UNIVERSITÀ
DEGLI STUDI
DI PADOVA

UNIVERSITÁ DEGLI STUDI DI PADOVA

SCUOLA DI DOTTORATO DI RICERCA
IN INGEGNERIA INDUSTRIALE
INDIRIZZO INGEGNERIA DELL'ENERGIA
CICLO XXVIII

Analysis and design procedures of permanent magnet machines for hybrid electric vehicles and rail-traction applications

DIRETTORE DELLA SCUOLA
Ch.mo Prof. Paolo Colombo

COORDINATORE D'INDIRIZZO
Ch.ma Prof.ssa Luisa Rossetto

SUPERVISORE
Ch.mo Prof. Nicola Bianchi

DOTTORANDO
Enrico Carraro

ANNO
2017

Analysis and design procedures of permanent magnet machines for hybrid electric vehicles and rail-traction applications

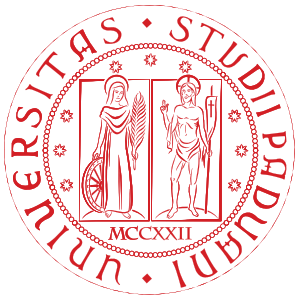

Enrico Carraro

Department of Industrial Engineering

University of Padova

This dissertation is submitted in partial fulfillment of the requirements for the degree of

Doctor of Philosophy in Industrial Engineering

2017

I would like to dedicate this thesis to Silvia.

"The brick walls are there for a reason. The brick walls are not there to keep us out. The brick walls are there to give us a chance to show how badly we want something."

Dr. Randolph Frederick "Randy" Pausch , PhD

Declaration

I hereby declare that except where specific reference is made to the work of others, the contents of this dissertation are original and have not been submitted in whole or in part for consideration for any other degree or qualification in this, or any other University. This dissertation is the result of my own work.

Enrico Carraro
2017

Acknowledgements

I would like to acknowledge Brose Fahrzeugteile GmbH & Co. KG, Würzburg, Germany, for supporting this project.

Abstract

English

The interest for Permanent Magnet (PM) synchronous machines has increased in the recent years. This is mainly due to important developments in the field of the electrical machine design, control systems and PM technology. These factors enable the possibility of designing electrical machines with a high torque density, power density, efficiency, low cost with wide degrees of freedom. Such requirements are highly sought in the automotive field, especially following the increasingly stringent energy efficiency and air pollution emissions policies. These conditions are pushing forward the transition from the conventional internal combustion engine mobility systems to the hybrid electric and full electric vehicles for the mass market production.

Moreover, further requirements, especially in high demanding traction and auxiliary machines, such as Electric Power Steering (EPS) motors, are nowadays getting more and more important. Flux weakening performance, torque quality (cogging torque and torque ripple), demagnetization, acoustic performance and robustness of the designs has to be taken into account, together with stringent dimensional, electrical and thermal constraints typical for compact integrated automotive electrical drives.

Due to recent sky-rocketing price, instability, critical availability of Rare Earth (RE) metals and the related environmental issue for their sourcing, Heavy (HR) RE free, RE-free and even PM free machines are hunted for in the automotive market. The novel PM motor topologies meet such a "market pull".

The main research subject of this PhD is the development of novel analysis and design procedures of PM synchronous machines for automotive applications. The latter range from low torque / low power auxiliary systems, i.e. EPS machines, to high torque / high power applications, such as traction machines. It provides a comprehensive evaluation of various synchronous machine topologies. Particular attention is devoted to the study of HRE-free solutions and the development of Finite Element Analysis (FEA) and analytical procedures for the optimization of the motor designs. As mentioned above These methodologies take into account several electromechanical constraints and various performance targets.

As regards the traction machines, the investigation is focused to the permanent magnet assisted reluctance (PMASR) topology. The interest around the PMASR motors has grown in the last years especially as consequence of the price crisis of rare earth magnets. In fact these machines represent a potential low cost replacement of conventional PM machines due to several technical advantages, such as wide speed range, competitive torque density and efficiency, high overload capability and robust structure. On the other hand, the most important drawback is represented by the high torque ripple.
In the area of the electric power steering motors, several topologies, both with isotropic and anisotropic rotor structures and equipped with fractional slot concentrated windings, are evaluated. Some novel motor designs, which employ the reluctance and flux concentration principle, are introduced, optimized by means of FEA procedures and experimentally validated in detail, including the acoustic and PM performance. Further considerations are derived on the robustness of the solutions against the manufacturing imperfections. Comparing to the isotropic topologies, these innovative motor configurations show higher torque density, extended speed range, optimal torque quality and acoustic performance, ensuring lower active cost and structural simplicity. Therefore, they represent attractive candidates for high performance automotive applications.

Italiano

Negli ultimi anni l'interesse nel settore delle macchine sincrone a magneti permanenti ha riscontrato una notevole crescita. Questo e' stato determinato principalmente da importanti sviluppi nel campo della progettazione delle macchine elettriche, nei sistemi di controllo e nelle tecnologie dei magneti permanenti. Questi fattori hanno reso possibile la progettazione di macchine elettriche con elevata densita' di coppia, densita' di potenza, rendimento, basso costo unitamente ad ampi gradi di liberta' nella geometria e struttura della macchina. Tali requisiti sono fortemente ricercati nel campo automotive, soprattutto a seguito dell'introduzione di sempre piu' stringenti normative sull'efficienza energetica e sulle emissioni atmosferiche inquinanti. Questi aspetti hanno accelerato la transizione da sistemi di mobilita' tradizionali con motori a combustione interna a veicoli ibridi-elettrici e puramente elettrici, nella produzione industriale di massa.
Inoltre, ulteriori requisiti, specialmente in macchine da trazione ed ausiliarie ad alte prestazioni, quali ad es. motori per servosterzo elettrico, stanno attualmente diventando sempre piu' importanti. Prestazioni in deflussaggio, qualita' della coppia (coppia di impuntamento ed oscillazione della coppia), smagnetizzazione, prestazioni acustiche e robustezza delle configurazioni devono essere tenute in conto, insieme a stringenti vincoli dimensionali, elettrici e termici tipici di azionamenti elettrici compatti ed integrati.
A causa dell'incremento significativo ed instabilita' dei prezzi delle terre rare, della criticita' dei loro approvvigionamenti ed i relativi impatti ambientali, soluzioni prive di terre rare pesanti, senza terre rare od addirittura senza magneti permanenti, sono fortemente ricercate nel settore automotive.

La principale tematica di ricerca di questo dottorato riguarda lo sviluppo di innovative procedure di analisi e sintesi di macchine sincrone a magneti permanenti per applicazioni automotive. Queste ultime spaziano da sistemi ausiliari a bassa coppia / bassa potenza, nella fattispecie motori per servosterzo elettrico, fino a applicazioni at alta coppia / alta potenza, quali ad es. motori da trazione. Questo lavoro fornisce una valutazione complessiva di differenti tipologie di macchine. Particolare attenzione e' dedicata allo studio di soluzioni con magneti permanenti privi di terre rare pesanti ed allo sviluppo di procedure di ottimizzazione ad elementi finiti ed analitiche della geometria del motore. Come menzionato precedentemente, tali metodologie tengono in considerazione numerosi vincoli elettromeccanici e differenti obiettivi.
Per quanto riguarda le macchine da trazione, la ricerca si e' focalizzata sulla topologia di motori a riluttanza assistiti da magneti permanenti. L'interesse attorno a tali macchine e' cresciuto negli ultimi anni soprattutto a seguito della crisi dei prezzi dei magneti permanenti

a terre rare. Infatti, tali macchine rappresentano una soluzione alternativa a basso costo rispetto a motori a magneti permanenti tradizionali a causa di importanti vantaggi tecnici quali ad es. un ampio regime di velocita', competitivi valori di densita' di coppia ed efficienza, elevata capacita' di sovraccarico ed una robustezza della struttura. D'altra parte, uno dei principali svantaggi e' rappresentato dall'elevata oscillazione della coppia.
Nel campo dei motori per servosterzo elettrico, differenti topologie, sia dotate di rotore isotropo che anisotropo ed equipaggiate con avvolgimenti concentrati, sono state valutate. Alcune nuove configurazioni, che sfruttano il principio della riluttanza e della concentrazione di flusso, sono introdotte, ottimizzate per mezzo di procedure ad elementi finiti ed infine validate per mezzo di misure sperimentali, includendo valutazioni delle prestazioni acustiche e quelle dei magneti permanenti. Ulteriori considerazioni sono tratte per quanto concerne la robustezza delle soluzioni nei confronti delle imperfezioni costruttive. Rispetto alle macchine isotrope, tali configurazioni sviluppano una densita' di coppia piu' alta, esibiscono un piu' ampio intervallo di velocita', maggiore rendimento raggiungendo un qualita' della coppia e prestazioni acustiche competitive ad un costo inferiore e con una buona semplicita' costruttiva. Esse si dimostrano, pertanto, dei candidati ottimali per applicazioni automotive ad alte prestazioni.

Contents

Preface

The subject matter covered in the thesis is organized into five thematic parts, each including a certain number of chapters. Hopefully the work presented in this thesis will further contribute to extend the knowledge on this subject.

Part I is a an introductory session summarizing the background of this work and the electromechanical model of a synchronous machines.
Chapter 1 describes the impact of the transportation on the world energy demand and its environmental sustainability highlighting the electric mobility systems, at the current state, as the only viable option. An overview the electrical machine typologies, especially in regards to the traction and EPS systems is reported. The chapter ends with an overview on the current PM technology, highlighting conventional, novel compounds and their properties.
Chapter 2 deals with the electromechanical model of a synchronous machines. The influence of the motor parameters is studied and an effective parameter selection procedure, which takes into account various electrical and electromechanical constraints is developed and applied for EPS application case study.

Part II deals wit the design, analysis and optimization of traction machines.
Chapter 3 provides a design methodology of a fractional slot concentrated winding interior permanent magnet synchronous motor according to the high demanding FreedoomCAR/US Drive specifications. A conventional and shaped rotor design are compared and the advantages of the latter configuration for achieving the torque quality and efficiency targets are highlighted.
Chapter 4 summarizes the design criteria and the electrical requirements of ferrite permanent magnet assisted synchronous reluctance machines for traction application. The electromechanical performance have been evaluated and compared and a overview of the power electronic supply system in is presented.
Chapter 5 is an extension of the previous chapter and it provides a comparative assessment

of the electromechanical performance of synchronous motors for a light electric vehicle, considering isotropic and anisotropic rotor designs, evaluating the efficiency in the whole operating area.
Chapter 6 investigates and compare in detail the experimental and simulated performance of a ferrite permanent magnet assisted synchronous reluctance motor, considering critical operating conditions, such as short circuit and demagnetization operation. The replacement of the ferrite with a novel hot-pressed Dy-free magnet is discussed and various measurements for the torque ripple reduction are studied.
Chapter 7 reports the design and optimization of a outer rotor interior permanent magnet generator. An optimization strategy aimed at maximizing the output power in a wide constant power speed range and minimizing the PM volume is presented.
Chapter 8 introduces the design and novel global optimization methodology of a ferrite permanent magnet assisted synchronous reluctance motor according to a driving cycle. A procedure is proposed to evaluate the most effective design areas by means of a series of representative points, which have been considered for the global optimization.
Chapter 9 is an extension of the previous chapter. In this case the robustness of some motor performances in two different representative operating point, namely the torque ripple and the losses, is considered in the optimization strategy.

Part III deals wit the design, analysis and optimization of EPS machines.
Chapter 10 investigate and compares different motor topologies for a EPS applications, taking into account with several constraints in terms of overall dimensions, torque quality, flux weakening, VA-rating, efficiency and demagnetization. Some novel motor designs are developed. A multiobjective optimization procedure is developed and for the definition of the final candidates for the prototyping stage.
Chapter 11 deals with the design criteria of a spoke type, fractional slot concentrated winding, interior permanent magnet motor, especially as regards the minimization of the magnet volume, maximization of the airgap flux density and optimization of the split ratio. An analytical procedure is presented and validated by means of FEA.
Chapter 12 investigates the influence of the slot/pole combination on the performance of a fractional slot concentrated winding spoke type EPS motors. Two different low cost heavy rare earths free PM typologies, ferrite and hot-pressed NdFeB, are considered. Design and optimization procedures, based upon FEA, are presented.

Part IV deals with the analysis of the acoustic performance of synchronous machines.

Chapter 13 deals with the influence of the slot/pole combination on the acoustic performance. Finally, an evaluation of the of the acoustic performance the final candidates reported in Chapter 10 is reported.

Part V deals with the measurement methodologies and influence of the manufacturing imperfections.
Chapter 14 summarizes a detailed measurement campaign on the PM properties and the electromechanical and acoustic performance of the EPS prototypes. The FEA model is validated. This chapter highlights the impact of the manufacturing tolerance on the torque quality performance and further considerations are reported.

Publications and scientific contributions

- E. Carraro, N. Bianchi, "Design and Comparison of Interior Permanent Magnet Synchronous Motors with Non-Uniform Airgap and Conventional Rotor for Electric Vehicle Applications", IET Electric Power Applications, vol. 8, no. 6, pp. 240-249, Jul. 2014.
- E. Carraro, M. Degano, N. Bianchi, "Permanent Magnet Volume Minimization in Permanent Magnet Assisted Synchronous Reluctance motors", IEEE International Conference and Exhibition on Ecological Vehicles and Renewable Energies (EVER), pp. 1-4, 27-30 Mar. 2013, Montecarlo, Monaco.
- E. Carraro, M. Degano, M. Mattia, N. Bianchi, "Formula SAE Competition: Electrical motor design", IEEE International Electric Machines & Drives Conference (IEMDC), pp. 1142-1148, 12-15 May 2013, Chicago, IL, USA.
- E. Carraro, M. Morandin, N. Bianchi, "Optimization of a Traction PMASR Motor According to a Given Driving Cycle", IEEE Transportation Electrification Conference and Expo (ITEC), pp.1-6, 15-18 Jun. 2014, Dearborn, MI, USA (extended and republished in IEEE Transaction of Industry Applications).
- E. Fornasiero, M. Morandin, E. Carraro, N. Bianchi, S. Bolognani, "Outer rotor IPM generator with a Wide Constant Power Region for Automotive Applications", IEEE Transportation Electrification Conference and Expo (ITEC), pp.1-6, 15-18 Jun. 2014, Dearborn, MI, USA, 15-18 Jun 2014.
- M. Degano, E. Carraro, N. Bianchi, "Robust Optimization of a Traction PMASR Motor According to Given Driving Cycles", IEEE International Conference on Electrical Machines (ICEM), 2-5 Sep. 2014, Berlin, Germany (extended and republished in IEEE Transaction of Industry Applications).
- E. Carraro, N. Bianchi, S. Zhang, M. Koch, "Permanent Magnet Volume Minimization of

Spoke Type Fractional Slot Synchronous Motors", IEEE Energy Conversion Congress and Exposition (ECCE), pp. 4180-4187, 14-18 Sep. 2014, Pittsburgh, PA, USA.

- E. Carraro, M. Degano, M. Morandin, N. Bianchi, "PM synchronous machine comparison for light electric vehicles", IEEE International Electric Vehicle Conference (IEVC), pp. 1-8, 17-19 Dec. 2014, Florence, Italy.

- N. Bianchi, E. Fornasiero, E. Carraro, S. Bolognani, M. Castiello, "Electric vehicle traction based on a PM assisted synchronous reluctance motor", IEEE International Electric Vehicle Conference (IEVC), pp. 1-6, 17-19 Dec. 2014, Florence, Italy.

- S. Zhang, E. Carraro, N. Bianchi, K. Wang, K. Vervaeke, "Industrial-scale Motor Cogging Torque Control for High-volume Motor Manufacturing", IEEE International Electric Machines & Drives Conference (IEMDC), 10-13 May 2015, Coeur d'Alene, ID, USA.

- E. Carraro, N. Bianchi, S. Zhang, M. Koch, Performance Comparison of Fractional Slot Concentrated Winding Spoke Type Synchronous Motors with Different Slot-Pole Combinations", IEEE Energy Conversion Congress and Exposition (ECCE), 20-24 Sep. 2015, Montreal, Canada.

Part I

Electrical machines for automotive applications: overview, theory and design

Chapter 1

Introduction

1.1 Role of the transportation on the energy supplies and environmental sustainability

Following the increase of the energy demand of the recent years, the problem of the depletion and diversification of energy supplies, energy efficiencies and pollution is becoming more and more important and critical. As reported in Fig. 1.1(a), it is expected that the world demand will continue to be dominated by asian economies, such as China and India which account up to half of the total growth of energy demand at 2040, while the traditional first 32 developed economies (Organisation for Economic Co-operation and Development, OECD) will remain in a substantial saturation.

As shown in 1.1(b), this is well highlighted considering the trend of the transportation energy demand in the OECD32 countries that predictably will contract by 10% from 2010 to 2040 while in the other countries will double or triple. Fig. 1.2 shows the impact of the transportation on the energy consumption and the distribution among the different vehicles platforms. As 2012, it is the second representative contribution, following the industrial sector, accounting of about 27% of the world energy consumption. Analyzing the distribution of the transport energy consumption, it is worth noticing that road transport, represented by Light Duty/Heavy Duty Vehicles (LDVs/HDVs), is the dominant factor with about 70% of the total energy consumption.

Since the birth of mechanical-powered vehicles, the propulsion energy has been mainly relied by the combustion of hydrocarbon (HC) fuels. Ideally, this chemical process which

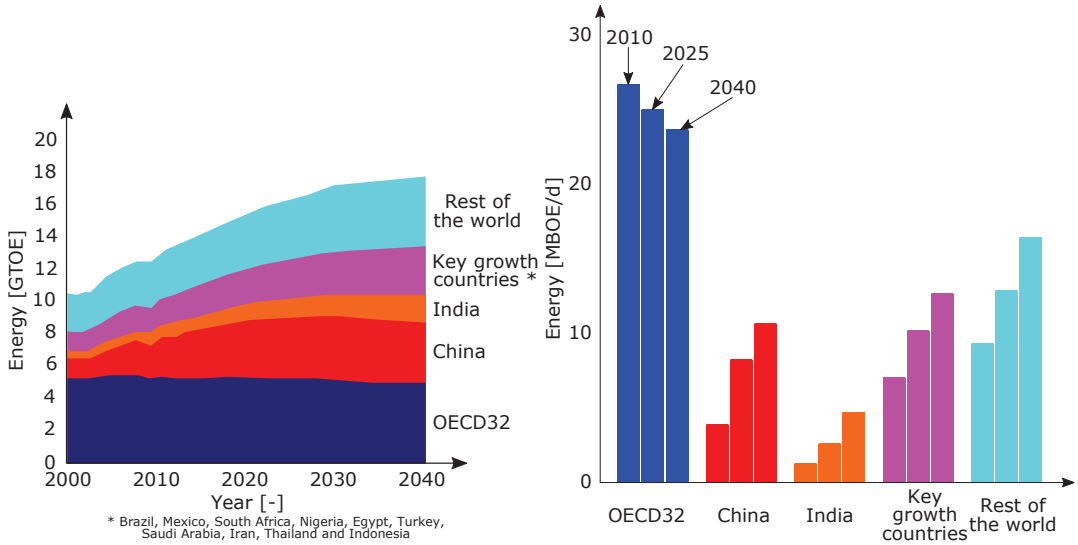

(a) Energy demand forecast [56]. (b) Transportation fuel demand forecast [56].

Fig. 1.1: Transportation fuel demand forecast.

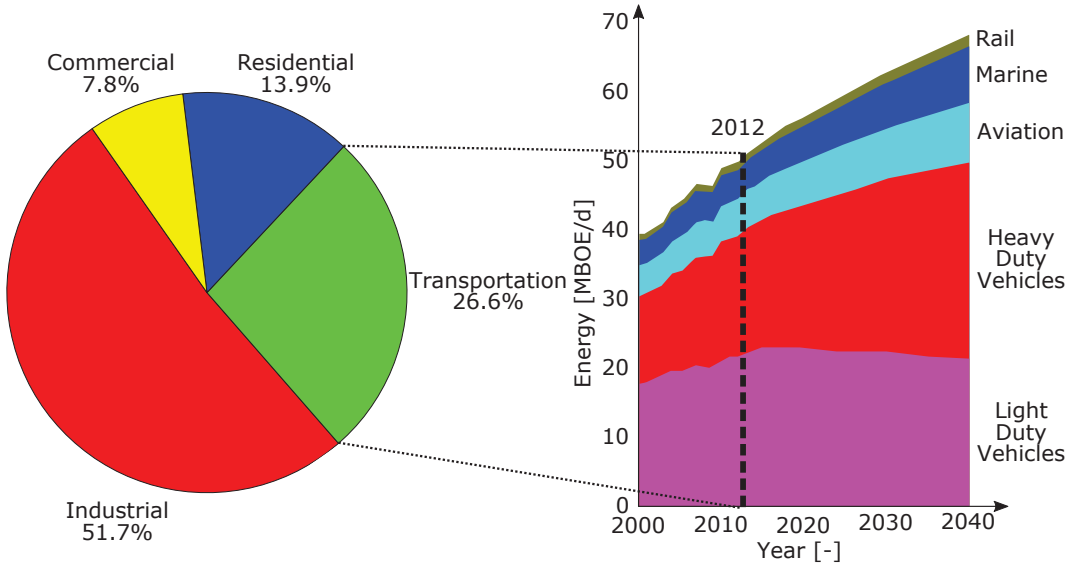

Fig. 1.2: Impact of the transportation to the energy consumption [56, 80]

involves the reaction of the HC fuel with air, produce carbon dioxide (CO_2) and water. The first compound is, in essence, not dangerous for the enviroment and human life under a given concentration because it is necessary to green plant for their photosynthesis. Actually, the combustion of HC produces several byproducts such as nitrogen oxides (NO_x), carbon monoxide (CO), sulfur dioxide (SO_x), methane (CH_4), nitrous oxide (N_2O), chlorofluorocarbons (CFC), perfluorocarbons (PFC), silicon tetrafloride (SF_6), unburned HCs (particulate,

benzene) and heavy metals (lead, zinc, chrome, copper, cadmium) [49, 143]. All these compounds are toxic to the human life. Most of these compounds represent the Green House gases (GHGs) which are responsible of the global warming phenomenon. Nowadays there is an ongoing debate in the scientific community regarding the impact of these anthropogenic sources to the climate change. However, as shown in Fig. 1.3(a) transportation account for about 14% of the total GHGs emission. According to different temperature rise scenario, reported in Fig. 1.3(b), the transport field is expected to contribute with about 21% CO_2 reduction in order to limit the increase of the average temperature up to $+2°C$ by 2050. In order to meet that target 75% of the vehicle would need to be electrical-powered [81].

Another fundamental issue is the diversification of the energy resource, which are for the transport field, mainly based upon the oil supply. As 2020, the transportation is the primary user of oil, accounting for about 65% and 48% of the total oil consumption for the industrialized and developing country, respectively [49]. Following the progressive depletion of the oil reserves together with the reduced growth of the discoveries of the new reserves and consequent increase of the cost of extractions, it is expected that, according to world trend of the oil consumption, the oil resources will be e exhausted by about the 2067. Conversely, EVs using electric energy as primary source, allow for a greater diversification of sources of supply. The transition from the conventional ICE to pure EV goes through different degree of electrification $DOE = 0-1$, defined as the ratio between the electric traction motor power and the total motor power (ICE and electric) [48]. According to this ratio an EV can be classified as follows [98]:

- Hybrid EV (HEV): $DOE < 1$, where the propulsion is provided by the combined contribution of a conventional ICE and an electric motor.
- Plug-In Hybrid (PHEV): $DOE < 1$, it is an HEV employing a rechargeable batteries or another energy storage system which can be connected to an external electric power source, which makes possible to restore the full charge during stops.
- Battery EV (BEV): $DOE = 1$, it employs a rechargeable battery as power source is provided.
- Fuel Cell EV (FCEV): $DOE = 1$, it employs a FC battery as primary energy source, generating electric energy by means of the reaction between hydrogen and oxygen.

1.1.1 Efficiency of the propulsion systems

Comparing to electric motor, conventional Internal Combustion Engine (ICE) vehicle are inherently not efficient. In the last years the research in improvement of the Although in

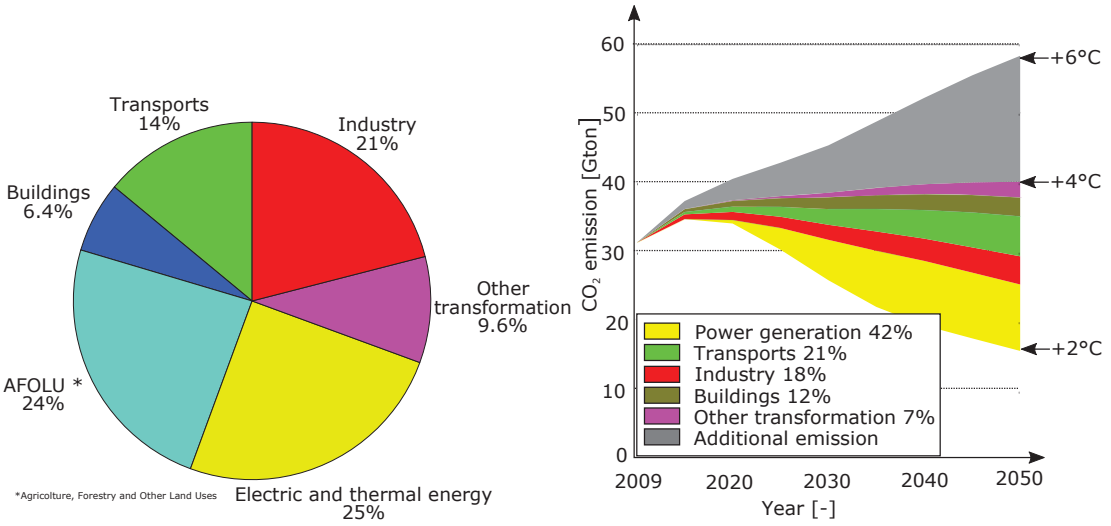

(a) Global GHGs emission by economic sector (2010) [77].

(b) Contribution of different economic sectors in CO_2 reduction [81].

Fig. 1.3: Role of the transport in the GHGs emission.

recent years there has been an improvement of ICE engines, both in diesel and in gasoline engine, greatly improved the motor efficiency (maximum theoretical value in the order of 35% for gasoline and 50% for diesel engine), the actual efficiency is, lower, in average, around 25%. On the other hand, electric motors can be designed in order to provide a very high efficiency up to 95%. As reported in 8.2, considering the oil as the same primary energy source of both a conventional ICE vehicle (ICEV) and BEV, the average tank-to-wheel efficiency of a pure EV is almost double of the corresponding ICE value, about 34% in comparison of 18% [114].

Table 1.1: Comparison of the efficiency between traction technologies. Note: for ICEV, tank-to-wheel efficiency comes from a weighted average between gasoline and diesel vehicles.

ICEV		**BEV**	
Oil refinery efficiency	$\sim 90\%$	Thermoelectric generation efficiency	$\sim 46\%$
Electric transmission efficiency	$\sim 93\%$	Oil transmission efficiency	$\sim 98\%$
Tank-to-wheel efficiency	$\sim 22\%$	Tank-to-wheel efficiency	$\sim 80\%$
Well-to-wheel efficiency	$\sim 18\%$	Well-to-wheel efficiency	$\sim 34\%$

In Fig. 1.4 the trend and forecast for Light Duty Vehicle (LDV) sales are reported. It is worth noticing the remarkable increase of the EVs which are expected, for the 2050, to cover up to 80% of the total sales of LDV. Therefore, this scenario is expected to have a significant impact in terms of reduction of oil consumption. In Fig. 1.4(b) is reported the trend of the

different design strategies aimed at increasing the fuel economy of a vehicle. Powertrain, hybridization and accessories improvement represents the most important research area and in these fields electric motors and related technologies have a dominant role in order to achieve these target.

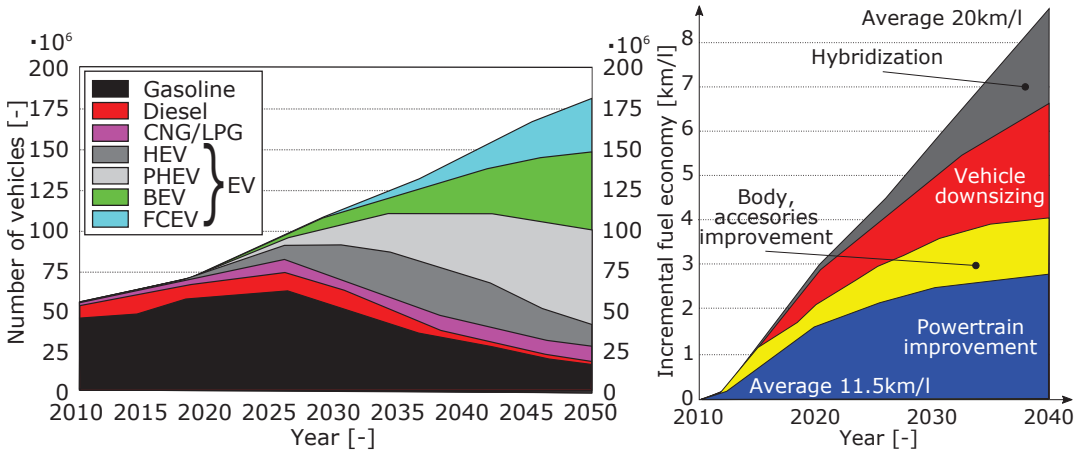

(a) LDV sales per technology type.

(b) Improvement of the fuel economy.

Fig. 1.4: LDV sales and vehicle efficiency improvement forecast [56].

1.2 Electric motors for automotive

Electric motors are the key devices for a "more electric" vehicle technologies. Fig. 1.8 shows the typical architecture of the electric system of a vehicle, highlighting the different motors, which can be summarized in two main groups:

- Traction motors.
- Auxiliary motors, which powered or assist the auxiliary mechanical systems of a vehicle. They are normally low torque / low power motors (in the order of kilowatt max), fed by the low DC bus system of the vehicle ($12V$, 36, $48V$). These machine are summarized as follows:
  - Electric Power Steering (EPS) which helps the steering action.
  - Heating, Ventilating and Air Conditioning (HVAC) blower.
  - Dual Clutch Transmission (DCT), for automatic transmission.
  - Electric Braking System (EBS) which assist to the braking system and which can be integrated with different electronic systems, such as Anti-lock Braking System

(ABS), Electronic Stability Control (ESC), Adaptive Cruise Control (ACC) and Automatic Traction Control (ATC).
- Cooling Fan Module (CFM) for engine cooling.
- Vacuum Pump used for powering pneumatic accessories, such as assisting the braking action.
- Seat adjusters.
- Window regulator.

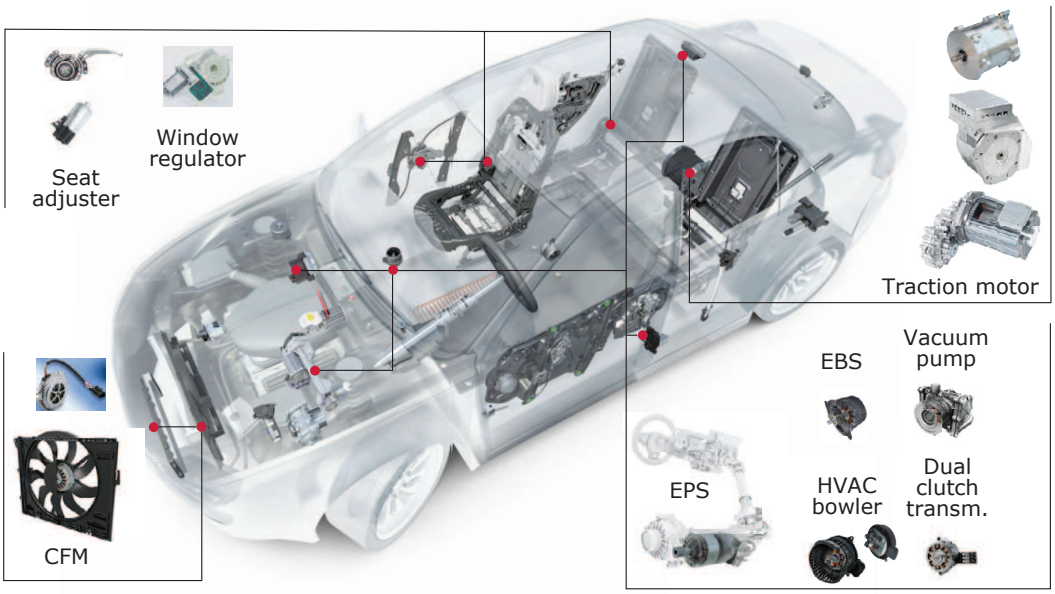

Fig. 1.5: Electric drives and motors in a vehicle (by kind permission of Brose).

In general, motors for automotive applications have to fullfill specific requirements which can bee summarized as follows [189]:

- High torque and power density, crucial in order to save weight and displacement thus improving fuel consumption.
- Wide speed range, with Flux Weakening (FW) with an expected Constant Power Speed Range (CPSR) typically in the order of $3-4$ times the base speed. This characteristic is researched especially in high power applications, such as EPS and especially in traction motor. For the latter machine, a higher speed range represents an attractive and researched feature [52, 53, 140, 141, 154, 162, 163, 174, 175].
- High efficiency over a wide and torque range, in order to increase the fuel consumption.

- Low torque ripple, cogging torque, noise and vibration for a comfortable and silent operation of the system.
- Overload operation. As highlighted before, the large majority of auxiliary motors does not work in continuous service, rather an intermittent periodic operation. Conversely, an attractive feature of traction motors is the capability of exhibiting an intermittent overload operation in the whole speed range for a short duration of time an acceleration is required at any speed [136].
- High robustness and reliability due the harsh condition of the vehicle environment.
- Low cost.

Electric motors can be divided in two main topologies, represented by the commutator (or brushed DC) and commutatorless (or brushless) machines, as shown in Fig. 1.6. Historically

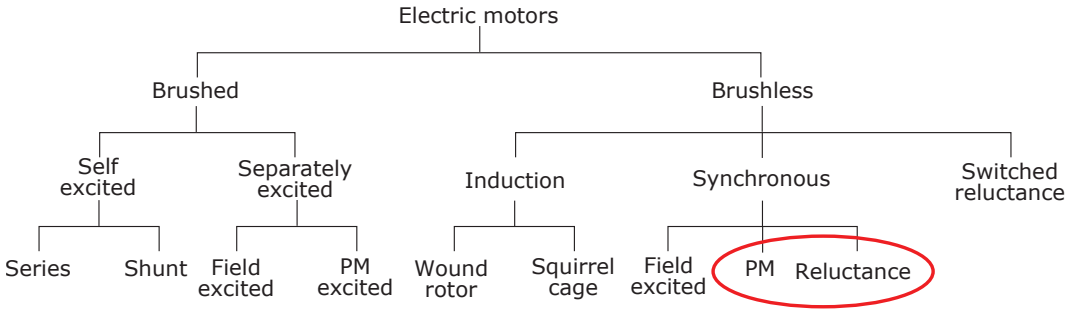

Fig. 1.6: Electric motor overview.

for many years auxiliary and traction motors were based completely on DC machines due the simplicity and maturity of the technology and the simple and cheap control system. On the other hand, these machines exhibit some important drawbacks due to the mechanical commutation: a limited lifetime (600h), high vibration and noise, Electro-Magnetic Compatibility (EMC) issues [130] and lower power density [49]. Starting from the last decades of the XX century, the development of the power electronic technology (controllable and semicontrollable electronic switches, such as thyristors, BJT, MOSFET, GTO, IGBT and MCT), miniaturization and digitalization of the control system (microcontrollers, microprocessors) and the evolution of the manufacturing and material technologies have yield to a strong evolution of the commutatorless machines. Thanks to the developement of the vector control of AC machines (K. Hasse and F. Blaschke, 1968 – 1970), an drastic improvement of the flexibility and performance of the commutatorless machines has been possibile. [168] Induction motors (IM) represent one of the most mature motor designs wich shows attractive features, such as low cost, robustness, maintenance-free operation and consolidated manufacturing technology [33, 49, 135]. On the other hand, they exibith low torque and

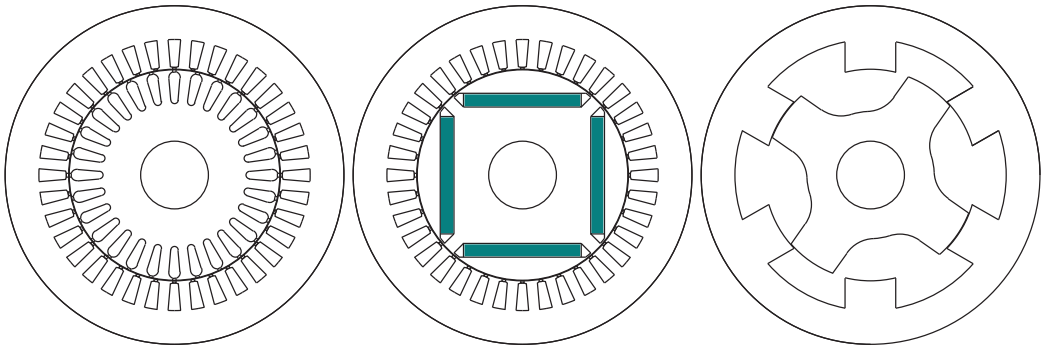

(a) IM. (b) PMSM. (c) SRM.

Fig. 1.7: Commutatorless motor typologies.

power density and low efficiency. In automotive they show an very limited use in traction application and although the abovementioned performance drawbacks, this is the typology selected for the first mass-produced EV, the GM EV1 (1996) and in the in the well known, high performance Tesla cars.

Switching Reluctance Motors (SRM) are recognized to have great potential in automotive applications, thanks to several features which are summarized as follows: simple, robust magnet-free structure which is desiderable in high speed or high temperature operation, low cost, excellent torque vs. speed characteristic and intrisic fault tolerance beahvior. On the other hand, they normally exbith relatively high torque ripple, noise and vibration and non standard power electronic system due to the unipolar control strategy [35, 49, 189].

Synchronous machines represent nowdays one of the attractive and powerful tecnologies. Representing historically the bulk in power generation, especially in traditional DC excited configuration, it has undergone a major development following the advancement of the PM techonologies, namely the development of high energy density magnets (see Sec. 1.3.4). PM synchronous machines, called also brushless (BL) machines, have been invented in the 1920s and become commercially available in 1979 (H. R. Johnson, patent $US4151431A$). They are classified according to the wafeworm of the back Electro Motive Force (EMF) in two main categories. The first is characterized by a sinusoidal wavweform of the back-EMF and it is normally fed with sinusoidal current normally generated by means of a Pulse Width Modulation (PWM) strategy, and therefore called BL Alternatig Current (BLAC) motors. The second exibiths a trapezoidal back-EMF and they are usually fed by a rectangular AC current: comparing to the BLAC motors they usually produce a higher torque and power density, on the other hand the torque quality performance are worse [35, 49], therefore their use is limited in specific applications.

The BLAC machines typology (by now called simply PM synchronous machines) combines the high torque, power density and efficiency with several degree of freedom in the design [12] ensuring potentially high torque quality and acoustic performance. In the last decade they have established themselves in high performance application and therefore with a great potential in automotive field. In this field, PM synchronous motors has been commercially used for the first time in the Toyota Prius cars (1997). Since then, they have spread in both auxiliary and traction applications with several example. In high power applications, typically traction motors, has been extensively commercially produced in different vehicle classes, which are briefly summarized as follows:

- Subcompact car, such as Mitsubishi i-MiEV, BMW i3.
- Compact car, such as Toyota Prius anddf Camry, Honda Civic Hybrid, Nissan Leaf, Chevrolet Volt, Volkswagen e-Golf.
- Midsize
  full size car, such as Lexus LS600h, Mercedes-Benz B-Class Electric Drive.
- Sport Utility Vehicle (SUV), Lexus RX400h, Ford Escape Hybrid, BMW X5 xDrive40e and 225xe Active Tourer Plug-In Hybrid, Volvo XC90 Plug-In Hybrid, Audi Q5 Hybrid, Porsche Cayenne S E-Hybrid.
- Sport car, such as BMW i8.

Since the beginning of the 2000s, it has been used in many low power applications, starting from CFM, HVAC till the most recent EPS motors.

As shown in Fig. 1.8(a), the requested output power and operating times of automotive motors varies from tens of watts of wipers till tens of kilowatts for powertrain units. Moreover, the duty cycles, qualitatively measured by the operating time where the machine actually works continuosly at nominal condition, varies significantly, from few seconds for the ABS and EBS motors up to tens minutes for the HVAC blowers and traction motors. Nowadays, in a Compact (C) segment car, there are in average 120 small electric motors installed. As shown in Fig. 1.8(b), there are around 36kg of motors distributed in about 27kg of brush motors and 9kg of brushless motors. It is expected that, due to the highest demand of performance, the motor technology will be gradually shifted to the commutatorless typologies.

1.2.1 Electric Power Steering (EPS)

Introduction

In a vehicle a power steering system assist the driver steering operation, in order to lead the vechile on a desired trajectory without requiring excessive phisical effort. Moreover it

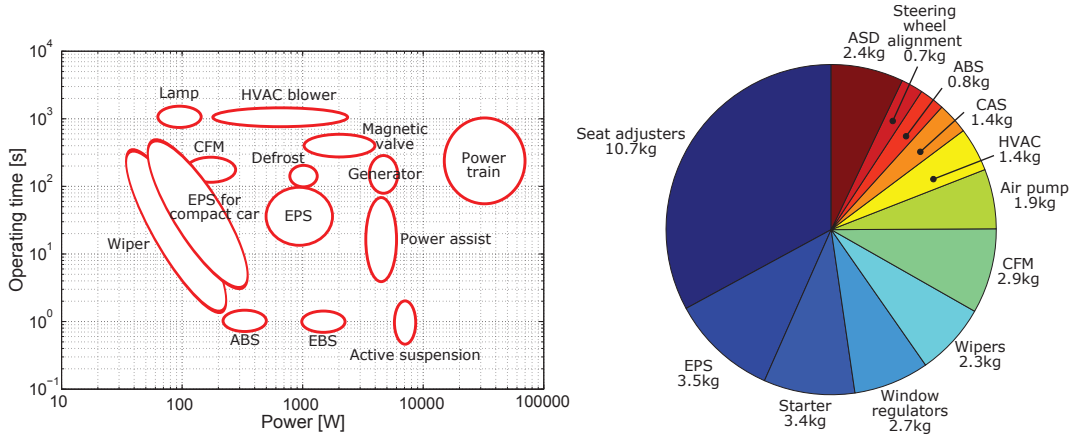

(a) Typical motor and actuator power classes and operating times of automotive motors [90].

(b) Mass distribution in a C-segment (compact) car. Note: ASD, Automatic Shut Down; CAS, Collision Avoidance System.

Fig. 1.8: Motor power classes and masses for an automobile.

has to provide to the driver a suitable level of feedback of the driving condition in order to minimize the error in which the vehcicle follows the abovementioned path. According to the power source, there are three main PS typology, reported in Fig. 1.9:

- Hydraulic Power Steering (HPS).
- Electro-Hydraulic Power Sterring (EHPS).
- Electric Power Steering (EPS).

[180]. Following some experimental designs at the beginning of the *XX* century, the HPS systems were commercially introduced after World War 2, following the increase of the demand of assisted steering capability of heavy duty military vehicles which boosted the research of new solutions. In 1950*s* the first HPS system was developed by Chrisler, GM in USA and Bishop in Australia [180]. in a HPS, as shown in Fig. 1.10(a), a pressurized fluid is provided by a gerotor or rotary vane pump driven by a engine's shaft. The hydraulic pressure is applied to a double-acting hydraulic cylinder connected to to the steering gear linked to the road wheels. A control valve is responsbile to manage the fluid flow in the two sides of the cylinder. According to the direction in which the steering wheel is rotated (clockwise or counterclockwise), more pressure is applied on more on one side or on the other side of the piston, allowing the steering action. When the steering wheel in the straight-ahead position the pressure on the both sides is equalized, thus the assist action is neutralized. The higher the torque applied by the driver to the steering wheel, the higher the pressure applied on the piston, thus more powerful the steering action. In the hydraulic system the delivered flow

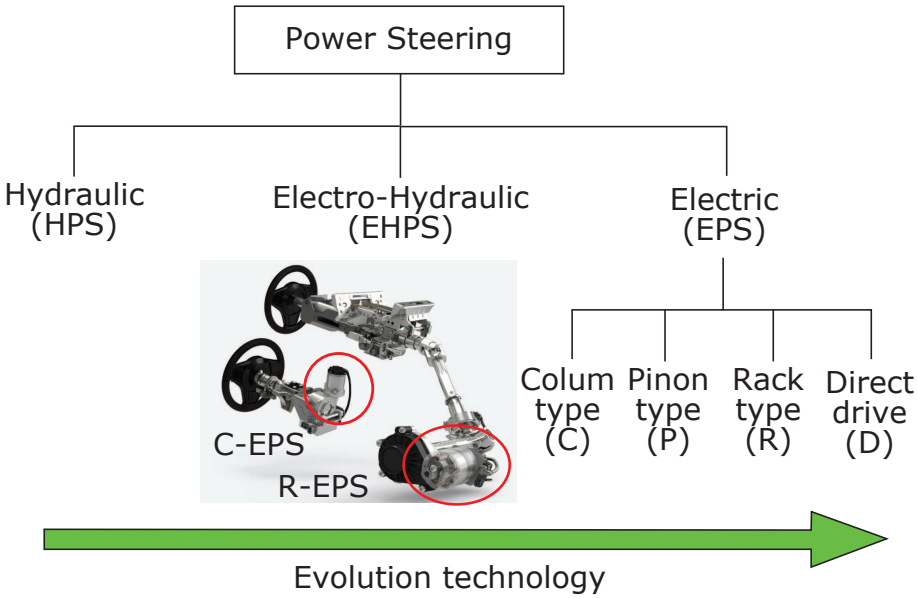

Fig. 1.9: Power steering systems.

rate is proportinal to the engine speed, therefore an HPS would become more effective as the speed increase. In order to avoid this behavior a flow-control valve is installed. In some modern designs, called variable-assist HPS (VAHPS), this valve is electronically controlled. The EHPS represents an hybrid configuration between the pure hydraulic and electric pow-

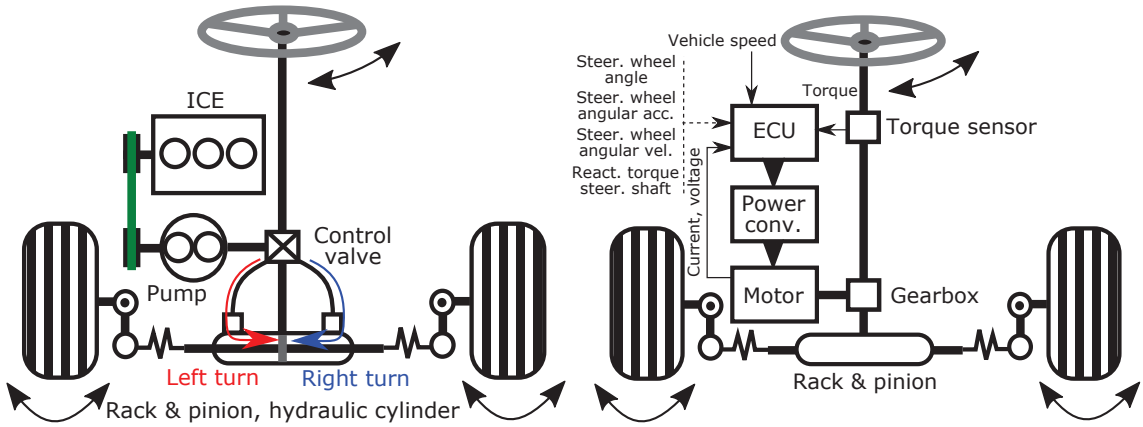

(a) HPS. (b) EPS.

Fig. 1.10: HPS and EPS architecture.

ered action. In this architecture, the hydraulic pump is driven by an electric motor insted of the engine while the other parts are retained. This designs was experimentally introduced by Ford in 1965 and started to become a consolidated techonologied for many car companies starting from the 1990*s*. Uncoupling the steering action with the working condition of the

engine, this system benefits from the flexibility of the electric motor, since it can provide a comfortable and safe operation reducing the motor rotation in non-steering action or when the vehicle runs at high speed, while increasing the motor rotation at low speed and when steering action is required.

EPS, also called Electric Power Assisted Steering (EPAS) or Motor-Driven Power Steering (MDPS) represents the last step in the evolution of PS system where the complete hydraulic architecture is replaced by an electromechanical system powered by an electric motor. The first EPS drive was introduced by Koyo in 1988. Starting from the 2000*s* (Fiat Punto, VW Lupo 3L, Honda) EPS has spread gradually in the market accounting, as 2010, for about 40% of the PS systems. Comparing to the HPS/EHPS designs, it is the most efficient in terms of energy saving and structure complexity. In fact one of the intrinsic drawback of HPS systems is represented by the parasitic losses due to the continuous operation of the hydraulic pump necessary to maintanin the oil in pressure, altough the steering assistance is practically required for only about $10-20\%$ of the time [116]. As reported in Fig. 1.11(a), almost 50% of the losses are represented by the over flow loss of the pump. Analysis show that modern HPS systems can drain from about 15% (for small cars) to 10% (larger vehicles) of the engine power [116], accounting for about of 3% of the total energy consumption in a car [180]. It is worth noticing that the maximum assistance power demand is required at low speed for cornering and parking, where the ICE efficiency is worse Fig. 1.11(b) reports the comparison of the RMS losses of a different PS technologies according to the japanese $10-15$ driving cycle. Comparing to a conventional HPS system, the EPS is able to reduce the power consumption of more than 90% [116]. This is expected to yield to a reduction of the fuel consumption of 5%, therefore the development of an efficient EPS techonlogy can only have a very positive effect in terms of reduction of the energy consumption of the private transport system [180]. Finally, the higher efficiency leads to a reduction of about 4.5% of the CO_2 emissions, representing, togheter with the start-stop technology, one the highest contribution in terms of automotive system [127]. Comparing to the EPS, a HPS motor is more complicated and require more maintanence (e.g. fluid leakage) and it is less flexible since it has to be phisically coupled with the engine and it is space consuming requiring sensible hydraulic lines. Finally EPS systems can be easily included in a electronic stabilit control sysyem aiding the driving operation in harsh condition.

Structure of an EPS system

Fig. 1.10(b) shows the typical layout of an EPS systems. Generally it consists of the following components:

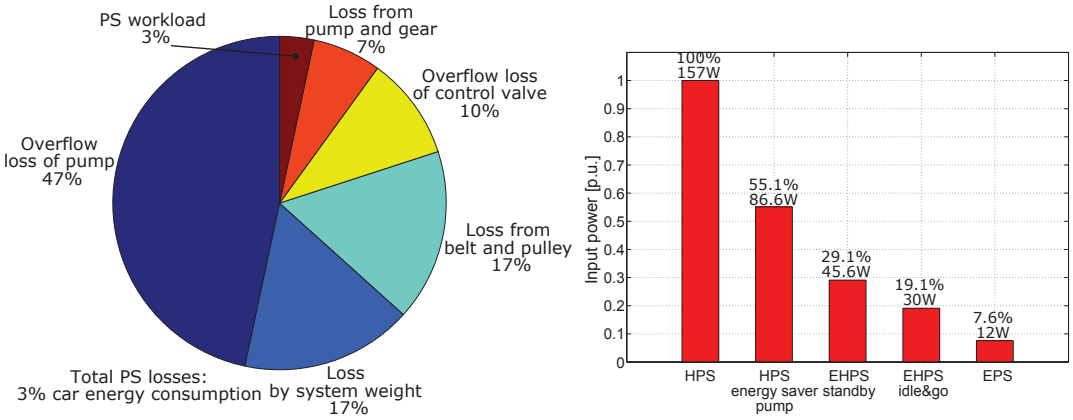

(a) Distribution of the losses in a HPS.

(b) Power demand comparison of PS systems over a japanese $10-15$ driving cycle.

Fig. 1.11: Energy consumption of PS systems. [116]

- Electric motor.
- Sensors.
- Electronic Control Unit (ECU) and power converter.
- Gear.
- Mechanical coupling to the steering wheels.

Thanks to the higher degree of flexibility, an ESP system can be managed according to several control strategies [150, 180].:

- **Base assist strategy**
  It is responsible of the fundamental function of an EPS, which is assisting the driver sterring in cornering. It requires a torque sensor which measures the effort produced by the driver to the steering wheel in order to adjust the value of the addtional torque produced by the electric motor. Normally, the relationship between the output of the sensor and the motor torque is linear. The heart of the torque sensor is the torsion bar which, under a torque load, produce an angular displacement $\Delta\theta$ (in the order of few degres). This is transduced in an electric signinal for to the control system
- **Returns control strategy**
  The "return control" feature represents the capability of a the EPS to improve return-to-center performance of the steering wheels, thus the vehcile dynamics. Normally, following a cornering, the energy stored in the mechanical system is able to produce a self alignment torque for steering wheel to the straight ahead postion. However, is some case, such as at low speed driving the return-to-center capability is inhibited due

to the friction of the road and steering system. This control logic requires an angular sensor for the measurement of the steering angle.

- **Damping control strategy**
  It is responsible to mitigate the oscillation of the steering systems. Proposed solutions require the measurement of the steering wheel angular velocity. The motor torque is controlled in order to oppose the alignment torque induced by the road. For most of the driving condition the "base assist" logic is almost able to manage this feature.
- **Inertia control strategy**
  If the steering wheel is quickly turned, a high counter-acting inertial torque is generated and it represent un uncomfortable feeling for the driver. This issue might not be effectively managed by "base assist" logic, therefor a interia control strategy, based on the measurement of the steering wheel angular acceleration as main input togethere with the vehicle speed and the steering wheel angle.
- **Impact control stategy**
  It is responsible of mitigating the oscillation induced on the steering wheel by the uneven conditions of the road surface. Solutions propose to estimate the reaction torque on the steering shaft [96] which requires the measurement of the steering wheel torque, motor current, steering wheel angular acceleration. Additional signal are the vehicle speed and and steering wheel angular velocity.

One of the most important parameter of a EPS system is the available steering force which is able to develop on the rack. Fig. 1.12(a) reports the typical steering rack force as a function of the gross mass of the vehicle. It is worth noticing that, comparing to an HPS system, the EPS is able to cover a wider operating range. The EPS systems are classified according to the postion of the motor in 4 main topologies reported as follows.

- **Column type EPS (C-EPS)**
  The first EPS commercially introduced in a car, it usually equips small size vehicle (A, B segment) with a rack force and output power up to $\sim 6kN$ and $\sim 500W$, respectively. This is a compact and easy to mount design because the motor, ECU and sensors (power assist unit) are attached to the steering column. It can be mounted to a fixed steering column, tilt-type steering column and other column type. It is inside the vehicle compartment, therefore as shown in Table 1.2, high torque quality and acoustic performance a requested, while the resistance against enviromental agents is not critical.
- **Pinion type EPS (P-EPS)**
  It normally equips medium size cars (C segment) with a rack force and output power

up to $\sim 8kN$ and $\sim 500W$, respectively. The power assist unit is attached to the steering gear's pinion shaft, outside the vehicle compartment, allowing to increase the performance without affecting the acoustic comfort. On the other hand the system has to be more carefully design as regards the enviromental and thermal condition, as reported in Table 1.2. It provide better handling chatacteristics.

- **Rack type EPS (R-EPS)**
  It usually equips large size cars (D, E, F segment, SUV and small trucks) developing a rack force and output power higher than $12kN$ and $600W$. The power assist unit can be placed freely on the rack, ensuring a reat flexibility in the architecture. This kind of motors normally requires a torque higher than $5Nm$ [128] with a FW performance up to 3.5 [18]. As regards the acoustic comfort and enviromental/thermal conditions, the same consideration are applied as for the P-EPS.
- **Direct drive EPS (D-EPS)**
  Direct drive design is the most recent desing in EPS systems. The steering rack is directly connected ot the power assist unit, without gearbox. The system is very compact and provides the lowest friction and inertia.

Table 1.2: Comparison of the requirements of different EPS type [128]

	Type		
Quantity	**Column**	**Pinion**	**Rack**
Output power	Low	Intermediate	High
Cogging torque	Intermediate	Intermediate	Intermediate
Torque ripple	Intermediate	Intermediate	High
NVH	High	Intermediate	Intermediate
Mechanical losses	Intermediate	Intermediate	High
Moment of inertia	Intermediate	Intermediate	Intermediate
Water resistance	Low	High	High
Thermal durability	Low	High	High

In Fig. 1.12(b) the typical motor technologies used for EPS applications as a function of the of the steering rack force and output power are reported. The brushed DC motor is still a common design for low power applications, for power lower than $500W$ while high power design are nowdays based upon PM synchronous motors. Finally EPS motor are

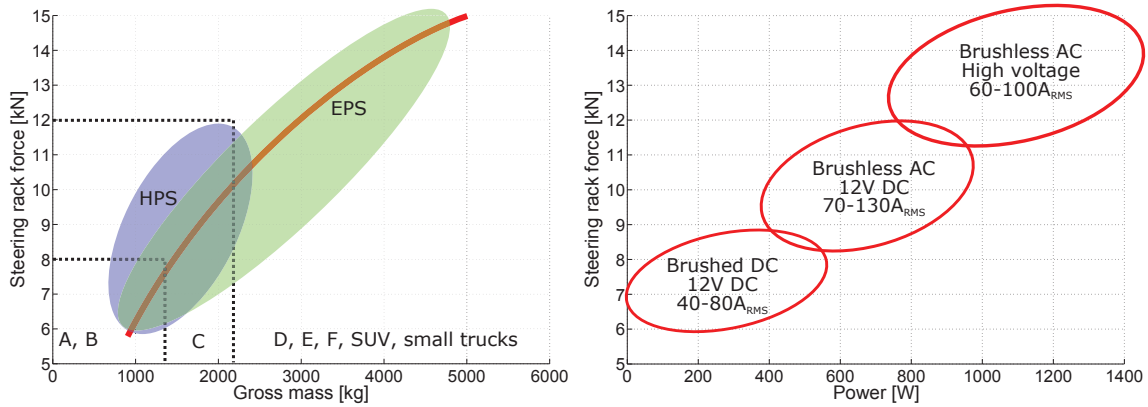

(a) Rack force requirments according to the vehicle size. [116]

(b) Typical motor typologies according to the rack force and power demand. [127]

Fig. 1.12: Steering rack force requirements.

1.3 PM technology

1.3.1 PM properties

PM materials, also called hard magnetic materials, respond to an externally applied magnetic field by developing an internal field, an induced field. An hysteresis loop describes the relationship between the external magnetic field and the flux density, as reported in Fig. 1.13(a). Two different loops can be defined, as follows,

- **Intrinsic characteristic**, represents the measure of the induced field, and it represents the actual magnet property of the magnet under test, and it describes the polarization J as a function of the magnetic field H.
- **Normal characteristic**, represents the measure of the contribution of the induced and applied field and it describes the flux density as a function o the magnetic field H.

As shown in detail in Fig. 1.13(b), PM material normally works in the 2^{nd} quadrant (reluctance in a closed magnetic circuit is negative). The representative quantity are defined:

- **Remanence flux density** B_r, represents the PM flux density forcing the magnetic field to 0.
- **Coercivity** H_{cB}, represents, on the normal curve, the magnetic field necessary to cancel the PM flux density.
- **Recoil permeability** μ_{rec}, represents the slope of the linear portion of the normal curve (recoil line).

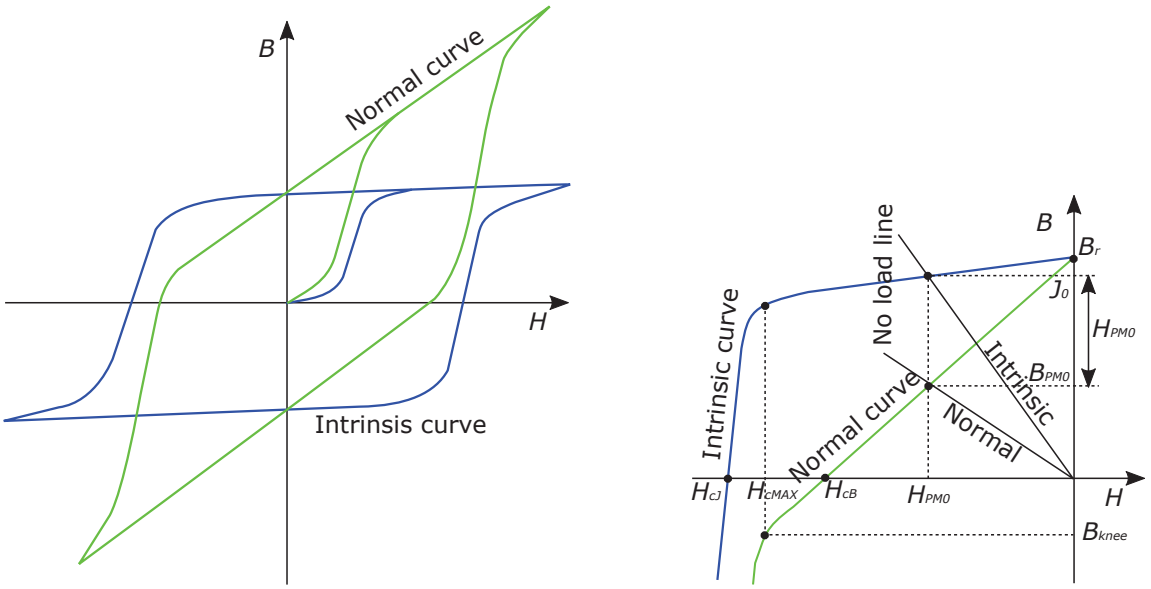

(a) PM hysteresis loop.

(b) 2^{nd} and 3^{rd} quadrant B-H curve.

Fig. 1.13: PM magnetization curves.

- **Intrinsic coercivity** H_{cJ}, represents, on the intrinsic curve, the magnetic field necessary to cancel the polarization. This parameter provides a quantitative indication of the resistance of the PM against the demagnetization.
- (H_cMAX, B_{knee}) is the limit of the reversible demagnetization. If the PM works below this point on the magnetization characteristic, the demagnetization is irreversible.
- **Maximum energy product** BH_{MAX}, represents the maximum storable magnetic energy in a PM, and is equivalent to the largest area of the rectangle which can be inscribed under the normal curve.
- B_r **reversible temperature coefficient** α_{B_r}, represents the ratio of variation of the remanence flux density per unit of temperature variation.
- H_{cJ} **reversible temperature coefficient** $\alpha_{H_{cJ}}$, represents the ratio of variation of the intrinsic coercivity per unit of temperature variation.
- **Permeance coefficient** PC, represents the ratio between the PM flux density and the PM flux density in the vacuum.
- **Temperature of Curie**, it is the temperature above which an irreversible demagnetization occurs and the material becomes paramagnetic.
- **Resistivity**, is related to the eddy current losses in the PMs, critical contribution of losses especially in high speed operation [181].

Between the two curve, the normal characteristic is the only one which can be actually measured, while the intrinsic characteristic is computed indirectly. The polarization J, equal to $4 \cdot \pi M$ (where M is the magnetization), is,

$$J = H_{PM} + B_{PM} = H_{PM} \cdot (1 + PC) \tag{1.1}$$

While all the above mentioned parameters represents, in principle, local quantity which are affected by in unavoidable variations due manufacturing tolerance, is usual to include in the characterization of the PM an integral quantity called magnetic moment M_m. It is equal to the ratio between the polarization and the PM volume. Defining dM the magnetic moment (in open circuit) of an infinitesimal volume dv_{PM} interested by a local polarization J_0, it results,

$$dM_m = J_0 \cdot dv_{PM} \tag{1.2}$$

Integrating in the total PM volume V_{PM}, the total magnetic moment M_m is,

$$M_m = \int_{V_{PM}} dM_m = \int_{V_{PM}} J_0 \cdot dv_{PM} \tag{1.3}$$

The measurement of the magnetic moment can be performed by means of Helmoholtz coil and many magnetic quantities discussed above, such as the remanence or the max energy product, can be estimated.

1.3.2 Evolution of the PM technology

The PM applications date back to ancient times. First evidences are found in the Greek, Roman and Chinese culture, where special stones, having the property of attract each other or iron pieces, called *lodestones* or *magnes* from the name Magnesia, an area in the current Turkey, at that time under Greek domination. This compound represents a variety of magnetite, an oxide of iron (Fe_3O_4) an it is naturally magnetic. Its first application was with the invention of the magnetic compass for navigation, and it is traced back to around $850 - 1050$, in use by Chinese sailors. A first comprehensive investigation of the PM technology was carried out by William Gilbert in his *De Magnete Magneticisque Corporibus et de Magno Magnete Tellure Physiologia Nova*, published in 1600. In this manuscript, Gilbert introduced different methodologies in order to improve the magnetic performance by means of iron expansion and for magnet production. These recommendation and procedures were still kept in use till the *XIX* century. Starting from the end of the *XIX* century, the Carbon-steel (C-steel), Tungsten-steel (W-steel) and the Cobalt-steel) become the first

Table 1.3: Permanent magnet development timeline [42].

Material	**Year**	**Reference**	**Max. energy product** $[kJ/m^3]$	**Intrinsic coercivity** $[kA/m]$
Carbon steel	~ 1600	Gilbert	1.6	3.98
Chrome steel	~ 1870	Hadfield	2.4	5.17
Cobalt steel	1916	Honda et al	7.2	18.3
Remalloy	1931	Seljesater	8.8	18.3
AlNiCo	1931	Mishima	11.1	40.0
New KS	1934	Honda et al	15.9	62.9
PtCo	1936	Jellinghaus	59.7	342
CuNiFe	1937	Neumann et al	14.3	47.0
CuNiCo	1938	Dannöhl & Neumann	8.0	35.8
AlNiCo, field treated	1938	Oliver & Shedden	43.8	50.9
Vicalloy	1940	Nesbitt & Kelsall	23.9	35.8
AlNiCo, DG	1948	McCaig, Bemius, Ebeling	51.7	54.1
Ferrite, isotropic	1952	Went et al	8	143
Ferrite, anisotropic	1954	Stuijts et al	28.6	175
Lodex ®	1955	Luborsky	27.9	74.8
AlNiCo 8	1956	Koch et al	35.8	115
AlNiCo 9	1956	Koch et al	73.2	119
$RECo_5$	1966	Strnat et al	127	557
$RECo_5$	1970	Benz & Martin	151	637
$RE_2(Co,Fe,Cu,Zr)_{17}$	1972	Strnat et al	255	1989
$RE_2TM_{14}B$	1984	Koon, Croat, Sagawa	$207-279$	$1989-875$
$RE_2TM_{14}B$	2010	-	$239-414$	$2785-875$

PM materials available in sufficient large quantities. By 1932, Mishima introduced the MK-steel regarded as the precursors of the AlNiCo PMs, the first modern PM material. In Table 1.3 are summarized the fundamental step in the evolution of the PM material, highlighting the progressive improvement of the maximum energy product. Modern PM material can be regrouped in AlNiCo PMs, ferrite (or ceramic) PMs and the group of the Rare Earth (RE) PMs represented by the SmCo ($RECoX$) and $NdFeB$ (RE_2X). Their features are briefly summarized as follows.

Aluminium Nickel Cobalt (AlNiCo)

AlNiCo PMs were developed in the 1940s leading to a revolution in the PM applications. They are composed by an alloy of Al, Ni and Co together with additives which enhance the PM properties. They exhibit high remanence flux density, high Curie temperature ($\sim$

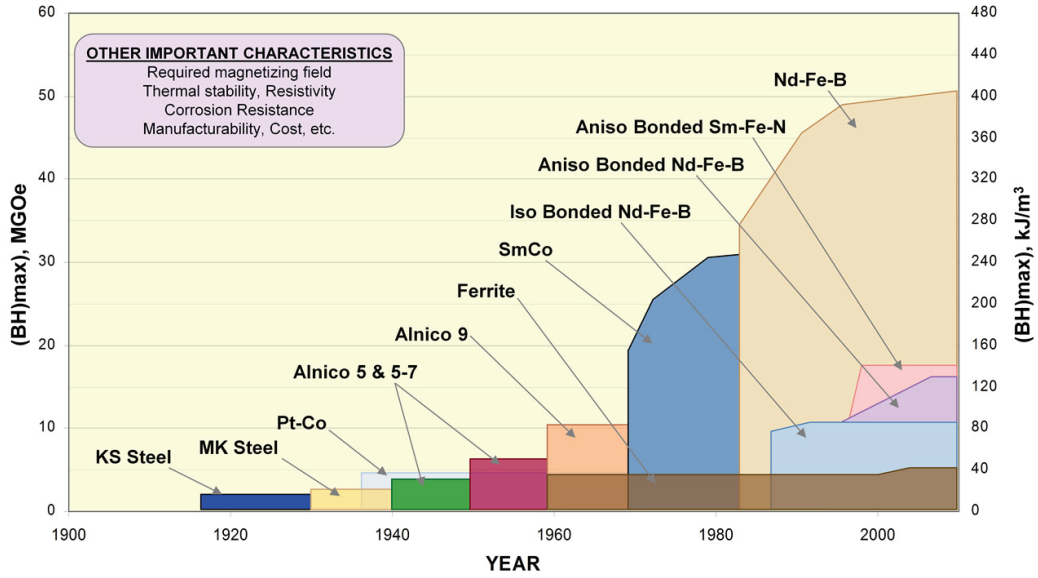

(a) Max energy product historical trend.

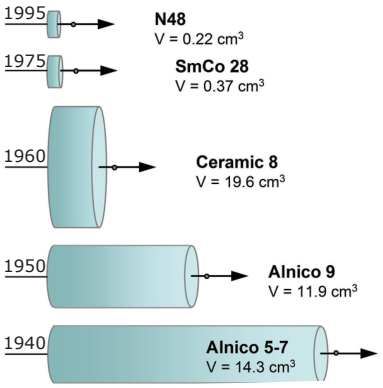

(b) Relative magnet size and optimal shape for developing $0.1T$ at $5mm$ from the PM surface.

Reversible Temperature Coefficients in %/°C

Temperature Stability	Material	Induction	Coercivity
Least Stable	Ferrite	-0.20	0.27
	La-Co Ferrite	-0.20	0.13
	NdFeB	-0.11	-0.50
	SmFeN	-0.08	-0.44
	SmCo 1:5	-0.045	-0.40
	SmCo 2:17	-0.035	-0.20
Most Stable	Alnico (8)	0.02	-0.01

(c) Temperature stability: reversible temperature coefficient.

Fig. 1.14: PM technology evolution [42] (Arnold Magnetic Technologies, all rights reserved).

$800°C$), excellent thermal stability, high corrosion resistant and mechanical strength. On the other hand, they are expensive and show a poor demagnetization strength (low H_{cJ} which make them unsuitable demanding requirements. Even if still used in the industry, they are phases out in favor of higher performance and and lower cost PMs.

Ferrite / ceramic

Ferrite (also called ceramic) PMs were introduced in the 1950s. They are composed by iron oxide and barium carbonate ($BaCO_3$) or strontium carbonate ($SrCO_3$). Ferrite PMs can be isotropic or anisotropic. The anisotropic types deliver the highest maximum energy product almost up to $30kJ/m^3$.
Ferrite are the cheapest magnet commercially available and, as shown in Fig. 1.15(a), is less influenced by price oscillation, being therefore the ideal candidate for mass market applications. Besides the price, they are the lightest among the PMs (density $5000kg/m^3$). Unlike other PMs typologies, ferrite magnets exhibit a positive H_{cJ} reversible temperature coefficient, which improve the demagnetization performance at high temperature and yielding to an easier demagnetization as the temperature decreases.
The drawbacks are the low remanence flux density $\sim 0.4T$ and the lowest energy products among the magnets. On the other hand, in the last years a novel ferrite composition (12 grade) doped with Lanthanum (La) and Cobalt (Co) has been developed, achieving remanence up to almost $0.5T$ with enhanced thermal stability and demagnetization strength [186]. They represent an attractive option in PM machines which employs flux concentration (spoke type) and anisotropic rotors. Moreover, they exhibit low mechanical properties (brittle consistency).

Rare Earth (RE)

RE PMs consist of a compound of alloys of elements of the Lanthanides group. Among them, the most important are the neodymium (Nd) and the samarium (Sm). Nd is a Light RE element (LRE) widely employed in RE PMs, since it is the third most abundant Lanthanide, following Cerium and Lanthanum. Sm is another important element which is less abundant than Nd. Nowadays RE PMs are widely used in motor applications due to the very high energy product (up to 5 times the previous AlNiCo magnet technology) making possible the development of high torque density and energy efficiency PM synchronous motors.

- **Samarium Cobalt (*SmCo*)**
  SmCo PMs were introduced in the market place in the 1970s. Two main compounds exists: $SmCo_5$ and $SmCo_{12}$, commonly defined as $1-5$ and $1-12$, respectively. *SmCo* have several advantages over the *AlNico* and Ferrite PMs, such as a higher energy (up to 3 times the AlNiCo), relative high remanence (up to $1T$), high Curie temperature ($800°C$) and the very high temperature stability (lowest reversible temperature coefficient among the PMs) and excellent corrosion resistance. Therefore they are an ideal

choice for high temperature applications for special environments. The drawbacks are are inherent to an extreme fragility and they generally more expensive than the $NdFeB$. As reported in Fig. 1.15(a), following sky-rocketing price and critical availability of RE-metals of $2011-2012$, the $SmCo$ has become an attractive choice with prices halved than conventional $NdFeB$ compounds. On the other hand, is expected that, if the demand of $SmCo$ starts to rise significantly, the price increases as well becoming comparable with the novel low cost $NdFeB$ compounds.

- **Neodymium Iron Boron ($NdFeB$)**
  $NdFeB$ PMs were discovered in 1983 by General Motors and Sumitomo Special Metals. Chemically defined as $Nd_2Fe_{14}B$, they have lead to a drastic step forward in the PM motor design due to the several advantages over all the other PM types, such as highest energy product (up to 10 times the ferrite), highest remanence up to $1.43T$ and an excellent demagnetization resistance (for conventional compounds). On the other hand, comparing to the $SmCo$, they exhibit a lower thermal stability and lower corrosion resistance. Nowadays the main disadvantages is the high price, up to 20 times the price of the ferrite. The main contribution to the high price is the addition to the compound of Heavy Rare Earth (HRE) elements, namely dysprosium (Dy) and terbium (Tb), used to improve the demagnetization performance (H_{cJ}). Being much more abundant than Tb, Dy plays a key role in NdFeB PMs, on the other hand it is almost 6 times more expensive than the Nd being of limited availingly and sourced from a single country, China. Therefore, as shown in Fig. 1.15(b), is more influenced by supply shortage and price variability [186]. On the other, following the recent crisis of the RE metals, this issue has been addressed by the research of lower cost, Dy-free replacements, discussed later.

1.3.3 Manufacturing technologies

PMs are manufactured following different procedures. Older PM typologies, such as $AlNiCo$, are normally produced by means of cast or extrusion process. The most recent PMs in the marked place are classified according to two production methodologies.

- **Sintered PMs**
  Sintering is widely use for manufacturing $NdFeB$, $SmCo$ and ferrite PMs. In this process, a suitable composition is pulverized into fine powder, compacted and heated to cause densification via *liquid phase sintering*. During sintering, the PMs shrink about $15-20\%$ of their original dimensions, require therefore a grinding process to

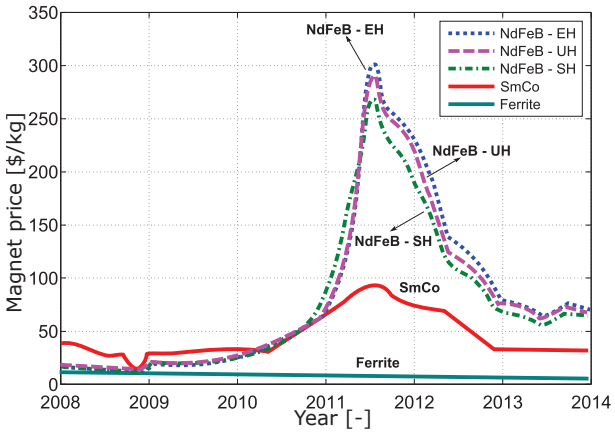

(a) Historical price trend of the most used PMs.

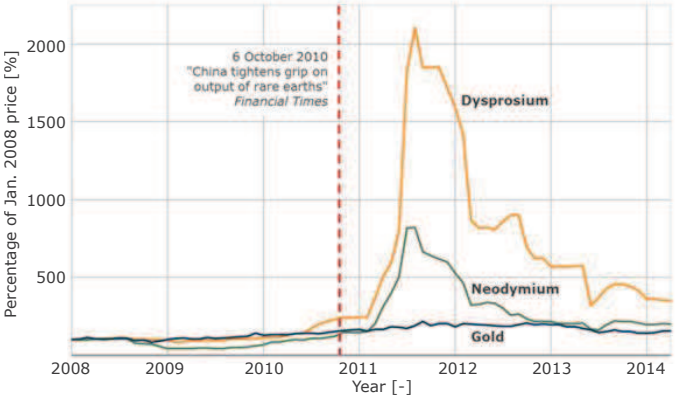

(b) Historical price trend of RE materials (source Bloomberg).

Fig. 1.15: Price trend of PM materials.

adjust the dimension to the requirements. Comparing to the bonded PMs, sintered PMs exhibit higher energy product.

- **Bonded PMs**

  Bonded PMs are made of hard magnetic powders (ferrite, *SmCo*, *NdFeB*) spreaded in a matrix of non-magnetic polymer or rubber binder. This latter material can be flexible (typically nitrile rubber or vynil) or rigid (generally nylon, polyphenylene sulfide, polyester, teflon, and thermoset epoxies). The bonded process allows to build PMs with any kind of shape, with precise sizes, examining the degrees of freedom in the motor design. Performance of bonded PMs are lower tha sintered PMs, on the other hand they are more stable and easier to produce without any finishing process, hence being an ideal candidates for mass market production.

1.3.4 The issue of the HRE compounds: novel Dy-free/reduced $NdFeB$ PMs

Together to the increase the intrinsic coercivity PMs, the addition of *Dy* in the NdFeB compounds reduces the dependence of the coercivity to the temperature, increasing therefore the thermal stability of the PM. On the other hand, it reduces the available remanence flux density and energy product. Fig. Fig. 1.16 reports the approximated trend of the intrinsic coercivity and remanence flux density of $NdFeB$ PM as a function of the *Dy* ratio. Most of electrical machine applications typically require more than 4% of *Dy*. On the other hand, based upon the current estimation of the abundance of this HRE material, the balance with the worldwide supply is achieved for a much more lower value, about 1.6% of the total PM mass. [42]

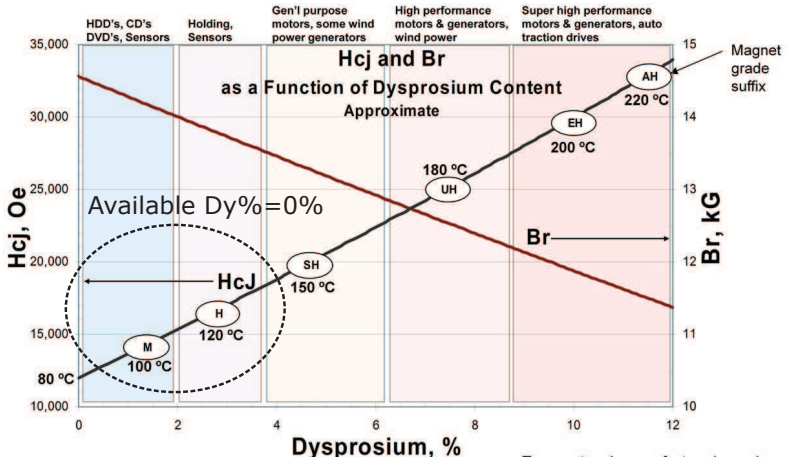

Fig. 1.16: *Dy* ratio in respect of the total mass of $NdFeB$ (Arnold Magnetic Technologies, all rights reserved). [42]

In the last years, industry has start to develop novel Dy-free or Dy-reduce $NdFeB$ compounds which try to address two contrasting target, high energy product and high intrinsic coercivity (demagnetization strength). They are briefly summarized hereafter.

- **Advanced Liquid Sintering (ALS) *Dy*-free NdFeB**
  Major part of the sintering technology is based upon the so called Liquid Sintering (LS). This methodology has been improved (i.e. advanced) by means of an optimization strategy of the several factors during manufacturing process. These factors are, for e.g., the grain size, oxygen content, conditions of the particle surface. Nowadays ALS technology allows to replace conventional *Dy*-with PMs up for intrinsic coercivity up to $\sim 1400 kA/m$ (M and H grade) and remanence up to $1.4T$. This has almost

halved the price of in comparison to conventional (*Dy*-with) *NdFeB*. ALS process oriented toward higher grades are under intensive development. [186]

- **Hot-Deformed (HD) fully-densed nanocrystalline *Dy*-free NdFeB**
  This methodology is used to produce fully-densed anisotropic NdFeB PMS. This process consists in two stages. In the first rapidly quenched ribbons with a grain size lower than $100nm$ are first coldly packed and then hot-pressed at about $700°C$ into a fully-densed form. In the second stage, a HD process is performed, allowing the compound to undergo a sufficient amount of plastic deformation at a higher temperature. During this latter stage the orientation of the grains takes place, with a direction normal to the direction of the plastic flow. The most important advantage is that, thanks to the finer grain size, a high intrinsic coercivity can be achieved without the addition of HRE elements like *Dy* or Tb. Moreover, the material usage is very efficient due to the fact that such a methodology is almost a net-shape technology. The major disadvantage is its relative slow process, limiting a high-volume production. [186]
  The most important compounds developed on the basis of this technology are represented by $NdFeB\ MQ-A$ powders: they are made starting from nanocrystalline melt spun powders ($MQ-P$), followed by a hot pressing into an isotropic compound ($MQ2$). Then, a HD followed by an extrusion deformation under high temperature, is performed producing an anisotropic $MQ3$ PMs. $MQ2$ and $MQ3$ exhibit a remanence flux density around $0.8T$ and $1.3T$, respectively. The $MQ3$ shows some cost advantages, over conventional $NdFeB$, if manufactured as a ring shape. On the other hand, the magnetization of a ring shape is not able to achieve the nominal performance, with an expected remanence flux density about 15% lower than the rated value. It exhibits a intrinsic coercivity in the order of $1500kA/m$. Conversely the $MQ2$ is about 20% more cheaper than *Dy*-free sintered $NdFeB$, with a very high intrinsic coercivity, up to almost $1800kA/m$.
- **Grain Boundary *Dy*-diffused (GBD) NdFeB**
  This technology allows to drastically reduce the content of *Dy* in the PMs, without affecting the thermal stability, intrinsic coercivity and remanence flux density. In fact, it is important to remaind that, the main drawback of the *Dy* in the $NdFeB$ compound (forming $Dy_2Fe_{14}B$), is the reduction of remanence flux density. Moreover it is recognized that microstructure and the grain boundary phase play a critical role in controlling the intrinsic coercivity of the $NdFeB$ PMs. By diffusing the *Dy* into the grain boundary, the intrinsic coercivity can be drastically enhanced adding a small quantity of *Dy*, without influencing the remanence flux density.

Due to the lower amount of *Dy*, this methodology leads to a reduction of the PM cost. [186]

- **Pressless Process (PLP) *Dy*-reduced NdFeB**
  Likewise the GBD technology, the PLP process is aimed to reduce the amount of *Dy* in the PM, using net-shape molding technology. The key of this methodology is the development of a strategy to handle the (sub)-micron fine magnetic powder which must be injected to a molding die. The fine powder is tapped in a carbon-made molding die under a vacuum system with very low oxygen content. Then, an external field is applied for aligning the grains. The most important advantage is that the NdFeB powder has a negligible reaction the carbon under the very low oxygen content. As a result, the deformation due to sintering shrinkage can be minimized or avoided.
  Thanks to the near net-shape technology, a very high material efficiency and a high product yield. Industrialization and further investment are currently the major challenges.

In Fig. 1.17 and Table 1.4 reports the comparison of the typical magnetization characteristics, magnetic data and indicative price of some of the *Dy*-free PMs discussed in this section.

Table 1.4: Summary of *Dy*-free PMs data. Values referred at the ambient temperature of $20°C$ for the sintered NdFeB and ferrite, $25°C$ for the *NdFeB* hot-extracted and hot-pressed.

Type	NdFeB sintered	NdFeB hot-extracted	NdFeB hot-pressed	Ferrite	
Grade	*N*45*H*	*MQ*3	*MQ*2	9	
Rem. flux density B_r	1.31	1.3	0.8	0.4	T
Rec. permeability	1.04	1.05	1.137	1.075	–
Intrinsic coerc. $-H_{cJ}$	-1353	-1500	-1750	-320	kA/m
B_r **rev. temp. coeff.**	-0.12	-0.09	-0.09	-0.2	$\%\cdot{}^\circ C^{-1}$
H_{cj} **rev. temp. coeff.**	-0.54	-0.48	-0.48	0.15	$\%\cdot{}^\circ C^{-1}$
Density	7600	7600	7600	5000	kg/m^3
Price	~ 50	~ 90 (ring) (~ 100 block)	~ 40	~ 5	€$/kg$

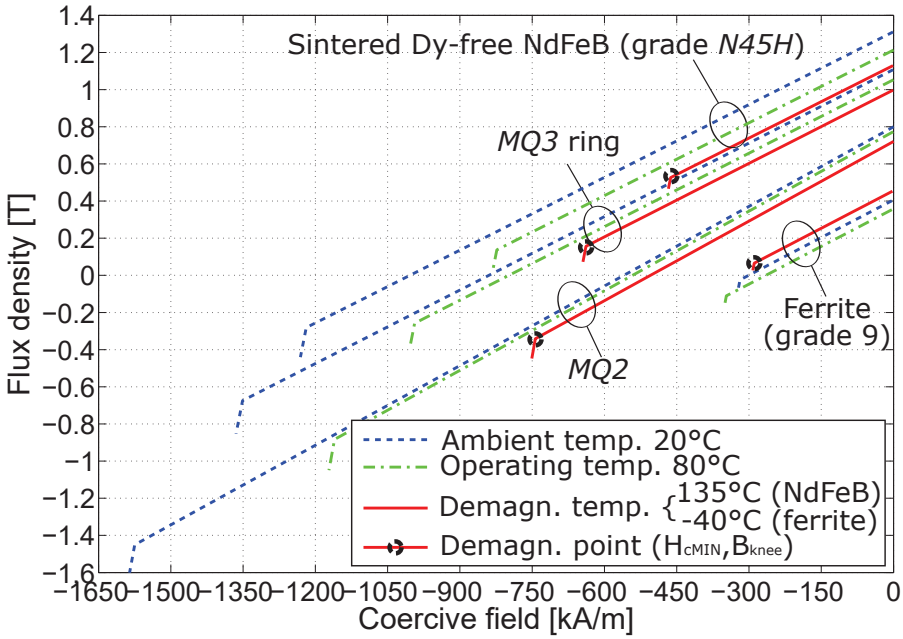

Fig. 1.17: Typical B-H characteristics of Dy-free PMs for different temperature (the temperature are related to an EPS application).

Part II

Design, analysis ed optimization of traction machines

Chapter 3

Design and comparison of IPM motors with non-uniform and conventional airgap

3.1 Introduction

In recent years, electric mobility is becoming a growing reality due to the increase of the oil demand and cost as well as the enviromental impact of conventional internal combustion engines. Since about a decade, in USA, a public-private cooperative research initiative, called FreedomCAR (US Drive since May 2012 [U.S. DRIVE]) has been working for developing high efficiency and cost competitive technologies for electrification of private transport. It is focused to develop the next generation electric and fuel technology for automotive applications. The last edition, FreedomCAR 2020, defines a sets of technical targets for the electric motors summarized in Table 3.1 and Fig. 3.1. The machine has to develop a continuous power of $30kW$, a peak of $55kW$ at $2800rpm$, ensuring a Constant Power Speed Range (CPSR) equal to $5:1$ up to $14000rpm$. In addition to the dimensional specifications, important constraints in terms of efficiency (95%), line-to-line back EMF ($600V_{peak}$), torque ripple (5%) are required. This paper deals with the design of an I-shape, radial magnetization, FSCW IPM motor suitable to this application. Based on the aforementioned specifications, it presents a comparison between two different rotor shape solutions, highlighting the influence on the electromechanical performance and losses. The first design presents a non-uniform airgap while the second is characterized by a conventional circular rotor shape. Although the advantages of the first solution are well established in many

low-torque applications, e.g., servomotors or electric power steering systems [87], limited attention has been given up to now to high-torque traction motors, such as this research aims to do.

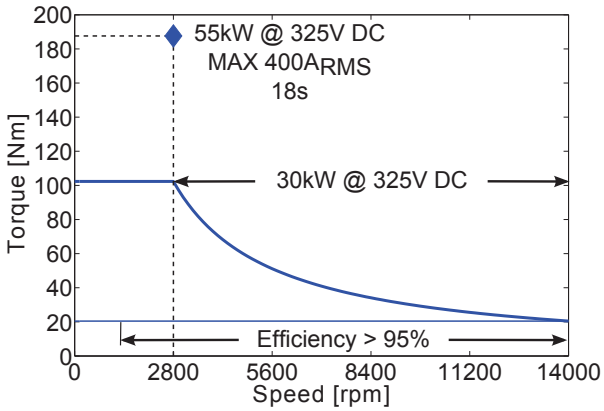

Fig. 3.1: FreedomCAR 2020 target available torque vs. speed.

3.2 Literature review

In the last years, many works were carried out aimed at the design of PM synchronous motors on the basis of FreedomCAR requirements. The first studies [154] investigated analytically the influence of these specifications on the choice of the motor parameters for a Surface-mounted Permanent Magnet (SPM) topology. In [140, 141] a FSCW SPM and V-shape IPM motor prototypes were developed and compared. In [162, 163], FSCW and Integral Slot Distributed Winding (ISDW) V-shape IPM motors are presented, investigating the effect of the PM geometry and the winding topology on the performance. The feasibility of a low cost ISDW ferrite-assisted synchronous reluctance machine has been evaluated in [133]. At last, different cooling systems of a FSCW spoke-type IPM motor are compared in [51]. All the topologies share an uniform airgap, provide comparable performance and are good candidates for the FreedomCAR application. On the other hands, they does not achieve the most challenging specifications that are efficiency (even only electrical) $> 95\%$ at partial load (20% rated torque), at high speed range, and line-to-line back EMF $< 600V_{peak}$ at maximum speed [51, 133, 140–142, 162, 163].

Both the previous targets are strictly related to the high speed requirement. As regards the efficiency, a noticeable reason is represented by the rotor losses, caused by the space Magneto Motive Force (MMF) harmonics. It proves to be not negligible and PM segmen-

Table 3.1: FreedomCAR 2020 specifications.

Specification	Target	Conditions
Max speed	14000rpm	
Rated power	$30kW$	$20-100\%$ speed rated voltage limited service 18s
Max power	$55kW$	20% speed rated voltage
Efficiency	$>95\%$	$10-100\%$ speed 20% rated torque
Torque ripple	$<5\%$	$0-100\%$ speed
DC operating voltage	$200-450V$ $325V$ rated	
Max phase current	$400A_{RMS}$	
Characteristic current	$<400A_{RMS}$	
Line-to-line back EMF	$<600V_{peak}$	100% speed
Min. isolation impedance	$1M\Omega$	terminals to ground
Mass	$\leq 35kg$	with frame
Volume	$\leq 9.7\ell$	with frame
Ambient operating temperature	$-40-140°C$	outside housing
Coolant inlet temperature	$105°C$	
Max. coolant flow rate	$10\ell/min$	
Max. coolant pressure drop	$13.8kPa$	
Max. coolant inlet pressure	$138kPa$	
Unit cost	$\leq 275\$$	in quantities of $100k$

tation is mandatory (axial, circumferential or both) in order to reduce the eddy current phenomenon. A "stator shifting" technique is proposed in [142] so as to reduce this harmonic content. The back EMF constraint is a safety-critical requirements in case of inverter failure at maximum speed (the motor operates as an uncontrolled generator [136]), such the Flux Weakening (FW) effect disappears, no longer supported by the d-axis current. As noted in [154], the constraints of the maximum EMF, together with the maximum current limit, proves to be a challenging target, as far as the motor design is concerned.

3.3 Preliminary analysis

The purpose of this section is to explore the more suitable motor configurations for the application. The optimal choice between one or the other configuration is related to the requested performance.

3.3.1 Rotor configuration: IPM vs. SPM rotor

The most important requirement is represented by the Flux weakening (FW) capability, defined as the speed range over the base speed during which the machine works at the rated voltage limit. For FreedomCAR application, the motor has to exhibits also a large CPSR. Such a capability is related to the characteristic current I_{ch}, defined as,

$$I_{ch} = \frac{\Lambda_{PM}}{L_d} \tag{3.1}$$

where Λ_{PM} is the PM flux linkage and L_d is the d-axis synchronous inductance. Analysis [153] proves that the rated current has to approximate the characteristic current in order to have an excellent CPSR performance. Based on the voltage, rated power specifications of Table 3.1 and assuming a power factor 0.9, efficiency 0.95, inverter linear modulation operation mode[154], the rated current is approximately $88A_{RMS}$. Unlike IPM motors, SPM machines exhibit, in general, a limited CPSR due to the low synchronous inductance. Only SPM solutions adopting FSCW show a large inductance so as to reach high CPSR [54]. Finally, SPM motors does not benefit from the presence of the reluctance torque that, for IPM machines, allows to reduce the PM flux linkage, the back EMF and the PM mass. Moreover, a reduction of Λ_{PM} yields a decrease of I_{ch}, making easier to achieve the optimal FW condition ($I_{ch} \cong I_n$).

3.3.2 Number of poles and slots

The number of poles $2 \cdot p$ and slots Q have a great effect on the machine performance and dimensions, particularly importance for reaching the specifications. The number of poles $2 \cdot p$ is directly proportional to the frequency, and so it affects the iron losses (more than proportionally). On the other hands, it is inversely proportional to the induced reaction and flux per pole. Therefore, its reduction leads to an increase of the back iron and PM height.

The number of poles, together with the number of slots, defines the motor winding topology (FSCW or DW) and its performance. It is useful to refer to some important motor quality indexes, represented by winding factor of the main harmonic k_{w1}, the rotor loss rate $Q/(2 \cdot p)$, the cogging torque index $\imath_{cog} = LCM(Q, 2 \cdot p)$ and the radial force index $\imath_{rf} = GCD(Q, 2 \cdot p)$. The last two indexes are well known to provide a preliminary evaluation of the most promising slot-pole candidate: the higher $\imath_{cog}$, the lower the cogging torque [54] while an even and high $\imath_{rf}$ is expected in order to achieve low radial forces and good radial symmetry [54, 107]. The last two issues are linked to the vibrations and noises of

the machines. Conversely, the rotor losses rate [16] is important in order to detect the solutions with the lower rotor losses that is lower over temperature and higher efficiency. As reported in Table 3.2, the global minimum of rotor losses is found in the area of DWs with $Q/(2\cdot p)=3$. Adopting FSCW, rotor losses gradually increase, however some local minima exist, identified by $Q/(2\cdot p)=5/2$, $3/2$ and 1 [16]. For this last reason, despite DW proves to be an ideal candidate, while also showing higher saliency ratio [41, 97, 164], FSCW offers some advantages, especially for automotive applications and that can be summarized in the following points. Manufacturing simplicity, lower end winding length [12] and lower total axial length [108], higher power density, higher fill factor (especially with segmented stator [54]), lower cogging torque and torque ripple[12], higher synchronous inductance [12] and better fault tolerant capability [112]. On the other hand, the noise and vibration might be a critical issue when the number of slots per pole and phase is fractional [39, 107, 177]. Since there are no clear specifications about this issue, it has not been quantitatively investigated in this research.

Table 3.2: Rotor losses minima for PM machines.

$Q/(2\cdot p)$	**Winding topology**	**Double layer**	**Single layer**
3	DW	Global min.	
$5/2$	DW	1^{st} local min.	–
$3/2$	FSCW	2^{nd} local min.	1^{st} local min.
1	FSCW	–	2^{nd} local min.

3.3.3 Motor selection

According to the previous remarks, an IPM motor equipped with a 3-phase, Y connection, double layer FSCW, has been selected. As regards the optimal slot/pole combination, reported in Table 3.3, there is no solution matching all the stated objectives simultaneously. Machines with the highest rotor loss rate, i.e. $Q/(2\cdot p)=3/2$, exhibit low winding factors ($k_{w1}=0.866$), yielding a reduction of efficiency due to the copper losses. Regarding the cogging torque level, the slot/pole configurations $15/14$ and $18/14$ exhibit an outstanding behavior. On the other hand, they require a very high frequency f_{MAX} so that the stator iron losses become dominant during high speed operations. For this reason, machines with lower number of poles are preferable. Finally, a 12-slot 10-pole machine has been selected.

Table 3.3: Possible FSCW slot / pole combinations.

$2 \cdot p$ [−]	f_{MAX} [Hz]	Q [−]	k_{w1} [−]	$Q/(2 \cdot p)$ [−]	ι_{cog} [−]	ι_{rf} [−]
4	467	6	0.866	1.5	12	2
6	700	9	0.866	1.5	18	3
8	933	9	0.945	1.13	72	1
		12	0.866	1.5	24	4
10	1167	12	0.933	1.2	60	2
		15	0.866	1.5	30	5
12	1400	18	0.866	1.5	36	6
14	1633	15	0.951	1.07	210	1
		18	0.902	1.29	126	2
		21	0.866	1.5	42	7

3.4 Analytical synthesis

The analytical synthesis procedure is based upon the electromagnetic model of the so called "SPM equivalent machine" [25]. Since the reluctance torque of FSCW IPM machine is quite negligible [97], the torque equation of SPM machines [18] can be considered. This procedure [117] is based on the transformation of the actual motor into an ideal machine, characterized by the following assumptions: (*i*) the stator is slotless, (*ii*) the iron core permeability is infinite, (*iii*) the PM B-H curve is linear, (*iv*) the no load airgap flux density B_{g0} is a square wave along the rotor circumference and (*v*) the electric loading $\widehat{K}_s$ (peak value) is sinusoidally distributed. The assumptions (*i*) and (*ii*) lead to define an equivalent airgap g^{II} considering the Carter and the saturation coefficients. The resulting design equations are,

$$\begin{cases} h_{PM} = k_\sigma \cdot \mu_{rec} \cdot g^{II} \cdot \dfrac{1}{k_\sigma \cdot \dfrac{B_r}{B_{g0}} - 1} \\ T_n = \widehat{K}_s \cdot B_{g0} \cdot D^2 \cdot L_{stk} \\ \Delta B = \mu_0 \cdot \dfrac{\widehat{K}_s \cdot D}{2 \cdot p \cdot \left(g^{II} + \dfrac{h_{PM}}{k_\sigma \cdot \mu_{rec}} \right)} \end{cases} \tag{3.2}$$

where h_{PM} is the PM thickness, k_σ is the leakage factor (ratio between airgap and PM pole surface), μ_{rec} is the PM recoil permeability, B_r is the PM remanence flux density, T_n is the rated torque, D is the airgap diameter, L_{stk} is the stack length, ΔB is the admitted flux density variation (in order to avoid demagnetization), μ_0 is the air permeability.

Since the thermal issue is critical in the motor design especially under the demagne-

tization point of view, in order to have a preliminary indication of the maximum motor temperatures, experimental thermal analysis performed on FreedomCAR IPM prototypes reported in [51, 140] have been considered. These analysis show that, with a coolant temperature of $105°C$, the winding achieves approximately 175-185$°C$, while rotor and magnets work at about $165-180°C$, in the worst operating condition reached at maximum speed. It is expected that the rotor losses are dissipated by forced air. As a consequence, a PM temperature of $180°C$ has been prudentially selected.

The PM is a medium class, high strength, sintered NdFeB magnet, whose magnetic data are reported in Table 3.4. A high quality steel grade M235-35A, whose electromagnetic properties are reported in Sec. VI, has been chosen in order to reduce the impact of the iron losses on the efficiency.

Table 3.4: PM parameters summary.

Grade	NdFeB N36EH
Remanence flux density	$1T$ @ $180°C$
Knee flux density	$0.15T$ ($0.25T$ design) @ $180°C$
Recoil permeability	1.05

At first, a parametric analysis has been carried out in order to define the starting machine geometry, assuming constant ΔB, B_{g0}. Consequently, on the basis of (3.2), h_{PM} and the slot current are constants. As reported in Fig. 3.2(a) D results to be inversely proportional to L_{stk}. As a consequence, in order to ensure the same iron flux density levels, tooth width, back iron height and slot width vary inversely with L_{stk}. Finally, having assumed the same current density and fill factor, the slot area is constant with L_{stk}. It is worth noticing that the mass remains below the $35kg$-limit, in most part of the considered stack length range between 20 and $180mm$, as shown in Fig. 3.2(b) (the analysis has been stopped when D becomes theoretically equal to the shaft diameter). Stator iron and copper mass remain almost the same, while higher variations are found in rotor iron mass. The total machine mass includes also the motor frame [141] even if it is difficult to assess with precision at this stage. For this reason, an airgap diameter $150mm$, stack length $87mm$ have been selected so as to have a safety margin.

3.5 Finite Element Analysis

The baseline geometry has been tuned and deeply analyzed by means of $2D$ Finite Element Analysis (FEA). Two different rotors have been considered: *Design A*, equipped with a non-

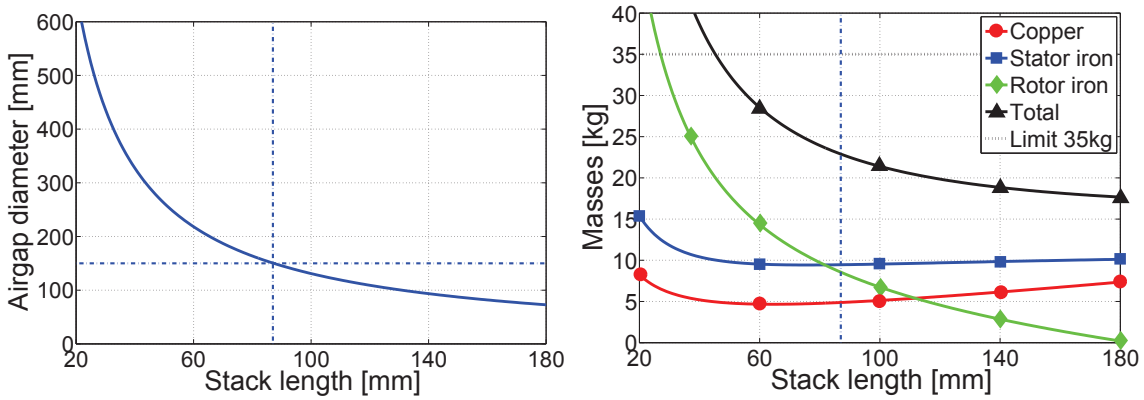

(a) Airgap diameter vs. stack length.

(b) Masses vs. stack length.

Fig. 3.2: Machine masses and geometry trends.

uniform airgap and *Design B*, characterized by a conventional smooth shape with uniform airgap.

3.5.1 Analysis of the profile of the rotor poles

An appropriate shaping of the rotor polar surface is an effective measure to improve the airgap flux density distribution, the EMF waveform and to reduce cogging torque, torque ripple, noise and vibration levels. [55, 87, 92, 129, 179]. Although there are shapes of different complexity [55, 129, 179], a simple "centre-offset arc" [55] pole shoe shape is considered hereafter, as shown in Fig. 3.3. The arc angle has been set to $\beta_e = 150$ elec. degrees. Simulations have been performed in order to find an optimal shape, fixing minimum airgap to $g = 0.7mm$ and changing the round shape height Δ_r from 0 to $3mm$.

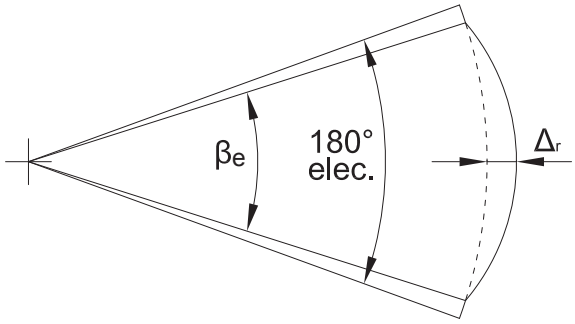

Fig. 3.3: Shaping of the rotor pole.

Figs. 3.4 and 3.5 show the distribution and the harmonic content of normal airgap flux density and phase EMF waveform, respectively, with different values of Δ_r, under no load

operation. Increasing this height, a harmonic reduction is achieved in both waveforms, with a minimum around $\Delta_r \cong 1.5mm$.

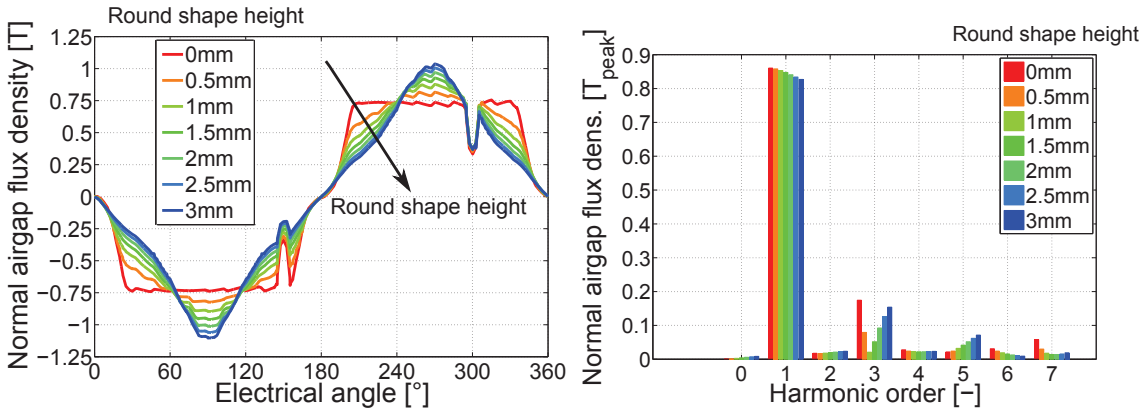

(a) Normal airgap flux density vs. electrical angle.

(b) Normal airgap flux density vs. harmonic order.

Fig. 3.4: Normal airgap flux density at no load operation.

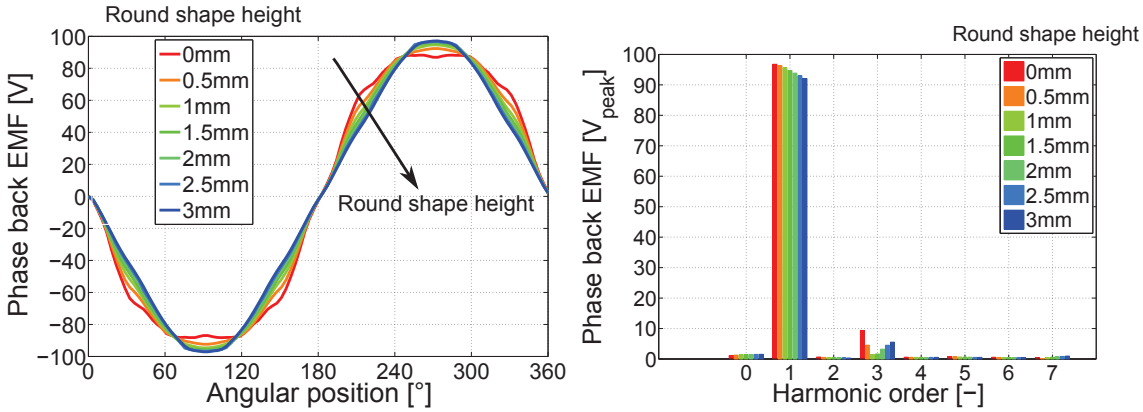

(a) Back EMF vs. angular position.

(b) Phase back EMF vs. harmonic order.

Fig. 3.5: Phase back EMF at no load operation.

Concerning the torque performance, Fig. 3.6 illustrates the benefical effect of the rotor shaping on the reduction of the cogging torque and torque ripple, which results around 96% and 72%, respectively. However, due to the increase of the equivalent airgap height, the average torque exhibits a reduction as well, estimated around 12%.

A round shape height $\Delta_r = 1.5mm$ has been selected so as to get the benefits of the reduction of the EMF harmonic content, cogging torque and torque ripple, without excessively affecting the average torque performance.

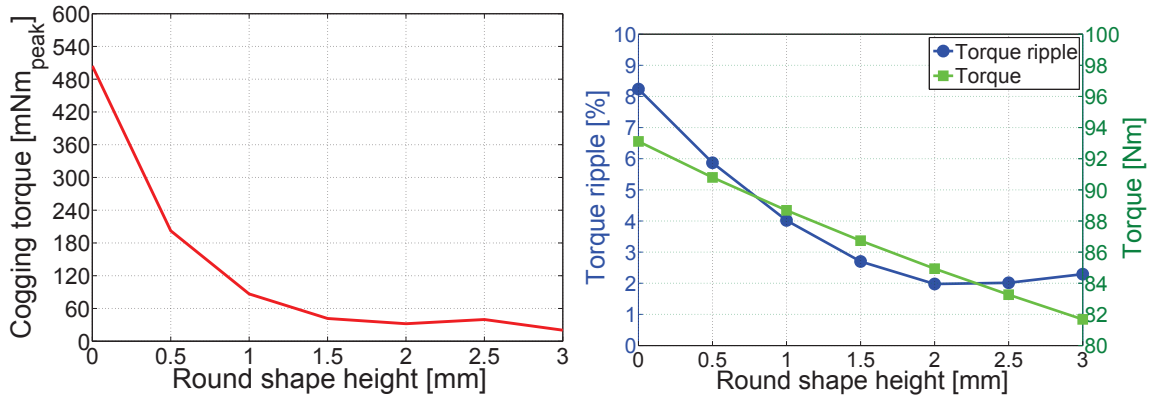

(a) Cogging torque vs. round shape height. (b) Torque vs. round shape height at $130A_{RMS}$.

Fig. 3.6: Torque trends.

3.5.2 Definition of the final geometry

A parametric analysis has been carried out on the *Design A* in order to satisfy the maximum torque at the requested base speed, ensuring a proper demagnetization level in order to prevent the irreversible demagnetization of PM. Finally, an analytical approach has been adopted to estimate the mechanical strength of the iron bridges due to the centrifugal stress. The resultant designs are reported in Fig. 3.7.

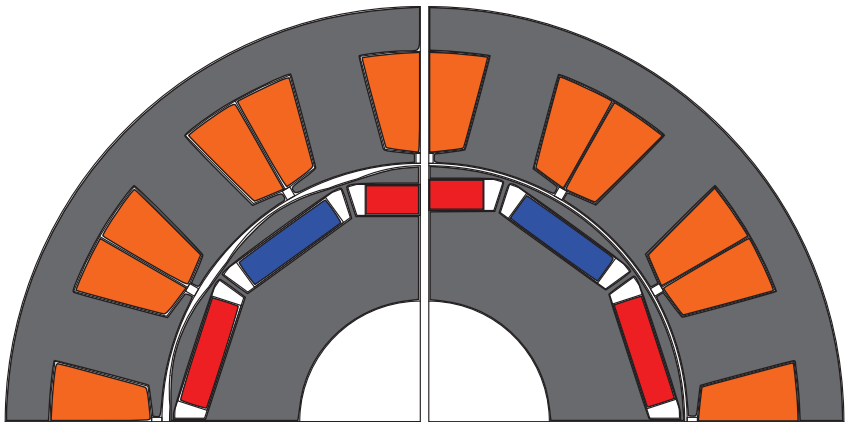

(a) *Design A* (non-uniform airgap). (b) *Design B* (uniform airgap).

Fig. 3.7: FreedomCAR final geometries.

3.5.3 Electromechanical performance

A parametric analysis has been carried out in order to estimate the trajectory of the current space vector. Fig. 3.8 shows the Maximum Torque Per Ampere (MTPA) and Maximum Torque Per Volt (MTPV) loci in the $(I_d - I_q)$ plane, for *Design A* and *Design B* respectively. These loci are superimposed with the contour lines of the constant output power $[kW]$ and speed [rpm] at rated voltage. The maximum torque, required by the application, is developed in point B' at the base speed of $2800rpm$. Both machines operate inside the rated voltage limit with a good safety margin. From 0 to base speed the machines work along the MTPA trajectory up to the base point B, where they develop the rated torque. From base speed to about $4200rpm$, both machines continue to operate in MTPA locus. The current is decreased up to intercept the rated $30kW$-power curve. The voltage increases up to the rated value, while the current is controlled in order to deliver a constant rated power. Finally, from $4200rpm$ to $14000rpm$, both machines are fed by rated voltage, developing a constant rated $30kW$-power, under FW control. It is interesting to note that this trajectory can be described by a straight line crossing the point $(-I_{ch}, 0)$, that represents the center of the voltage limit (speed limit) ellipses and the point where the MTPV locus intersects the I_d-axis.

Both designs exhibit a satisfactory FW capability, since I_{ch} is close to the rated current, that are, $89A_{RMS}$ for *Design A* and $95A_{RMS}$ for *Design B*. As reported in Table 3.5, they generate a line-to-line back EMF in the order of $760V_{peak}$, at maximum speed. It is higher than $600V_{peak}$-limit. It is worth noticing that a reduction of the back EMF, to down about $622V_{peak}$, at maximum speed, is achievable only in *Design B*, reducing the number of conductors per each slot, series configuration, from 16 to 13. This yields an increase of the maximum current to about $394A_{RMS}$, anyway lower than the maximum limit. This is not possible for *Design A*. From this point of view, this represents a drawback of the solution with a non-uniform airgap.

Fig. 3.9 shows the resulting mechanical characteristics. The PM and the reluctance components are segregated according to the method proposed in [5]. The predicted trend of the torque components of the two motors is almost the same and the cylindrical component results clearly higher than the reluctance component. In fact, an evaluation of the average saliency ratios, 1.45 and 1.3 for *Design B* and *Design A*, respectively, confirms the low anisotropy of FSCW machines. The expected reduction of the saliency ratio, caused by the rotor shape design [55], is limited to 10%.

The torque ripple amplitude vs. speed is shown in Fig. 3.10, according to the predicted current space vector trajectory. Although *Design A* does not ensure completely the FreedomCAR limit, the torque ripple levels are lower than 5% at low and medium speed, with

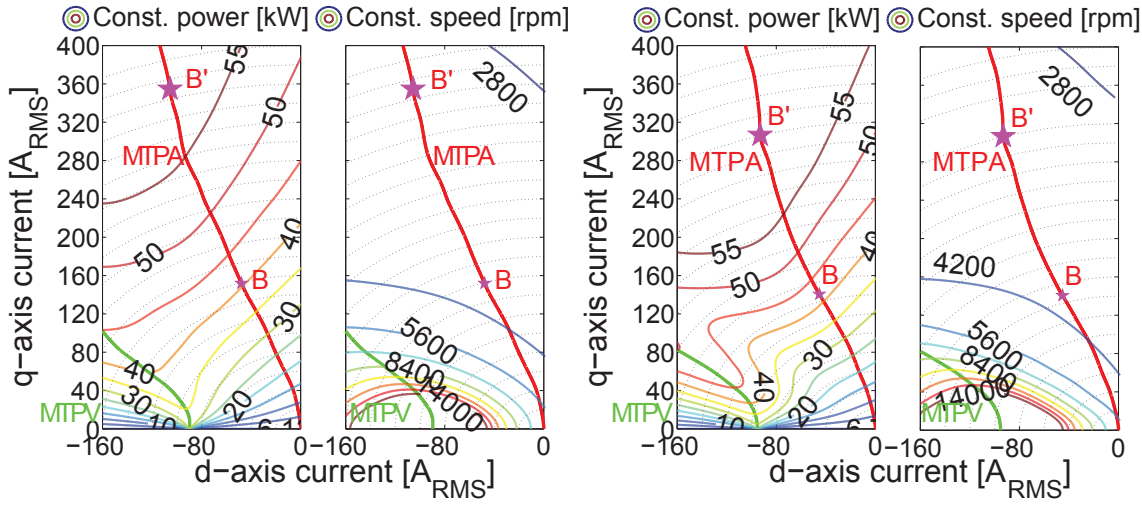

(a) *Design A*. (b) *Design B*.

Fig. 3.8: Current space vector trajectory.

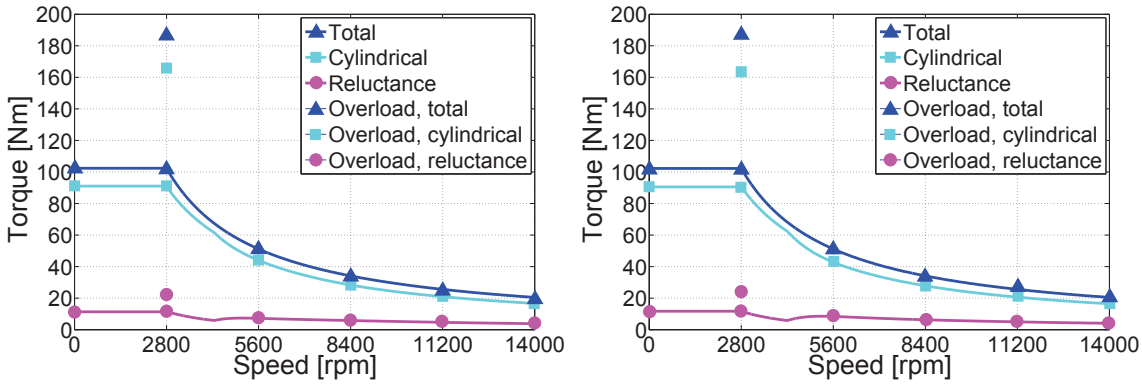

(a) *Design A*. (b) *Design B*.

Fig. 3.9: Torque vs. speed at rated load.

a maximum of 8% at the highest speed. *Design B* exhibits always higher values, reaching 40% at maximum speed. This confirms the benefical impact of the pole shaping in a wide operating speed range. Then, it is difficult to fall within the specific, for a conventional motor, without additional measures, such as skewing or optimal design of flux barriers [12].

3.5.4 Losses and efficiency performance

Figs. 3.11 and 3.12 show the electrical losses trends at rated and partial load, respectively, for both machines.

The computation of the copper losses neglects the contribution of the skin and proximity

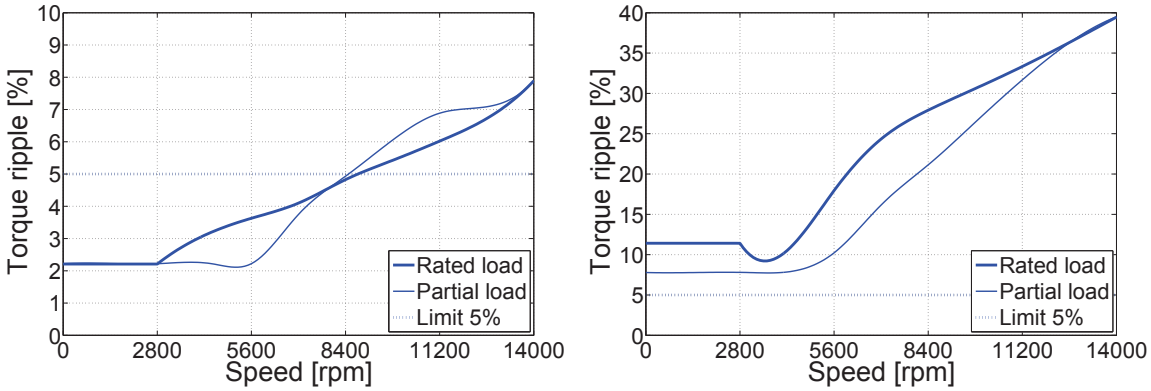

(a) *Design A*. (b) *Design B*.

Fig. 3.10: Torque ripple vs. speed.

effects (AC losses) that might be rather remarkable at maximum speed. While the first phenomena could be easily controlled employing a proper paralleled wire strand, the second can be suppressed adopting a Litz wire [141]. However, at base speed, due to the higher equivalent airgap, the copper losses of *Design A* result about 15% higher than those of *Design B*.

Regarding the iron losses, a transient calculation has been performed. Due to the high operating speed, these losses represent a noticeable contribution on the total losses. They are the main loss component at speeds higher than $4200rpm$. For the same reason, the rotor iron losses are non-negligible at maximum speed. They are approximately one third of the stator losses. Although both machines exhibit similar trends at low speeds, the difference in FW operating region is remarkable. The predicted iron losses, for *Design A*, at maximum speed, are about half of those evaluated for *Design B*. This emphasizes that a non-uniform airgap rotor drastically reduces the impact of the MMF harmonic on the iron and PM losses. As highlighted in Sec. *I.B* and confirmed by FEA, eddy current losses in the PMs are not negligible at high speed range. To the aim of reducing their impact, a segmentation is performed [181]. As a consequence of the considered 2D formulation, only a circumferential segmentation is implemented, splitting each magnet in 6 pieces of $5.3mm$ each. However, it is enough to decrease these losses, for both designs, of about 80%.

Finally, the resultant electrical efficiency has been evaluated and reported in Fig. 3.13. Although both machines exhibit comparable maximum electrical efficiency, in the order of about 97%, as the speed increases, the gap gradually widens. In fact, due to the lower iron losses in FW operation, only *Design A*, at partial load, ensures an electrical efficiency higher of almost 96% up to $14000rpm$. On the contrary, in the same loading condition, *De-*

sign B exhibits an electrical efficiency higher than the FreedomCAR target only up to about $10000rpm$, falling to about 93% at maximum speed. However, including friction, ventilation losses and the "building factor" [23], it is expected that the total efficiency slightly decreases by a few percentage points for both machines.

It is worth noticing that different choices could yield a reduction of the iron losses even though increasing the copper losses. On the other hand, this could further reduce the efficiency at low speed range, where the iron losses have low impact.

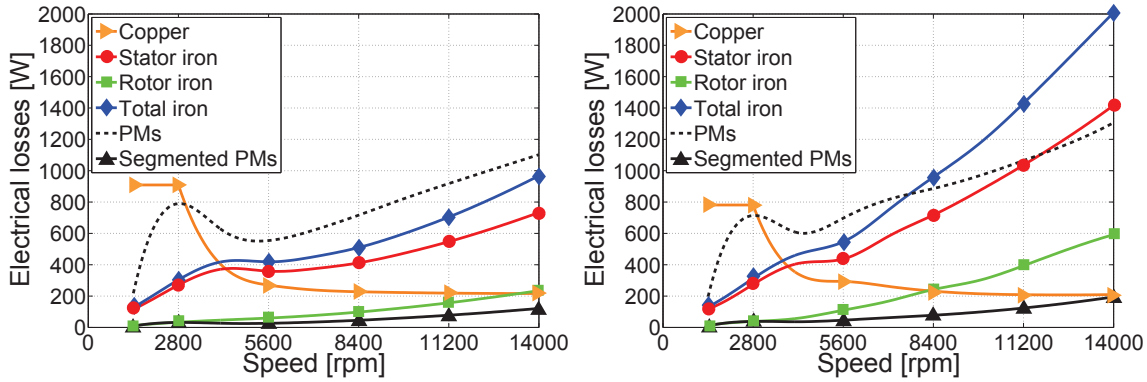

(a) *Design A.* (b) *Design B.*

Fig. 3.11: Losses vs. speed at rated load.

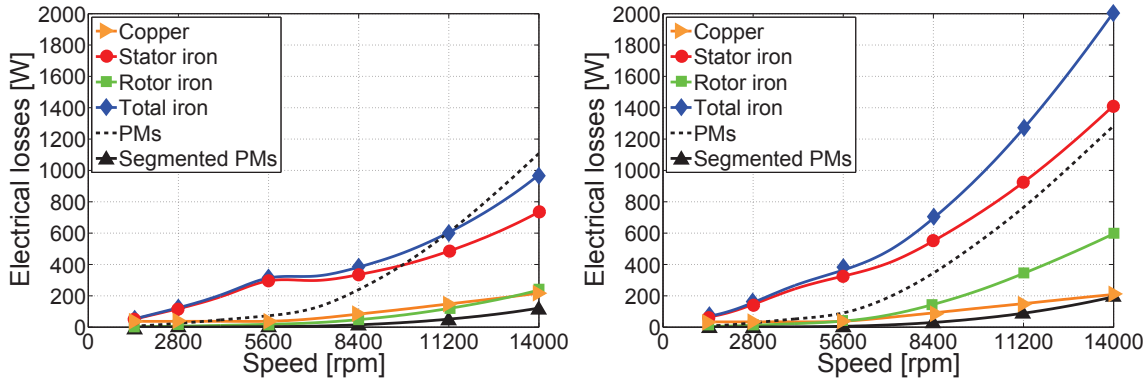

(a) *Design A.* (b) *Design B.*

Fig. 3.12: Losses vs. speed at partial load.

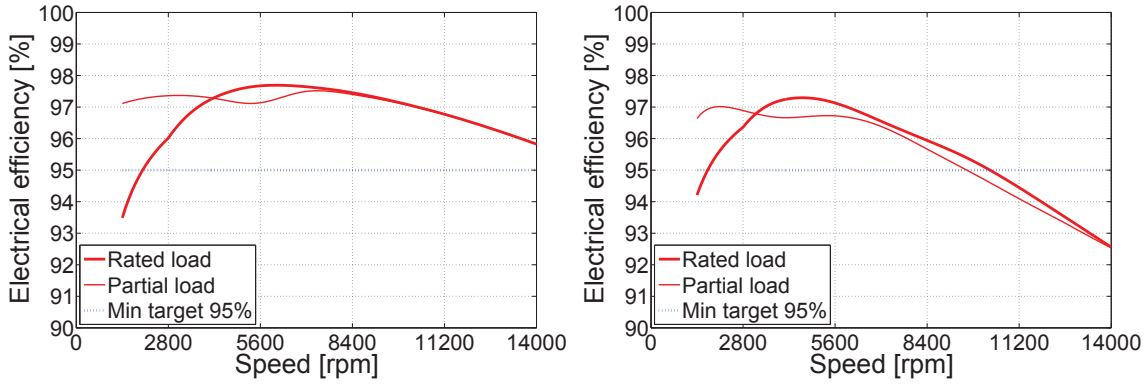

(a) *Design A*. (b) *Design B*.

Fig. 3.13: Electrical efficiency vs. speed.

3.6 Conclusions

This paper investigates the feasibility of a high performance IPM synchronous motor according to FreedomCAR specifications, comparing two solutions, with a non-uniform airgap and a traditional smooth rotor. A preliminary analytical analysis has allowed to define the machine fundamental characteristics and the main geometry. A FEA has been performed in order to find an optimal shape, reducing the back EMF harmonic contents, cogging torque and torque ripple.

Although both machines satisfy most of the requirements, this research highlights that the adopted non-uniform airgap geometry exhibits clear advantages also when employed in traction motors for which is required a high torque quality and high efficiency in a wide speed range. The benefit is mainly achieved when operating at maximum speed. The torque ripple results about one fifth while a remarkable reduction of the iron losses, of about one half, is expected. This last effect is currently under further investigations in high speed, flux weakening operation. Consequently, only the motor with shaped rotor design achieves the target electrical efficiency, higher than 95% at partial load, up to $14000 rpm$.

Table 3.5: Key machine parameters summary.

Rotor configuration	***Design A***	***Design B***	**Unit**
Number of slots	12		–
Number of poles	10		–
Airgap diameter	150		mm
Stack length	87		mm
Stator outer diameter	241		mm
Airgap height	0.7		mm
Round shape height	1.5	0	mm
# of conduc. per phase, series config.	64		–
# of conduc. per slot, series config.	16		–
Conductor area, series config.	21.21		mm^2
PM dimensions per pole	9×32		mm
Rated power	30		kW
Max power	55		kW
Rated phase current	159	148	A_{RMS}
Max phase current	372	320	A_{RMS}
Characteristic current	89	95	A_{RMS}
Back EMF line-to-line @ $14000rpm$	752	766	V_{peak}
PMs mass	1.90		kg
Copper mass	4.88		kg
Iron mass	17.52	18.59	kg
Total mass	24.30	25.37	kg
Total volume	3.97		ℓ

Chapter 4

Formula SAE Electric competition: electric motor design

4.1 Introduction

Formula SAE is an international, university student, vehicle design competition, promoted by SAE International started at the beginning of 1980*s*. The idea underlying this competition is that a fictional manufacturing company has contracted a student design team to develop a small Formula-style race car [79]. The prototype race car is to be evaluated for its potential as a production item, through a series of tests regrouped in Static events ("Technical Inspection", "Cost and Manufacturing", "Presentation", "Design") and Dynamic events ("Acceleration", "Skid Pad", "Autocross", "Efficiency & Endurance") [78]. Every year, this competition is organized in several official races all over the world, in USA, Australia, Brazil, Italy, UK, Germany, Japan. Recently, due to the growing interest in electric mobility, alongside the traditional internal combustion engine races, a purely electric formula takes places, for e.g. in Formula Student Electric Germany. The current trend in the research of high performance electric motor for traction application highlights the permanent magnet (PM) synchronous motor as the best candidate [140, 141, 154, 162, 163], due to the high torque density, high efficiency, high degree of freedom in the design of the motor [12]. On the other hand, the increase and the instability of the price of rare earth PM is pushing the research of rare earth free alternatives. The most interesting solution is represented by the synchronous reluctance machine. It seems to be suitable for traction application due to the robust structure, high operating speed range, high overload capability, no electro motive force, leading to a safe behavior in case of inverter failure. Thanks to the appropriate vector control algorithm, the performance in terms of efficiency and torque become competitive

Fig. 4.1: MG0712, formula SAE car, year 2012, Race UP team, University of Padova, Italy.

[110]. Conversely, the most important drawbacks of reluctance machines are the intrinsically higher torque ripple[65] and usually a low power factor. A reduction of the torque ripple can be achieved by means of a careful choice of the number and the shape of the flux barriers, in addition to the skewing [12, 170]. An increase of the power factor is achievable by the inset of PMs in the high saliency rotor structure. This last configuration, known as permanent magnet assisted synchronous reluctance (PMASR) or Interior Permanent Magnet motor (IPM), exhibits comparable performance to surface mounted (SPM) PM machine needing a limited amount of high cost rare earth magnets, such as NdFeB or SmCo. It is otherwise a cost effective solution when flux barriers are filled with ferrite [9, 169]. This chapter deals with the design criteria of PM synchronous motors according to Formula SAE requirements. A preliminary analysis has been carried out in order to define the motor electrical requirements. The analysis is based upon the performance required by the various dynamic events. Two different stator geometries, with the same number of slots and different outer diameter, have been considered as further constraints. For each stator laminations and a given gear ratio, two Integral Slot Distributed Winding (ISDW) ferrite IPM motors have been developed and optimized with the objective to minimize the torque ripple. The best candidate, in terms of final mass and performance, has been scaled for a double gear ratio and finally compared with two equivalent outer diameter and stack length $NdFeB$ SPM motors. One is characterized by the same stator lamination, while the second is equipped with a fractional slot concentrated winding (FSCW). Finally, some considerations on the power supply inverters have been presented.

4.2 Preliminary analysis and design considerations

The 2013 Formula SAE edition introduces important electrical constraints and specifications in the design of a traction system for an Electric Vehicle (EV). The electrical constraints that limit the degrees of freedom in the design of electric motors for traction are: (i) the maximum power that can be developed by the battery pack, equal to $85kW$ and (ii) the maximum DC voltage, lower than $300V$ or $600V$ depending on the competition [78].

Considering the previous constraints, the requested torque vs. speed is evaluated in order to achieve excellent performance during the "Acceleration" event as well as the maximum speed. Assuming an uniformly accelerated motion during the $s = 75m$-track of the "Acceleration" competition in a top time of $t = 4s$, the predicted acceleration is equal to

$$a = \frac{2 \cdot s}{t^2} \cong 10m/s^2 \tag{4.1}$$

The total mass of the vehicle, including the $80kg$-pilot, is assumed to be prudentially in the order of $400kg$. Consequently, the total traction force is

$$F_n = m \cdot a \cong 4000N \tag{4.2}$$

The consequent evaluation of the maximum frictional force tire-road, assuming a frictional coefficient $\mu_f = 2$ and two driven rear-wheels, must ensure the capacity to transfer the traction force without wheel slip. It results

$$F_{MAX} = \frac{1}{2} \cdot m \cdot g \cdot \mu_f \cong 4000N \tag{4.3}$$

Considering a wheel diameter $D_w = 500mm$, the rated torque per each wheel is finally

$$T_{wn} = \frac{1}{2} \cdot F_n \cdot \frac{D_{wn}}{2} \cong 500Nm \tag{4.4}$$

The requested maximum speed is $v_{MAX} \cong 140km/h$, equivalent to a rotation wheel speed $n_w \cong 1480rpm$. Two different gear ratios, $1:4$ and $1:8$, have been selected. The rated torque T_n and maximum speed n_{MAX} have been evaluated consequently. According to the $85kW$ power limitation, two traction motors have been analyzed. The predicted base speed n_B has been evaluated in order to achieve a rated power of $P_n = 40kW$ for each unit. Finally, the DC bus rated voltage V_{DCn} has been fixed to the lowest value established by SAE rules, $300V$. Although a lower voltage, for e.g. $48V$, allows automotive class components to

be employed [64, 122], high voltage yields to a reduction of the size of the power supply system and line connections.

The resultant motor specifications are reported in Table 4.1.

Table 4.1: Motor specifications.

Gear ratio	1 : 4	1 : 8	**Unit**
n_{MAX}	6000	12000	rpm
n_B	~ 3000	~ 6000	rpm
T_n	125	63	Nm
P_n	~ 40	~ 40	kW
V_{DCn}	300		V

4.3 IPM motors: design and analysis

Two existing $Q = 36$ slot stator laminations, one with an outer diameter $D_e = 337mm$ (A) and the second $D_e = 276mm$ (B), has been considered in the design of the electric motors. The corresponding airgap diameter D and slot area S_{slot} are reported in Table 4.2.

Table 4.2: Motor specifications.

Lamination type	**A**	**B**	**Unit**
Q	36	36	–
D_e	337	276	mm
D	230	180	mm
S_{slot}	183.2	148.0	mm^2

These lamination geometries meet the overall dimensions of a $600cm^3$ 4-cylinder ICE that equips an existing Formula SAE conventional race car and that will be replaced by electric motors. In order to reduce the maximum supply frequency, the number of poles has been selected to $2 \cdot p = 4$. As a consequence, an ISDW has been designed. This winding arrangement proves to be the most effective solution when an high anisotropic rotor is adopted, because, comparing to Fractional Slot Concentrated (FSCW), it drastically increases the saliency ratio [41, 162]. On the basis on the geometry constraints and a gear ratio 1 : 4, two motors, IPM-A ($D_e = 337mm$) and IPM-B ($D_e = 276mm$), have been designed, as reported in Fig. 4.2. The rotor structure is characterized by three symmetrical flux barriers per pole, filled by ferrite (remanence flux density $0.4T$ @ $20°C$, knee flux density $0.1T$ @ $20°C$, recoil permeability 1.05, density $4800kg/m^3$).

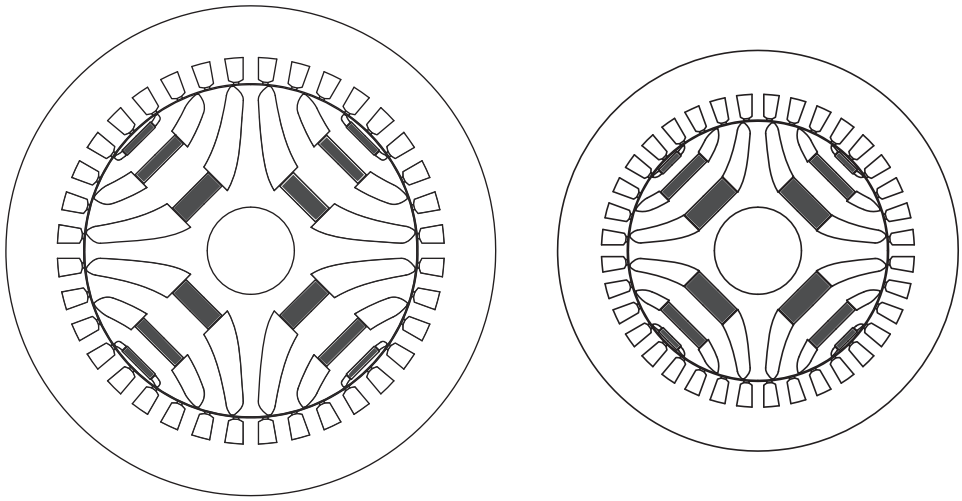

(a) IPM-A: 36-slot 4-pole, outer diameter $337mm$.

(b) IPM-B: 36-slot 4-pole, outer diameter $276mm$.

Fig. 4.2: IPM designs.

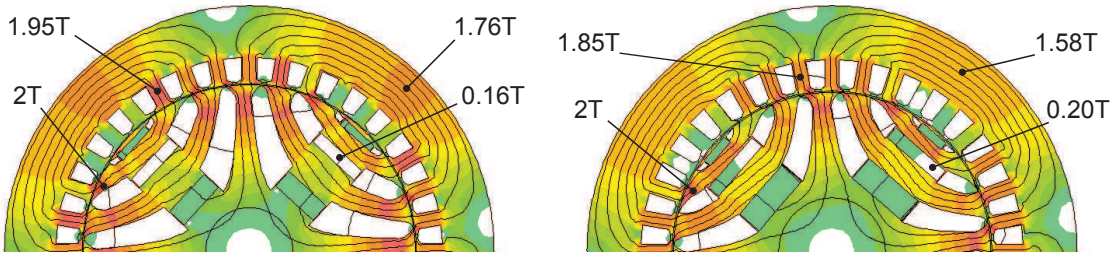

(a) IPM-A: 36-slot 4-pole, $D_e = 337mm$.

(b) IPM-B: 36-slot 4-pole, $D_e = 276mm$.

Fig. 4.3: IPM machines: flux density map at rated load.

The geometry has been tuned and analyzed by means of $2D$ FEA. The stack length L_{stk} has been scaled in order to achieve the rated torque T_n, taking full advantage of the iron, working up to the knee of the iron $B-H$ characteristics, as reported in Fig. 4.3. However, the flux density maps show some critical areas for the demagnetization in the PMs, although their values are higher than the knee value of $0.1T$ at $20°C$.

In the same loading condition, a Non-dominated Sorted Genetic Algorithm (NSGA) has been performed in order to minimize the torque ripple. Since the stator geometries are fixed, only the rotor structure has been optimized for both designs. The optimization variables considered are the flux barrier angles and the ratio between air and iron path along the q-axis. At the end of the automatic procedure, the minimum torque ripple is 12%, achieved in IPM-B, while IPM-A exhibit an higher value, around 18%.

The number n_{cs} has been changed in order to set the base speed close to the requested

$3000rpm$, ensuring the feasibility of double layer winding. The rated current I_n, rated current density J_n (assuming a fill factor of 0.4), PM flux linkage Λ_{PM} and the characteristic current I_{ch} have been computed as well as the machine masses (copper G_{Cu}, PMs G_{PM}, stator iron G_{Fes}, rotor iron G_{Fer}, total iron G_{Fe}, total G).

Both machines exhibit similar torque, power and power factor (PF) characteristics, as reported in Fig. 4.4. Table 4.3 summarizes the main electromechanical results. IPM-A presents an overload current density of about 12% higher than that in IPM-B, while the current is slightly higher. However, due to the selected number of series conductors per each slot n_{cs}, the rated current densities values implies an adequate cooling system. If this increases the complexity of the systems, on the other hand it yields to reduce the machine mass, improving the car dynamic performance. Conversely to $NdFeB$, the ferrite PM has got a positive reversible temperature coefficient of coercivity. This improves the demagnetization strength as the temperature increases, leading to better car dynamic performance.

Analysis proves that a characteristic current (given by the ratio between PM flux linkage and q-axis inductance) closes to the rated current, yields the machine to show an excellent Constant Power Speed Range (CPSR) [153]. Although this condition is not verified by the considered motors, due to the limited requested FW ratio (2 : 1), the performance over the base speed is well suited. As shown in Figs. 4b, 4c, the higher value of the characteristic current of IPM-B produces a slightly better CPSR and power factor than those of IPM-A.

Finally, the mass of both machines is equal, emphasizing that there are not substantially advantages selecting higher stator diameters. However, due to the higher airgap diameter, the impact of the end winding on the copper mass in IPM-A is two times higher than that in IPM-B.

4.4 Comparison to SPM motors

In order to achieve a further reduction of the masses, a gear ratio 1 : 8 has been considered, leading to a scaling of the stack length of an half. As IPM-A become practically not feasible in terms of 2D FEA analysis, due to the noticeable effects of the end winding, only the smaller stator, called IPM-B', has been evaluated. This design has been compared with two equivalent size SPM machines, as reported in Fig. 4.5. The first, SPM-B, equipped with the same 36-slot stator and 4-pole rotor, while the second, SPM-C, presents a 12-slot and 8-pole, equipped with a FSCW. The PM used in the machine is $NdFeB$ (remanence flux density $1.1T$ @ $20°C$, knee flux density $0.1T$ @ $20°C$, recoil permeability 1.05, density $7500kg/m^3$).

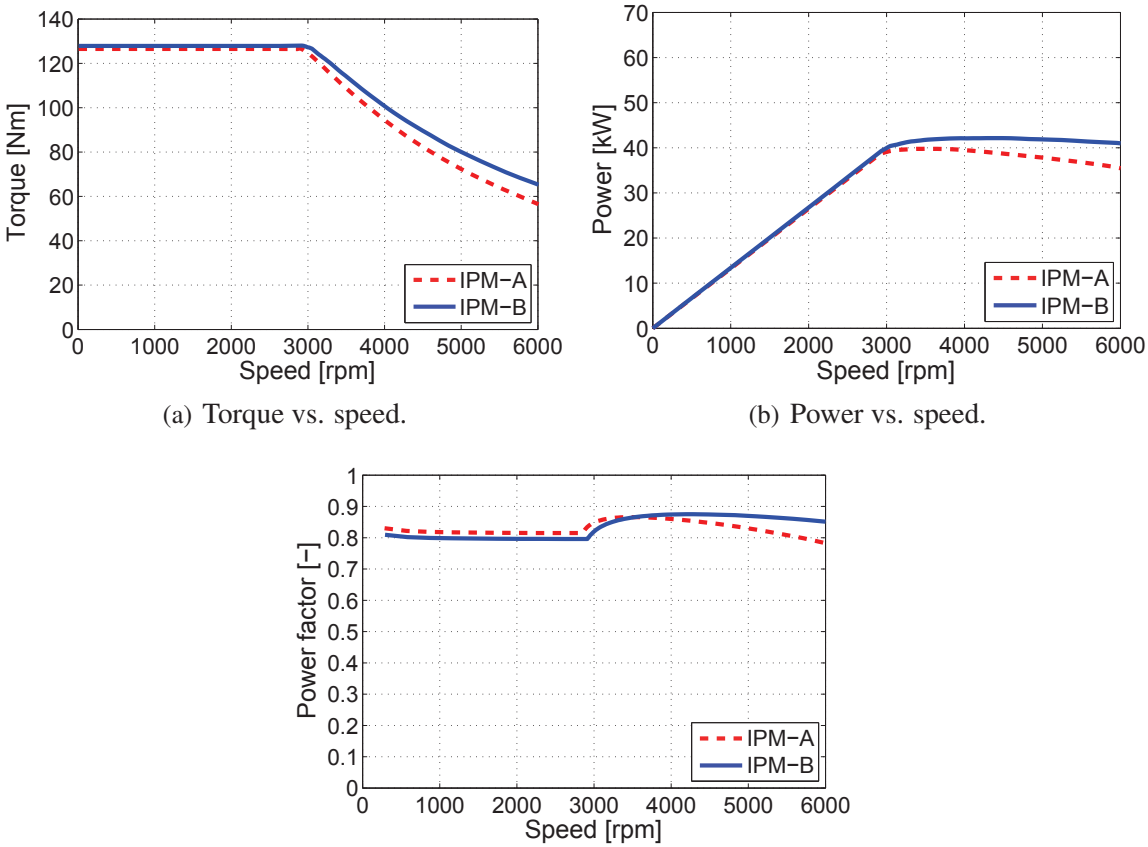

(a) Torque vs. speed.

(b) Power vs. speed.

(c) Power factor vs. speed.

Fig. 4.4: Performance comparison.

A load simulation has been performed in order to evaluate the flux density levels at rated load, as reported in Fig. 4.6. The number n_{cs} of SPM machines has been changed in order to include the requested torque vs. speed curve up to the maximum speed $12000rpm$.

As regards the electromechanical characteristics, SPM-B shows a wider FW range than SPM-C, about 60% higher. In order to meet the final torque in SPM-B and especially SPM-C, their base speeds has been increased highly, thus requiring an higher phase current. It is worth noticing that IPM-B' and SPM-B have approximately the same rated slot current. Both SPM machines shows characteristic current higher than the rated current, yielding to a torque vs. speed characteristic with a zero torque at the maximum speed. Regarding the PF trends, SPM machines ensure a better value than IPM machines, higher than 0.9 up to almost $12000rpm$. On the other hand, it shows a great reduction trend when higher speeds are required.

The evaluation of the masses shows that the lowest values are achieved with IPM-B' and

Table 4.3: Key machine parameters summary, gear 1 : 4.

Design	IPM-A	IPM-B	Unit
D_e	337	276	mm
D	230	180	mm
L_{stk}	50	80	mm
n_{MAX}	6000	6000	rpm
n_B	2857	2915	rpm
T_n	125	125	Nm
I_n	133	127	A_{RMS}
J_n	14.5	12.9	A_{RMS}/mm^2
Λ_{PM}	29.2	32.5	mVs
I_{ch}	30	48	A_{RMS}
n_{cs}	8	6	$-$
G_{Cu}	7.9	5.8	kg
G_{PM}	0.9	1.4	kg
G_{Fes}	15.9	18.0	kg
G_{Fer}	8.9	8.4	kg
G_{Fe}	24.8	26.4	kg
G	33.6	33.6	kg

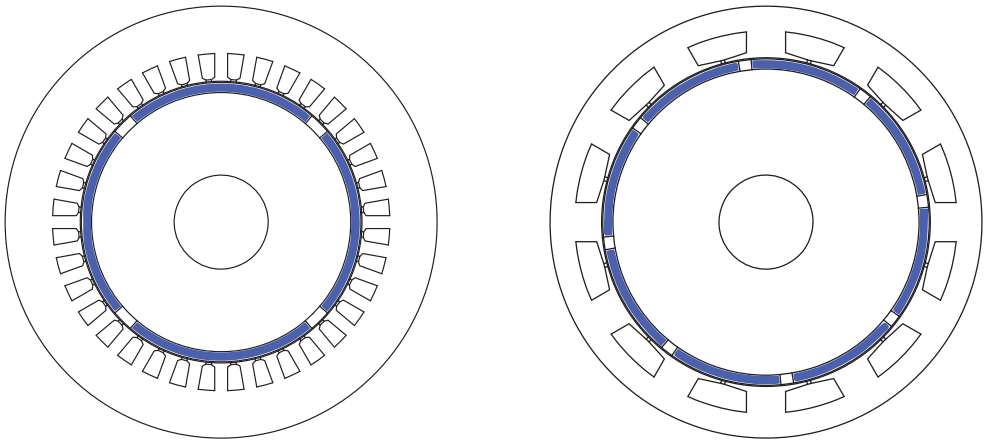

(a) SPM-B: 36-slot 4-pole, outer diameter 276mm.

(b) SPM-C: 12-slot 8-pole, outer diameter 276mm.

Fig. 4.5: SPM designs.

SPM-C. It is worth noticing that, contrarily to IPM machines, the rotor mass of SPM motors

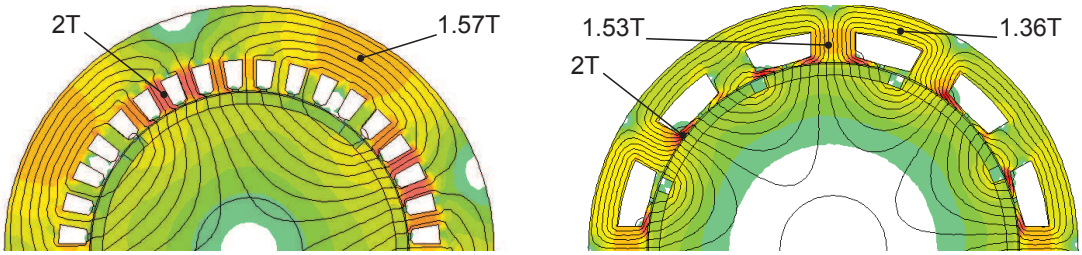

(a) SPM-B: 36-slot 4-pole, $D_e = 276mm$. (b) SPM-C: 12-slot 8-pole, $D_e = 276mm$.

Fig. 4.6: SPM machines: flux density map at rated load.

can be further reduced introducing flux barriers in proximity of the rotor shaft, without affecting the motor performance. This is especially true for the high pole number machine, SPM-C, for which a predicted reduction of about 30% is achievable.

The previous arguments emphasize as the most promising candidates the IPM-B' and SPM-C. The first machine exhibits the best torque and power vs. speed trends, especially in FW operation. The SPM-C machine, although does not show a suitable traction characteristic, offer its own advantage in view of a reduction of the motor mass due to the combination between the FSCW and the SPM configuration.

Table 4.4: Key machine parameters summary, gear ratio 1 : 8.

Design	**IPM-B'**	**SPM-B**	**SPM-C**	**Unit**
D_e	276	276	276	mm
D	180	180	210	mm
L_{stk}	40	40	40	mm
n_{MAX}	12000	18320	13280	rpm
n_B	5832	7639	8717	rpm
T_n	63	63	63	Nm
I_n	127	156	168	A_{RMS}
J_n	12.9	13.2	11.2	A_{RMS}/mm^2
Λ_{PM}	13.6	101	43.8	mVs
I_{ch}	30	163	425	A_{RMS}
n_{cs}	6	5	13.5	–
G_{Cu}	5.0	5.0	2.1	kg
G_{PM}	0.7	1.0	1.1	kg
G_{Fes}	9.0	9.0	6.0	kg
G_{Fer}	4.2	5.8	8.5	kg
G_{Fe}	13.2	14.8	14.5	kg
G	18.9	20.8	17.7	kg

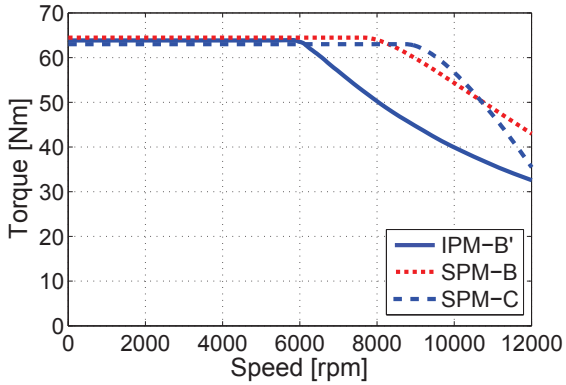

(a) Torque vs. speed.

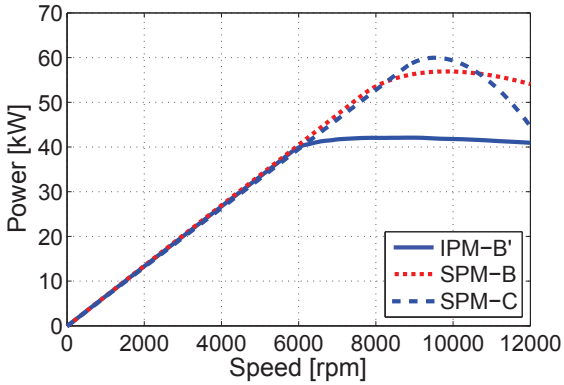

(b) Power vs. speed.

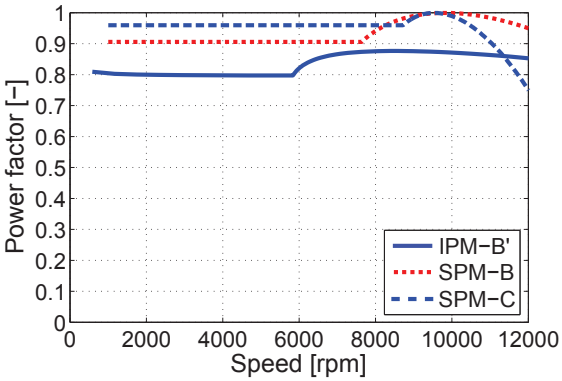

(c) Power factor vs. speed.

Fig. 4.7: Performance comparison.

4.5 Electric drive

In order to reduce the car mass, a simple power-train architecture has been selected. It is composed by a synchronous electric motor directly connected at the rear wheel by a fixed gear, a bi-directional single stage power converter and a battery pack. The block scheme of the system is shown in Fig. 5.6.

The power converter, that has been adopted for this electric vehicle, is a simple but effective single stage three phase inverter. Its DC bus is directly connected to the vehicle Energy Storage System (ESS) whose voltage V_{DC} is fixed to $300V$. The main power converter characteristics are reported in Table 5.2. A losses analysis has been carried out in order to estimate the inverter efficiency. The losses in a power converter are the conduction losses and the switching losses in its devices. The estimate efficiency has been computed by using the device characteristics [6]. In IGBT devices the switching losses $P_{switching}$ and

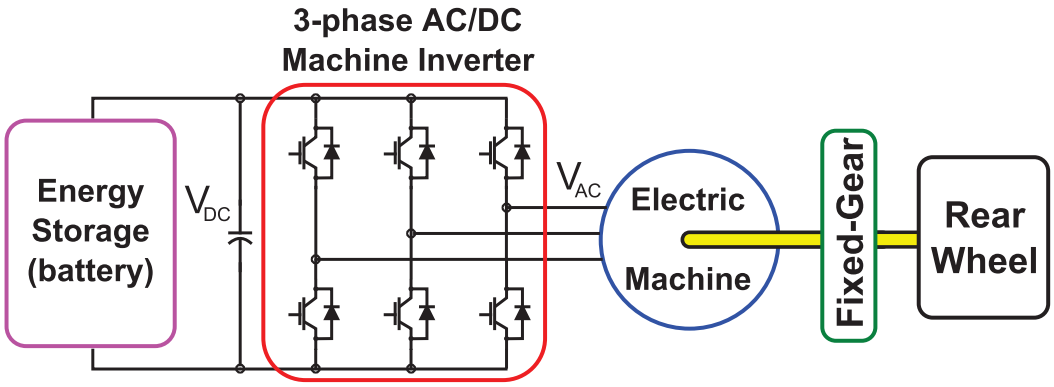

Fig. 4.8: EV power-train sketch overview.

Table 4.5: three-phase inverter parameters.

Parameter	Value
Number of phases	3
Type of switch	IGBT
Switching frequency	$10kHz$
Dead time	$2\mu s$
Maximum DC bus voltage	$300V$
Rated AC current	$180A_{RMS}$
Rated AC voltage	$120V_{RMS}$

conduction losses $P_{conduction}$ have been calculated by following formulae [119]

$$P_{switching} = (E_{ON} + E_{OFF}) \cdot f_{sw} \tag{4.5}$$

$$P_{conduction} = v_{ON} \cdot i_D \tag{4.6}$$

where v_{ON} is equal to $2V$ when the devices is in conduction, i_D is the device current, f_{sw} is the switching frequency, E_{ON} is the turn-on switching energy and E_{OFF} is the turn-off switching energy. These energies are roughly proportional to the device current and as an example are $E_{ON} = 16mJ$ @ $150A_{RMS}$ and $E_{OFF} = 8mJ$ @ $150A_{RMS}$. The converter constant efficiency loci are reported in the torque vs. speed plane of Fig. 4.9 for the most promising candidates, IPM-B' and SPM-C. It highlights that IPM-B' drive exhibits higher efficiency starting from $4000rpm$ with respect to SPM configuration. This is due to a lower rated current (about 70%). From the base speed working point, the converter efficiency of SPM-C machine decreases and the PF reduces, as previously mentioned.

In order to choose a proper ESS, a few preliminary consideration are introduced. With the rated total power fixed to $80kW$ it is necessary an ESS size of about $8-10kWh$ [61].

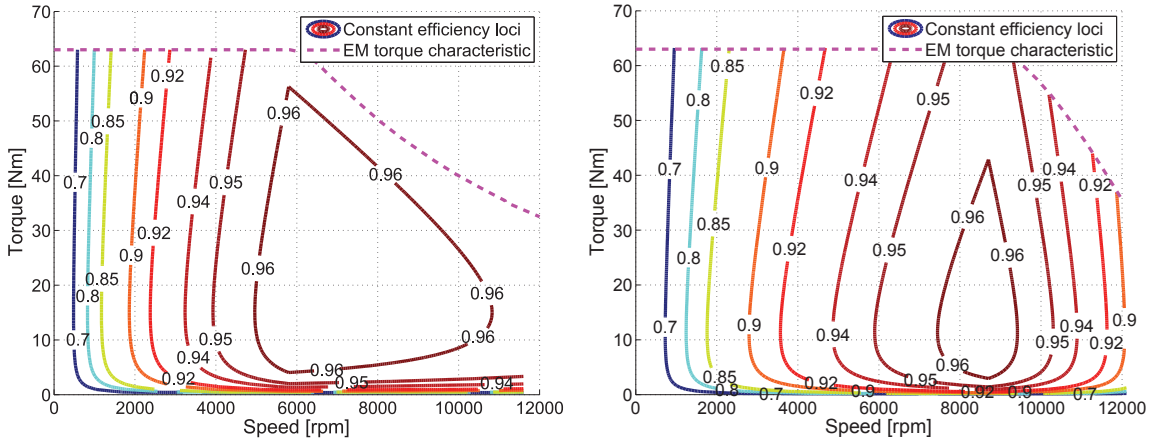

(a) IPM-B'. (b) SPM-C.

Fig. 4.9: Power converter efficiency map.

Considering the ESS data reported in [61], the mass of the battery has been estimated to be about 80kg and 140kg for Li-ion and Ni-MH technology respectively. Fig. 4.10 shows a typical spiderchart for the two battery type, representing the multiobjective function that allows to choose the best ESS. A comparison of the two solutions with the goal to choose the best trade-off between cost, volume and mass, emphasizes as the best candidate the Li-ion type, especially in the perspective of a minimization of the total mass.

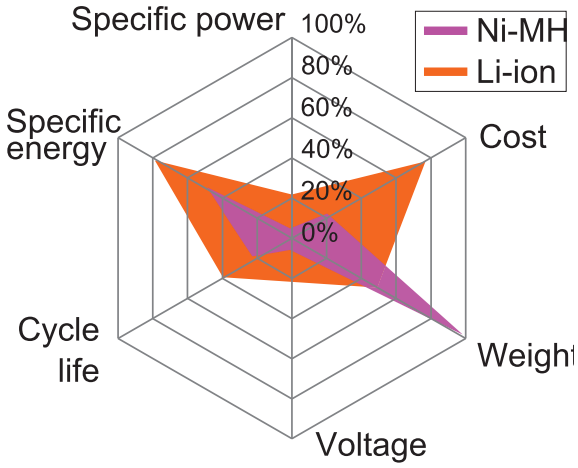

Fig. 4.10: Batteries comparison.

4.6 Conclusions

This research confirms the manufacturing feasibility of a high performance ferrite IPM motor for a formula SAE EV. The motor specifications have been estimated in accordance with the performance requirements of the competition and two gear ratios have been considered in order to achieve a size reduction. On the basis of different stator laminations, two ISDW IPM motors, with the same number of slots and poles, have been designed, optimized in terms of torque ripple and compared. Finally, a further comparison has been carried out with two equivalent size rare earth SPM machines, one equipped with the same stator lamination and number of poles, while the second is provided with a FSCW.

The results highlight that the proposed IPM design exhibits the best torque vs. speed trend for the application. Even if the proposed SPM machines show the highest torque density, especially for the FSCW configuration, the electromechanical performance over the base speed prove to be not suitable although the short FW area. In order to satisfy the torque requirements at high operating speed, a reduction of the number of conductors proves to be necessary. This is an important drawback because it yields to an increase of the phase current, making mandatory an oversizing of the power supply system (inverter and ESS). For these reasons this research emphasizes that the proposed IPM design is the most suitable solution because combines high performance in a wide speed range with a cost reduction due the adoption of rare-earth free magnet.

Chapter 5

PM synchronous machine comparison for light electric vehicles

5.1 Introduction

The current trend in the research of high performance electric motor for traction application highlights the Permanent Magnet (PM) synchronous motor as one of the best candidate [26, 53, 140, 141, 154, 162, 163], due to the high torque density, high efficiency, high degree of freedom in the design of the motor [12]. On the other hand, the increase and the price instability of rare earth PMs, such as NdFeB and SmCo, is pushing heavily the research of rare earth free alternatives. The most interesting solution is represented by the synchronous Reluctance machines (REL).

They are suitable for traction application due to the robust structure, high operating speed range, high overload capability, no electro motive force, leading to a safe behavior in case of inverter failure.

Thanks to an appropriate vector control algorithm, the performance in terms of efficiency and torque become competitive [110]. Conversely, the drawbacks of reluctance machines are the intrinsically higher torque ripple[65] and low power factor. A reduction of the torque ripple can be achieved by means of a careful choice of the number and the geometry of the rotor flux barriers, in addition to the skewing [12, 170] while an increase of the power factor is achievable by the insertion of PMs in the anisotropic rotor structure. This last configuration is known as Permanent Magnet Assisted Synchronous Reluctance (PMASR). It exhibits comparable performance to Surface mounted PM machines (SPM) needing a limited amount of expensive rare earth magnets. The same capability can be achieved filling the flux barrier with ferrite PMs, obtaining a low cost solution [9, 169].

Four different machine topologies have been considered and compared in terms of electromechanical performance and efficiency in the whole operating area. All the machines share the same stator geometry, overall dimensions and number of poles. The ferrite PMASR motor has been developed and optimized to maximize the torque density, minimize the torque ripple and PM volume and it has been considered as reference machine. All the machines are feed by the same power supply system, which rating represent a further constraint in this analysis. Finally, the efficiency of inverter coupled with the machines, has been investigated and some considerations are reported.

5.2 Machine Design and Optimization

A 36-slot stator lamination geometry is given as a constraint. The outer diameter D_e and the airgap diameter D are 276 mm and 180 mm, respectively. The airgap is fixed to $g = 0.7$ mm. The slot area is $S_s = 148$ mm^2, the fill factor is assumed to be $k_{fill} = 0.4$ while the peak current density has been fixed to $J_{MAX} = 13$ A_{RMS}/mm^2. The stack length is constrained to 40 mm. A $M470-50$ steel grade is considered for the lamination. Finally, a 300 V DC bus feeds the traction system.

The specifications, used for the motor design, are computed on the basis of the dynamic performance requested for a Light Electric Vehicle (LEV). This car, currently in development, is designed for a racing competition.
The main electromechanical requirements are summarized as follows:

- Peak torque, $T_{MAX} = 60$ Nm.
- Base speed, $n_B = 6000$ rpm.
- Maximum speed, $n_{MAX} = 12000$ rpm.
- Flux weakening range, $1:2$ [28].

With the aim of reducing the maximum supply frequency and thus the iron losses, the number of poles has been selected to $2 \cdot p = 4$. On the other hand, unlike PMASR machines with a high number of pole, designs with lower number of poles exhibit a higher anisotropy [8]. An integral slot distributed winding has been considered. This winding arrangement proves to be the most effective solution when a high anisotropic rotor is adopted. A high saliency ratio is expected especially if compared to a Fractional Slot Concentrated Winding (FSCW) solution [41, 162].

The motor topologies, considered in this analysis, are shown in Fig. 5.1. The PMASR motors of Figs. 5.1(a) and 5.1(b) are characterized by a symmetrical rotor with three flux

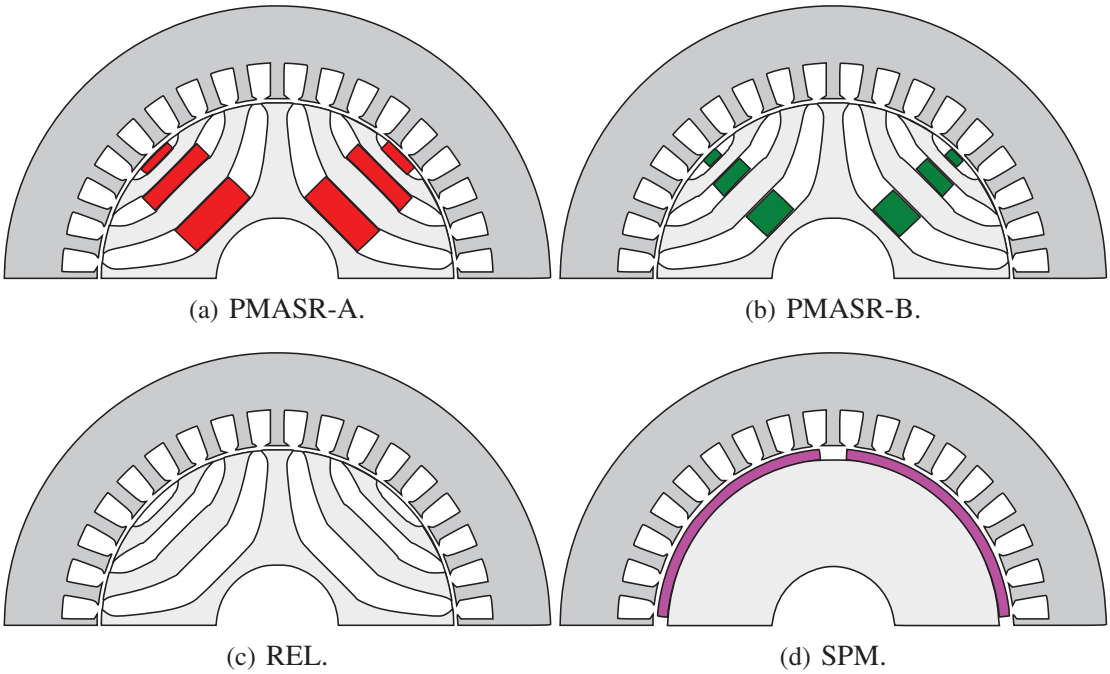

(a) PMASR-A. (b) PMASR-B.

(c) REL. (d) SPM.

Fig. 5.1: Motor sketches.

barriers per pole. The PMASR-A is filled with ferrite (remanence flux density 0.4 T @ 20 $^{\circ}C$, knee flux density 0.1 T @ -40 $^{\circ}C$, recoil permeability 1.05, density 4800 kg/m^3). In PMASR-B a more valuable $NdFeB$ PMs has been used (remanence flux density 1.1 T @ 20 $^{\circ}C$, knee flux density 0.1 T @ 140 $^{\circ}C$, recoil permeability 1.05, density 7500 kg/m^3). PMASR-A has been considered as reference machine. The torque ripple, the torque density and the PM volume, have been optimized under peak load condition by means of a multiobjective non-dominated sorted genetic algorithm. The stator geometry has been fixed during the optimization procedure and the optimization variables are the flux barrier angles and the insulation ratio [60], defined as follows,

$$k_{air} = \frac{2 \cdot \sum_i t_{bi}}{D_r - D_{sh}} \tag{5.1}$$

where t_{bi} is the thickness i-th of the flux barrier, D_r is the rotor diameter and D_{sh} is the shaft diameter.

Moreover, for each iteration, the PM demagnetization levels at the peak current density have been verified in order to provide effective solutions. A motor design is accepted when the minimum flux density in the PM is higher than the flux density at the knee of the BH curve (the demagnetization test temperature is considered, $-40^{\circ}C$).

Finally, an optimal solution has been selected. It shows a peak torque of 60 Nm with a torque ripple of 14 %. The number of conductors per each slot, series configuration, n_{cs}, has been changed in order to adjust the base speed close to the requested target of 6000 rpm.

On the basis of the PMASR-A rotor lamination, a PMASR-B and a REL topology, shown in Figs. 5.1(b) and 5.1(c), have been introduced. Finally, a SPM machine, reported in Fig. 5.1(d), has been designed. It is equipped with a rotor characterized by 4 C-shape $NdFeB$ PMs. It is important to highlight that the minimum PM thickness has been evaluated in order to ensure a safe demagnetization under deep flux weakening operation.

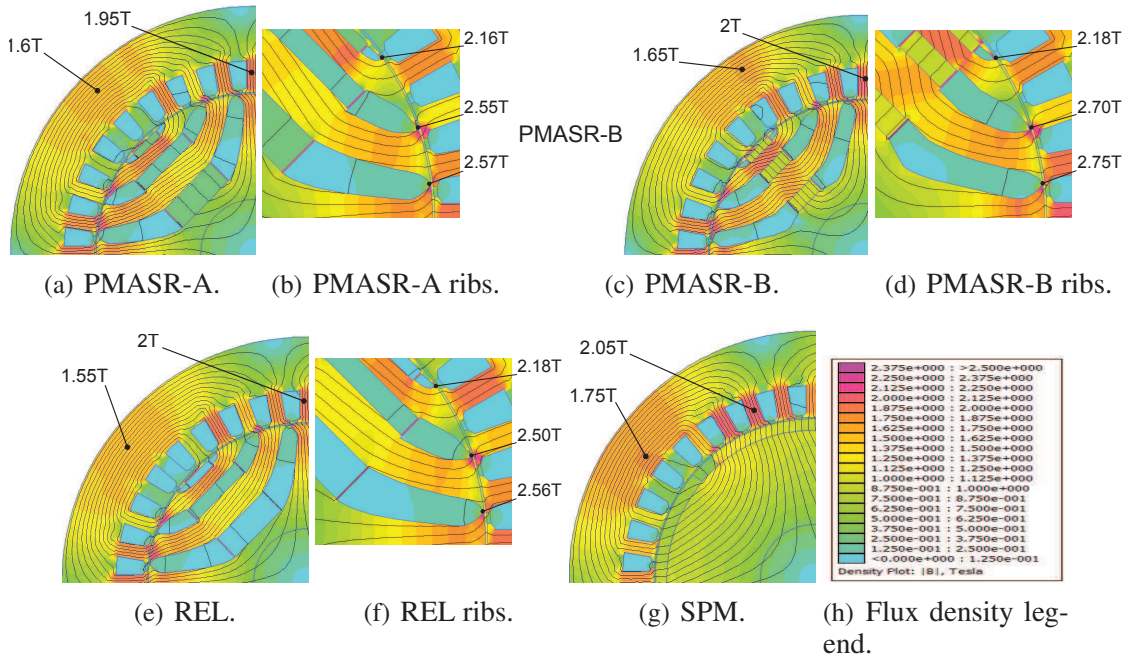

(a) PMASR-A. (b) PMASR-A ribs. (c) PMASR-B. (d) PMASR-B ribs.

(e) REL. (f) REL ribs. (g) SPM. (h) Flux density legend.

Fig. 5.2: Flux density maps at peak load operation.

In order to provide a meaningful comparison, PMASR-B, REL and SPM are characterized by the same number of conductors of PMASR-A. Therefore, they exhibit equal peak current and VA-rating, thus leading to employ the same inverter.

Since the machines are designed in overload operation, a proper cooling system is mandatory. Even if it increases the complexity of the traction system, it yields to reduce the machine mass, improving the car dynamic performance. Conversely to $NdFeB$, the ferrite has got a positive reversible temperature coefficient of coercivity. This increases the demagnetization strength as the temperature increases, leading to an improvement of the motor performance.

Table 5.1: Key machine parameters summary

Design	PMASR-A	PMASR-B	REL	SPM	Unit
T_{MAX}	60	61	53	72	Nm
n_B	5738	5981	5853	5632	rpm
n_{MAX}	>12000	>12000	>12000	10626	rpm
I_{MAX}	129	129	129	129	A_{RMS}
PF_B	0.80	0.84	0.72	0.96	$-$
γ_B	61	60	64	9	$^\circ$
Λ_{PM}	16.3	29.5	0	138	mWb_{peak}
L_{dB}	0.233	0.230	0.239	0.207	mH
L_{qB}	1.52	1.42	1.64	0.325	mH
ξ_B	6.5	6.2	6.9	1.5	$-$
I_{ch}	42	76	0	263	A_{RMS}
P_{CuB}	2530	2530	2530	2530	W
P_{FeB}	654	697	625	662	W
η_{eB}	91.8	92.1	91.2	93.0	%
n_{cs}	6	6	6	6	$-$
G_{Cu}	5.8	5.8	5.8	5.8	kg
G_{PM}	0.71	0.45	0	1.1	kg
G_{Fes}	9.0	9.0	9.0	9.0	kg
G_{Fer}	5	5.5	5	6.8	kg
G_{Fe}	14	14.5	14	15.8	kg
G	20.5	20.75	19.8	22.7	kg
$Cost$	1	1.39	0.93	2.08	$p.u.$

5.3 Comparison of the topologies

The electromechanical performance of the machines have been evaluated on the basis of the synchronous space vector control in the d/q reference frame. The machine is controlled in order to exhibit a constant torque up to the base speed, working along the Maximum Torque per Ampere (MTPA) locus. For speeds higher than the base one, the motor is operated in FW, along the current limit and the Maximum Torque Per Voltage (MPTV) locus, if included [84, 151, 153].

An overload analysis has been performed in order to evaluate the flux density levels at the peak load. The flux density maps are shown in Fig. 5.2.

PMASR-A and PMASR-B motor, in Figs. 5.2(b) and 5.2(d) respectively, show local saturation, especially in the areas corresponding to the stator teeth and the rotor iron ribs, as expected at peak load condition. As regards the REL machine, reported in Fig. 5.2(f), the saturation is lower due the absence of PMs in the rotor structure. Conversely, the stator saturation for the SPM motor is higher, due to the higher flux contribution of the PMs which are placed on the rotor surface.

Table 5.1 summarizes the main electromechanical results, masses and cost indexes. They are represented by the peak torque T_{MAX}, the peak current I_{MAX}, the base speed n_B, the maximum speed n_{MAX}, the Power Factor PF_B, the commutation angle γ_B, the PM flux linkage Λ_{PM}, the d-axis synchronous inductance L_{dB}, the q-axis synchronous inductance

L_{qB}, the saliency ratio ξ_B and the characteristic current I_{ch}. As regards the losses, the copper losses P_{CuB}, the iron losses P_{FeB} and the electrical efficiency η_B are reported. The subscript B highlights that the quantity has been evaluated at the base point, along the MTPA locus. Finally the mass quantities have been computed as well, including the copper G_{Cu}, PMs G_{PM}, stator iron G_{Fes}, rotor iron G_{Fer}, total iron G_{Fe} and total G.

Let us consider PMASR-A motor as reference machine for the following comparisons. Even if the volume of $NdFeB$ PMs used in the PMASR-B motor is about 40 % lower, the PM flux linkage is almost doubled. The SPM motor instead, which exhibit a volume of rare earth PMs 60 % higher, shows a PM flux linkage about 4.5 times higher.

5.3.1 Constant torque capability

As regards the operation in the constant torque region, PMASR-B and SPM motors exhibit respectively a peak torque of 1 % and 20 % higher than that of PMASR-A. Conversely, the REL motor torque is almost 12 % lower. It is well known that the PMs, assisting a reluctance machine, are using part of their flux to saturate the internal iron bridges and the iron ribs located on the rotor periphery, which are necessary for mechanical reasons. For this reason, REL machines require a higher current in order to provide the same saturation effect ensured by the PMs in the PMASR motors. For the REL motor under study, to reach the peak torque specification of 60 Nm the corresponding current has to be increased up to around 142 A_{RMS}.

Concerning the anisotropy of the reluctance machines, the results show comparable saliency ratio, in the range $6-7$. The highest is achieved by the REL machines, while the lowest is exhibited by the PMASR-B. An analysis of the ratio between the $d/q-$axis synchronous inductances of PMASR-B shows that the L_{dB} is the lowest among the designs due to the higher rib saturation. On the other hand, the L_{qB} is reduced as well due to the higher saturation of the iron paths between flux barriers, as shown in Figs. 5.2(c) and 5.2(d). It is worth noticing that the SPM machine provides a limited anisotropy, with a saliency ratio in the order of 1.5.

5.3.2 Flux weakening capability

Torque, power and PF trends are reported in Fig. 5.3.
Analysis shows that a characteristic current (given by the ratio between PM flux linkage and d-axis inductance) close to the peak current I_{MAX}, ensures an excellent Constant Power Speed Range (CPSR) capability [153]. Although this condition is not achieved for all the

considered motors, as shown in Table 5.1, due to the limited requested Flux Weakening (FW) ratio (2 : 1), the performance over the base speed are well suited for the PMASR-A and PMASR-B machines.

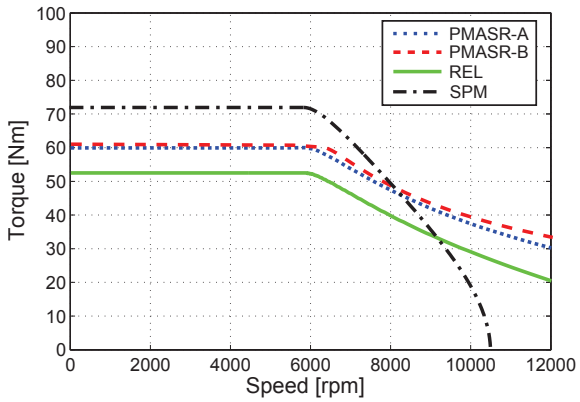

(a) Torque vs. speed.

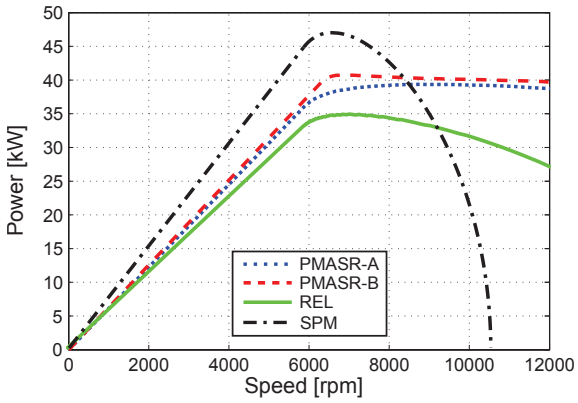

(b) Power vs. speed.

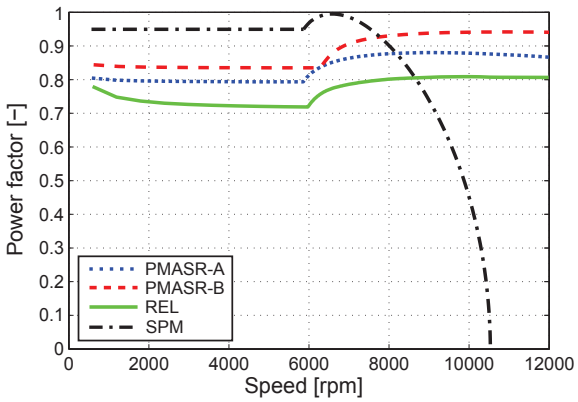

(c) Power factor vs. speed.

Fig. 5.3: Electromechanical performance.

The higher value of the characteristic current I_{ch} of PMASR-B motor produces a slightly better CPSR and power factor with respect to the PMASR-A, as shown in Figs. 5.3(b) and 5.3(c), respectively. These results confirm the wide speed range capability of synchronous reluctance machines. The PMASR and REL machines outmatch the maximum speed target of $12000rpm$. Since the characteristic current is lower than the rated one [153], the current space vector is controlled in order to work along the MTPV locus machine in deep FW operation, and the maximum speed is only limited by the mechanical strength of the rotor and bearing design.

Despite the SPM motor exhibits a higher overload torque, in the FW region the torque and power characteristics decrease down quickly to 0 up to a maximum speed $n_{MAX} =$

10500 *rpm*. In fact, the characteristic current of the SPM machine is higher than the peak current, yielding to a torque vs. speed characteristic not suitable for traction application. It is worth noticing that the combination of the SPM with a FSCW is able to provide an optimal FW performance [54].
In order to provide a torque profile which encloses the PMASR motors torque vs. speed curve, the base speed has to be increased to 8900 *rpm*, reducing the number of conductors per each slot, series configuration n_{cs} down to 4. On the other hand, this measure requires an oversizing of the supply converter. An improvement of the constant torque region is achievable by means of a reduction of the PM flux linkage, i.e. the peak torque, reducing the machine stack length of about 17 %. The base speed and the maximum speed are expected to increase of about 20 %, up to 7200 *rpm* and 11700 *rpm* respectively and the same inverter size can be used.

Regarding the PF trends, shown in Fig. 5.3(c), SPM machines provides the highest value in the constant torque region, in the order of 0.95 up to 6000 *rpm*. Similarly to the power trend, the PF falls quickly as the speed increases.

The performance of the REL motor in terms of torque power and PF, are lower than the other motor topologies. The SPM machine, although provides the highest torque density, it is not suitable for the applications considered in this research, which require a wider speed range. However, its behavior in FW operation might be suitable for those application which require a less extended speed range, such as electric vehicle for urban mobility [30].

5.3.3 Losses and efficiency

The computation of the losses and electrical efficiency has been performed, according to the vector control strategy in the $I_d - I_q$ plane, mentioned in Sec. II. The Bertotti's equation is used for the evaluation of the iron losses, on the basis of the hysteresis and eddy current coefficients extracted from the losses curve data available for the lamination.

As reported in Table 5.1, a comparison of the losses at the base point, show similar results among the machines. On the other hand, since the study has been performed at the same overload current and not at the same torque, an analysis of the losses and the efficiency in the whole operating area is more meaningful.
Fig. 5.4 reports the trend of the losses in the torque vs. speed plane for PMASR-B and SPM machine. It is worth noticing that in both cases the losses profile tends to follow the trend of the torque.
Fig. 5.5 shows the comparison of the machines electrical efficiency maps in the torque vs.

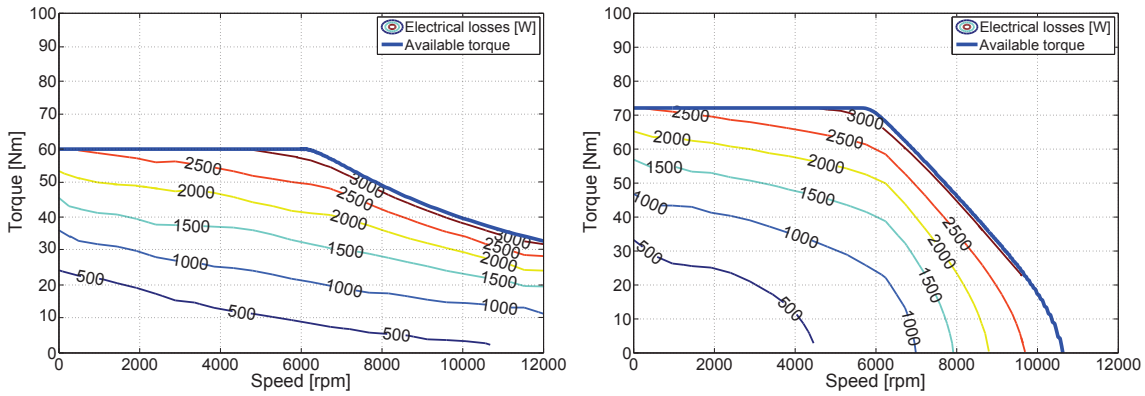

(a) PMASR-B. (b) SPM.

Fig. 5.4: Constant electrical losses loci in the torque-speed plane.

speed plane. The available overload torque profile is highlighted. The highest electrical efficiency, in the order of 94 %, is provided by the PMASR-B and SPM. Comparing to the PMASR-B, the PMASR-A and REL motors show a lower efficiency due to the worser FW capability.

On the other hand, the distribution of efficiency is different between the reluctance and SPM machines. The SPM machine exhibits an higher efficiency operation in medium speed range, around the base speed. Due to the remarkable reduction of the torque as the speed increases over the base one, the efficiency falls quickly in FW operation.

5.3.4 Economical comparison

As regards the masses, the lowest values are achieved by the REL and PMASR-A motor, due to the absence and lower mass density of the ferrite PMs in comparison to that of *NdFeB*, respectively. Contrarily to PMASR machines, the rotor mass of SPM motors can be further reduced introducing flux barriers in proximity of the rotor shaft, without affecting the motor performance.

Finally, the total machine costs are evaluated in p.u., considering the average cost of the iron lamination and PMs as for 2014. It is worth noticing that the noticeable increase of about 40 % of the PMASR-B machine cost due to the more valuable *NdFeB* PM, leads to a negligible increase of the performance in terms of peak torque and PF. While the REL motor exhibit the lowest total cost, about 7 % lower than that of PMASR-A, the SPM solution shows a doubling of the cost.

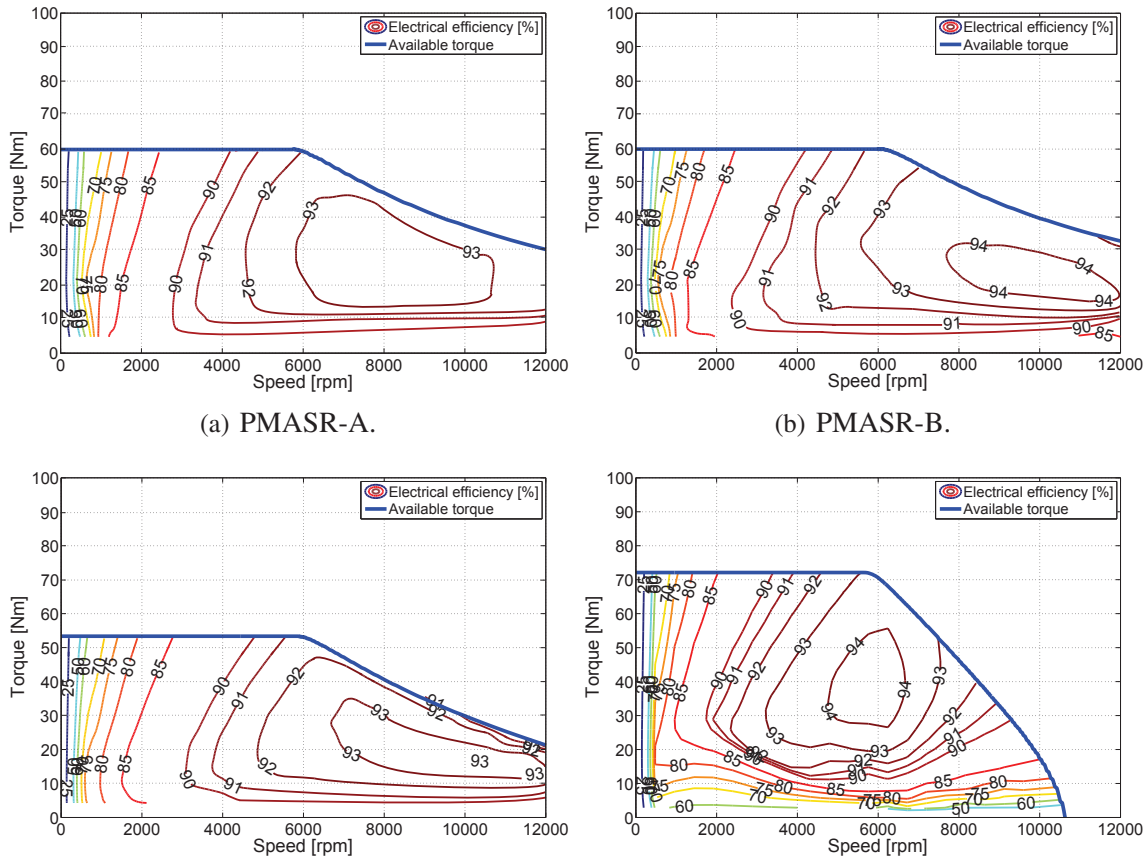

(a) PMASR-A. (b) PMASR-B.

(c) REL. (d) SPM.

Fig. 5.5: Constant electrical efficiency loci in the torque-speed plane.

5.3.5 Overview of the electric supply system

In LEVs mass represents a critical aspect. For this reason, the car power-train architecture considered in this work is quite simple. It is composed by synchronous electric machine (EM) direct connects at the rear wheels by a fixed gearbox, a bi-directional single-stage power converter and an battery packs. Fig. 5.6 reports a block scheme of the considered system architecture.

The power converter, that has been considered for this LEV, is a simple but effective half bridge three-phase inverter. Its DC bus is direct connected to the vehicle energy storage whose voltage, V_{DC}, is fixed to 300 V. The power converter features are summarized in Table 5.2.

As reported in Fig. 5.7, the power converter efficiency maps has been studied for the considered motor topologies, highlighting the overload torque profile.
Fig. 5.7 shows that the highest efficiency, about 96%, is provided by all electric machines.

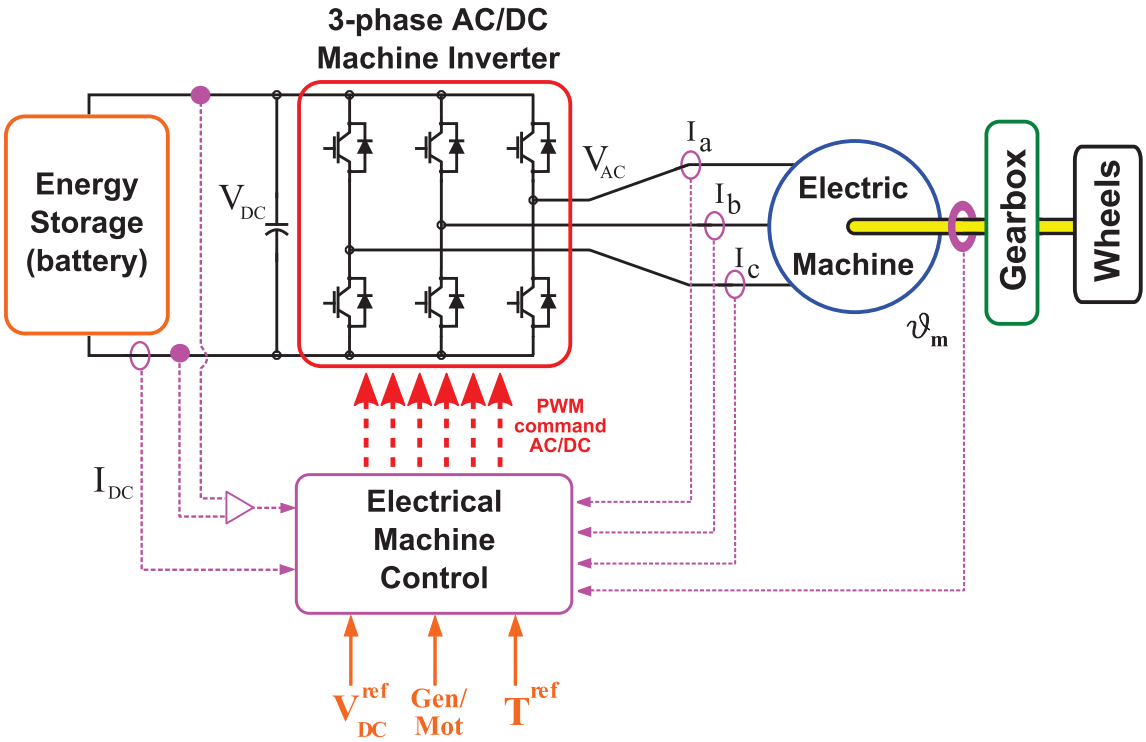

Fig. 5.6: LEV power-train sketch overview.

As already reported in Fig. 5.7(d), the SPM machine exhibits an higher efficiency around the base speed and medium speed range. Moreover, in FW region the efficiency falls quickly as the speed increases principally due to the high reduction of the torque. Conversely to the PMASR-A, the PMASR-B and REL motors show a higher efficiency in the FW operation.

These losses analysis has been carried out in order to estimate the inverter efficiency in the different EMs working points. The principle reasons of the losses in a power converter are the conduction losses and switching losses in its devices, [119]. The switching losses, p_{sw}, and conduction losses p_{cond} with IGBT devices have been calculated by following formulae, [120, 124]:

$$p_{sw} = (E_{ON} + E_{OFF}) \cdot f_{sw} \tag{5.2}$$

$$p_{cond} = v_D \cdot i_D \tag{5.3}$$

where v_D and i_D are the device voltage and the current, respectively. E_{ON} the turn-on switching energy, E_{OFF} turn-off switching energy and f_{sw} is the switching frequency. As reported in the device characteristics, these energies are roughly proportional to device current and as example are $E_{ON} = 16\ mJ\ @\ 150\ A_{RMS}$ and $E_{OFF} = 8000\ mJ\ @\ 30\ A_{RMS}$.

Table 5.2: Three-phase inverter parameters.

Parameter	Value
Number of Phases	3
Type of switch	IGBT
Maximum DC bus voltage	300 V
Rated AC current	200 A_{RMS}
Rated AC voltage	120 V_{RMS}
Type of switch modulation	SVM
Switching frequency	20 kHz
Dead time	2 μs

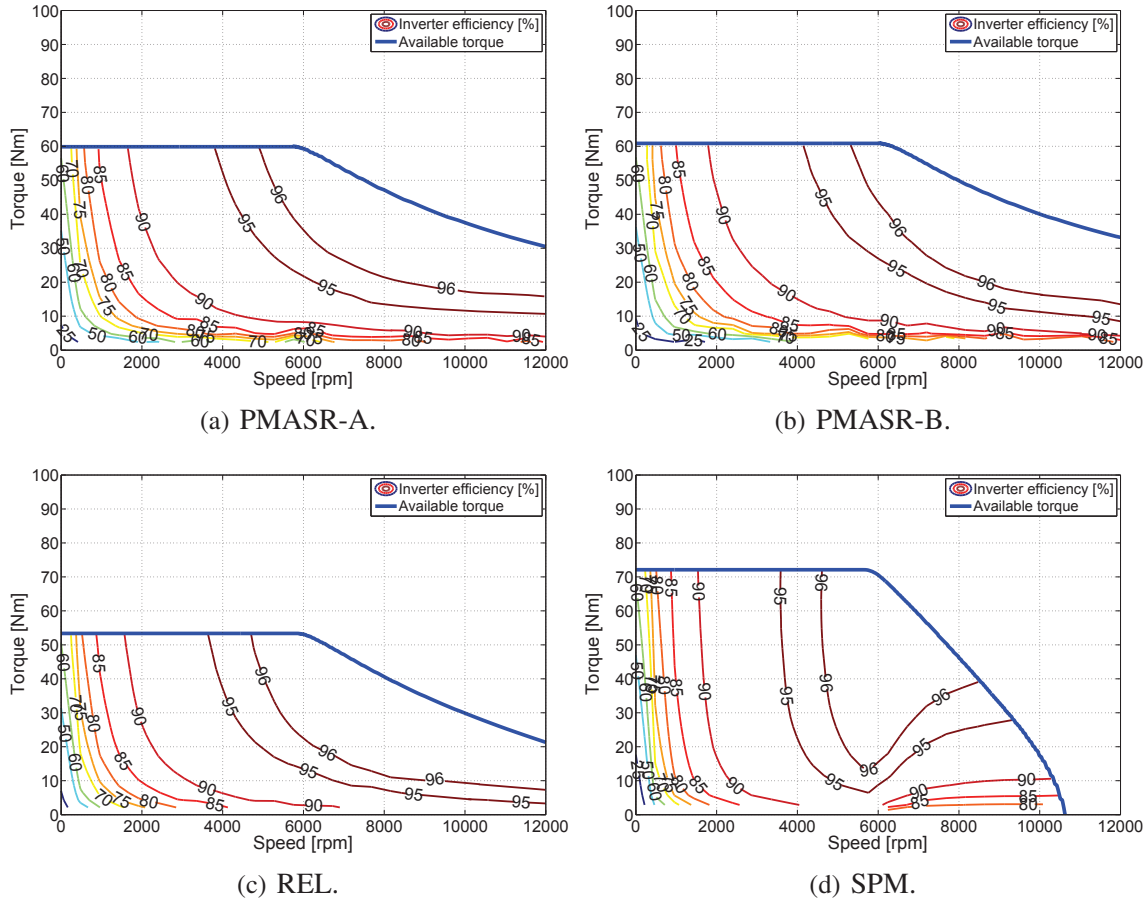

(a) PMASR-A.

(b) PMASR-B.

(c) REL.

(d) SPM.

Fig. 5.7: Constant inverter efficiency loci in the torque-speed plane.

5.4 Conclusions

This research confirms the feasibility of the realization of an high performance ferrite PMASR for traction applications. The motor capabilities have been computed on the basis of the dynamic performance requested for a LEV. A ferrite PMASR machine has been designed and optimized with the aim of minimizing the torque ripple, PM volume and maximizing the torque density. On the basis of the same stator laminations, winding arrangement and number of poles, four different machine have been analyzed and compared. The results highlight that the proposed PMASR motor exhibits an optimal torque vs. speed behavior for the application.

Even if the proposed SPM machine shows the highest torque density, due to the limited FW area, the electromechanical performance over the base speed are not suitable. In order to satisfy the torque requirements at high operating speed, a reduction of the number of conductors proves to be necessary. This is an important drawback because it yields an increase of the phase current and an oversizing of the power supply system. For these reasons, this research emphasizes that the proposed PMASR machine is an excellent solution. It combines high efficiency in a wide speed range with a cost reduction due the adoption of ferrite PMs or with a small volume of rare-earth PMs. Moreover, this research shows that the adoption of the $NdFeB$ in PMASR design, does not provide significant advantages requiring a complete redesign of the rotor geometry.

Chapter 6

Electric vehicle traction based on a PM assisted synchronous reluctance motor

6.1 Introduction

The electric motors are key devices in an electric powertrain. Among the various typologies, the synchronous motors provide the best performance, in terms of high torque and power density, high speed capability, wide speed range, high efficiency and mass saving. Interior Permanent Magnet (IPM) motors with rare-earth magnets are mainly used for Electric Vehicles (EVs) and hybrid EVs (HEVs). They exhibit high torque density and constant power operation in a wide speed range. However, due to the high cost of rare-earth magnets and to the limited supply, IPM motors are becoming too expensive.

Therefore, the synchronous reluctance (REL) machine is becoming of great interest in the recent years. If properly designed, it represents a valid alternative for EVs and HEVs for its simple and rugged construction and for hazard-free operations [137, 159]. The REL motor as well as the ferrite PM assisted REL (PMASR) motor are becoming competitors of both surface–mounted PM machines and induction machines not only in automotive but also in many other applications [9].

A four–pole REL machine is sketched in Fig. 6.1, whose rotor has three flux barriers per pole. Rotor configurations with several flux barriers per pole allow to achieve a high rotor saliency, that is, a high average torque. The rotor geometry has a high influence on the machine performance [170]. In designing such a REL motor, the main attention has to be given (i) to maximize the average torque, (ii) to minimize the torque ripple and (iii) to maximize the motor efficiency in an extended speed range.

The synchronous PMASR motor is achieved when PMs are inset within the flux barriers

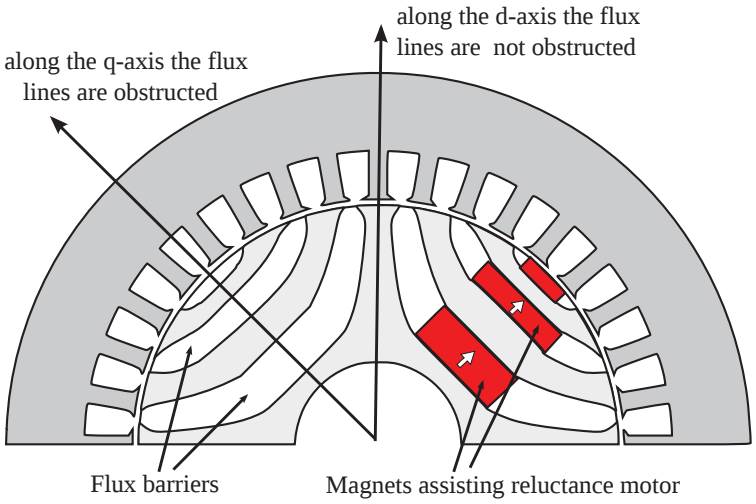

Fig. 6.1: Scheme of the synchronous reluctance motor.

[93]. They increase not only the average torque but also the power factor (PF), which is commonly quite low in a REL motor. In fact, the PM flux saturates the iron bridges, reducing the magnetizing stator current, and tends to rotate the flux linkage vector out of phase of 90 degrees with respect the current vector.

6.2 Torque versus current vector angle

Some motor prototypes (main data are given in Appendix) designed for electric vehicle application were tested experimentally. Rotors with and without skewing were tested, and with and without assisting PMs in the rotor flux-barriers.

Fig. 6.2(a) shows the measured torque versus the current angle for the REL machine, according to different current amplitudes. It refers to the motor without skewing. With skewed rotor, the torque is about 6% lower, as shown in section 6.10.

Fig. 6.2(b) shows the torque versus the current angle of the PMASR machine, without skewing, according to different current amplitudes. ferrite PM is used, which is characterized by a remanence $B_r = 0.4T$ (at $20^{\circ}C$). With a step–skewed rotor, the torque is about 5% lower.

As expected, comparing the torque exhibited by the REL motors (Fig. 6.2(a)) and by PMASR motors (Fig. 6.2(b)) it is verified that there is a higher average torque when the PMs assist the motors. As an example, according to a current of $10A_{peak}$, the average torque increases from $11.3Nm$ to $12.1Nm$. According to a current of $10A_{peak}$, the average torque increases from $17.7Nm$ to $19.0Nm$.

In addition, in the PMAREL motor the current angles along the MTPA trajectory are slightly lower: the current vector rotates towards the PM flux linkage vector.

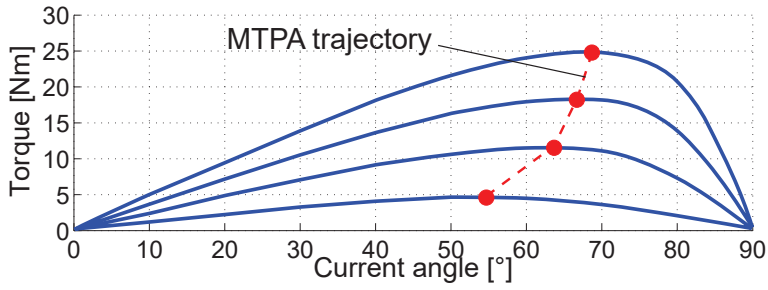

(a) REL.

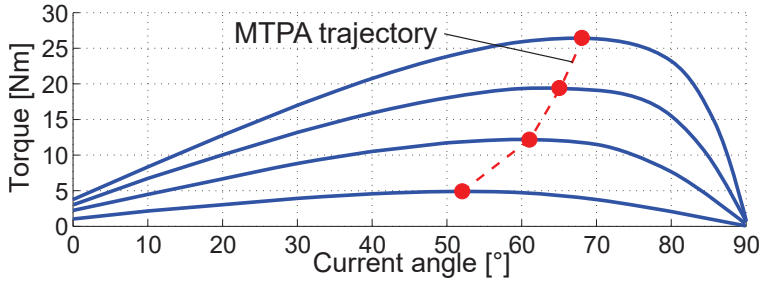

(b) PMAREL.

Fig. 6.2: Average torque versus current angle of non skewed motors (experimental results). Currents used in the tests are $5A_{peak}$, $10A_{peak}$, $15A_{peak}$ and $20A_{peak}$.

6.3 No-Load Voltage of PMASR motor

Fig. 6.3 shows the no-load voltage induced by the ferrite magnets in the PMAREL motor. The motor prototype has been designed for a industrial voltage so as to test it in laboratory test bench. The measured no-load voltage is quite low with respect the nominal voltage of the motor. From the test, the PM flux linkage results in $\Lambda_{PM} = 0.117 Wb_{peak}$.

6.4 Steady-state operations

Table 6.1 reports some measurements at steady-state operations. The tests have been carried out feeding the motors by different currents I in order to produce a given output torque, varying in the range between 2 and $12Nm$, at given rotation speeds. The d– and q–axis currents are selected so as to operate along the MTPA trajectory (see Figs. 6.2(a) and 6.2(b)).

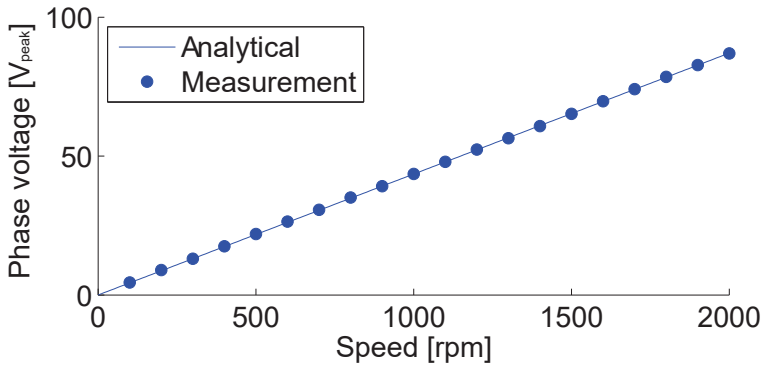

Fig. 6.3: No load voltage of the ferrite-based PMAREL motor

Even though the PM is a low–energy (ferrite) magnet, it is worth noticing that the use of the PMs reduces the required stator current. The losses are reported as a percentage of the output power. Since the test speed is quite low, the output power is quite low, then the loss percentage results to be quite large. However, the comparison between REL and PMAREL motors highlights the high loss reduction when PMs are added to assist the motor, especially at part loads.

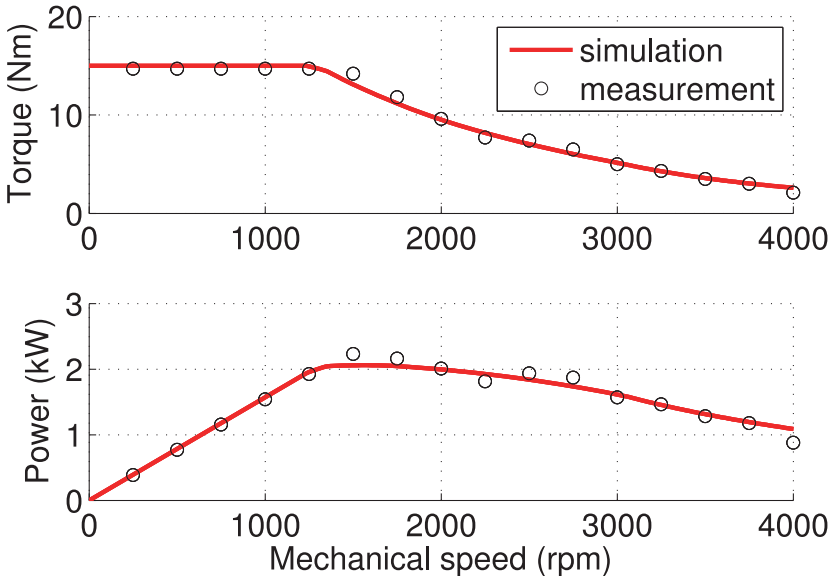

Fig. 6.4: REL motor: torque and power versus speed. Experimental versus simulated results.

The Power Factor (PF) is also reported. The voltage is measured adding a filter between the inverter and the wattmeter, so as to extract the fundamental voltage harmonic. It is possible to observe an increase of PF in the PMAREL motor.

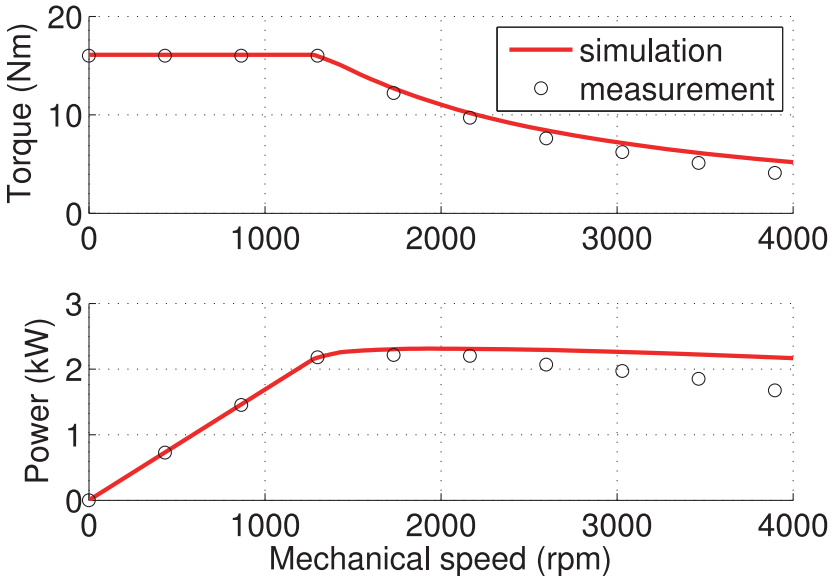

Fig. 6.5: PMAREL motor: torque and power versus speed. Experimental versus simulated results.

Table 6.1: REL motor: steady state operations.

		REL motor			PMAREL motor		
Speed	**Torque**	**Current**	**Power factor**	**Eff.**	**Current**	**Power factor**	**Eff.**
$[rpm]$	$[Nm]$	$[A_{peak}]$	$[-]$	$[\%]$	$[A_{peak}]$	$[-]$	$[\%]$
250	2	2.26	0.64	92	2.00	0.71	47
	4	3.35	0.72	72	3.07	0.78	51
	6	4.4	0.78	72	4.06	0.84	56
	8	5.39	0.81	75	5.03	0.87	61
	10	6.42	0.83	85	6.03	0.88	69
	12	7.43	0.85	92	6.99	0.90	75
500	2	2.25	0.70	64	2.00	0.77	27
	4	3.34	0.75	45	3.07	0.81	30
	6	4.38	0.79	41	4.06	0.86	30
	8	5.38	0.82	43	5.03	0.87	33
	10	6.38	0.83	45	6.03	0.88	37
	12	7.44	0.84	49	6.99	0.89	41

6.5 FW performance

The motors have been tested at various rotating speeds to determine their Flux-Weakening (FW) performance [93]. Fig. 6.4 shows the torque and power versus speed of the REL machine. Solid line refers to the simulated curve, while circles refer to the measurements.

The current has been limited to $12A_{peak}$. Similarly, Fig. 6.5 shows the torque and power versus speed for the PMAREL machine. There is a good agreement between the simulated and the measured operating points, even if at higher speeds the predicted torque of the PMAREL motor is higher than the measured one.

The comparison highlights not only the higher torque at low speed, but also the higher torque and power at higher speeds, under the FW control.

6.6 Short-circuit currents in PMAREL motor

The three phases of the PMAREL motor have been short-circuited to simulate a winding fault. Fig. 6.6 shows the short-circuit current amplitude, measured at different rotor speed. It is observed that the current always increases with the speed, approacing the characteristic current, that is, Λ_{PM}/L_q.

When the short-circuit currents flow in the stator winding, a braking torque arises. This is in undesidered phenomenon in several applications and sometimes it could be dangerous. In fact, the short-circuit event might produce a quick brake of the vehicle. In case of ferrite-based PMAREL motor, the contribution of PM flux is quite low, so that the corresponding braking torque is low as well. From Fig. 6.6, it is observed that the peak braking torque is lower than 1 Nm.

6.7 Measurements under overload

Fig. 6.7 shows the measured torque versus current of the REL motor. The current vector has been chosen along the MTPA trajectory. The current is increased up to about four times the nominal current. After a parabolic trend at lower current, as expected when the motor works without reaching iron saturation, the torque results to vary almost liniearly with the stator current.

Dashed lines in Fig. 6.7 refer to the maximum and minimum peaks that have been measured on the torque behaviour. As expected, the torque ripple increases with the average torque, but its percentage value remains almost the same.

Fig. 6.8(a) shows the k_T factor versus the current. Such a factor is computed as the ratio between the measured average torque and the current (peak value) corresponding to such a torque. It is worth noticing that such a k_T factor tends to remain constant in the whole overload operating region. Roughly speaking, the d-axis flux remain constant, since the d-axis path is saturated, and the torque is then proportional to the q-axis current.

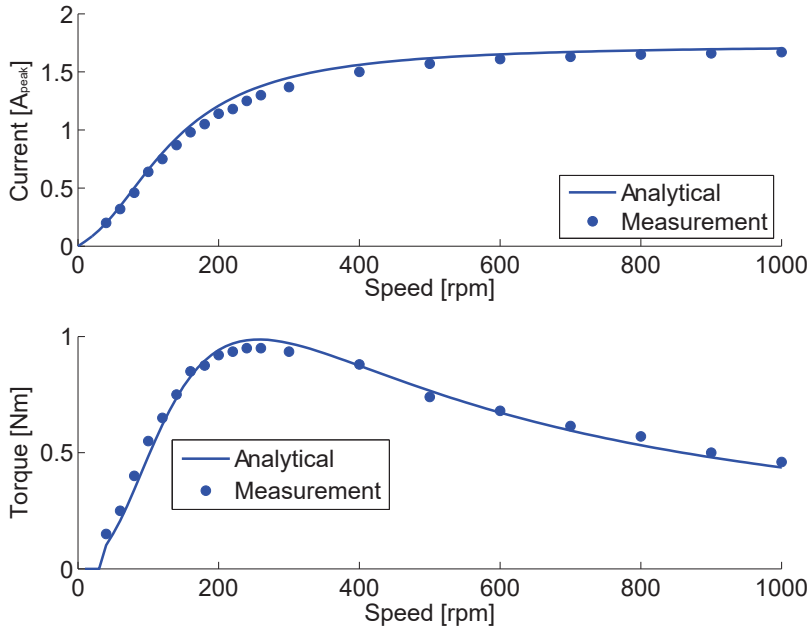

Fig. 6.6: Current and braking torque in the event of a three-phase short circuit in the PMAREL motor.

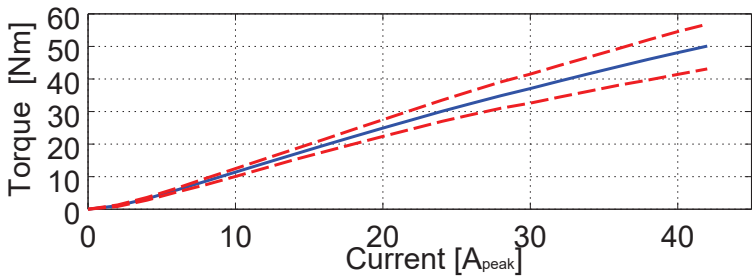

Fig. 6.7: Torque versus current (experimental test).

Fig. 6.8(b) shows the k_T^* factor versus the current. Such a factor is computed as the ratio between the torque and the corresponding current square. As expected, it decreases monotically, as the iron saturation increases with the current.

6.8 PM demagnetization

Some FEAs have been carried out so as to investigate the impact of the stator current on the demagnetization of the magnets. A positive q-axis current is considered, which represents the demagnetizing current, since the PM is oriented along the negative q–axis, as sketched

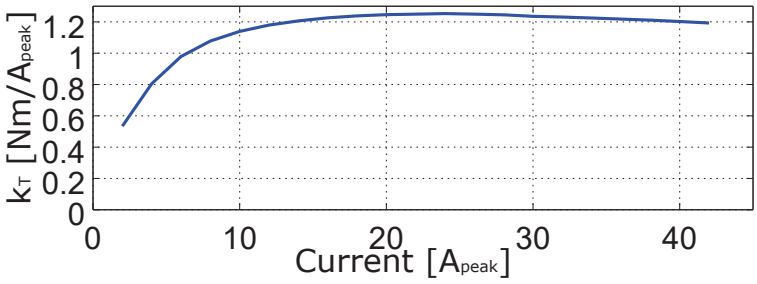

(a)

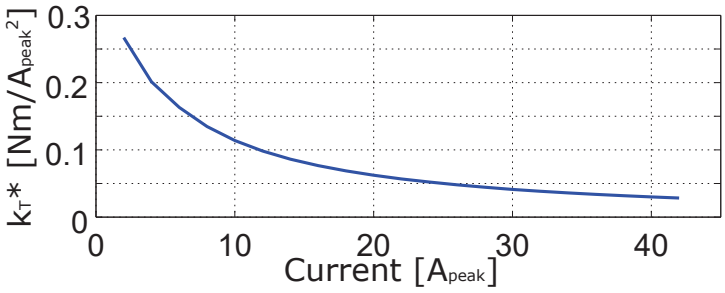

(b)

Fig. 6.8: The k_T and k_T^* factors versus the current amplitude (experimental test).

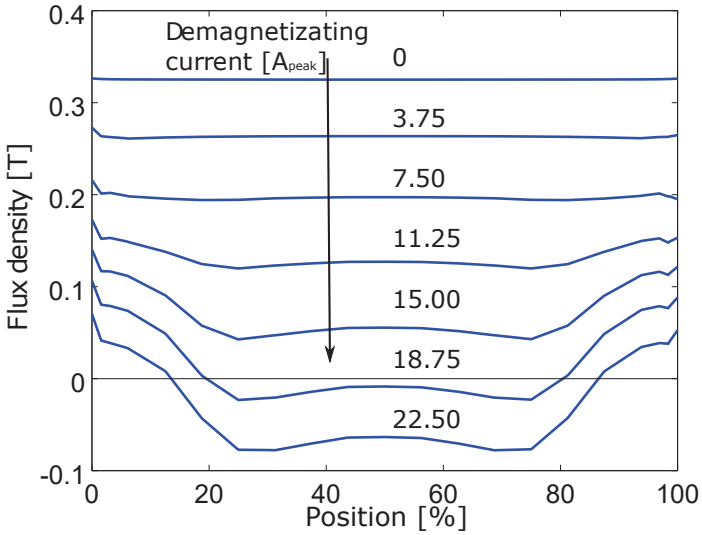

Fig. 6.9: PM flux density at different current amplitudes (ferrite magnet).

in Fig. 6.1.

The PM inset in the external flux barrier is considered in this study. Since it is closer to the air gap, it results to be more stressed by the stator current. Fig. 6.9 shows the flux density on the top of the PM, normal to the magnetization direction, when current varies

from 0 to $22.5A_{peak}$. The flux density of the PM decreases rapidly with the current, and it becomes negative at the higher currents. This result highlights that it is not safe to increase the currents above the rated current when ferrite magnets are used. An alternative design is necessary, increasing the PM thickness and the corresponding flux barrier thickness, so as to increase the overload capability. However, this implies a reduction of the d-axis paths, and of the d-axis flux linkage as well [59].

Fig. 6.10 shows the flux lines together with the maps of flux density, for some stator currents: 0, $7.5A_{peak}$, $15A_{peak}$, and $22.5A_{peak}$. Increasing the current, it is worth noticing that the flux lines in the PMs tend to disappear. In addition, the flux density reduces to zero (i.e., the colour of the PMs turns towards white).

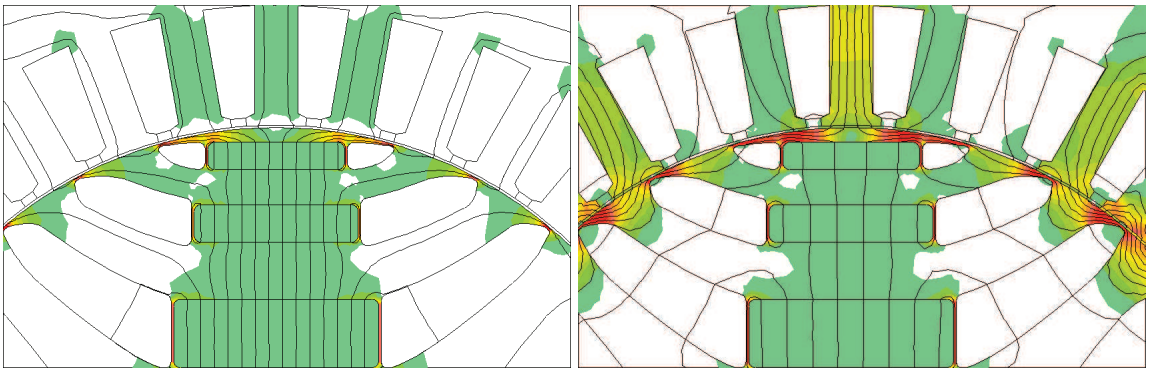

(a) No load (b) Phase current $7.5A_{peak}$

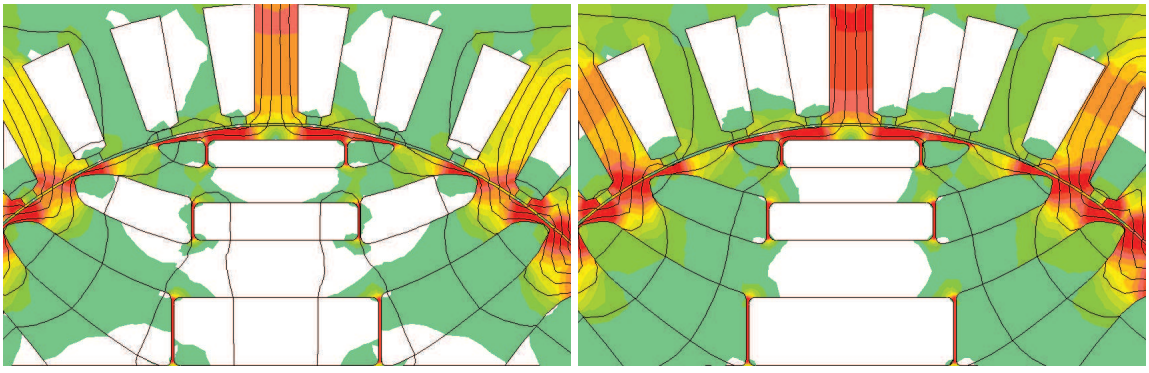

(c) Phase current $15A_{peak}$ (d) Phase current $22.5A_{peak}$

Fig. 6.10: Flux lines with positive (demagnetizing) q-axis stator currents.

6.9 Use of MQ2 permanent magnet

However, Dy-free NdFeB compounds have been recently developed so as to overcome the drawback of high and variable price of the commonly used NdFeB magnets [186]. The high cost is due to the combination of some heavy rare-earth compounds, such as Dysprosium (Dy) and Terbium (Tb), which are added to increase the thermal stability and the intrinsic coercivity of the permanent magnet material. The research interest is growing around the Dy-free sintered $NdFeB$ and the hot pressed Dy-free $NdFeB$, commercially called $MQ2$ [101, Molycorp Magnequench]. The recent developments of manufacturing processes yielded MQ2 compound exhibiting an excellent thermal stability, comparable to $NdFeB$ with Dy and Tb.

As discussed in Ch. 1 an reported in Fig. 1.17, the $MQ2$ remanence flux density at room temperature is 40% lower than the sintered NdFeB one, but double of ferrite one. In addition, it is worth noticing that the coercive field is comparable to that of the sintered Dy-doped NdFeB at high temperature. The adoption of some such magnet compounds allows to get safe demagnetization levels and high FW capability. In addition, the price is halved, ranking nowadays in an intermediate position between ferrite and heavy rare-earth NdFeB.

The use of ferrite magnets in synchronous PMAREL machines have been investigated in the last years [9], while the hot pressed MQ2 magnet has been less investigated in the literature, mainly about the spoke type motor design [27, 111]. A further improvement of torque density, FW performance, power factor and efficiency is expected.

Fig. 6.11 shows the flux density in the external flux barrier PMs, normal to the magnetization direction, considering $MQ2$ magnet. As above, the current varies up to $22.5A_{peak}$. The flux density of the PM decreases rapidly with the current, but remaining positive even at the higher currents. This result highlights the higher strength of such a magnet against the demagnetization with respect the ferrite magnets.

6.10 Torque ripple reduction

The torque ripple in synchronous reluctance motors is due to the interaction between the spatial harmonics of magneto-motive force (MMF) and the rotor geometry. Even if there is a variety of works which investigated the reduction of the torque ripple [65, 75, 85, 134], a few results and considerations are reported hereafter.

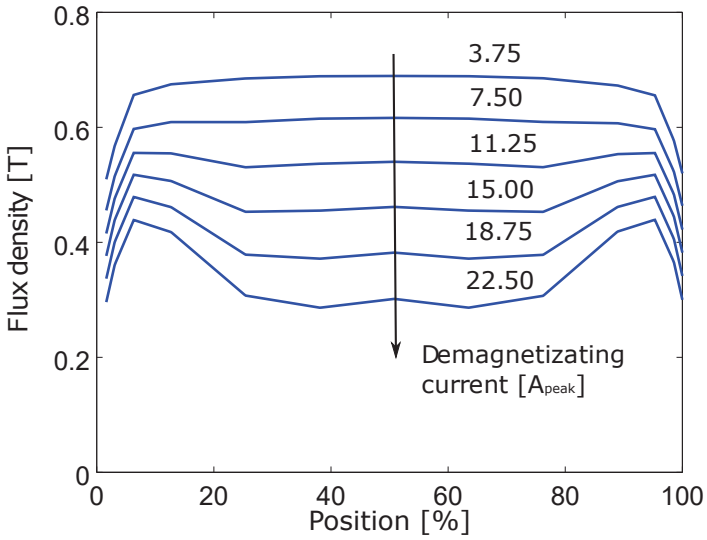

Fig. 6.11: PM flux density at different current amplitudes (MQ2 magnet).

6.10.1 Rotor skewing effect

Fig. 6.12 shows the measured torque versus the mechanical position for the REL motor, when it is supplied with a stator current $I = 10A_{peka}$, without and with rotor skewing. The torque ripple is halved, decreasing from about 17% to about 9% of the average torque. Similar results are measured in the PMAREL. When PMs are used a step–skewing is adopted: the rotor is split in three parts, each of them is skewed with respect to the others. Fig. 6.13 shows the measured torque behaviour of the PMAREL motors, according to the same stator currents $I = 10A_{peak}$. As described in [170], the torque ripple can not be completly reduced by the rotor skewing. In fact, the same stator current yields different d and q-axis components along the rotor axial length when the rotor is skewed.

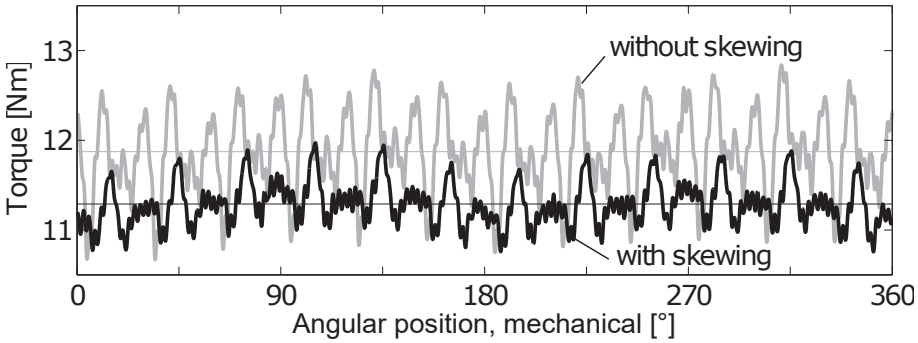

Fig. 6.12: REL motor: measured torque versus mechanical position $I = 10$ A

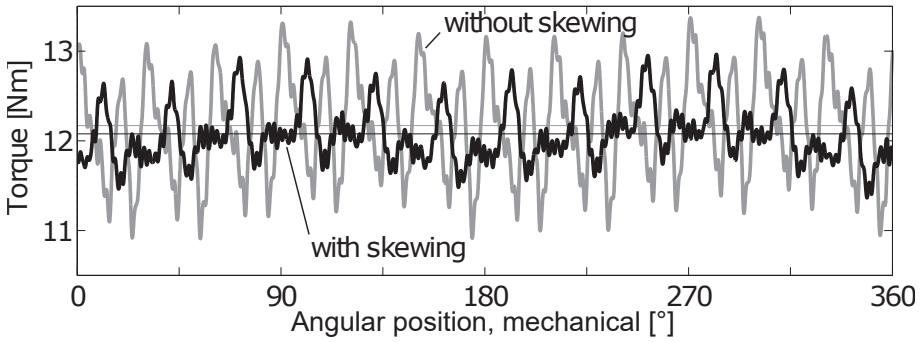

Fig. 6.13: PMAREL motor: measured torque versus mechanical position $I = 10$ A

6.10.2 Asymmetric Rotor Flux-Barriers

To the aim of a further torque ripple reduction, the authors proposed rotor flux barriers with different geometry in adjacent poles [2, 10, 14]. When asymmetric flux barrier geometries are adopted (large and small alternatively), there is a sort of compensation of the torque harmonics between the poles [21]. The resulting motor is referred to as *machaon* motor.

Fig. 6.14 shows the analysis of the torque versus rotor position θ_m of the REL motor. The motors are fed with the same current, amplitude and phase angle. The motors with symmetric rotors exhibit a higher torque ripple. The harmonic of 18^{th} order is well recognized (i.e., with three periods each 30 mechanical degrees). This is expected since this is the slot harmonic. Let's note that the motors with these two symmetric geometries exhibit such a torque harmonic of 18^{th} order with almost the same amplitude but out of phase of about 180°. Thus, when these two geometries are combined together, and the machaon–type rotor is achieved, there is a sort of compensation of the harmonic of $18th$ order. The torque ripple of the machaon–type motor exhibits no harmonic of $18th$ order, and the torque harmonic of 36^{th} order is more evident (i.e., with six periods each 30°, mechanical).

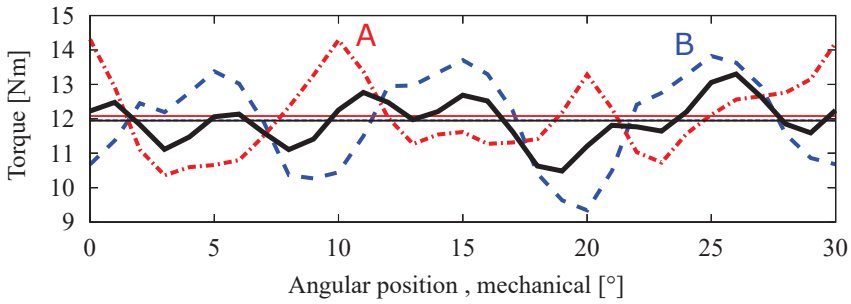

Fig. 6.14: REL motor: torque behaviour with symmetric and asymmetric rotor ($I = 10A_{peak}$, $\alpha_{ie} = 64°$)

With this geometry the torque ripple has been found to be reduce to two thirds, in both REL and PMAREL motors. In addition, the skewing angle can be reduced. On the other hands, the average torque remains almost the same, as highlighted in Fig. 6.14 by the thin solid line.

6.11 Conclusions

A synchronous reluctance motor, without or with assistance of PMs, has been analysed for traction applications in electric vehicle. Several simulation results and experimental tests are reported to highlight the motor capabilities.

The synchronous reluctance motor exhibits a high torque density. When PMs are introduced in the rotor flux barriers, the torque increases of about 10%. In flux-weakening operations a wider constant power–speed range is achieved. Finally, the power factor improves in the whole operating region.

However, a lower overload capability is recognized, due to the possible demagnetization of the ferrite PMs. When a high overload is requested, the synchronous reluctance motor is to be preferred. Alternatively, higher energy PMs have to be adopted. The increase of strength against demagnetization have been analyzed, according to the Dy-free $MQ2$ magnet.

As far as the torque ripple reduction is concerned, two techniques have been revised: rotor skewing and asymmetrical flux barriers. They both reduce the torque ripple down to about one third, with a slight decrease of the average torque.

Finally, the synchronous reluctance motor results to be a good competitor for electric vehicles. Its construction is robust and it is free from rare–earth magnets, making it very actractive from the cost point of view.

6.12 Appendix: test motor data

The synchronous REL motors under test adopts the stator of an induction motor. The slot number is 36 and the back iron is designed according to four poles. Outer and inner diameter are $D_e = 200mm$ and $D_i = 125mm$, respectively, and the stack length is $L_{stk} = 40mm$. Rated stator current is in the range between $10A_{peak}$ and $15A_{peak}$, corresponding to a current density in the conductors between 6 to $9A_{RMS}/mm^2$, depending on the cooling system.

Fig. 6.15 shows a picture of the test bench used for these measurements. The motor under test is on the left hand side. The machine on the right hand side is used as a brake.

The torque-meter is coupled between the two shafts.

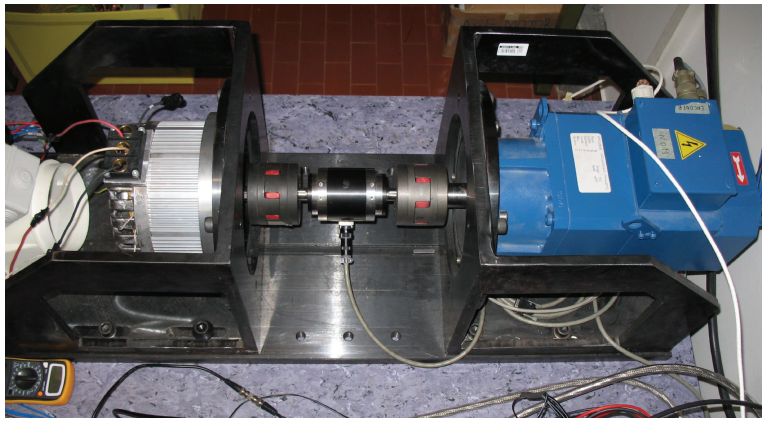

Fig. 6.15: Test bench for motor test.

Chapter 7

Outer Rotor IPM generator with wide constant power region

7.1 Introduction

Outer rotor machines generally present higher torque if compared with inner rotor machines [58]. However, outer rotor machines have not been widely investigated in literature, expecially when a wide constant power–speed range is required.

Outer rotor machines are designed with Permanent Magnets (PMs) mounted on the rotor surface to achieve a Surface Permanent Magnet (SPM) machine [123]. The main advantages are that they yield a thick rotor structure and a high torque density, and PMs do not need retain cover against the centrifugal force [32, 104]. On the other hand, SPM machines do not exhibit a wide Constant Power versus Speed Range (CPSR) [157].

Interior Permanent Magnet (IPM) machines are widely used in Electric Vehicles (EVs) [82], since they present high torque density, efficiency [3] and extended Flux–Weakening (FW) region [22, 38], that is, a wide CPSR [19]. This peculiarity is interesting in those cases where the output power should be quite constant independently from the speed, for example in generator applications, where a constant power production is desired in a wide speed range.

However, Interior Permanent Magnet (IPM) machines with external rotor have not a wide diffusion, since they present some difficulties in the manufacturing. Moreover, IPM outer rotors needs more space to address the PMs and the flux barriers, and sometimes it is difficult to achieve good design with more than one flux barrier per pole.

The proposed study aims to design an IPM machine to be used as a generator in an hybrid EV. The rotor includes one flux–barrier per pole, each containing two PMs arranged

in lateral position. To obtain a proper rotor geometry, a multi–objective optimization has been carried out. The rotor geometry is optimized to fit the desired objectives. The goals of the final machine are here described:

- higher output power, so as to increase the power–to–volume ratio;
- lower permanent magnet volume, so as to decrease the cost of the machine;
- a CPSR above the base speed, at least equal to eight times the base speed. The machine has to operate as a generator, the output power is quite constant with the speed, up to a given speed. In this optimization, the ratio between the maximum and the base speed (CPSR) is fixed to be 8;
- among all the optimized machines, the final machines will be chosen on the basis of the voltage drop between load and no load operation, and on the basis of other design considerations (demagnetization, poles, rotor losses).

7.2 Machine design

A sketch of the geometry of the outer rotor IPM generator is shown in Fig. 7.1. The aim is to optimize the rotor geometry. The rotor structure is that of an IPM machine, with one barrier per pole. The PMs are only on the lateral sides of the air barrier. There are some constraints on the dimensions, since the machine will be used as a generator in a hybrid vehicle with limited space. Such constraints are the outer rotor diameter, $D_{e,r}$, that should be at most 318 *mm* wide, and the stack length, L_{stk}, that is limited to 45 *mm*.

The main dimensions of the machine, together with the slot–pole number, are summarized in Table 7.1. The stator of all the machines is the same. The choice of the slot–pole combination allows to obtain a winding arrangement called concentrated coil winding [62]. Such winding configuration consists of coils that are wound around a single stator tooth, as represented in Fig. 7.2. The main advantage of this configuration is that the length of the end winding connections is minimized, with consequent reduction of copper used (less cost) and hence reduction of Joule losses.

The optimization algorithm works together with the Finite Element (FE) analysis. The rotor geometry is automatically drawn on the basis of some geometry variables, which are managed by the optimization algorithm. At the beginning, a random set of variables is created, then the variables are optimized during each step of the optimization algorithm in order to match the objectives. The FE software performs the analysis, which gives the machine performance as output. A Differential Evolution (DE) algorithm performs the objective

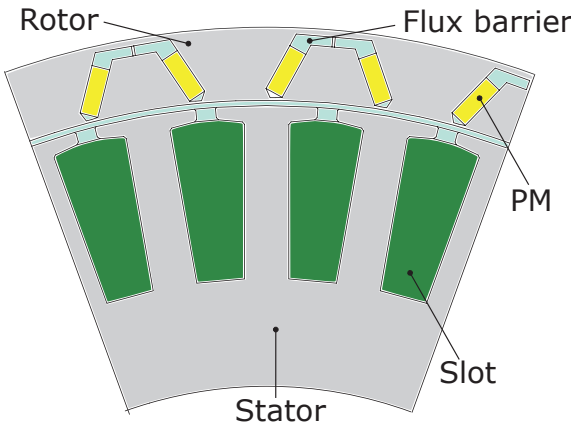

Fig. 7.1: Sketch of 1/9 of the machine.

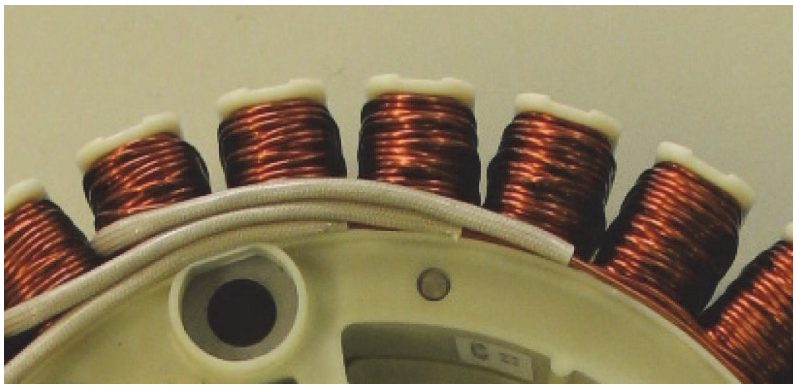

Fig. 7.2: Detail of the stator with the concentrated coil windings.

Table 7.1: Main machine dimensions

Dimension	Symbol	Value
Inner stator diameter	$D_{i,s}$	286 *mm*
Air–gap	g	1.1 *mm*
Inner rotor diameter	$D_{i,r}$	288.2 *mm*
Outer rotor diameter	$D_{e,r}$	318 *mm*
Stack length	L_{stk}	45 *mm*
Number of slots	Q	36
Number of poles	p	24

calculation and evaluation on the basis of the objective definitions. Then the DE creates next generation performing selection, crossover and mutation up to the last generation. At the end of the computation the Pareto front is given, which is the set of optimum solutions

which match all the objectives. Fig. 7.3 shows the rotor variables that are considered: R_b is the radius of the outer part of the barrier, h_b is the height of the air in the central part of the barrier, R_m is the radius measured in the center of the lateral magnets, w_m and h_m are the width and the height of the lateral magnets, α_b is the angle with respect to the center of the lateral magnets, α_m is the angle that determines the position of the lateral magnets of the barrier, and α_r represents the angle between the tips of the barrier, with respect to the center of the rotor. All these variables are changed during the optimization, so that the barrier can assume different shapes. The resulting machines will present different behaviors.

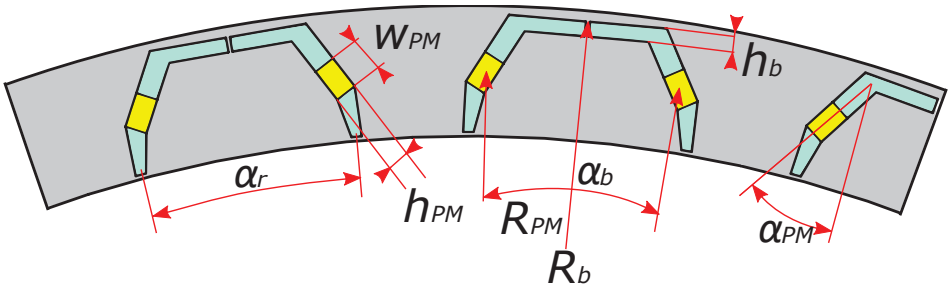

Fig. 7.3: Variables modified in the optimization process.

7.3 Optimization objectives

The optimization algorithm has been designed with two objectives. The first objective is to maximize the nominal power (base power) of the machine, P_n, in order to have a machine with high power density. The second objective is to minimize the PM volume so as to reduce the costs.

Moreover, a constrain on the machine design is related to the capability of the generator to support the nominal power for a wide speed range above the base speed ω_b. Fig. 7.4 shows the output power and torque versus speed of a generic Electrical Machine (EM) together with the same characteristics of a generic Internal Combustion Engine (ICE). When the EM is operated as a generator, both torque and power of the ICE should be higher than those of the EM, in the desired speed range. In this way, the output base electric power from the EM can be pulled out in a wide speed range, allowing the ICE to be operated at different speeds. Furthermore the ICE can be operated maximizing its efficiency.

In order to address this constrain, the ideal machine should exhibit a power versus speed characteristic as shown in Fig. 7.5.

For such ideal machine, once the nominal power P_n is reached, at the base speed ω_b, the

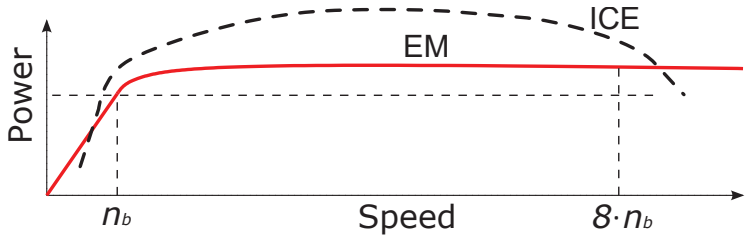

Fig. 7.4: Power of ICE and EM.

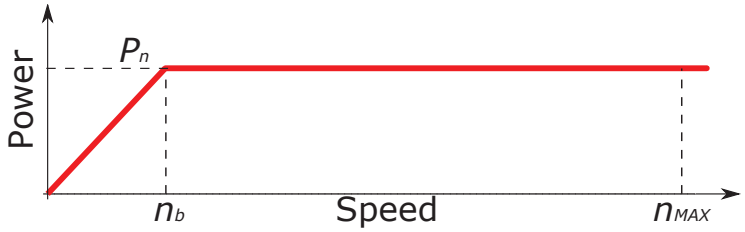

Fig. 7.5: Ideal behaviour: infinite CPSR, from ω_0 to ω_{max}.

output power is constant up to the maximum speed ω_{max}. In this case, the CPSR is only limited by the maximum speed which is determined by evaluating the mechanical stresses.

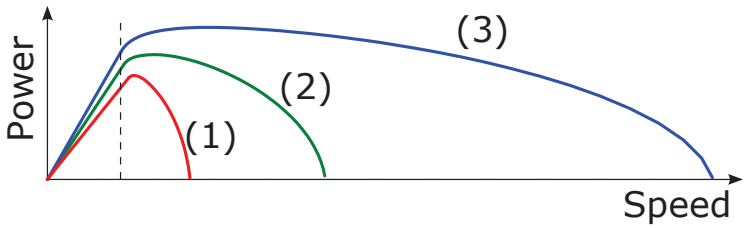

Fig. 7.6: Real constant power versus speed range.

However, actual machines differ from the ideal behavior. Fig. 7.6 reports more realistic power versus speed curves. Once the base speed and power are reached, the power is not constant for higher speeds. At the beginning it tends to increase, and then, according to the machine design, the power decreases down. The power could decrease rapidly with the speed up to a zero power, as shown in Fig. 7.6, or it could decrease more slowly and maintain a value near the base power for a wide speed range. The behavior of curve (1) and (2) is commonly found in SPM machines, since they exhibit a limited flux weakening range [156]. The behavior of curve (3) is instead typical of IPM machines, in which the design plays an important role on the flux weakening capability.

In the case of actual machines, the CPSR is determined on the basis of the speed below which the power is higher or equal to the nominal power, ω_0 in Fig. 7.6. Hence, the ratio

between n_b and n_0 is commonly referred to as CPSR. In the speed range from n_b to n_0 the power is at least equal to the base power, and the speed n_0 represents the maximum speed of the CPSR.

In the optimization process, n_0 has been chosen to be eight times the base speed, to have a ratio 1 : 8 between the base and the maximum speed of the constant power region. It follows,

$$obj_2 = \frac{n_0}{n_b} \tag{7.1}$$

This ratio has been chosen according to the output characteristic of an ICE. Considering both a diesel oil and a gasoline fed ICE, the chosen CPSR ensures that the EM can be operated between the minimum and the maximum ICE speed. This is true if the base speed of the EM is similar to the minimum speed of the ICE, so that the CPSR matches the range of speeds of the ICE. Moreover, the EM used as a generator when the ICE is operating, could be operated as a motor when the ICE needs to be turned on. This considerations led to a further constrain on the algorithm: a machine is accepted if and only if its base speed is higher than the ignition speed of the ICE. In this way, the same EM can be used to turn on the ICE and allows to exploit the full ICE speed range. A reasonable value for such base speed is $n_B = 1000rpm$.

There is no constrain about the maximum speed of the EM, that can be generally considered higher than the maximum speed of the ICE. Mechanical problems related to mechanical stress on the rotor ribs can be solved with an accurate rotor design, even by introducing a containing jacket on the external part of the rotor to contain centrifugal stresses.

In order to match such constrain (CPSR ≥ 8), and to avoid that the algorithm rejects some solutions, a particular strategy has been adopted. Let's refer to Fig. 7.7. Fig. 7.7(a) shows the possible output power of a machine that is going to be managed by the optimization algorithm. Such a machine presents a ratio (7.1) at the nominal power P_n that is lower than 8. If such curve were processed by the algorithm, it would be rejected since it does not match the desired CPSR. A way to make the CPSR suitable for the application, and hence to be accepted by the algorithm constrains, is to apply a power derating, as shown in Fig. 7.7(b). The nominal power of the machine is decreased down to the power P_n' (and then also the corresponding nominal speed) until the corresponding CPSR is at least equal to 8. The power P_n' becomes the new nominal power of the machine, and now the machine satisfies the desired CPSR requirement and the algorithm returns this value of power.

In this way, the set of optimal solutions will include some machines with lower power, but all solutions exhibit a CPSR at least equal to 8. Anyways, the optimization algorithm

will force the solutions toward machines with high power, as well.

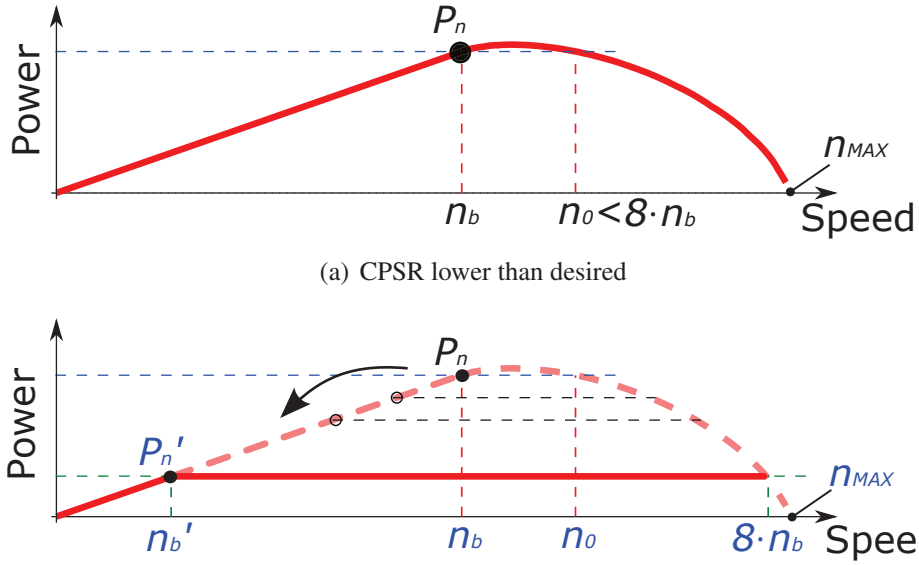

(a) CPSR lower than desired

(b) Nominal power lowered to increase CPSR

Fig. 7.7: Strategy to verify the CPSR constrain.

The FE simulations are performed at constant current, the same for all machines. The stator current has been selected in order to operate the machine in continuous mode operation, according with the winding insulation class, and to avoid over temperature in the winding. The stator geometry, as said above, is the same for all machines, so that also the Joule losses are the same for all machines, as well. Mechanical and stator iron losses can be considered similar for each simulated machine, since the iron flux density is supposed to be the same for any machine. It results that the amount of losses can be considered the same during the optimization process, and the optimization goes toward machines with increasing efficiency, since one of the objectives is to maximize the output power. In regard to the torque ripple, its reduction is not relevant from the point of view of the application. In fact, the ICE torque ripple is certainly higher than the EM torque ripple, and a minimization of it will not lead to any improvement.

7.4 Optimization results

This section presents some optimization results. Fig. 7.8 shows the set of solutions obtained from the optimization process in the plane PM volume–base power. The Pareto front is also shown, formed by the best results. The two objectives of the optimization, high con-

stant power versus speed capability and low PM volume, require opposite design choices. Fig. 7.9 shows the power versus speed curve of a machine chosen along the Pareto front. The solution has been chosen with a high base power, and with high PM volume too. This solution yields a higher strength against demagnetization. From the application point of view, interesting solutions are those with high base power, that are found in the lower part of the Pareto front. The solutions along the Pareto front helps to choose, among the various designs that lead to high base power, those who present lower PM volume. Other choices could be selected with a good agreement between the two objectives. It can be noted that the CPSR is very wide as requested. Moreover, the output power and torque are quite high.

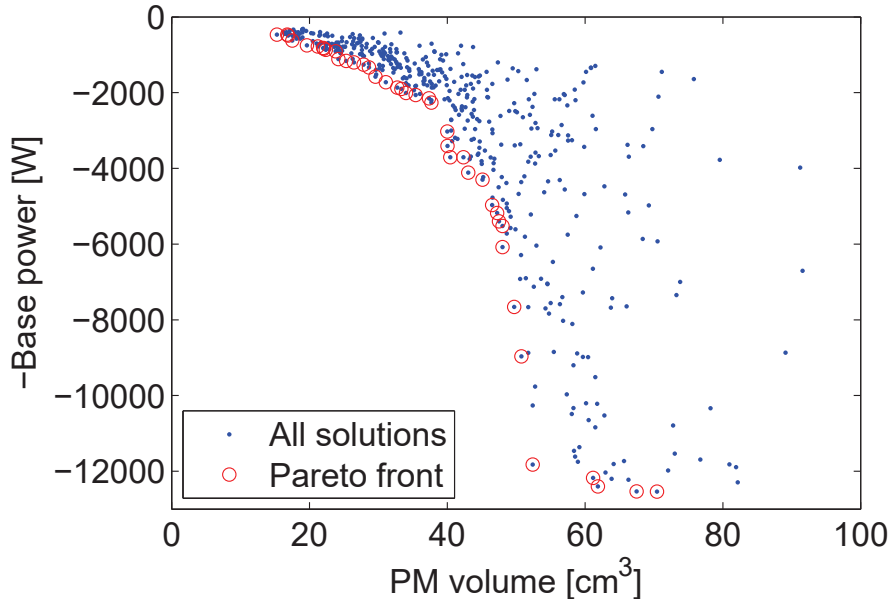

Fig. 7.8: Pareto front.

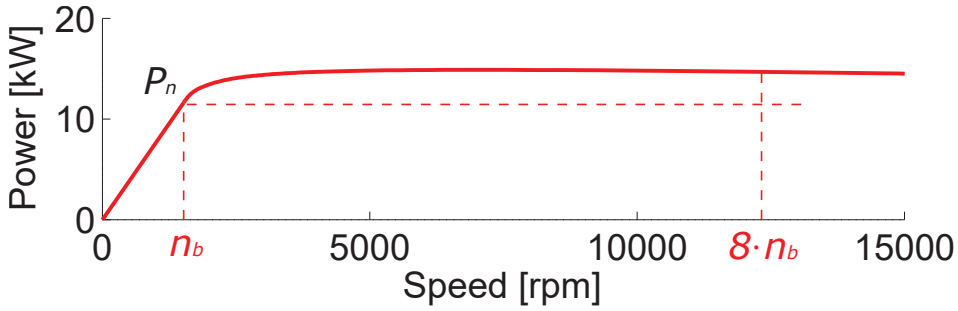

Fig. 7.9: Power versus speed referred to a solution selected along the Pareto front.

If moving along the Pareto front, the rotor geometry changes in order to match the

objectives. Analyzing the main changes, it is found that:

- the PM size changes, according to the objective that aims to reduce PM volume;
- the shape of the bridges in front of the airgap modify, to get a different inductance that play a decisive role for determining the desired CPSR [155], together with the PM flux linkage.

The performance that are achievable from the optimized machine are a torque up to $110Nm$, a PM volume of $15-70cm^3$, a base power up to $12.5kW$ and a base speed of $1150-1500rpm$.

To compare the IPM rotor design with an SPM one, Fig. 7.10 shows the power versus speed of an IPM and a SPM rotor design. Both machines have external rotor, and the same main dimensions. The SPM machine presents a lower torque, but is characterized by a higher base speed. This aspect lead to a machine with a higher base power. On the other hand, the torque of the IPM machine is higher and the base speed lower, resulting in a lower base power. However, the IPM machine has an extended CPSR, that allows the machine to be operated at higher speeds with a good output power.

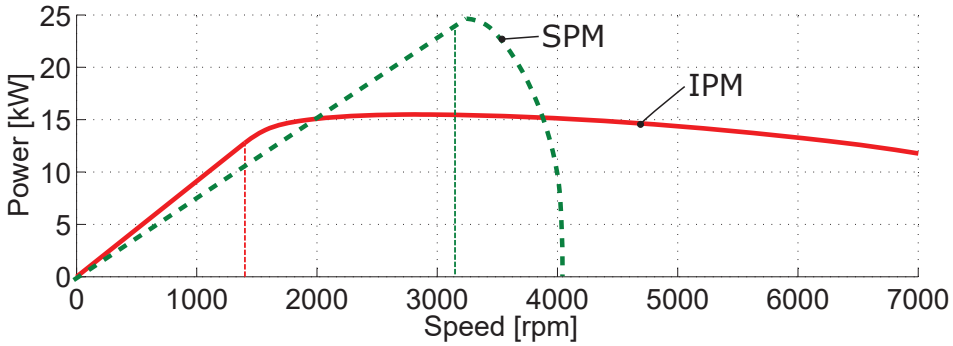

Fig. 7.10: SPM versus IPM power versus speed.

7.5 Rotor parametric analysis

The result of the optimization process, as shown above, is a set of optimal solutions, the Pareto front. The rotor geometries along such front are the best found by the GA. They are different from the objective point of view; going toward one side of the front there are geometries with higher PM volume and lower base power, and viceversa going toward the opposite side.

In any case, the generic rotor geometry found from the Pareto front is similar to that of Fig. 7.11, which shows the flux lines of a FE simulation.

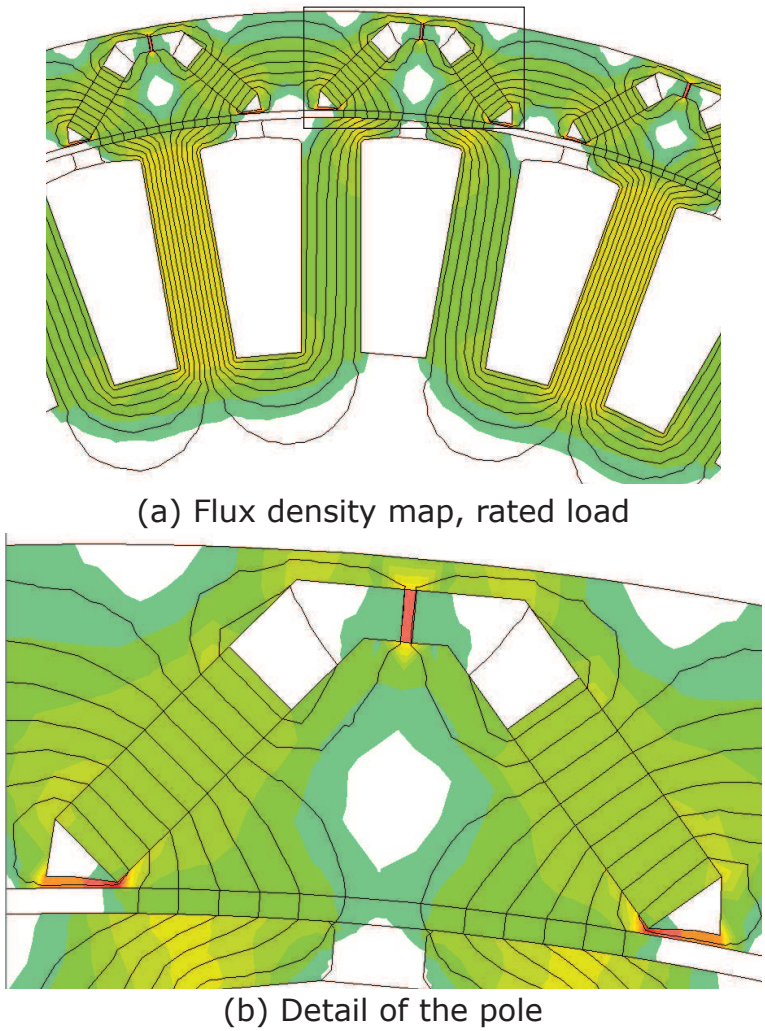

(a) Flux density map, rated load

(b) Detail of the pole

Fig. 7.11: Rated load operation of the selected optimized geometry.

It can be noted, from a particular view in Fig. 7.11(b), that some flux lines go from the PMs to the rotor ribs without crossing the airgap. This means a loss of PM flux for torque production. Moreover, the PMs housing is larger than the PMs size, that suggests that the rotor geometry can be further improved to save space.

The main idea is to remove the external part of the rotor with the ribs and to substitute it with a containing jacket, made by non magnetic material, with the function to assembly the rotor parts, as Fig. 7.12 shows.

In this way the rotor mechanical resistance to centrifugal forces is solved by this containing jacket, and the rotor iron paths could be also made by Soft Magnetic Composites

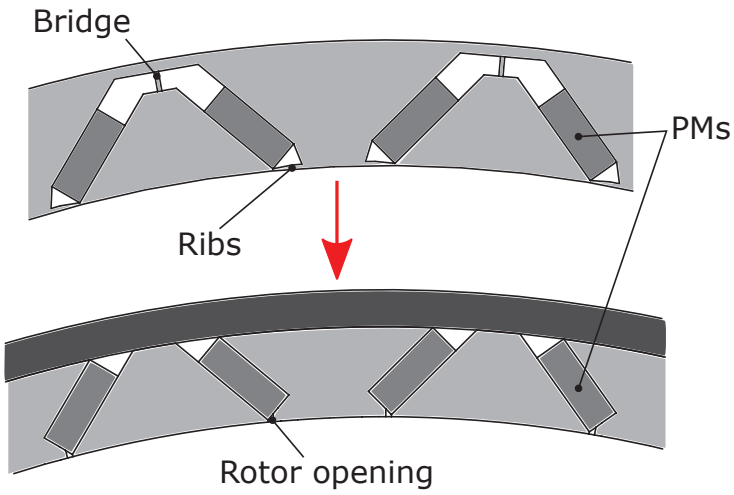

Fig. 7.12: Rotor modification to improve the rotor.

(SMC), with advantages in assembly, rotor losses [74] and manufacturing costs [103]. Another thing that has been changed, in order to improve the rotor assembly, is the removal of the ribs in front of the stator. In the place of those, openings have been introduced.

As said in Section 7.4, both the shape of the ribs in front of the stator and the PM flux linkage determine the amplitude of the CPSR, and hence the introduced rotor changes, modify the CPSR, as well.

In fact, the PM size affects the PM flux linkage (λ_{PM}), and the shape of the barrier tip affects the d–axis inductance (L_d). It is well known [155] that the ratio Λ_{PM}/L_d determines the field weakening performance.

In order to get hints in the rotor design, a FE parametric analysis has been carried out on the modified rotor. It allows the designer to know which are the parameters to act on to adjust the desired performance. Starting from a good solution found on the Pareto front, the rotor been modified as said above, and the width of both PMs and rotor openings has been modified, as shown in Fig. 7.13. The PMs height is kept constant since it derives from demagnetization considerations.

Fig. 7.14 shows the power versus speed of all simulated machines. Each subplot reports the variation of the rotor openings with fixed PM width, starting from the smaller PM width (first subplot), to the higher PM width (last subplot). In each subplot, it is noted that decreasing the rotor opening width there is a corresponding increasing on the power versus speed range. This is true for the higher PM widths, while the behaviour is a little different when the PM width is small.

The CPSR always increases with the rotor opening width, except for the lowest PM

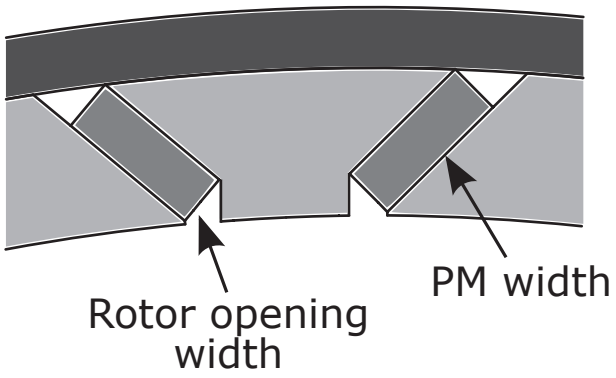

Fig. 7.13: Rotor dimensions changed during parametrization.

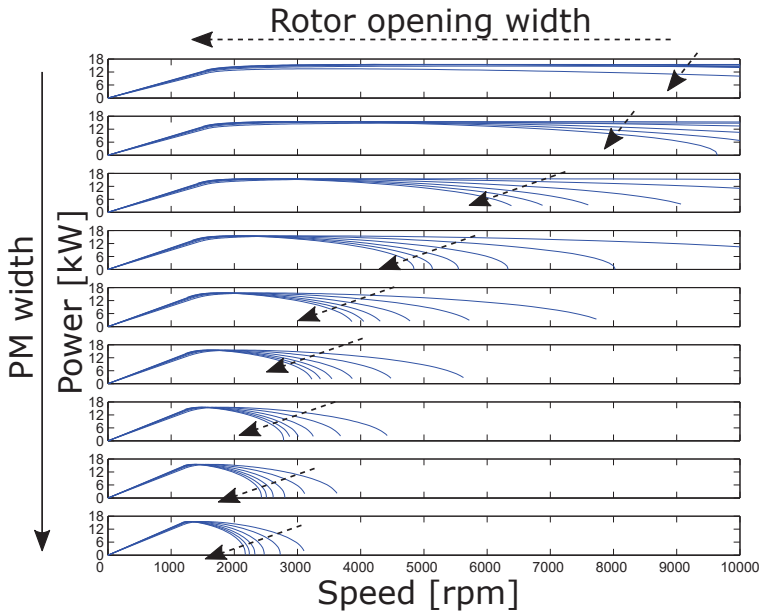

Fig. 7.14: Power vs speed for the parametric optimization.

width. For such case there is an initial increasing, then the CPSR decreases. In any case, increasing the PM width it is more difficult to obtain a high CPSR since the PM flux linkage is too high to be weakened by the stator current. The behaviour of the IPM machine in this case is similar to that of the SPM machine. The parametric simulations show that also the base torque (and hence the base power and the base speed) is a function of the PM and rotor opening dimension. It is therefore possible to select both the PM width and the rotor opening width according to the desired CPSR as well as to achieve the desired output characteristics.

7.6 Conclusions

This chapter presents the design of an outer rotor IPM generator for EV applications. An outer rotor solution has been chosen in order to increase the torque density of the generator, while an IPM configuration has been selected so as to achieve a wider CPSR. The preliminary rotor design has taken advantage by a multi–objective optimization genetic algorithm. Such an optimization is carried out minimizing the PM volume and maximizing the generator nominal power. Moreover, since a wide speed range operation is also required, such constrain has been introduced in the optimization process. A preliminary optimized result has been reported, then improvements on the rotor geometry have been introduced, which also give to the rotor modularity and better resistance to mechanical stresses. A parametric analysis on the improved rotor has been carried out, to give hints on the rotor design oriented to maximize the output power and achieve a wide CPSR. A sample generator is going to be prototyped to test its performance.

Chapter 8

Traction PMASR motor optimization according to a given driving cycle

8.1 Introduction

The progressive electrification of the private transport system seems to be a well-established reality and it is expanding significantly in these last years. Electric mobility is seen as a possible solution to the problem of air pollution, global warming, depleting and dependance of oil resources and energy efficiency [49]. Electric motors are the key devices in an electric powertrain and among the typologies, the synchronous motors provides the best performance, in terms of high torque and power density, high speed capability, wide speed range, high efficiency and mass saving.

Several researches have been carried out in the design and optimization of synchronous motor for traction application, including all the main typologies such as surface mounted permanent magnet (PM), interior PM, switching flux PM, and PM Assisted Synchronous Reluctance (PMASR) motors [26, 51, 88, 99, 109, 136, 160, 163]. In these works, generally, the design and optimization procedure are based upon rated motor specifications and they do not consider the actual working cycle of the electric car. As emphasized in some recent studies [36, 37, 66], an optimization performed only on the rated conditions might not yield to an optimal results in the whole driving cycle and a global optimization proves to be an effective solution. As shown in [71, 125, 182], the motor during a city profile mainly works in low torque operation, far from the rated condition. In [76] a simplified global optimization procedure has been performed. Since typical driving cycles are described by hundreds or thousand of operating points, for each of them the design has to be analyzed, a high amount of computation time is required. In order to overcome this limit, in [100], the concept of the

"energy center of gravity" has been introduced, showing that, the computation cost of the optimization along the driving cycle can be drastically reduced selecting a limited number of representative operating points in which the energy is concentrated.

This paper aims to present an optimization procedure of a ferrite PMASR motor for traction considering a given driving cycle of the vehicle. The interest in ferrite PMASR motors [9, 28, 40, 169] has grown in the last years, following the instability and the increase of the price of rare earth magnets. Moreover, it provides a high flux-weakening range, which is an important requirement in traction applications. Conversely, the most important drawback is the intrinsically higher torque ripple [65] that can be reduced by means of different strategies, such as an appropriate number and shape of the flux barriers and skewing [13, 102, 146, 170].
The proposed technique is based upon the evaluation of equivalent operating points along the driving cycle, based upon the analysis of the density pattern of the working points in the whole operating area. Each representative points is related to a weight coefficient which provides a quantitative indication of the operating rate at such a working condition. As urban mobility is currently seen as one of the most suitable and effective application fields for electric vehicles [118], a typical city and mixed driving cycle have been considered in this analysis.

8.2 Evaluation of the motor specification and operating areas

The motor performance has been assessed on the basis of two US driving cycles used to evaluate the fuel efficiency, exhaust emission of light-duty vehicles. They are represented by:

- Urban Dynamometer Driving Schedule (UDDS), reported in Fig. 9.1(a) referring to a city driving. It represents a $31min$, $18km$ urban route characterized by 23 stops with an average speed of $32km/h$ and a top speed of $90km/h$. [United States Environmental Protection Agency (
- US06 Supplemental Federal Test Procedure (US06/SFTP), reported in Fig. 8.1(d), combines the city profile with highway driving, providing a more accurate description of the actual operating conditions. It includes 4 stops along a $10min$, $13km$ route with an average speed of $78km/h$ and a maximum speed of $130km/h$. [United States Environmental Protectio

In the following analysis, it has been assumed that these driving cycles have to be performed on a flat route by a medium size two-wheel drive car, with a mass of about $m = 1500kg$. A

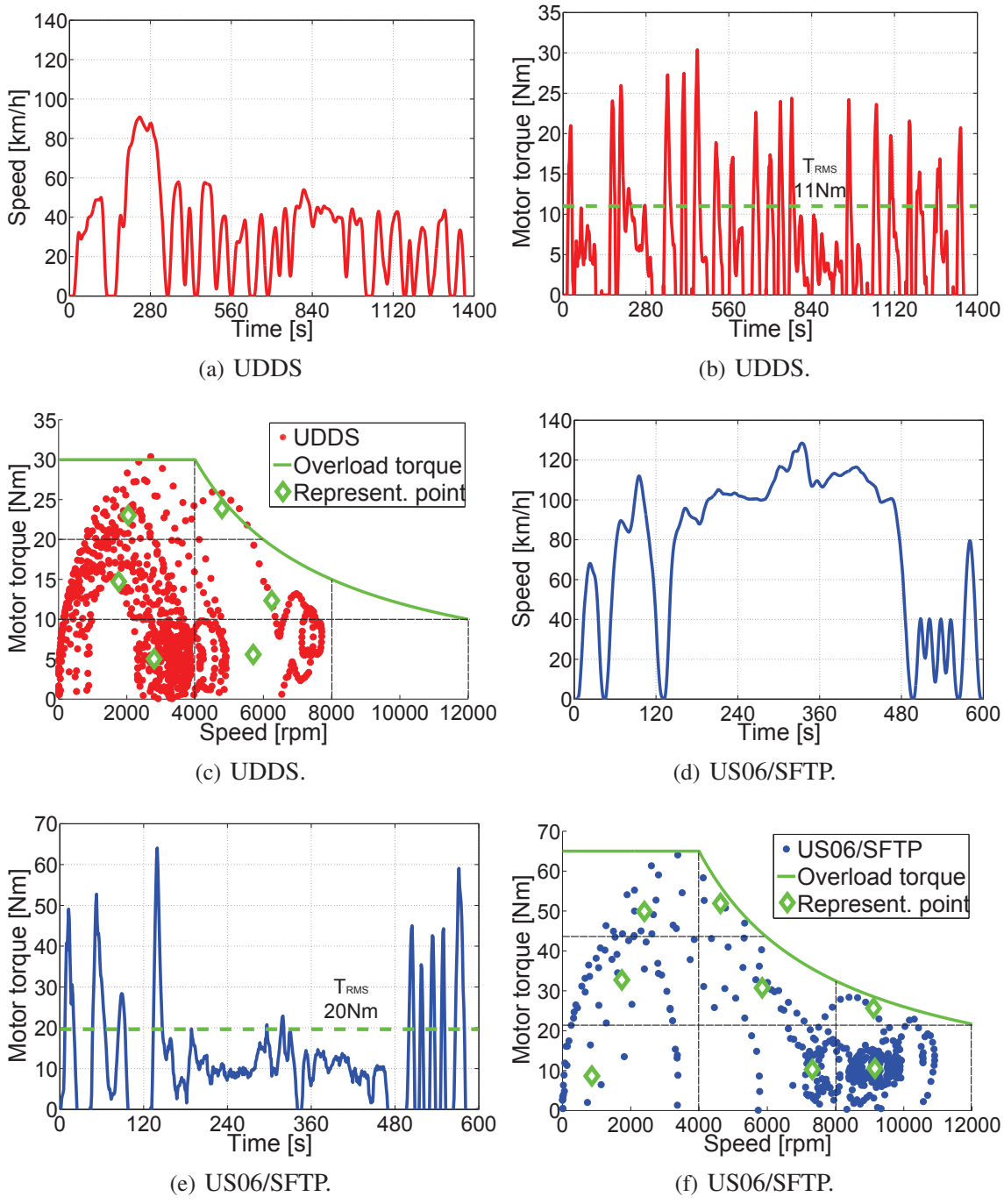

(a) UDDS (b) UDDS.

(c) UDDS. (d) US06/SFTP.

(e) US06/SFTP. (f) US06/SFTP.

Fig. 8.1: Driving cycle speed and torque distribution profiles.

gearbox with a $1:8$ ratio is used between each wheel and motor. The requested motor torque vs. speed characteristic has been computed according to the method proposed in [49]. This procedure considers the inertial F, rolling F_r and drag force F_d. Some suitable parameters

are considered, such as the wheel diameter, the air density, the frontal area and the drag coefficient, equal to $500mm$, $\rho = 1.225kg/m^3$, $S = 1.85m^2$ and $c_x = 0.4$ respectively. The wind resistance is considered negligible.

$$\begin{cases} F = m \cdot a & \text{(8.1a)} \\ F_r = 0.01 \cdot \left(1 + \dfrac{v}{44.4}\right) \cdot m \cdot g & \text{(8.1b)} \\ F_d = \dfrac{1}{2} \cdot \rho \cdot c_x \cdot S \cdot v^2 & \text{(8.1c)} \\ F_t = F + F_f + F_d & \text{(8.1d)} \end{cases}$$

Where a and g are the vehicle and gravitational acceleration, respectively. The motor torques, reported in Figs. 8.1(b) and 8.1(e), have been computed on the basis of the traction force F_t of (9.1a), while the motor speed has been evaluated from the vehicle speeds v, Figs. 9.1(a) and 8.1(d), for the given wheel diameter and gearbox ratio. Since the machine has been designed and optimized in motor operation, the regenerative area has not been included in the analysis.

As highlighted in Sec. 12.1, due to the high dynamic of the operating conditions, the torque is distributed along the whole electromechanical characteristics. The machine works at high torque operation, i.e. near the overload torque profile, for a short time. The effective utilization areas are located at low torque operations, medium and high speed range for the UDDS and US06/SFTP, respectively. The most significant torque value is the RMS torque that is related to the allowable thermal limits, equal to,

$$T_{RMS} = \sqrt{\frac{1}{t_p} \cdot \int_{t_p} T^2(t) \cdot dt} \tag{8.2}$$

Where t_p is the time period, $T(t)$ is the instantaneous torque and t is the time. The RMS torque is about $11Nm$ for the UDDS and $20Nm$ for the US06/SFTP, which are about 37% and 30% of the respective peak torque. The operating area with the highest use is located at different speeds of the driving cycles, being about $3500rpm$ for the UDDS and $8500rpm$ for the US06/SFTP.

The final torque distributions along the whole motor speed range, for both driving cycles, are reported in Fig. 8.1(c) and 8.1(f). The ideal target peak torque profile that includes all the operating points, is highlighted, assuming a hyperbolic trend over the base speed such as to ensure an ideal constant power speed range.

In order to provide a simplified representation of the torque distribution, the motor speed

range has been conveniently superimposed on a grid of (i-th, j-th) uniformly rectangular areas. For each of these areas, a representative equivalent torque $T_{eq,ij}$ and speed $\Omega_{meq,ij}$ have been evaluated, in terms of geometrical center of gravity. Each equivalent torque-speed combination is related to a weight coefficient $w_{eq,ij}$ which represents the relative time in which the motor runs in such areas. It is worth noticing that areas with a higher weight coefficient corresponds to regions with higher clustering of working points. Therefore, on the view of driving cycle optimization, such operating areas weigh more than others.
Finally,

$$\begin{cases} T_{eq,ij} = \dfrac{\sum_k T_{k,ij}}{p_{t,ij}} & \text{(8.3a)} \\ \Omega_{meq,ij} = \dfrac{\sum_k \Omega_{mk,ij}}{p_{t,ij}} & \text{(8.3b)} \\ w_{eq,ij} = \dfrac{p_{t,ij}}{p_t} & \text{(8.3c)} \end{cases}$$

Where:

- $T_{k,ij}$, $\Omega_{mk,ij}$ are the k-th torque and k-th speed in each considered (i-th, j-th) area, respectively.
- $p_{t,ij}$, p_t are the number of torque-speed points of the (i-th, j-th) area and the total number of torque-speed points of the driving cycle, respectively.

Table 9.1 reports the values of the equivalent torque, speed and weight coefficient in the working areas above mentioned, for both the driving cycles. It is highlighted in Fig. 8.1(f) and 8.1(c). The torque-speed distribution has been properly described by 6 points for the UDDS and 8 points for the US06/SFTP. The machine work with a torque lower of $1/3$ of the peak one for more than 60% and 80% of the time for the UDDS and SFTP/US06, respectively. It is worth noticing that the flux-weakening range specification is not critical for the city driving, since about 77% of the time, the motor operates at speeds lower than the base one. Conversely, it becomes mandatory when considering the combined driving cycle SFTP/US06, since the motor operates at speed range between $4000-12000$rpm for about 84% of the time. The grid structure and the number of the representative points is a critical issue for the effectiveness of the cycle optimization and it comes from a trade-off choice between the computation cost and the accuracy. Table 8.2 reports the comparison between the mechanical energies computed along the actual cycle profile and only on the representative points. It is worth noticing that the error is negligible for the selected grid layout.

Table 8.1: Equivalent torque, speed and weight coefficient in the operating areas of the driving cycles.

(a) UDDS.

Torque / Peak torque	**Speed** [rpm] 0−4000	4000−8000	8000−12000	**Tot.** [%]
0−1/3	5Nm 2801rpm 45.7%	5.5Nm 5704rpm 18.2%	–	63.9
1/3−2/3	14.7Nm 1761rpm 22.6%	12.3Nm 6246rpm 4.2%	–	26.8
1/3−2/3	23Nm 2041rpm 8.4%	23.9Nm 4787rpm 0.9%	–	9.1
Tot. [%]	76.7	23.3	–	100

(b) US06/SFTP.

Torque / Peak torque	**Speed** [rpm] 0−4000	4000−8000	8000−12000	**Tot.** [%]
0−1/3	8.7Nm 860rpm 5.6%	10.3Nm 7318rpm 14.1%	10.5Nm 9153rpm 61.6%	81.3
1/3−2/3	32.7Nm 1738rpm 6.7%	30.8Nm 5851rpm 5.1%	25.6Nm 9113rpm 1.7%	13.5
1/3−2/3	49.9Nm 2398rpm 4.1%	51.9Nm 4631rpm 1.1%	–	5.2
Tot. [%]	16.4	20.3	63.3	100

Table 8.2: Comparison between mechanical energy along the driving cycle.

Driving cycle	**Mech. energy all points** [MJ]	**Mech. energy repres. points** [MJ]	**Error** [%]
UDDS	2.49	2.47	−0.8
US06/SFTP	4.60	4.57	−0.7

8.3 Design procedure

8.3.1 Preliminary design of the baseline geometries

A 36-slot, 4-pole PMASR motor, equipped with an integral slot distributed winding, reported in Fig. 8.2, has been considered. It shares the same stator geometry of a prototype manufactured and tested for a low torque application [59]. The rotor is symmetric and it is equipped with 3 flux barriers per pole filled with 3 blocks of high quality (grade 9) ferrite magnets.

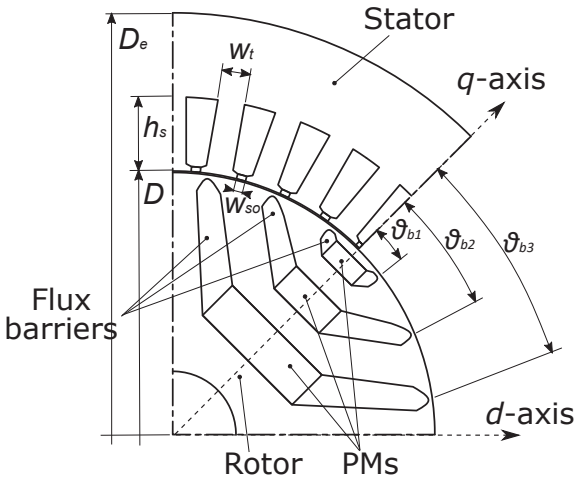

Fig. 8.2: 1/4 PMASR cross section.

On the basis of the aforementioned stator lamination and the requested motor specifications, a baseline geometry has been evaluated. The machine has been designed in order to meet the target peak torque profile at the operating temperature of $140°C$. The copper resistivity and PM properties have been prudentially considered at such a temperature. An overload current density of $9A_{RMS}/mm^2$, equivalent to a slot current of about $\widehat{I}_s = 508A_{peak}$, has been fixed. The fill factor has been assumed to be $k_{fill} = 0.4$.

In order to define the preliminary optimized geometry, a multi-objective Differential Evolution (DE) optimization procedure aimed to the maximization of the torque and minimization of the torque ripple, copper and iron losses, has been carried out. The main stator dimensions (tooth width, slot height and opening width), the insulation ratio [59] and the flux barrier angles have been considered as optimization variables. As shown in Table 8.3, the airgap height, the inner and outer stator diameter together with the slot current, have been kept as constraints.

Fig. 8.3(a) shows the resultant Pareto front for the optimization of the US06/SFTP cycle

Table 8.3: Machine constraints summary.

Name	Symbol	Value
Outer diameter	D_e	$200mm$
Airgap diameter	D	$125mm$
Shaft diameter	D_{ri}	$30mm$
Airgap height	g	$0.35mm$
Fill factor	k_{fill}	0.4
Overload slot current (base point)	$\widehat{I}_{sB}$	$508A_{peak}$
DC bus rated voltage	V_{DCn}	$300V$
Operating temperature	T_{op}	$140°C$

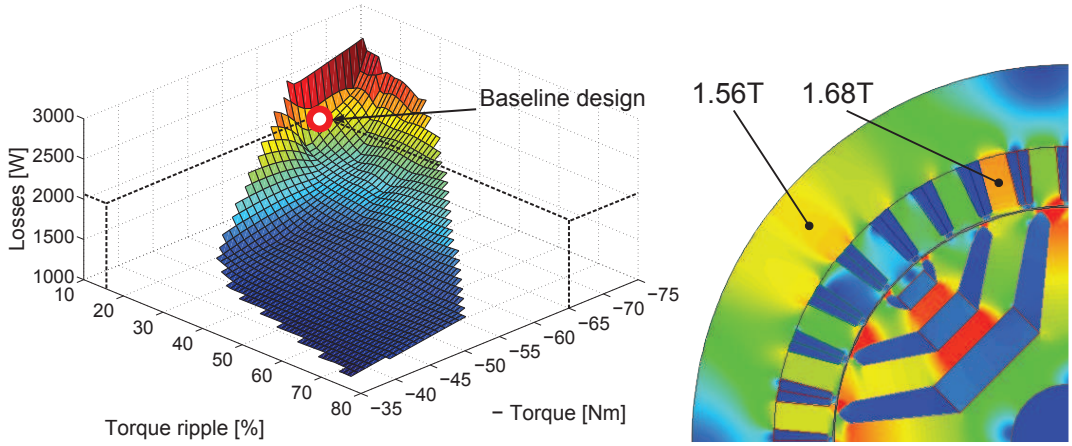

(a) Pareto front (interpolation) of the 3-objective preliminary optimization for the US06/SFTP design.

(b) Flux density map at the base point.

Fig. 8.3: Baseline design.

and the selected baseline design. The optimization has been performed only at the base point along the Maximum Torque Per Ampere (MTPA) locus, selecting the appropriate current phase angle of the starting geometry. Although the optimization process does not ensure the invariance of the machine parameters (PM flux linkage and synchronous inductances), the optimized designs exhibit a slight variation of the current angle that is limited in few degrees.

The demagnetization levels of the PMs have been verified, in order to exhibit a safe operation (PM flux density higher than $0.2T$) down to temperature of $-40°C$ in deep flux-weakening condition, feeding the machine only with the rated q-axis current.

Finally, the stack length and the number of conductors have been adjusted to meet the different peak torque specifications of the UDDS and the US06/SFTP while providing a base speed around the target value of $4000rpm$. The power supply is provided by a $300V$

DC bus.

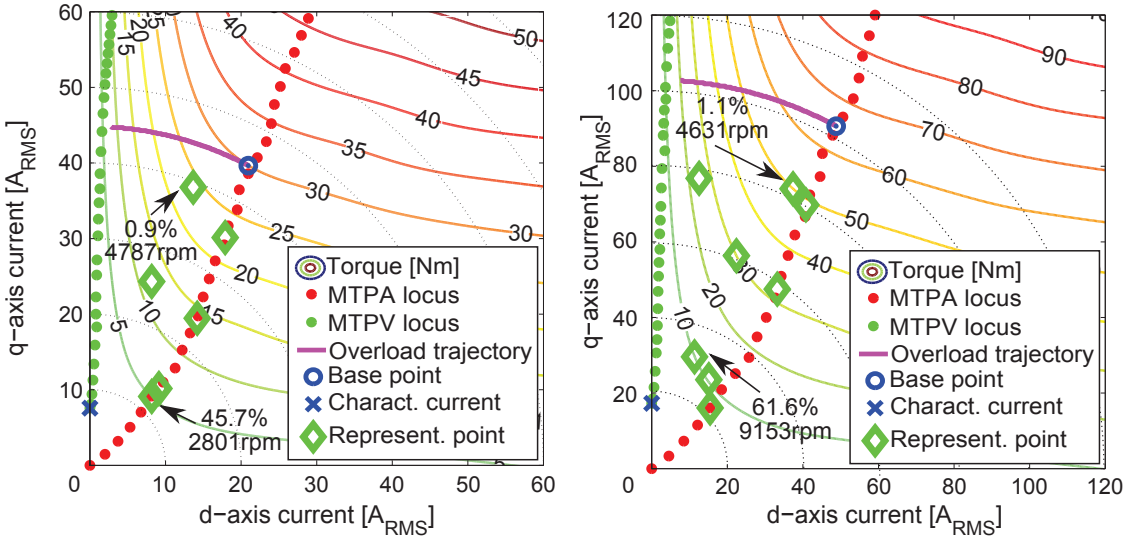

(a) UDDS. (b) US06/SFTP.

Fig. 8.4: Constant torque loci and trajectory in the $I_d - I_q$ plane.

Fig. 14.35 shows the resultant constant torque loci in the I_d–I_q plane computed by means of Finite Element Analysis (FEA), highlighting the MTPA, the Maximum Torque Per Voltage (MTPV) loci, the overload trajectory, the characteristic current [153], the base point and the representative operating points. For both the solutions, the operating points are distributed in the whole working area, far from the overload trajectory. It is worth noticing that the machines work for most of the time (45% for the UDDS and 60% for the US06/SFTP) with a current of about 30% of the peak one, in the proximity or along the MTPA locus. In fact, for the UDDS, the point with the highest utilization is also a MTPA point, while for the US06/SFTP it is placed close to the MTPA, in FW operation. Finally, it is also observed that, for the requested maximum speed, the MTPV trajectory is never reached.

8.3.2 Driving cycle optimization

A multi-objective DE optimization algorithm has been performed to optimize the torque T_{obj} and the losses $P_{l,obj}$, including the copper and the iron losses. They are defined as,

$$\begin{cases} max\left\{T_{obj}\right\} = max\left\{\sum_h \left(w_{eq,h} \cdot T_{eq,h}\right)\right\} & \text{(8.4a)} \\ min\left\{P_{l,obj}\right\} = min\left\{\sum_h \left(w_{eq,h} \cdot P_{leq,h}\right)\right\} & \text{(8.4b)} \end{cases}$$

These quantities represent the weighted sum of the respective value in the representative operating points over the driving cycle. As outlined in Sec. 12.2 and reported in (8.4), for each h-th operating point, the torque $T_{eq,h}$ and losses $P_{leq,h}$ have been weighted with the corresponding weight coefficients $w_{eq,h}$. Since a further optimization of the rotor geometry might yield to noticeable variation of the torque ripple and the torque-speed profile, the optimization variables have been limited to the slot dimensions (tooth width and slot height). For each iteration, the voltage limit has been verified, for the given space current vector and speed (i.e. frequency). This ensures an effective control of the machine in the representative operating points.

Fig. 8.5 shows the Pareto front for both the machines, highlighting the selected final solutions. Since an optimization of the torque ripple has not been included, due to the high computation time, the optimal geometries have been chosen in order to exhibit comparable torque ripple in the base point, while providing the same peak torque. For this last reason, the objective torque is equal to the correspondent one of the baseline design.

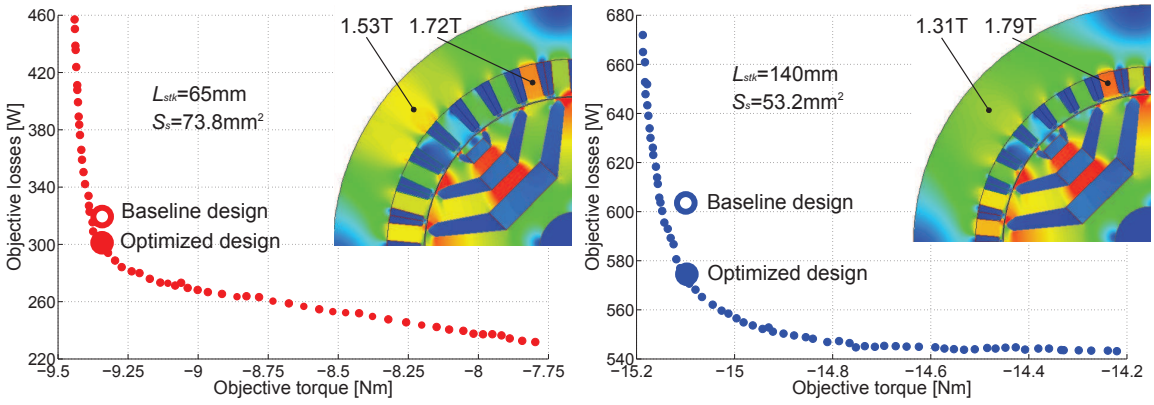

(a) UDDS. (b) US06/SFTP.

Fig. 8.5: Pareto front and flux density map of the optimized design at the base point.

8.4 Results and comparison

The main geometrical parameters and main electromechanical data of the baseline motor solutions and those that has been optimized along the driving cycles, are reported in Table 8.4.

The torque profiles at the base point are reported in Fig. 8.6 together with their respective torque ripple ΔT_r. As mentioned in Sec. 11.3.2, the optimization of the torque ripple over the driving cycle has not been included. On the other hand, the optimization procedure has not worsened much the torque ripple at the base point in comparison to the baseline design, with an increase of few percent points.

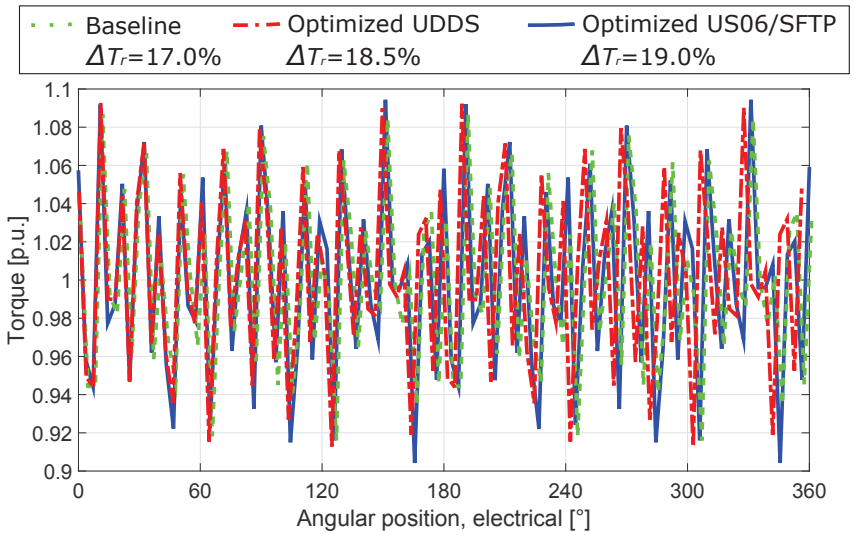

Fig. 8.6: Torque vs. angular position (electrical) at the base point.

Fig. 8.7 shows the copper and iron losses distribution, over the representative points, are reported. The baseline machines and the driving cycle optimized motors have been finally simulated according to the respective speed profiles, evaluating the cycle energy efficiency given by,

$$\eta_{e,cycle} = \frac{\sum_h \left(w_{eq,h} \cdot T_{eq,h} \cdot \Omega_{meq,h}\right)}{\sum_h \left(w_{eq,h} \cdot \left(T_{eq,h} \cdot \Omega_{meq,h} + P_{leq,h}\right)\right)} \tag{8.5}$$

The optimized UDDS motor exhibits a slot area about 5% higher than those of the baseline motors. However, the optimized US06/SFTP machine requires a copper area about 25% lower. This can be explained by the different behavior of the iron and copper losses along the driving cycle. Considering, for example, the working points with the highest use (61.6% and 45.7% for the US06/SFTP and UDDS, respectively) some remarks can be done.

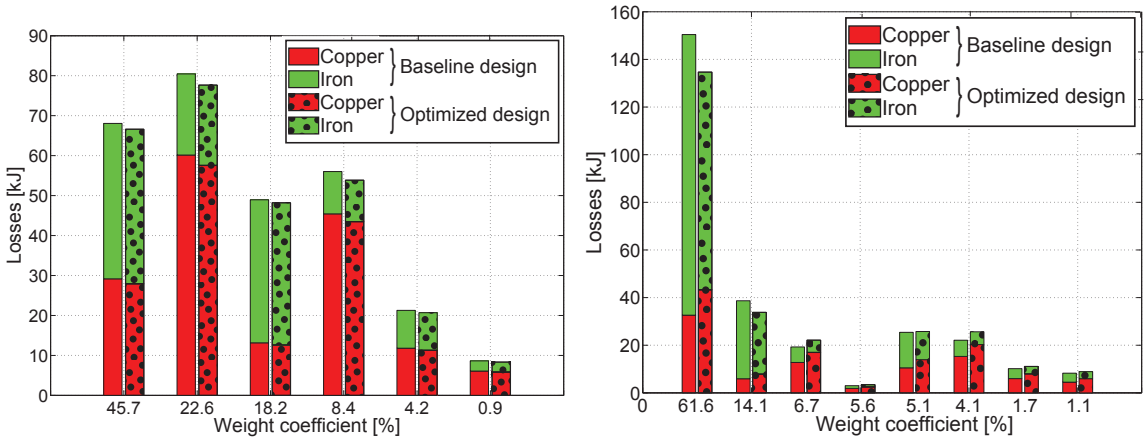

(a) UDDS. (b) US06/SFTP.

Fig. 8.7: Losses distribution over the representative points.

Fig. 8.8 report the comparison between the electrical losses and efficiency loci for the US06/SFTP driving cycle. The highest and lowest weight representative point is highlighted. Since the US06/SFTP operation is concentrated at high speed, the iron losses are the dominant component, resulting almost 4 times the copper losses. For the selected design, the back iron mass is the main part of the stator mass, thus the yoke losses results to be the prevalent contribution of the iron losses, being about 1.7 times the teeth losses. For this reason, the optimization is mainly addressed to reduce this contribution. As shown in Figs. 8.3(b) and 8.7(b), this is carried out decreasing the flux density levels in the yoke from about $1.6T$ to $1.3T$. This yields to a reduction of the iron losses in the cycle of more than 20%.

On the other hand, it leads to an increase of about 33% of the current density and thus the copper losses, which are, under the efficiency point of view, critical at low speed and base point operation. In fact, the base point electrical efficiency of the baseline machine is about 93.3%, one percent higher than that of the cycle optimized design.

As reported in Figs. 8.8(f) and 8.8(e), the optimization works extending the high efficiency area to the low torque, high speed operation. In the optimized design, this goes to the detriment of the efficiency at high torque, low speed operation.

Conversely, as shown in 8.7(a), the UDDS design mainly works at low speed, where the copper losses are noticeable. In this case, the increase of the efficiency is mainly achieved by means of an increase of the slot area.

Comparing the baseline designs with those optimized along the driving cycle, a limited increase of the cycle efficiency is expected. The increase is slightly higher for the

US06/SFTP since the optimization is focused on the reduction of the iron losses at high speed operation, far from the base operating point where copper losses are otherwise remarkable.

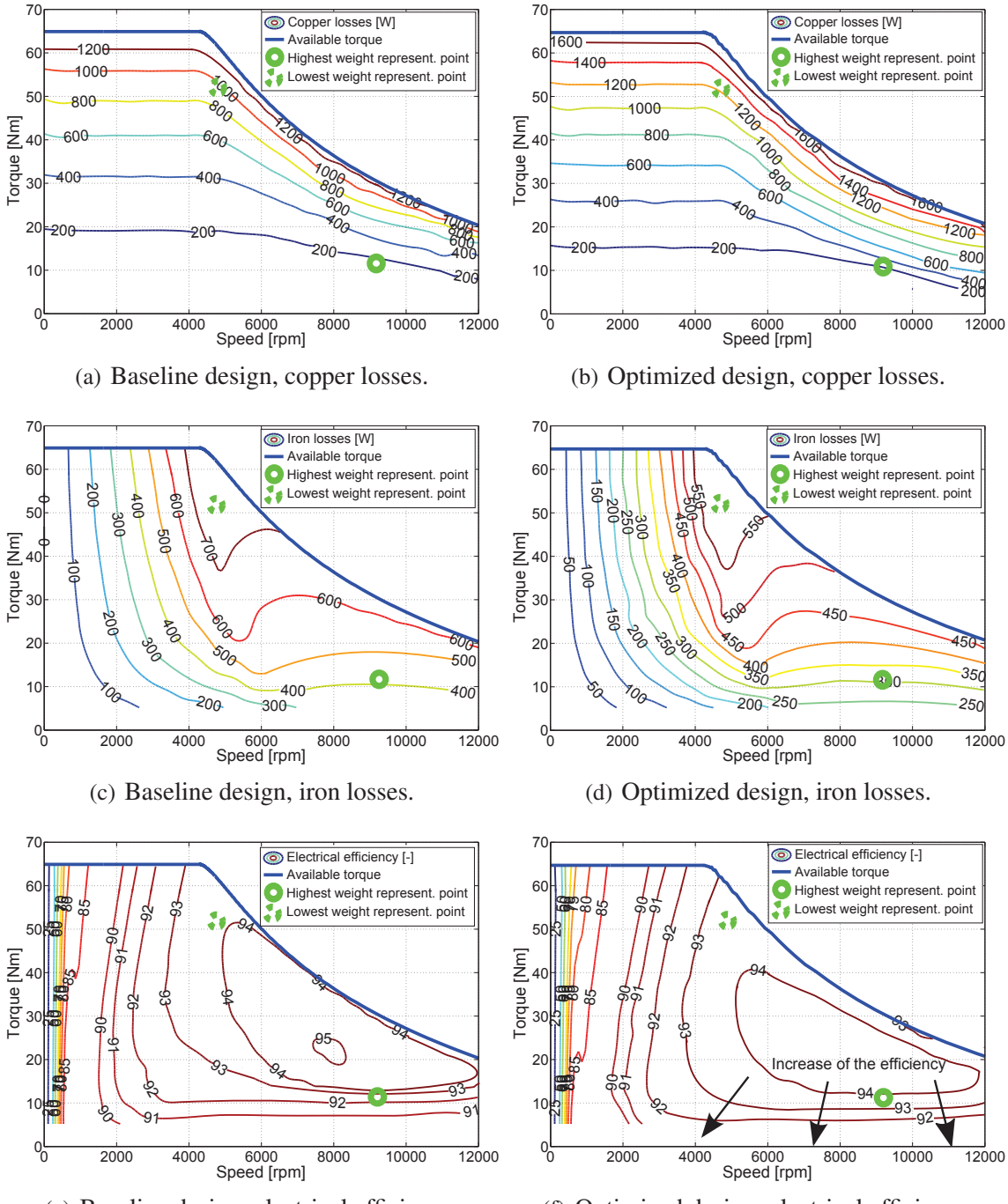

(a) Baseline design, copper losses.

(b) Optimized design, copper losses.

(c) Baseline design, iron losses.

(d) Optimized design, iron losses.

(e) Baseline design, electrical efficiency.

(f) Optimized design, electrical efficiency.

Fig. 8.8: Constant electrical losses and efficiency loci for the US06/SFTP driving cycle.

8.5 Conclusions

This research investigates the design and optimization of a PMASR motors for traction applications. The most profitable working area is considered according to two duty cycles, one for city driving while the second suitable for mixed driving operation. A preliminary optimization of the motor design has been carried out in the base point. A cycle optimization over a group of representative points has been introduced and subsequently performed in order to reduce the losses during the operation along the driving cycle.

This research shows that an increase of the efficiency over the driving cycle is achieved performing a global optimization. The effectiveness of the cycle optimization is emphasized in comparison of the base point optimization. The cycle optimization works balancing the ratio between the copper and iron losses, according to the different operating conditions of the driving cycle. In machines designed for low speed operation, the advantages of the cycle optimization are negligible. Conversely, better results are got when the machine operation is concentrated at high speed range.

Table 8.4: Key machine parameters summary.

Name	**Symbol**	**Baseline designs**		**Optimized designs**		**Unit**
		UDDS	**US06/ SFTP**	**UDDS**	**US06/ SFTP**	
Stack length	L_{stk}	65	140	65	140	mm
Tooth width	w_t	7.48		7.07	6.72	mm
Slot height	h_s	15.7		15.3	11.4	mm
Slot area	S_s	70.6		73.8	53.2	mm^2
Slot opening width	w_{so}	2.09				mm
Flux barrier angle 1	θ_{b1}	7.0				$^\circ$
Flux barrier angle 2	θ_{b2}	23.6				$^\circ$
Flux barrier angle 3	θ_{b3}	38.4				$^\circ$
Insulation coefficient	k_{air}	0.48				$-$
Overload current dens. (base point)	J_B	12.7		12.1	16.9	A_{RMS}/mm^2
Overload torque (base point)	T_B	30	65	30	65	Nm
Overload torque ripple (base point)	ΔT_{rB}	17.0		18.5	19.0	$\%$
Overload losses (base point)	P_{lB}	1309	2105	1234	2302	W
Overload elec. eff. (base point)	η_{eB}	90.5	93.3	91.0	92.5	$\%$
Objective torque	T_{obj}	9.36	15.1	9.36	15.1	Nm
Objective losses	P_{lobj}	314	602	305	576	W
Cycle copper losses	E_{Cu}	166	89.4	159	119	kJ
Cycle iron losses	E_{Fe}	117	188	118	147	kJ
Cycle elec. energy efficiency	$\eta_{e,cycle}$	89.8	94.0	90.1	94.5	$\%$

Chapter 9

Traction PMASR robust optimization according to a driving cycle

9.1 Introduction

The progressive electrification of the private transport systems is becoming a well-established reality in the international scenario since it is seen as the most promising solution to reduce air pollution, oil dependency and to improve energy efficiency. As for convention internal combustion engine vehicles, the performance of an electric vehicle are strictly related to the driving conditions of the car in which the motor is installed. On the other hand, the actual working conditions of the electric motors are rarely considered when an optimization procedure is adopted. For this reason, since the machine works in different conditions, it becomes mandatory to optimize the design in the most profitable areas in which the motor operates, in order to improve the overall performance. On this basis, some recent researches [31, 36, 37, 100] have introduced new design and optimization techniques for traction motors, in order to enhance the efficiency against a defined driving cycle. However, previous researches have investigated neither the optimization of the torque ripple, nor the robustness of the solutions, over the aforementioned driving cycle.

This work aims to present an optimization procedure of a Permanent Magnet Assisted Synchronous Reluctance (PMASR) motor for traction application, considering a city and a highway driving operation. The motor is equipped with a 36-slot 4-pole and an integral-slot distributed winding. A high grade Ferrite Permanent Magnet (PM) is considered. The interest in Ferrite-based PMASR motors [4, 9, 40, 169] is spreading in the last years, as a consequence of the instability and the increase of the price of rare earth magnets. Moreover, it has been shown, such as in [29], that PMASR motors exhibit a better FW range with re-

spect to other PM machines. Conversely, it is well known that the most important drawback for the PMASR is the intrinsically higher torque ripple [65] which can be reduced by means of different strategies, such as an optimization of the shape of the flux barriers and skewing [12, 170].
In this chapter a novel optimization strategy that takes into account both high efficiency and low torque ripple performance is introduced. The proposed method helps in searching a robust PMASR motor with optimal performance for more operating points over the driving cycle.

9.2 Evaluation of the motor requirements

9.2.1 Driving cycles

The motor performance have been assessed on the basis of two US driving cycles used to measure the fuel consumption and gas emission of light-duty vehicles.

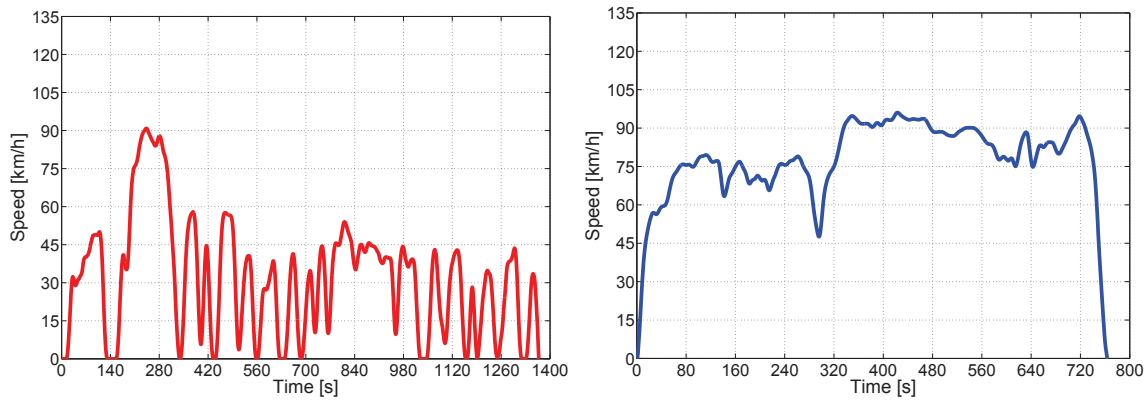

(a) UDDS (b) HWFET

Fig. 9.1: Driving cycle speed vs. time profiles.

The first, the Urban Dynamometer Driving Schedule (UDDS), is reported in Fig. 9.1(a). It is suitable for city driving. The cycle simulates an urban route of about 12 km with frequent stops and accelerations, with a maximum speed of about 91 km/h. It includes 23 stops over a period of 23 min for an average speed of 32 km/h.
The second, the Highway Fuel Economy Driving Schedule (HWFET), is reported in Fig. 9.1(b). It represents the highway driving cycle. It is characterized by a no-stop operation over a route of 16 km, with an average speed and a top speed of 77 km/h and 97 km/h, respectively [United States Environmental Protection Agency (USEPA)].

9.2.2 Torque and power distributions

In the analysis presented in this chapter these driving cycles are assumed to be performed by a medium size car with a mass of about $m = 1500\ kg$, equipped with two high speed PMASR motors. Each of them is connected to the respective wheel, with a diameter of $D_w = 500\ mm$, by means of a gearbox with a $1:8$ ratio. According to the method proposed in [49], the motor torque vs. speed distributions have been evaluated on the basis of the traction forces F_t computed, from the inertia force F, rolling force F_r and drag force F_d, as reported in (9.1). The grading force has not been accounted since the route covered by the vehicle is flat.

$$\begin{cases} F_t = F + F_r + F_d & \text{(9.1a)} \\ F = m \cdot a & \text{(9.1b)} \\ F_r = 0.01 \cdot \left(1 + \dfrac{v}{44.4}\right) \cdot m \cdot g & \text{(9.1c)} \\ F_d = \dfrac{1}{2} \cdot \rho \cdot c_x \cdot S \cdot v^2 & \text{(9.1d)} \end{cases}$$

where v is the car speed, a is the car acceleration, g is the gravitational acceleration and ρ is the air density. The frontal area and the drag coefficient, have been estimated on the basis of the average values of a typical medium size car, which are $S = 1.85m^2$ and $c_x = 0.4$, respectively.

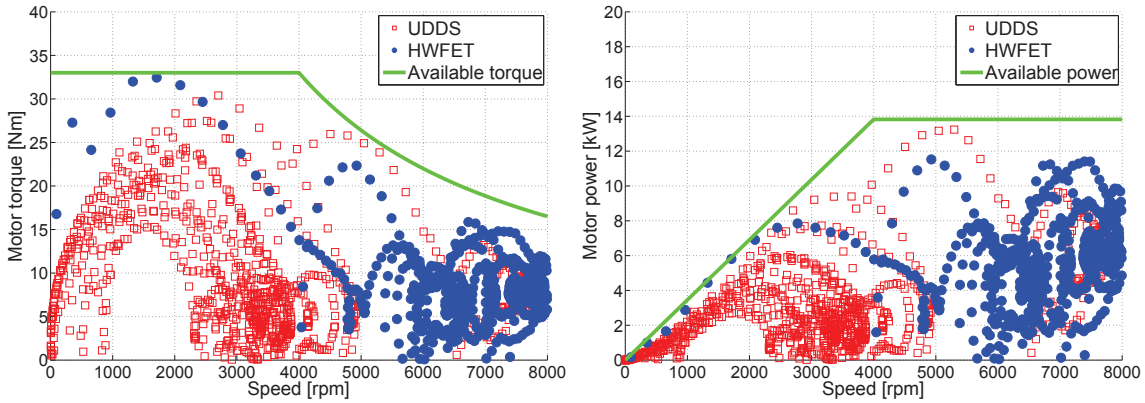

(a) Torque vs. speed.

(b) Power vs. speed.

Fig. 9.2: Electromechanical characteristics.

The torque and power vs. speed distributions, for both the driving cycles, are reported in Fig. 9.2. Since the optimization has been performed in the motor operation, the regenerative working area has been neglected in the present analysis.

The available torque and power curves target are highlighted, assuming a hyperbolic trend

over the base speed such as to ensure an ideal constant power speed range. The motor has to develop a rated torque of about $33Nm$ up to the base speed of about $4000rpm$, with a maximum speed in the order of $8000rpm$.

It is worth noticing that, for both the driving cycles, the machine operates mainly at low torque. The RMS torque, that provides an assessment of the thermal state of the machine, is about $11Nm$ for the UDDS and $9Nm$ for the HWFET. It follows that, even if the motor has to be designed for the rated torque, the optimization have to be effectively addressed in low torque operation.
Two representative operating torque-speed points (T_{eq}, n_{eq}), the first for the city, the second for the highway driving, have been evaluated. They are related to the operation at the highest working rate. They are computed on the basis of the calculation of the centre of gravity in the torque vs. speed distribution, according to the following equations,

$$\begin{cases} T_{eq} = \dfrac{\sum_k T_k}{p_t} & \text{(9.2a)} \\ n_{eq} = \dfrac{\sum_k n_{mk}}{p_t} & \text{(9.2b)} \end{cases}$$

Where:

- T_k, n_k are the k-th torque and k-th speed in the torque-speed plane, respectively.
- p_t the total number of torque-speed points of the driving cycle.

Table 9.1: Representative operating points of the driving cycles evaluated in the PMASR motor prototype.

Name	**Symbol**	**UDDS**	**HWFET**	**Unit**
Torque	T_{eq}	5	7.5	Nm
Speed	n_{eq}	3500	7000	rpm
Current density	J	2.2	3	A_{RMS}/mm^2
Current angle	α_{ie}	53	73	$^\circ$
Frequency	f	116	233	Hz

These points, in which the machine works for most of the duration of the driving cycle, are $T_{eq} = 5Nm$ at $n_{eq} = 3500rpm$ for the UDDS and $T_{eq} = 7.5Nm$ at $n_{eq} = 7000rpm$ for the HWFET.

9.3 Design and optimization

A 36-slot 4-pole PMASR, integral slot distributed winding design, has been considered. The main motor dimensions are based on an existing prototype [59], designed and optimized for automotive application. A sketch of the motor cross section is reported in Fig. 9.3(a). The outer and airgap diameter are $200mm$ and $125mm$ respectively, while the airgap height is equal to $0.35mm$. The prototype has been manufactured and tested. As shown in [59], a good agreement between the experimental results and Finite Element Analysis (FEA) is achieved. A further improvement of the existing machine is aimed. The stator outer diameter has been kept as a constraint in order to maintain the same motor frame and the overall volume. For these reasons the design concentrate on the cross section optimization.

As reported in Table 9.1, the city and highway operating points, evaluated in 9.2.2, correspond to specific space current vectors and frequencies. As shown in Fig. 9.3(c) the city driving point is located along the maximum torque per ampere locus, while the HWFET is in FW working area.

9.3.1 Pre-optimization analysis

On the basis of the aforementioned stator lamination and the requested motor specification, a new optimized design has been evaluated. The machine has been designed in order to meet the target torque and power profile ensuring a safe demagnetization at the operating temperature in the range between $150°C$ and $180°C$, working at a rated current density of about $9A_{RMS}/mm^2$. The stack length and the number of conductors have been adjusted to meet different rated torque specifications and providing a base speed around the target value of $4000rpm$. An optimization algorithm has been performed to the aim of minimizing torque ripple T_r and losses P_l.

An evaluation and optimization of the robustness of the machine has been carried out. The robustness is a concept complementary to the sensitivity. A robust machine is defined as that machine configuration that exhibits the minimum sensitivity to any variation of the system parameters [20, 24, 131], which can be dimensional or operational (working conditions). This latter system variation is investigated in the current analysis. This is achieved imposing comparable performance in terms of torque ripple and losses in both the UDDS and HWFET operating points. Thus, the performance difference ΔT_r and ΔP_l, has to be minimized, as described by (9.3e) and (9.3f). Based upon the abovementioned argumentations,

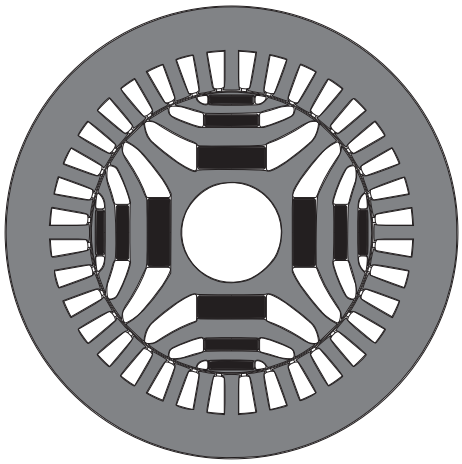

(a) PMASR motor cross section.

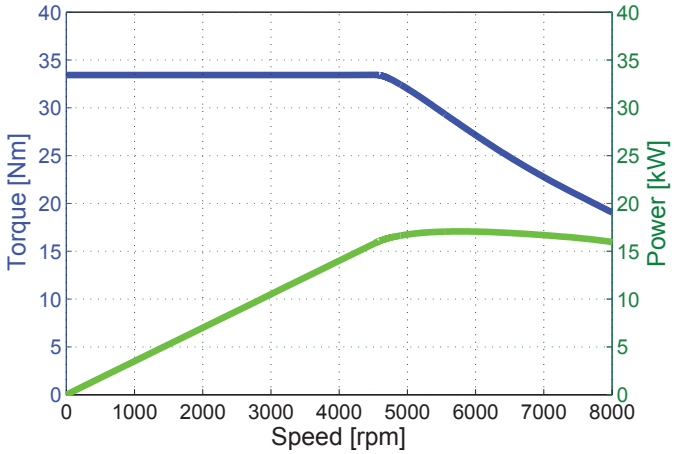

(b) Torque and power vs. speed.

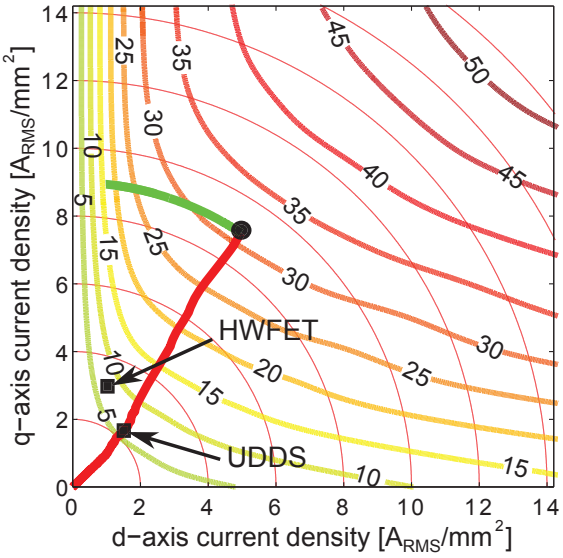

(c) d/q-axis current density plane. The representative operating points are highlighted.

Fig. 9.3: Baseline motor design data and performance.

the objective functions are defined as follows.

$$\begin{cases} min(T_{rUDDS}) & \text{(9.3a)} \\ min(T_{rHWFET}) & \text{(9.3b)} \\ min(P_{lUDDS}) & \text{(9.3c)} \\ min(P_{lHWFET}) & \text{(9.3d)} \\ min(\Delta T_r) = min|T_{rUDDS} - T_{rHWFET}| & \text{(9.3e)} \\ min(\Delta P_l) = min|P_{lUDDS} - P_{lHWFET}| & \text{(9.3f)} \end{cases}$$

Before selecting the optimization variables, it is important to consider their influence with respect to the objective functions. The sketch in Fig. 9.4 shows the main geometrical parameters that have been considered for the current study of this PMASR motor.

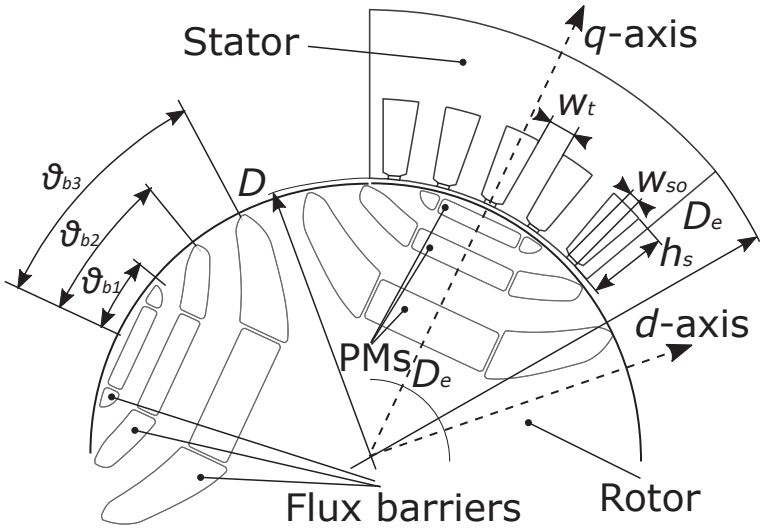

Fig. 9.4: PMASR geometrical variables.

The airgap and outer diameter, D and D_e respectively, have been kept as geometry constraints. It is well known that the motor performance are influenced by several parameters, since PMASR motors have intrinsically many degrees of freedom (especially the rotor geometry).

The torque ripple is determined by the interaction between the spatial harmonics of magnetomotive force (MMF) due to the stator currents and the rotor geometry and it is one of the main drawbacks of these motors. In [20] it has been shown that the torque ripple is very sensitive to the geometry along the airgap region. For instance, there is a strong impact of the flux barrier ends position, determined by the flux barrier angles (i.e. ϑ_{b1}, ϑ_{b2}, ϑ_{b3} of Fig. 9.4 assuming a rotor with three flux barriers per pole).

Other influential parameters are the slot opening width w_{so} and the iron bridges height (also called iron ribs) h_{rib}. The first is suitable to be optimized, even if there is a minimum threshold to be considered, depending on the diameter of the elementary conductor that has to be placed into the stator slot. The second parameter has to be designed with respect to the mechanical stress due to the mechanical forces arising at high rotational speed.

Regarding the thickness of the flux barriers and the permanent magnet dimensions, some considerations can be done. The portion of air (or PMs) with respect to the iron along the

Table 9.2: Input variables range properties.

Name	Symbol	Boundaries		Unit
		Lower	Upper	
Flux barrier angle 1	ϑ_{b1}	13	16	°
Flux barrier angle 2	ϑ_{b2}	25	28	°
Flux barrier angle 3	ϑ_{b3}	38	40	°
Insulation coefficient	k_{air}	0.35	0.45	–
Slot opening	w_{so}	1	4	mm
Slot height	h_s	12	22	mm
Tooth width	w_t	4	8	mm

q-axis, is defined as insulation coefficient. This parameter is defined as follows:

$$k_{air} = \frac{2 \cdot \sum_i h_{PMi}}{D_r - D_{ri}} \tag{9.4}$$

where h_{PMi} is the PM thickness of the *i-th* flux barrier (i.e. PM), D_r is the rotor diameter, D_{ri} is the shaft diameter. The choice of k_{air} is strongly related with two main design specifications. The first is the iron saturation level in the machine, whose effect has been deeply investigated in [59]. The second is the high saliency ratio ξ, in order to guarantee a proper reluctance torque. Conversely, PM dimensions have to be chosen taking into account the demagnetization, which can occur when the machine is working in deep flux weakening condition (high speed). Let us remember that the main role of the PMs in these types of motors is to saturate the iron bridges as well as enhance the power factor.

For these reasons, in order to explore the effect of the most influent parameters of both rotor and stator of the PMASR under study, the selected optimization variables are:

- the flux barriers angles ϑ_{b1}, ϑ_{b2}, ϑ_{b3},
- the insulation coefficient k_{air},
- the slot opening w_{so},
- the slot height h_s,
- the tooth width w_t.

Table 9.2 reports the range of variation of these optimization variables.

9.3.2 Optimization procedure

Once the input motor variables are set, an automatic optimization procedure is carried out, as follows:

1. Definition of the FEA model, setting of the sources and boundary condition.
2. Evaluation of the UDDS and HWFET points by means of a FEA parametric analysis in d/q-axis current density plane. For each (J_d, J_q), the torque, d/q-axis flux linkage and copper losses have been computed.
   On the basis of the voltage equations, the speed (i.e. the frequency) and the iron losses have been finally evaluated. Finally, the d/q-axis current density of the UDDS and HWEFT have been extracted from the resultant look-up table.
3. Load analysis for an accurate evaluation of the torque ripple in the UDDS and HWFET working points.

A multi objective genetic algorithm has been used. It works on a set of design configurations which are periodically updated when one generation is completed. It uses a smart multi-search elitism. The concept of elitism enhances the convergence properties towards the Pareto-optimal set. This operator is able to preserve some solutions without bringing premature convergence to local-optimal frontiers. These are the closest to the Pareto front exhibiting the best dispersion. Elitism is introduced storing all non-dominated solutions discovered so far, including the initial population. The operators of crossover, mutation and selection have been set in order to provide robustness and efficiency to the optimizer. At each step of the reproduction process, one operator is chosen and applied to each individual. A new set of variables, selected among the boundaries reported in Table 9.2, is then reassigned and the FEA is carried out again for the next generation.

9.3.3 Evaluation of the robustness

As mentioned in the previous section, the robustness concept has been introduced as an objective function of the optimization procedure. In order to evaluate quantitatively the robustness of the solutions of the final Pareto front a general mathematical procedure is presented hereafter.
Even this method can be easily extend to a hyperspace, two objective functions y_1 and y_2 in the bidimensional space are considered in this analysis. They are reported in Fig. 9.5.

The solutions which show the same value of the objective function ${y_1}^* = {y_2}^*$ are the most robust in the Pareto front. Thus, a robustness locus exists and it is described by a linear relationship $y_2 = y_1$. Considering the general solution $({y_1}^*, {y_2}^*)$ in the design space, a representative distance of this combination to the robustness curve is evaluated along the perpendicular line between the point $({y_1}^*, {y_2}^*)$ and the line $y_2 = y_1$. As shown in (9.6), the intersection point coordinate $(< y^* >, < y^* >)$ is equal to the mean value of the two

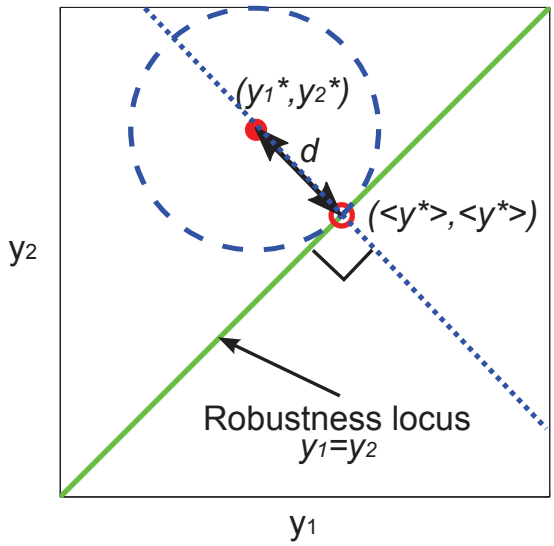

Fig. 9.5: Concept of the robustness for a 2 - objective functions design space.

objective functions.

$$< y^* >= \frac{{y_1}^* + {y_2}^*}{2} \tag{9.5}$$

Every solution that exhibits the same mean value lies on the same straight line perpendicular to the robustness locus. The distance of the solution $({y_1}^*, {y_2}^*)$ to the intersection point $(< y^* >, < y^* >)$ is defined as,

$$d = \sqrt{({y_1}^* - < y^* >)^2 + ({y_2}^* - < y^* >)^2} \tag{9.6}$$

As a consequence, among the solutions exhibiting the same mean value, i.e. lying on the same straight line perpendicular to the robustness locus, the most robust solution results to be that showing the lowest distance d from the mean value.

9.3.4 Results

Fig. 9.6 reports, for each iteration, the value of the torque ripple and the losses corresponding to the UDDS and HWFET operating points. Since the optimization procedure is aimed to find a robust design, the distribution of the points are concentrated around the robustness curves.

As shown in Fig. 9.6(a), the torque ripple distribution exhibits a high variation, in particular in the region above the robustness locus. The reason of this effect is mainly due to the higher

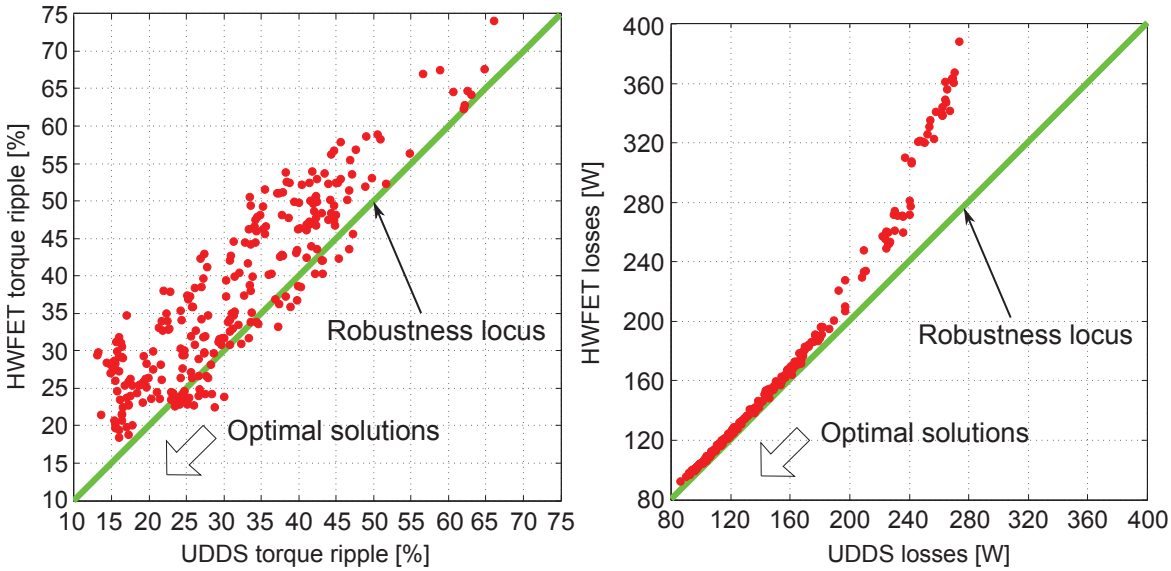

(a) Torque ripple trend.

(b) Losses trend.

Fig. 9.6: Torque ripple and losses distributions in UDDS and HWFET cycles.

torque ripple in flux weakening operation [84], i.e. in the HWFET point. It is worth noticing that the average distance, between the solutions and the robustness locus, is quite high. This confirms that torque ripple is very sensitive to the geometrical parameters variation.
Similarly to the torque ripple, Fig. 9.6(b) reports the losses distribution. In this case the optimization results are more concentrated along the robustness locus. The solutions are shifted above for all cases due to the higher contribution of the iron losses at the higher speed (HWFET operating point) with respect to the UDDS point.
Finally, the losses distribution diverges gradually from the robustness locus once the power loss exceeds $200W$. For lower values, the distance d is low, showing that losses are less sensitive to the geometrical variation within the range of variables.

Fig. 9.7 shows the trend of the solution distance with respect to the robustness locus vs. the mean torque ripple and the losses, evaluated comparing UDDS and HWFET operating points, according to the concept introduced in Sec. 9.3.3.
In Fig. 9.7(a), the most representative robust designs for the torque ripple are highlighted with blue filled circles, between A and B. These points exhibit the highest robustness, since the distance d from the robustness locus is approximately zero, while the mean torque ripple, in UDDS-HWFET operation, increases from A to B.

Always referring to Fig. 9.7(a), the solution C is also considered. It exhibits a mean torque ripple lower than 20% and the lower distance d from the robustness curve.

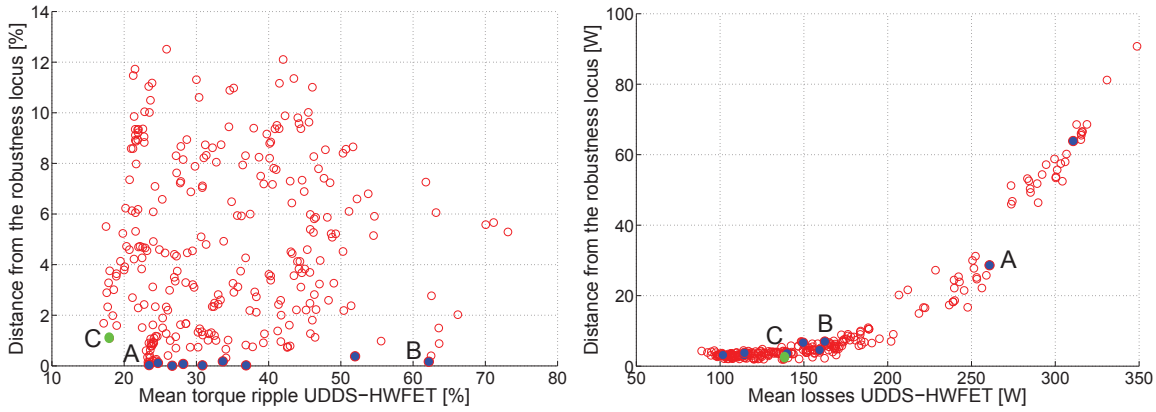

(a) Torque ripple trend. (b) Losses trend.

Fig. 9.7: Distance of the solution from the robustness locus in UDDS and HWFET cycles.

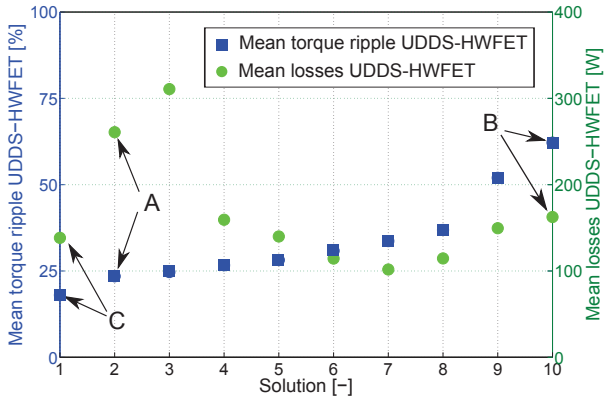

Fig. 9.8: Mean torque ripple (blue squares) and losses (green circles) trend of the most robust solutions ($d \simeq 0\%$).

The corresponding losses are highlighted in Fig. 9.7(b). It is worth noticing that the robust designs for the torque ripple do not correspond to the robust solutions as far as the losses are concerned. For instance, the solution A, which is robust in terms of torque ripple, shows a noticeable distance from the robustness losses curve (see Fig. 9.7(b)), while the B exhibits good robustness for both torque ripple and losses.

In order to help in the optimal solution selection, Fig. 9.8 reports the mean torque and losses trends of the most robust solutions ($d \simeq 0$) which, from the torque ripple point of view, are highlighted in Fig. 9.7(a). This representation confirms that a solution with a robustness satisfying one of the two objective functions, for instance solution A, does not necessarily satisfy the other one.

As usual, the selection of the best solution is a tradeoff between the results that better sat-

Table 9.3: Robust machines.

Name	**Symbol**	**A**	**B**	**C**	**Unit**
Flux barrier angle 1	θ_{b1}	13.9	13.9	14.5	*degrees*
Flux barrier angle 2	θ_{b2}	26.7	25.6	26.5	*degrees*
Flux barrier angle 3	θ_{b3}	38.7	38.7	38.6	*degrees*
Insulation coefficient	k_{air}	0.39	0.41	0.35	–
Slot opening	w_{so}	1.6	2.5	2.1	*mm*
Slot height	h_s	16	13.2	14.4	*mm*
Tooth width	w_t	6.4	6.2	7.6	*mm*

Table 9.4: Torque ripple and losses performance of design C.

	UDDS	**HWFET**	**Unit**
Torque ripple	16	17.6	*%*
Copper losses	33	68	*W*
Iron losses	103	72	*W*
Losses	136	140	*W*

isfy all the objective functions. In this case, considering these motor topologies and the application, the best compromise among the losses variation is resulting in design *C*, which is robust and exhibits low torque ripple and losses for both the considered driving cycles. In Tab. 9.3 are reported the dimensional parameters for machines A, B and C, which are sketched in Fig. 9.9.

Finally, comparing to the previous solutions, design C is robust in terms of losses but, it is not for the torque ripple. Table 9.4 reports the comparison between the torque ripple and losses in the UDDS and HWFET for design C. The copper losses and iron losses are highlighted. The results are confirming the comparable total losses for both the considered driving cycles.

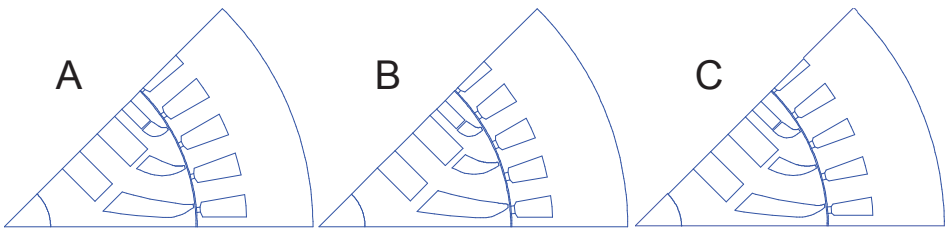

Fig. 9.9: Motors A, B and C.

Analysing more in detail the machines resulting from the optimization and represented in Fig. 9.7(a), it is worth noticing that there is a set of solutions, which are not the most

robust under the definition espressed by eq. 9.6, presenting a mean torque ripple lower than 20%.

Depending on the application and the requirements it is possible to consider solutions in a wider range of robustness, for instance the ones with d lower than 4%. In this case, similarly to the representation of Fig. 9.8, the machines performances are shown in Fig. 9.10. Always considering the enlargement at the bottom of Fig. 9.10, the motors highlighted with filled triangles are exhibiting a mean torque ripple lower than 20%. All these machines have a lower torque ripple in UDDS with respect to HWFET operating points. Finally, in Fig. 9.11 the optimized torque ripple trend calculated for the motor C is shown.

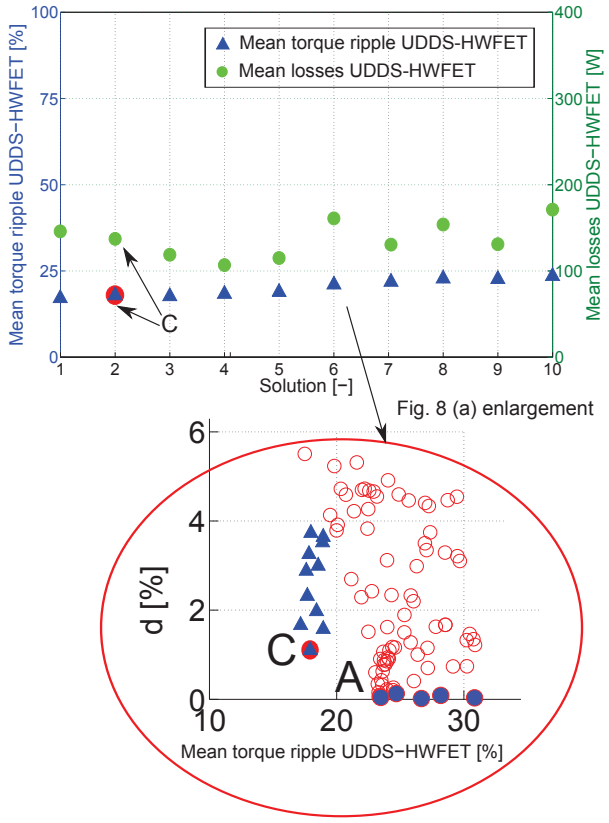

Fig. 9.10: Mean torque ripple (blue triangles) and losses (green circles) trend of the solutions considering a robustness range with $d < 4\%$); bottom: Enlargement with machines presenting a torque ripple lower than 20% (blue triangles).

9.4 Conclusions

To the aim of designing a PMASR motor for traction application, different driving cycles have to be considered. In this analysis, two driving cycles are taken into account, the first for

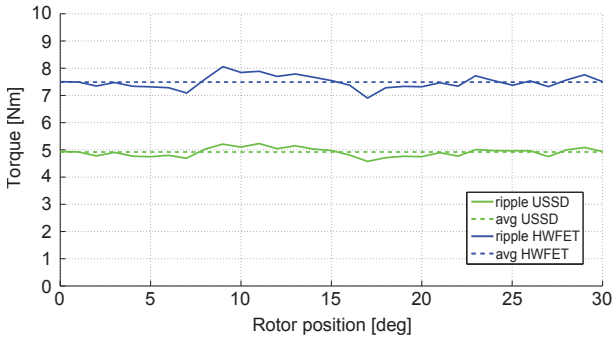

Fig. 9.11: Torque ripple vs. rotor position for motor C: comparison for two driving conditions (UDDS and HWFET).

the city driving USSD and the second for the highway driving HWFET. The electromechanical specification and the most profitable working areas have been predicted. The analysis of the geometrical parameters to be selected as optimization inputs has been done to this purpose.

The design has been optimized by means of genetic algorithm aimed to the minimization of the torque ripple and the losses in the considered driving cycles. The robustness concept has been defined in order to find the best solution in the design space.

It has been shown that the difference between torque ripple and losses can be introduced as additional objective functions. It is demonstrated that this help in the selection of a machine among the others, when presenting comparable performance for the two representative working points.

The analysis of the optimized solutions emphasizes that a robust solution for the torque ripple might not necessarily be a robust solution with respect to the losses.

The best candidate has been selected as a trade off between the lower torque ripple and the most robust results.

This method is suitable for the analysis over a wider range of representative points where the motor normally operates during a driving cycle. Hence, a robust design, in terms of working conditions, is achievable converging to a final solution which presents similar torque ripple and losses in the considered operating points.

Part III

Design, analysis ed optimization of EPS machines

Chapter 11

Analytical model and PM minimization of spoke type FSCW motors

11.1 Introduction

Interior Permanent Magnet (IPM) synchronous motor equipped with Fractional Slot Concentrated coil Winding (FSCW) are nowadays widely considered due to attractive features. The IPM motor offers high efficiency, wide constant power speed range, high torque density, sensorless capability, robustness, reliability [84, 151] and potential magnet mass saving [50]. The adoption of FSCW yields manufacturing simplicity, lower end winding length [12] and lower total axial length [108], higher power density, higher fill factor [54], lower cogging torque and torque ripple[12], higher synchronous inductance [12] and better fault tolerant capability [112]. On the other hand, the increase and the instability of the price of rare earth PMs is pushing the research of rare earth free/less PM alternatives. A high airgap flux density is achieved using the IPM configuration that employs flux concentration with the I-shape tangential magnetization topology. It is also called spoke type motor [89, 95] and it is reported in Fig. 12.1. On the other hand, comparing to other IPM machines, spoke type machines exhibit important drawbacks that are summarized in a limited flux-weakening capability, lower saliency ratio [22] and lower demagnetization strength [57, 89, 95].

Regarding the magnet technology, an attractive low cost PM for spoke type motor, is represented by ferrite PM. As shown in Fig. 1.17, a high grade ferrite PM provides about $1/3$ of the remanence flux density at room temperature of an high grade, conventional sintered NdFeB (N45UH), with a price that is approximately 10%. Most of the researches on spoke type motor have been focused on ferrite motor designs showing the benefit of flux concentration in terms of the airgap flux density increase. On the other hand, it seems to be

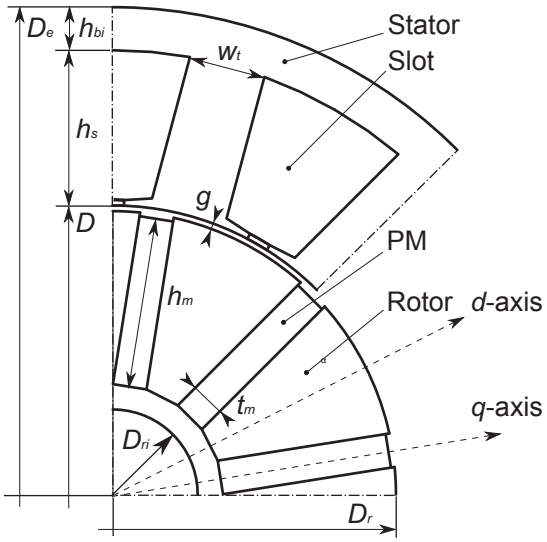

Fig. 11.1: 1/4 IPM spoke type sketch.

difficult to achieve airgap flux density levels comparable to rare-earth (RE) IPM machines [46, 57]. In order to overcome this limitation, a ferrite spoke-ring combination is proposed in [138] and a wing-shaped configuration has been introduced in [139].

When high torque density is required, the more valuable RE iron-boron based PM seems to be an effective solution and the combination of the NdFeB together with the spoke type motor is able to provide the highest torque density among the IPM topologies [57]. In a conventional NdFeB, the dominant cost component is due to the addition of Heavy RE (HRE) compounds, such as Dysprosium (Dy) and Terbium (Tb), which increase the thermal stability and intrinsic coercivity. In order to overcome the drawback of high and variable price, Dy-free NdFeB compounds have been recently developed [186]. Besides to the Dy-free sintered NdFeB, additional interest is growing around the less known hot pressed Dy-free NdFeB, commercially called MQ2 [101]. By means of particular manufacturing process, this compound exhibits an excellent thermal stability, comparable to Dy-with NdFeB. This allows to employ magnets with lower thickness, ensuring safe demagnetization levels and improving the flux-weakening performance. On the other hand, as shown in Fig. 1.17 the remanence flux density at room temperature is 40% lower than the sintered NdFeB one, but double of ferrite one. In addition to the absence of Dy, the most important advantage is the halving of the price, ranking nowadays in an intermediate position between ferrite and heavy HRE NdFeB.

During the last decade, several researches have been carried out on the design of spoke type motors. In [115, 173] an analytical procedure based on the reluctance model of the

machine have been used, while in [86] an analytical model, based on the concept of the equivalent machine [117] has been considered. Some Finite Element Analysis (FEA) have been performed in [158, 187, 188], evaluating the influence of some design factors, such as the number of poles, magnet thickness and shaft arrangement. On the other hand, a comprehensive study of the influence of the machine dimensions on the motor performance has not been already carried out. At last, the price issue of RE NdFeB makes mandatory an accurate study of the optimal motor dimensions to the aim of PM minimization.

This research deals with the design criteria of a spoke type FSCW IPM motor, focusing on the maximization of the airgap flux density, minimization of the PM volume and evaluation of the optimal split ratio. An analytical procedure is presented and validated, by means of FEA, on a motor designed for Electric Power Steering (EPS) system. An hot pressed Dy-free NdFeB PM has been considered in this analysis. Various slot/pole configurations are analyzed and compared in order to achieve general considerations about the motor design. To the same purpose, dimensionless parameters are used in order to compare different designs choices.

11.2 Preliminary considerations

The EPS systems require high performance in terms of torque density, torque quality and noise. Since these performance are mainly related to the combination of the number of slots and poles, a preliminary selection of the most promising slot-pole configurations has been carried out. It is useful to consider some quality indexes: (*i*) the winding factor of the main harmonic k_{w1}, (*ii*) the cogging torque $i_{cog} = LCM(Q, 2 \cdot p)$ and (*iii*) the radial force index $i_{rf} = GCD(Q, 2 \cdot p)$. These last two indexes provide a qualitative indication of the cogging torque and radial force levels. Let us to remember the higher the indexes, the lower the cogging torque and the unbalanced magnetic radial forces. An optimal slot combination should exhibit a high k_{w1}, a high i_{cog} [54] and even and high i_{rad} [26, 54, 107].

The flux concentration is effective when the number of poles $2 \cdot p \geq 6$ [22]. Table 12.1 summarizes FSCW slot-pole combinations with a number of slots per pole and phase $1/4 < q < 1/2$, exhibiting a winding factor higher than 0.866. For limiting the frequency, spoke type motors for automotive applications are usually designed for $2 \cdot p \leq 16$. For the above mentioned reasons, the $9/8$, $12/10$, $18/12$, $12/14$, $18/16$ configurations have been finally considered since they provide the best overall performance.

Table 11.1: Comparison of the motor quality indexes.

$Q/(2\cdot p)$	q	k_{w1}	$LCM(Q,2\cdot p)$	$GCD(Q,2\cdot p)$
9/6	1/2	0.866	18	3
6/8	1/4	0.866	24	2
9/8	**3/8**	**0.945**	**72**	**1**
12/8	1/2	0.866	24	2
9/10	3/10	0.945	90	1
12/10	**2/5**	**0.933**	**60**	**2**
15/10	1/2	0.866	30	5
9/12	1/4	0.866	36	3
18/12	**1/2**	**0.866**	**36**	**6**
12/14	**2/7**	**0.933**	**84**	**2**
15/14	5/14	0.951	210	1
18/14	3/7	0.902	126	2
21/14	5/14	0.866	42	7
6/16	5/14	0.866	48	2
12/16	3/8	0.866	48	4
15/16	5/14	0.951	210	1
18/16	**5/14**	**0.945**	**144**	**2**
21/16	7/16	0.890	336	1
24/16	1/2	0.866	48	8

11.3 Analytical model

An analytical model of the spoke type IPM machine is presented hereafter. This procedure is based on the transformation of the actual motor into an equivalent machine [117], characterized by the following assumptions:

1. the stator is slotless;
2. the iron core permeability is high enough to neglect the iron magnetic drop ($\mu_{Fe} = \infty$);
3. the PM B-H curve is linear, i.e. the operating flux density is higher than of the knee of the curve;
4. the no load airgap flux density B_{g0} is a quasi-square wave distribution.

A rectified section of the equivalent machine is reported in Fig. 11.2. The magnetic voltage drop is across an equivalent airgap g". It is derived from the mechanical airgap g , multiplying by the Carter k_{Cart} and the saturation k_{sat} coefficient, i.e. $g" = k_{Cart} \cdot k_{sat} \cdot g$. When the stator is segmented [50], the airgap has to be further increased. Let B_g be the airgap flux density, B_m the PM flux linkage, B_{rem} the remanence flux density and B_h the bridge

flux density. H_g is the airgap magnetic field and H_m is the no load PM magnetic field. μ_0 is the air permeability and μ_{rec} is the recoil permeability. U_s is the stator magnetic potential, computed performing the Ampere's law along the magnetic circuit. A_g, A_m and A_h are the airgap, the PM and the bridge cross section, respectively. They are given by,

$$\begin{cases} A_g = (\tau_p - t_m) \cdot L_{stk} & \text{(11.1a)} \\ A_m = h_m \cdot L_{stk} & \text{(11.1b)} \\ A_h = h \cdot L_{stk} & \text{(11.1c)} \end{cases}$$

where h_m is the PM width and L_{stk} is the stack length and $\tau_p = (\pi \cdot \delta \cdot D)/(2 \cdot p)$ is the pole pitch. $\delta = D/D_e$ is the split ratio.

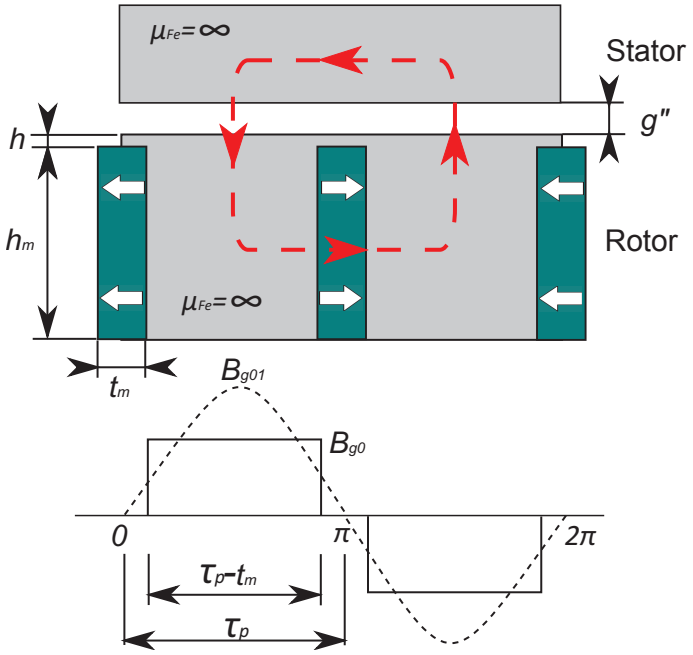

Fig. 11.2: Model of the equivalent machine and flux density distribution in no load operation.

According to this equivalent model, it is possible to define the system of equations reported hereafter.

$$\begin{cases} B_g \cdot A_g = 2 \cdot B_m \cdot A_m - 2 \cdot B_h \cdot A_h & \text{(11.2a)} \\ H_g \cdot 2 \cdot g" + H_m \cdot t_m = 2 \cdot U_s & \text{(11.2b)} \\ B_g = \mu_0 \cdot H_g & \text{(11.2c)} \\ B_m = B_{rem} + \mu_0 \cdot \mu_{rec} \cdot H_m & \text{(11.2d)} \end{cases}$$

It is useful to introduce three dimensionless coefficients: the cross section ratio $k_{cs} = h_m/t_m$, the thickness ratio $k_m = t_m/\tau_p$, and the PM volume ratio $\psi = (8 \cdot p \cdot w_m \cdot h_m) / \left(\pi \cdot {D_e}^2\right)$. This last coefficient represents ratio between the PM volume and the motor volume. It provides an effective indication of how cheap is the solution under investigation. It is worth noticing that it is not depending on the motor motor size.

11.3.1 No load operation

Solving (11.2), with $U_s = 0$, the no load airgap flux density is given by,

$$B_{g0} = \frac{B_{rem} - B_h \cdot \dfrac{h \cdot 2 \cdot p}{\pi \cdot k_{cs} \cdot k_m \cdot \delta \cdot D_e}}{\dfrac{4 \cdot \mu_{rec} \cdot g" \cdot p}{\pi \cdot k_m \cdot \delta \cdot D_e} + \dfrac{1}{2} \cdot \dfrac{1}{k_{cs}} \left(\dfrac{1}{k_m} - 1\right)} \tag{11.3}$$

The fundamental harmonic $\widehat{B}_{g1}$ is,

$$\widehat{B}_{g01} = \frac{4}{\pi} \cdot B_g \cdot \sin\left[\frac{\pi}{2} \cdot (1 - k_m)\right] \tag{11.4}$$

Assuming the leakage flux to be negligible, the flux concentration ratio $\chi = \widehat{B}_{g01}/B_{rem}$ is,

$$\chi = \frac{4}{\pi} \cdot \frac{sin\left[\dfrac{\pi}{2} \cdot (1 - k_m)\right]}{\dfrac{4 \cdot \mu_{rec} \cdot g" \cdot p}{\pi \cdot k_m \cdot \delta \cdot D_e} + \dfrac{1}{2} \cdot \dfrac{1}{k_{cs}} \left(\dfrac{1}{k_m} - 1\right)} \tag{11.5}$$

11.3.2 Load operation

The FSCW spoke type motor has a negligible anisotropy. The rated torque is basically achieved feeding the machine with stator current vector only along the q-axis. Moreover, as reported in Fig. 11.3, this winding arrangement yields a distribution of the magnetic scalar potential that can be assumed to be a square wave (dashed line). From the Ampere's law, the magnetic scalar potential is equal to the slot current, i.e. $\widehat{U}_s = \widehat{I}_{slot}$. Consequently, the maximum value of the stator airgap flux density is,

$$B_{sg} = \mu_0 \cdot \frac{\widehat{I}_s}{2 \cdot g"} \tag{11.6}$$

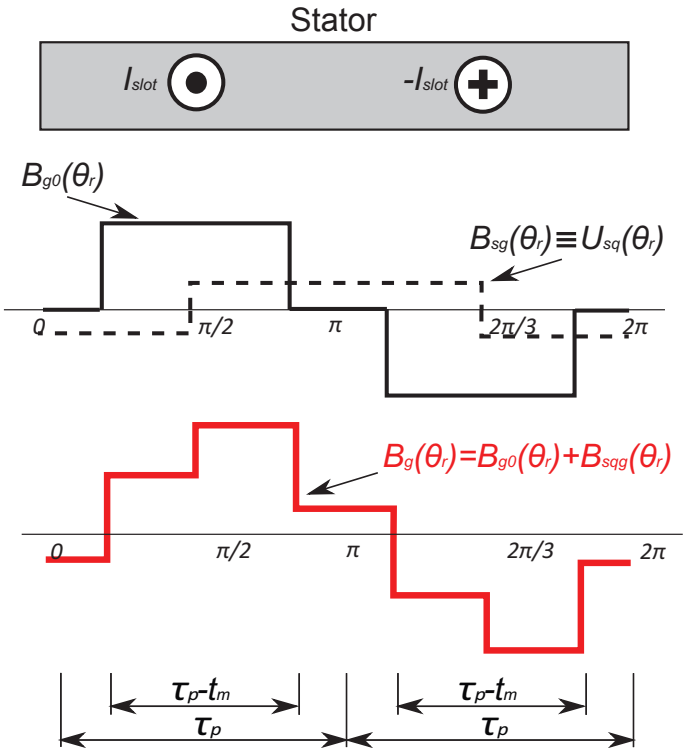

Fig. 11.3: Model of the airgap flux density distribution in q-axis load operation.

11.3.3 Motor synthesis

The stator dimensions have been evaluated on the basis of the airgap flux density, in order to ensure adequate flux density levels in the teeth $B_t \cong 1.7T$ and in the back iron $B_{bi} \cong 1.5T$. At this stage, the armature reaction is assumed to be negligible. The slot current $\widehat{I}_{slot}$ is evaluated according to the constraint of the copper losses P_{Cu}. As the machine is FSCW with $Q \cong 2 \cdot p$, the pole pitch τ_p is comparable to the slot pitch p_s. Fig. 11.4 shows a simplified model of the flux density distribution in front of a stator tooth, at no load and under load operation. Neglecting the leakage flux and the iron saturation of the tooth tip, the tooth width w_t can be estimated on the basis of the tooth flux that flows from one pole, that is,

$$\phi = \int_{p_s} B_{g0} \cdot dl \qquad if\ \tau_p \cdot (1-k_m) \geq p_s \tag{11.7a}$$

$$\phi = \int_{\tau_p \cdot (1-k_m)} B_{g0} \cdot dl \quad if\ \tau_p \cdot (1-k_m) < p_s \tag{11.7b}$$

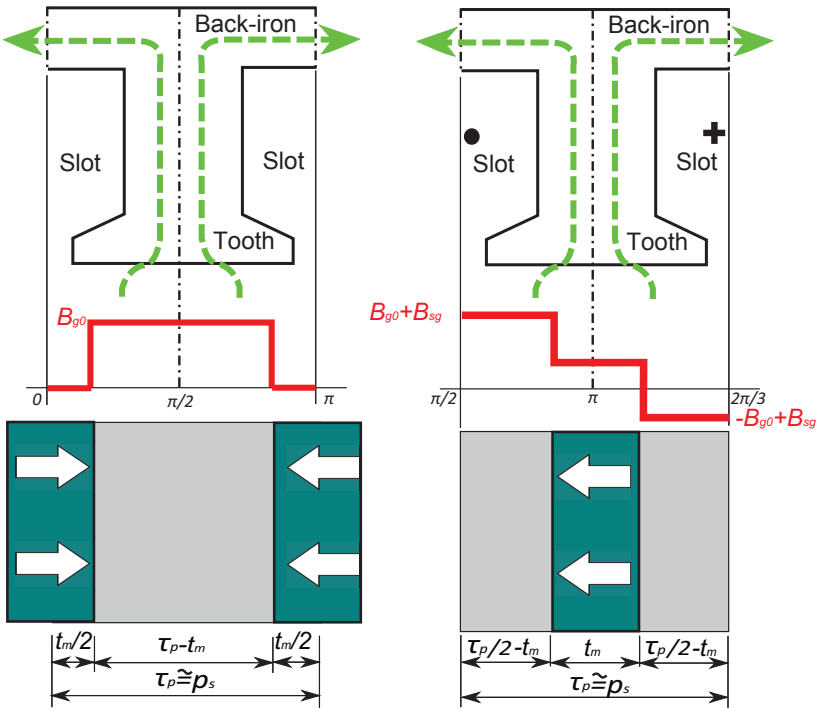

(a) No load. (b) Load.

Fig. 11.4: Stator flux density distribution.

The slot and tooth width, w_t and w_s respectively, are therefore,

$$w_t = \frac{\phi}{B_t} \tag{11.8}$$

$$w_s = p_s - w_t \tag{11.9}$$

As shown in Fig. 11.4, the flux in the back iron is assumed to be half of the airgap flux. The back iron height is therefore,

$$h_{bi} = \frac{1}{2} \cdot \frac{\phi}{B_{bi}} \tag{11.10}$$

Finally, the slot height h_s is constrained by the outer diameter D_e and it is equal to,

$$h_s = \frac{1}{2} \cdot D_e \cdot (1-\delta) - h_{bi} - w_t \tag{11.11}$$

The slot ending width w_{se} is,

$$w_{se} = \frac{\pi\,(\delta \cdot D_e + 2 \cdot h_s)}{Q} - w_t \tag{11.12}$$

Assuming a trapezoidal shape of the slot and neglecting the tooth tip, the slot area S_s is given by,

$$S_s = \frac{h_s}{2} \cdot (w_s + w_{se}) \tag{11.13}$$

For a given active copper losses P_{Cu}, the slot current $\widehat{I}_{slot}$ (peak value) is finally given by,

$$\widehat{I}_{slot} = \sqrt{\frac{2 \cdot k_{fill} \cdot P_{Cua} \cdot S_s}{\rho_{Cu} \cdot Q \cdot L_{stk}}} \tag{11.14}$$

Since the reluctance torque of FSCW IPM machine is quite negligible [97], the relationship used for SPM machines can be considered [17]. Thus, the torque density T_d, for a given motor volume $V = \frac{\pi}{4} \cdot {D_e}^2 \cdot L_{stk}$ is

$$T_d = \frac{1}{\pi \cdot D_e} \cdot \widehat{B}_g \cdot k_w \cdot Q \cdot \widehat{I}_{slot} \cdot \delta \tag{11.15}$$

An iterative algorithm based upon the aforementioned procedures has been implemented and summarized in Fig. 11.5. The machine design is carried out on the basis of the airgap flux density and slot current. The control of the iteration is operated on the saturation coefficient that is updated in each step. It is estimated, evaluating the magnetic voltage drop of the magnetic circuit knowing the magnetic characteristic of the iron. The magnetic path is represented by the tooth, back iron and airgap.
As reported in Fig. 11.4, under load operation the airgap flux density along one pole pitch due to the current can be considered constant and equal to B_{sg}. On the basis of this value, the machine design has been then adjusted and a load saturation coefficient has been computed in order to evaluate the torque density.

Finally the geometrical feasibility of the PM dimension has been taken into in account in order to avoid superimposition between two adjacent PMs. According to Fig. 12.1, it results,

$$\begin{cases} D_r - D_{ri} - 2 \cdot h \geq 2 \cdot h_m & \text{(11.16a)} \\ [D_r - D_{ri} - 2 \cdot (h + h_m)] \cdot \tan \dfrac{\alpha_r}{2} \leq t_m & \text{(11.16b)} \end{cases}$$

11.4 Validation and optimization

According to the analytical procedure proposed in Sec. 12.2, a spoke type motor has been designed. The constraints are the stator outer diameter $D_e \cong 90mm$, the stack length $L_{stk} \cong$

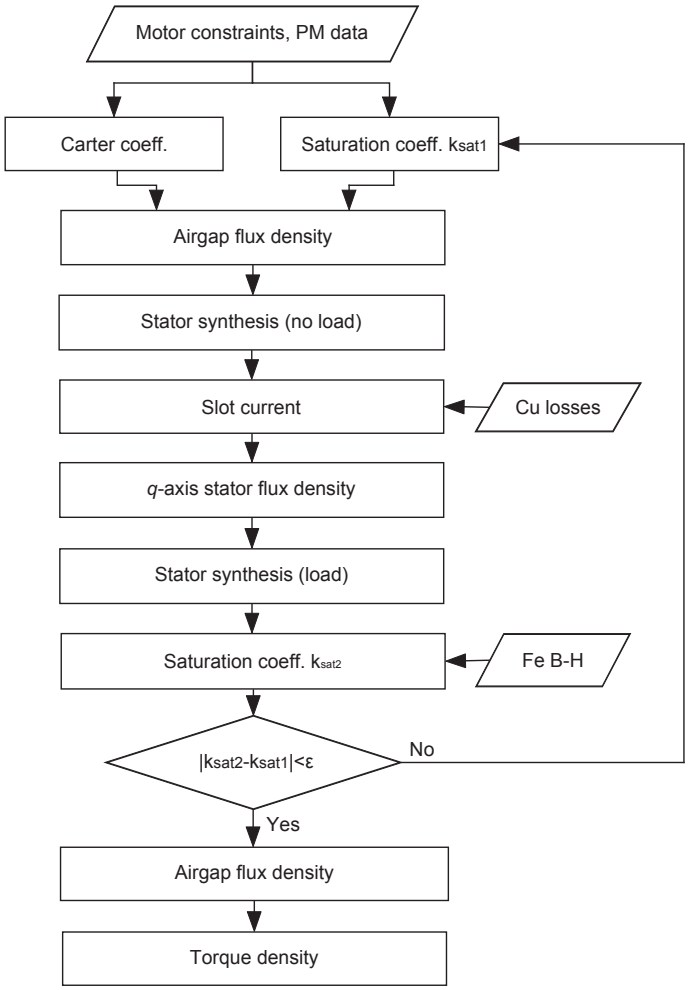

Fig. 11.5: Overview of the flow chart of the analytical procedure.

60mm, the copper losses $P_{Cu} = 180W$ and the shaft diameter D_{ri}. The slot opening height and width together to the wedge height are considered to be fixed.

11.4.1 Influence of the number of poles and PM cross section

According to (11.5), it is interesting to analyze the influence of the number of poles and the PM cross section on the flux concentration ratio χ. It is evaluated at no load operation, considering the PM dimensions and its possible minimization. The rotor leakage flux flowing in the iron ribs has been neglected. Finally, the split ratio has been fixed to $\delta = 0.5$. Fig. 11.6 reports the constant flux concentration ratio loci χ as a function of the PM volume ratio ψ and the thickness ratio k_m. As described in Sec. 11.3.3, the limit of feasibility is highlighted. The area under this limit represents the design area. Moreover, the design area

has a lower limit represented by the $\chi = 1$ curve, above which there is the flux concentration effect. In order to validate these results, some validation points, highlighted in the letters of the alphabet, have been considered. As reported in Table 11.2, a good agreement between FEA and analytical results has been got.

A locus of minimum PM volume maximizing the flux concentration ratio exists. Such a locus is defined as Maximum Flux Per PM Volume (MFPV). Considering for e.g. the $12/10$ machine, the point $B1$ provide a flux concentration ratio $\chi = 1$ along the limit of the feasibility. The same performance can be achieved in the points $B2$ with the same PM volume of the point $B1$. On the other hand, the minimum PM volume is got in the point B, along the MFPV.

Increasing the number of poles, these MFPV loci translate from lower value to higher value of k_m. Depending on the limit of feasibility, the MFPV locus is located partially within the design area. In particular, as the number of poles increases, the MFPV curve tends to fall completely within the design area (i.e. $18/12$, $12/14$, $18/16$).

The maximum flux concentration ratio is achieved along the limit of feasibility in correspondence of specific values of the thickness ratio, highlighted by the points A_{MAX}, B_{MAX}, C_{MAX}, D_{MAX}, E_{MAX} in Fig. 11.6. It is worth noticing that, if the MFPV locus falls within the design area (i.e. $18/12$, $12/14$, $18/16$) the above mentioned points are the optimum points under the PM minimization point of view. As a consequence, for the given rotor constraint, low pole machines do not provide the most exploitation of magnets.

Finally, in the design area, the thickness ratio k_m has to be selected in the range $0.2-0.4$ for the $9/8$, $0.25-0.4$ for the $12/10$, $0.3-0.45$ for the $18/12$, $0.4-0.5$ for the $12/14$ and $18/16$. Fig. 11.7 shows the flux concentration ratio χ, evaluated along the MFPV locus, as a function of the PM volume ratio ψ for the machines $12/10$, $18/12$, $12/14$, $18/16$. All the machines provide comparable flux concentration ratio, for the same PM volume in the considered range of number of poles. In general, the analytical procedure exhibits an under estimation of the actual flux concentration ratio. This is particularly evident with high PM volume ratio and number of poles. This is caused by an overestimation of the saturation factor.

As regards the torque density, a load analysis has been been carried out, according to the procedure described in Sec. 11.3.3. The results are reported in Table 11.2. While the model provide an accurate evaluation of torque density with linear iron and low poles motors, it shows some limits when the iron saturation in included or with high pole machines. The not uniformity between the torque results is explainable due to the saturation, mainly of the tooth shoes, that is not considered in the model. Without increasing the complexity of the

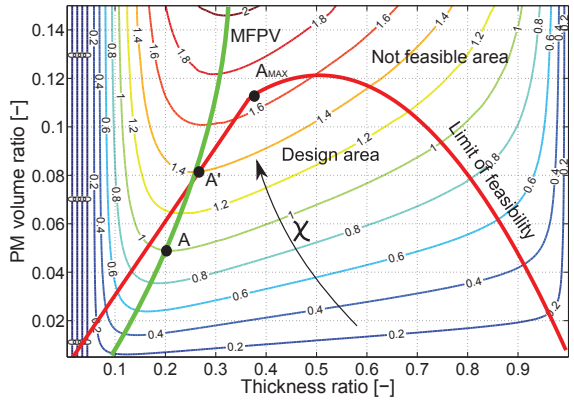

(a) 9-slot, 8-pole.

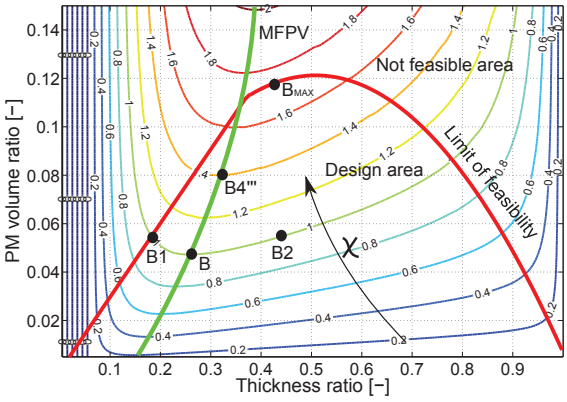

(b) 12-slot, 10-pole.

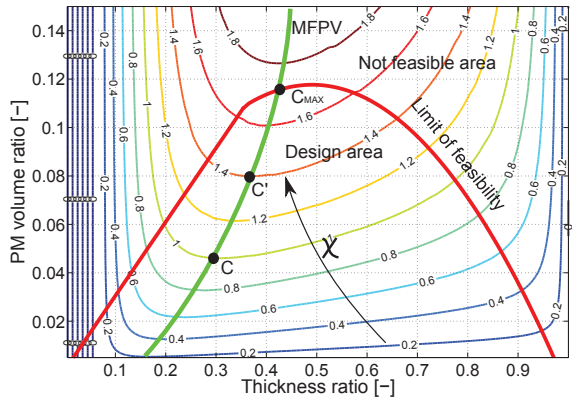

(c) 18-slot, 12-pole.

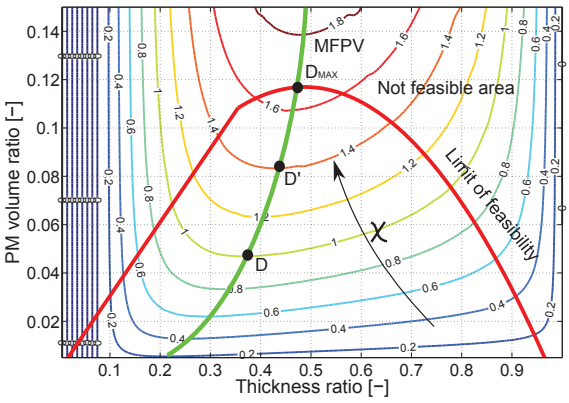

(d) 12-slot, 14-pole.

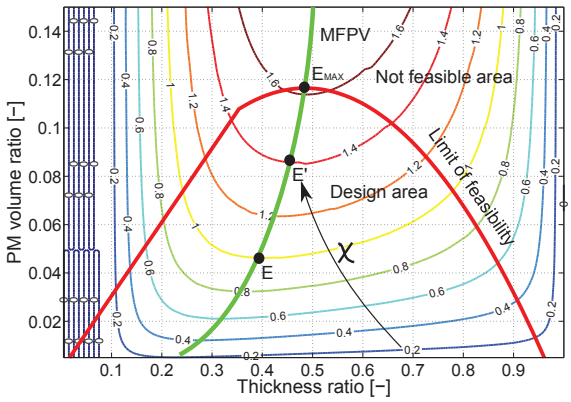

(e) 18-slot, 16-pole.

Fig. 11.6: Flux concentration ratio as a function of the PM volume ratio and thickness ratio for different number of poles (split ratio 0.5).

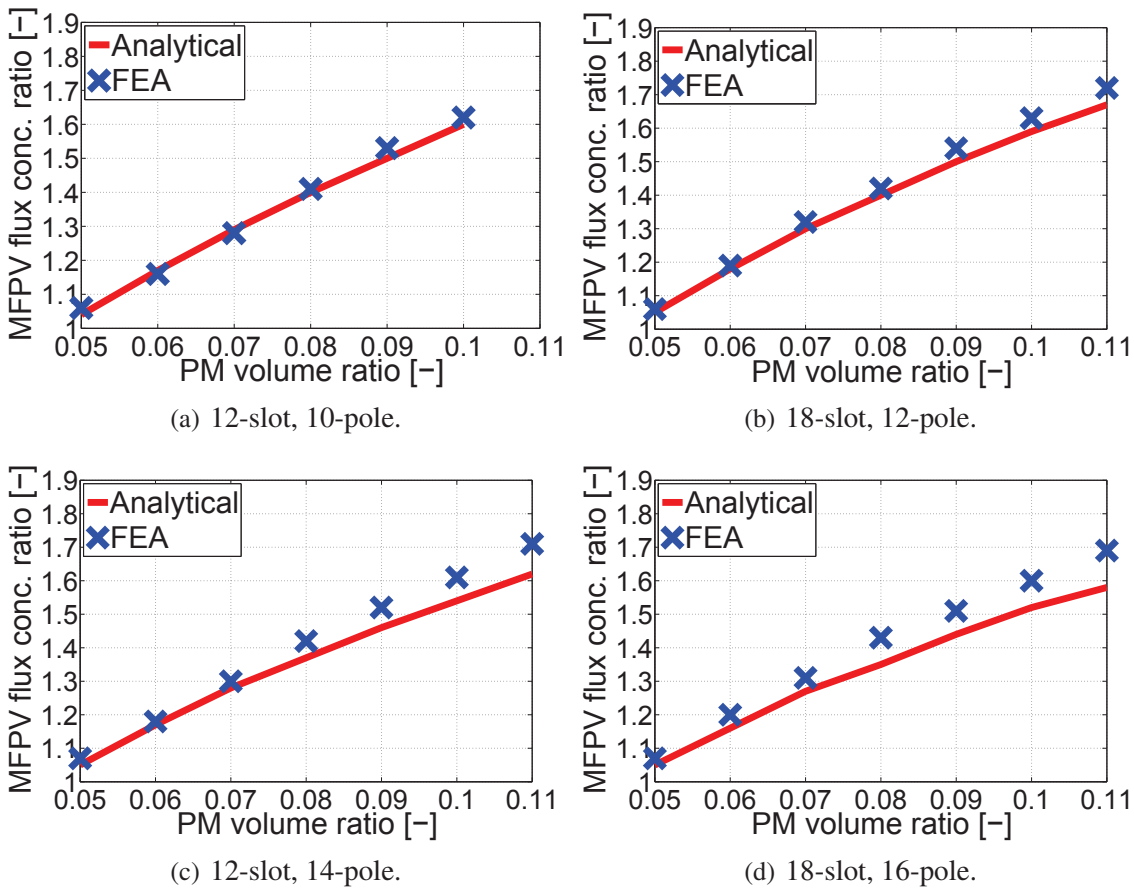

(a) 12-slot, 10-pole.

(b) 18-slot, 12-pole.

(c) 12-slot, 14-pole.

(d) 18-slot, 16-pole.

Fig. 11.7: MFPV flux concentration ratio vs. PM volume ratio (split ratio 0.5).

model, such a phenomenon can be taken into account by introducing a variable saturation factor to the airgap. On the other hand, the analytical computation requires a very short time for achieving a full design map, in comparison with the FEA approach. Thus, it is an important tool for preliminary design considerations.

11.4.2 Influence of the split ratio

It is also possible to represent the contour lines of the flux concentration ratio χ as a function of the split ratio δ. Fig. 11.8 shows an example referring to the $12/10$ configuration, highlighting the limit of feasibility, the design area and the not feasible region. Similarly to what has been shown previously, a locus of optimal split ratio that minimizes the PM volume, called MFPV', exists. For the selected slot-pole combination, such a locus is located in the non-feasible area. The point $B3$, $B4$, $B5$ refer to motor designs with $\delta = 0.55$ and $\chi = 1$,

Table 11.2: Comparison between analytical and FEA results.

Design					Analytical		FEA		
	δ [−]	k_m [−]	ψ [−]	k_{cs} [−]	χ [−]	T_d [Nm/dm^3]	χ [−]	T_d, linear Fe [Nm/dm^3]	T_d [Nm/dm^3]
A	0.5	0.210	0.049	2.83	1.00	19.5	0.99	19.1	15.1
A"	0.5	0.285	0.082	2.76	1.40	23.2	1.39	22.8	21.0
A_{MAX}	0.5	0.395	0.114	1.86	1.66	22.4	1.65	21.7	21.1
B	0.5	0.26	0.048	2.26	1.00	20.5	1.01	20.1	15.3
$B1$	0.5	0.165	0.050	5.85	1.00	19.2	0.99	20.7	13.6
$B2$	0.5	0.355	0.050	1.27	1.00	19.8	0.97	19.4	17.8
$B3$	0.55	0.200	0.050	3.45	1.00	22.2	0.98	21.8	17.1
$B4$	0.55	0.250	0.080	2.35	1.30	25.2	1.30	25.2	21.8
$B4'$	0.35	0.500	0.050	2.25	1.30	19.6	1.34	19.4	12.8
$B4''$	0.4	0.450	0.080	2.67	1.45	23.2	1.47	23.2	17.8
$B4'''$	0.5	0.315	0.080	2.57	1.40	25.3	1.41	25.5	22.0
$B5$	0.55	0.330	0.123	3.03	1.60	27.2	1.64	28.2	25.2
B_{MAX}	0.5	0.400	0.113	2.24	1.71	24.6	1.74	24.0	22.9
C	0.5	0.300	0.047	1.99	1.00	19.5	1.01	18.1	13.3
C'	0.5	0.375	0.080	2.17	1.40	24.1	1.42	23.2	19.9
C_{MAX}	0.5	0.425	0.114	2.40	1.71	24.8	1.75	23.3	22.0
D	0.5	0.360	0.047	1.61	1.00	21.0	1.01	20.1	15.2
D'	0.5	0.445	0.084	1.89	1.40	25.7	1.45	25.3	22.2
D_{MAX}	0.5	0.465	0.115	2.30	1.65	28.0	1.75	28.6	25.2
E	0.5	0.400	0.047	1.50	1.00	21.3	1.02	20.1	15.5
E'	0.5	0.460	0.086	2.07	1.40	24.9	1.48	23.2	21.6
E_{MAX}	0.5	0.490	0.115	2.44	1.61	25.2	1.72	24.0	22.4

1.3 and 1.6 respectively. With the above mentioned split ratio value, they do not exhibit the minimum PM volume. This minimum could be obtained with a lower δ, for a given χ. The minimization of the PM volume, i.e. of ψ, is achieved selecting the design parameters in the cross points between the constant-χ curves and the limit of feasibility curve. An example is represented by the point $B4'$, achieved with $\chi = 1.3$ with an optimal δ computed around 0.35.

However, the motor designed where the PM volume is minimum (e.g. $B4'$) does not exhibit an optimal torque for given losses. For instance, in the design point $B4'$, the motor torque results about 20% less than the torque in the point $B4$. A similar results is achieved if the motors are designed with the same PM volume ratio ($\psi = 0.08$), i.e. points $B4$, $B4''$, $B4'''$.

Fig. 11.9 shows the torque density as a function of the split ratio δ, referring to the $12/10$ configuration with the given $\psi = 0.08$. Points $B4$, $B4''$ and $B4'''$ of Fig. 11.8, are

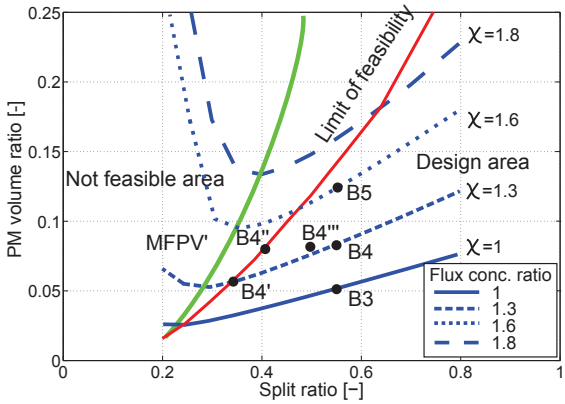

Fig. 11.8: PM volume ratio vs. split ratio for a given flux concentration ratio (12-slot 10-pole).

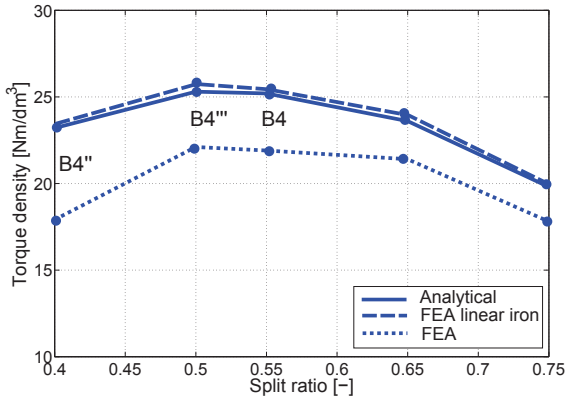

Fig. 11.9: Torque density vs. split ratio (constant PM volume ratio 0.08, 12-slot 10-pole).

highlighted. Even though the PM volume ratio remains the same, an optimal split ratio that exhbit the maximum torque exists. It is achieved corresponding to $\delta = 0.5$ (point $B4'''$). Finally, a slight variation of the split ratio around its optimal value does not cause a significant reduction of the motor torque from the maximum value. These results can be extended to the other poles configuration, providing comparable results.

11.5 Conclusions

This research investigates analytically the optimal design of a spoke type FSCW IPM with the aim objective of the minimization of the PM volume. The constraints are the motor outer dimensions and the maximum copper losses. Variables are the PM cross section, split ratio and number of poles. Optimal designs are achieved when the parameters are selected so as to remains along the Maximum Flux Per PM Volume curve. The thickness ratio results in

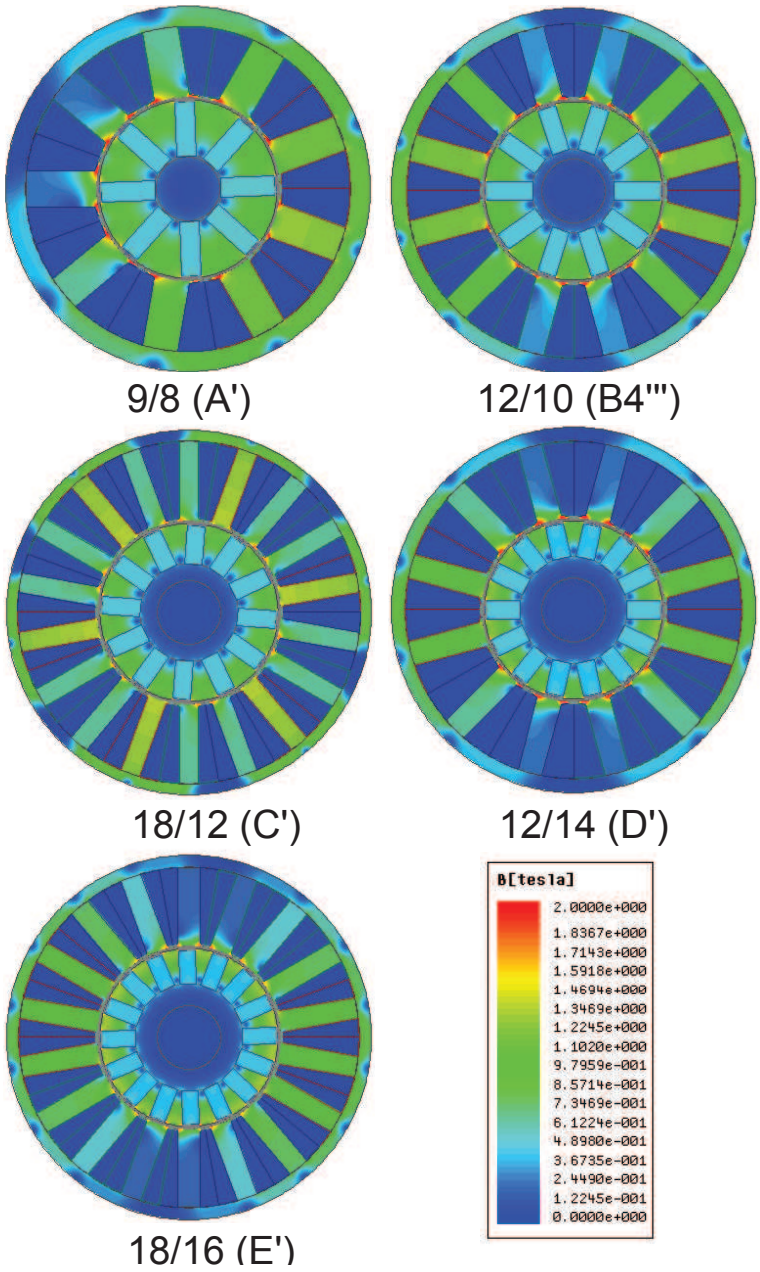

Fig. 11.10: Flux density maps under no load operation for different slot-pole combinations.

the range $0.2-0.4$ for low pole machines and (i.e. $9/8$, $12/10$), $0.4-0.5$ for high pole motors (i.e. $18/12$, $12/14$, $18/16$).

The optimal split ratio results to be around $\delta = 0.5-0.55$ for all configuration. In this range the maximum torque density is achieved. However, it is also shown that minimization of the PM volume and maximization of the torque density are not obtained with the same design choices.

Chapter 12

Influence of the slot-pole combination on the performance of spoke type FSCW motors

12.1 Introduction

In automotive applications, the research of high torque density, torque quality and manufacturing simplicity for mass production, emphasizes the Fractional Slot Concentrated Winding (FSCW) Interior Permanent Magnet (IPM) synchronous motor as one of the most attractive candidates [12, 50, 54, 108, 112]. Among the IPM topologies, one of the most interesting is represented by the tangential magnetization or spoke type machine [45, 89, 95, 160, 167, 184], reported in Fig. 12.1. Taking advantage of the flux concentration, spoke type motors provide the highest flux and torque density among the PM synchronous machines [57]. By means of the enhancing of the airgap flux density, the flux concentration yields to fully exploit Heavy Rare Earths (HRE) free, low cost and low remanence PM compounds such as ferrite or the recently introduced hot pressed NdFeB [101, 186]. The interest in these PM compounds has grown in the recent years following the skyrocketing of the price of RE materials, such as Dysprosium (Dy) and Terbium (Tb). Recent researches proposed some novel rotor geometries such as a ferrite spoke-ring combination [138], a wing-shaped configuration [139] and a semi-modular dual-stack rotor [147]. However, spoke type motors exhibit important drawbacks which are summarized in a limited flux weakening (FW) capability, lower saliency ratio (i.e. reluctance torque) [22, 34, 97] and lower demagnetization strength [57, 89, 95].

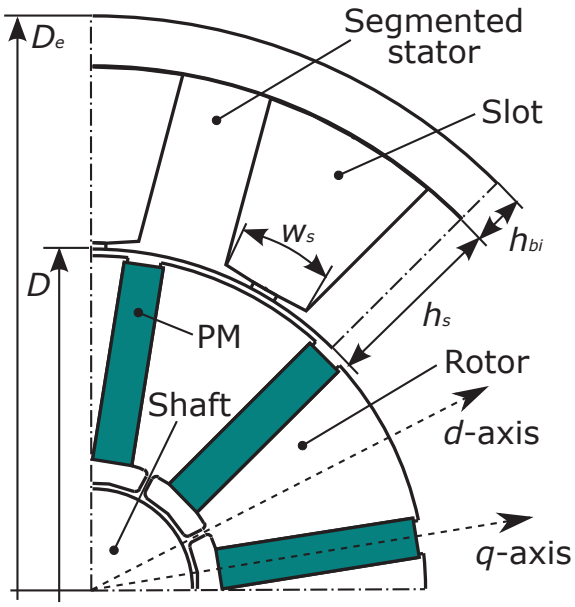

Fig. 12.1: 1/4 sketch of a spoke-type 12-slot 10-pole motor.

In [158, 187, 188], the influence of some design factors in a distributed winding spoke type motor has been investigated, considering different number of poles, magnet thickness and shaft arrangement. In [27], an analytical procedure for FSCW IPM spoke type motor has been introduced in order to provide some design criteria aimed to PM volume minimization, considering different slot-pole arrangement. On the other hand, a detailed analysis of the influence of the slot-pole combination on the motor performance, including torque quality, flux weakening performance has not been performed yet.

This work aims to fill this gap. It deals with the design and analysis of FSCW IPM spoke type motors for an Electric Power Steering (EPS) application. In order to provide a comprehensive evaluation of the problem, eight promising slot/pole combinations, between 6 and 16 poles, have been selected. The comparison of the electromechanical performance has been carried out, highlighting the advantages and drawbacks of such solutions.

12.2 Preliminary analysis

12.2.1 Selection of the optimal slot/pole combinations

EPS systems require high performance in terms of torque density, torque quality and NVH. Since these requirements are firstly influenced by the combination of the number of slots Q and poles $2 \cdot p$, a preliminary selection of the most promising $Q/(2 \cdot p)$ configurations has

been carried out. The choice is based upon an evaluation of the following motor quality indexes:

1. High winding factor (main harmonic) k_{w1}, in order to improve the torque density.
2. High Least Common Multiple $LCM(Q, 2 \cdot p)$, in order to reduce the cogging torque [54].
3. High and even Great Common Divisor $GCD(Q, 2 \cdot p)$ in order to reduce the unbalanced magnetic radial forces and increase the radial symmetry [54, 107].

As regards the number of poles, it is worth noticing that the flux concentration practically exists when the number of poles $2 \cdot p \geq 6$ [22, 27, 167]. As the number of pole increases, the flux concentration become effective. On the other hand, an excessive increase of the number of poles does not yield a reduction of the PM volume for a given flux concentration ratio [27]. Even if a machine with a high number of poles $(2 \cdot p > 16)$ can be theoretically designed, the higher supply frequency of the inverter and the higher manufacturing complexity make these solutions to be not attractive for mass market production.

Based upon the previous argumentations, the most promising FSCW slot/pole candidates are evaluated and reported in Table 12.1. Only the configurations with a number of slots per pole and phase $1/4 < q < 1/2$ have been considered since they exhibit a winding factor conveniently higher than 0.866. Finally, the selected configurations are $9/6$, $9/8$, $12/8$, $12/10$, $18/12$, $12/14$, $18/14$ and $18/16$. It is worth noticing that the combination with $GCD(Q, 2 \cdot p) = 1$, for e.g. $9/8$ are usually avoided in automotive applications since they exhibit an asymmetric radial force distribution, hence a poor NVH behavior [83].

12.2.2 Rotor design

One of the most intrinsic drawbacks of spoke type motors is the leakage flux, close to the shaft. For this reason, these machines are usually designed with a non magnetic shaft and joints between the rotor lamination and the shaft. Even if this rotor arrangement provides the best use of the magnet, it exhibit some drawbacks under the point of mass market production which are: (*i*) higher complexity of the manufacturing process because the rotor is not manufactured from a single mold and (*ii*) the torque quality and NVH might be practically less controllable if the rotor lamination is not structurally a single piece (higher manufacturing tolerances).

For these reasons, a single rotor lamination equipped with an interlink inner bridge for each pole, has been considered in this analysis. In order to reduce the leakage flux, these bridges have to be designed to work in saturation.

Table 12.1: Comparison of the motor quality indexes.

$Q/(2\cdot p)$	q	k_{w1}	$LCM(Q,2\cdot p)$	$GCD(Q,2\cdot p)$
9/6	**1/2**	**0.866**	**18**	**3**
6/8	1/4	0.866	24	2
9/8	**3/8**	**0.945**	**72**	**1**
12/8	**1/2**	**0.866**	**24**	**4**
9/10	3/10	0.945	90	1
12/10	**2/5**	**0.933**	**60**	**2**
15/10	1/2	0.866	30	5
9/12	1/4	0.866	36	3
18/12	**1/2**	**0.866**	**36**	**6**
12/14	**2/7**	**0.933**	**84**	**2**
15/14	5/14	0.951	210	1
18/14	**3/7**	**0.902**	**126**	**2**
21/14	5/14	0.866	42	7
6/16	5/14	0.866	48	2
12/16	3/8	0.866	48	4
15/16	5/14	0.951	210	1
18/16	**5/14**	**0.945**	**144**	**2**
21/16	7/16	0.890	336	1
24/16	1/2	0.866	48	8

12.3 Design and optimization

The machines have been designed and optimized on the basis of the following constraints: outer diameter $D_e = 86mm$, airgap height $g = 0.5mm$, shaft diameter $D_{ri} = 15mm$, fill factor $k_{fill} = 0.435$ and active copper losses $P_{Cua} = 141W$ at $80°C$. The stack lengths L_{stk} have been adjusted in order to meet a $7.5Nm$ rated torque target. The maximum speed is fixed to $2500rpm$. According to the inverter rating, a further constraint is given by the phase current $I_n \leq 100A_{RMS}$ and DC bus fixed at $12V$. It follows that the number of conductors per each slot is defined and it has been selected for ensuring a double layer feasibility. The resistance of the converter and the DC bus have been taken into account.

The constraint of the fixed copper losses, assuming the iron losses to be negligible, ensures a comparable thermal behavior among the machines. Hence, for a given torque, i.e. stack length, the thermal losses density through the housing is constant. In order to have a comprehensive comparison, two different HRE-free PMs, a ferrite (grade 9) and a Dy-free hot pressed NdFeB have been selected. Their B-H characteristic is reported in Fig. 1.17. As

shown in Fig. 12.1, the machine is equipped with a segmented stator [50]. This introduces an additional airgap but yields a high winding factor and easy winding process, especially in relation to the very limited overall motor dimensions. As a result of the segmented stator, for the mechanical feasibility, the slot opening is hybrid (sandwiched open and close slots). This configuration offers the advantage of comparable low cogging torque as for closed slot solutions without worsening the torque density in comparison to the open slot designs. It has been modeled considering an equivalent B-H curve, according to the method proposed in [7]. As reported in Fig. 12.1, the rotor ribs have been avoided in order to reduce the leakage flux.

The minimum thickness of the inner bridge has been preliminary evaluated on the basis of an analytical estimation, considering the worst case, taking into account the steady state centrifugal pressure at the maximum speed and the magnetic pressure p_m.

A grade M330-50A iron lamination has been considered in this analysis. The estimated force acting on the inner bridge is,

$$F_b = \frac{1}{n_b} \cdot \left(m_r \cdot R_m \cdot {\Omega_{MAX}}^2 + A_r \cdot p_m \right) \tag{12.1}$$

Where $n_b = 2 \cdot p$ is the number of bridges, m_r is the estimated rotor mass, R_m is the average rotor diameter related to the position of the center of mass of the rotor iron, Ω_{MAX} is the maximum speed and A_r is the rotor outer surface and p_m is the radial magnetic pressure. Such a parameter is assumed to be constant along the rotor periphery. Considering a homogenous rotor (PMs ad flux barriers have the same density of the iron) and assuming an average split ratio (airgap diameter D over D_e) $\delta = 0.6$, $p_m \cong 400kPa$ (equivalent to typical airgap flux density of about $1T$) the force on the bridge has been evaluated. Hence, the minimum thickness of the bridges has been computed by (12.2), assuming a safe factor $k_s = 3$.

$$w_b = k_s \cdot \frac{F_b}{\sigma_y \cdot L_{stk}} \tag{12.2}$$

where $\sigma_y = 354MPa$ is the iron yield stress and L_{stk} is the stack length. On the basis of the punching feasibility, the minimum thickness is $0.33mm$. This value is largely higher than those evaluated and reported in Table 12.2, hence it has been selected for all the configurations.

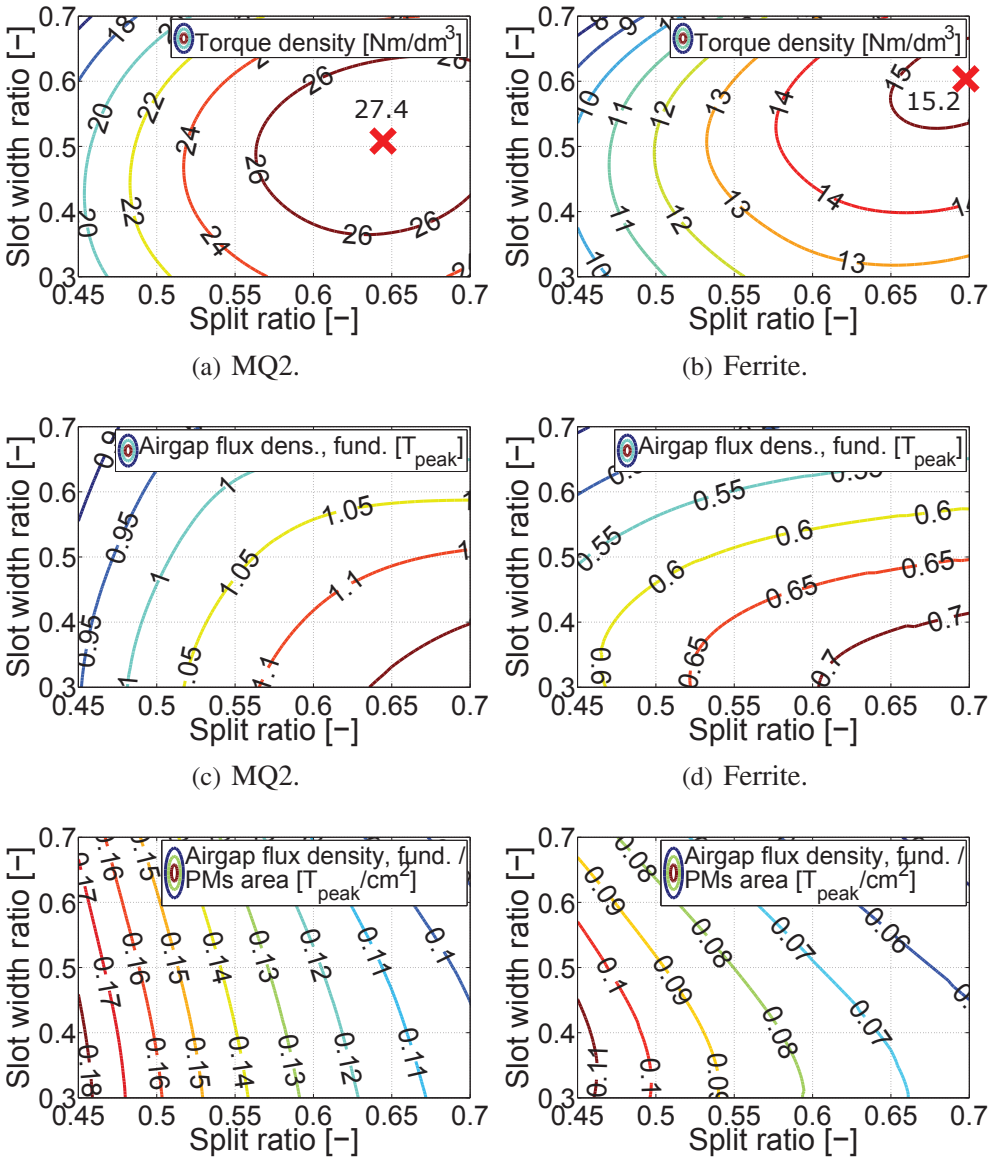

(a) MQ2.

(b) Ferrite.

(c) MQ2.

(d) Ferrite.

(e) MQ2.

(f) Ferrite.

Fig. 12.2: 12-slot 10-pole motor: torque density and no load airgap flux density as a function of the main motor dimensions.

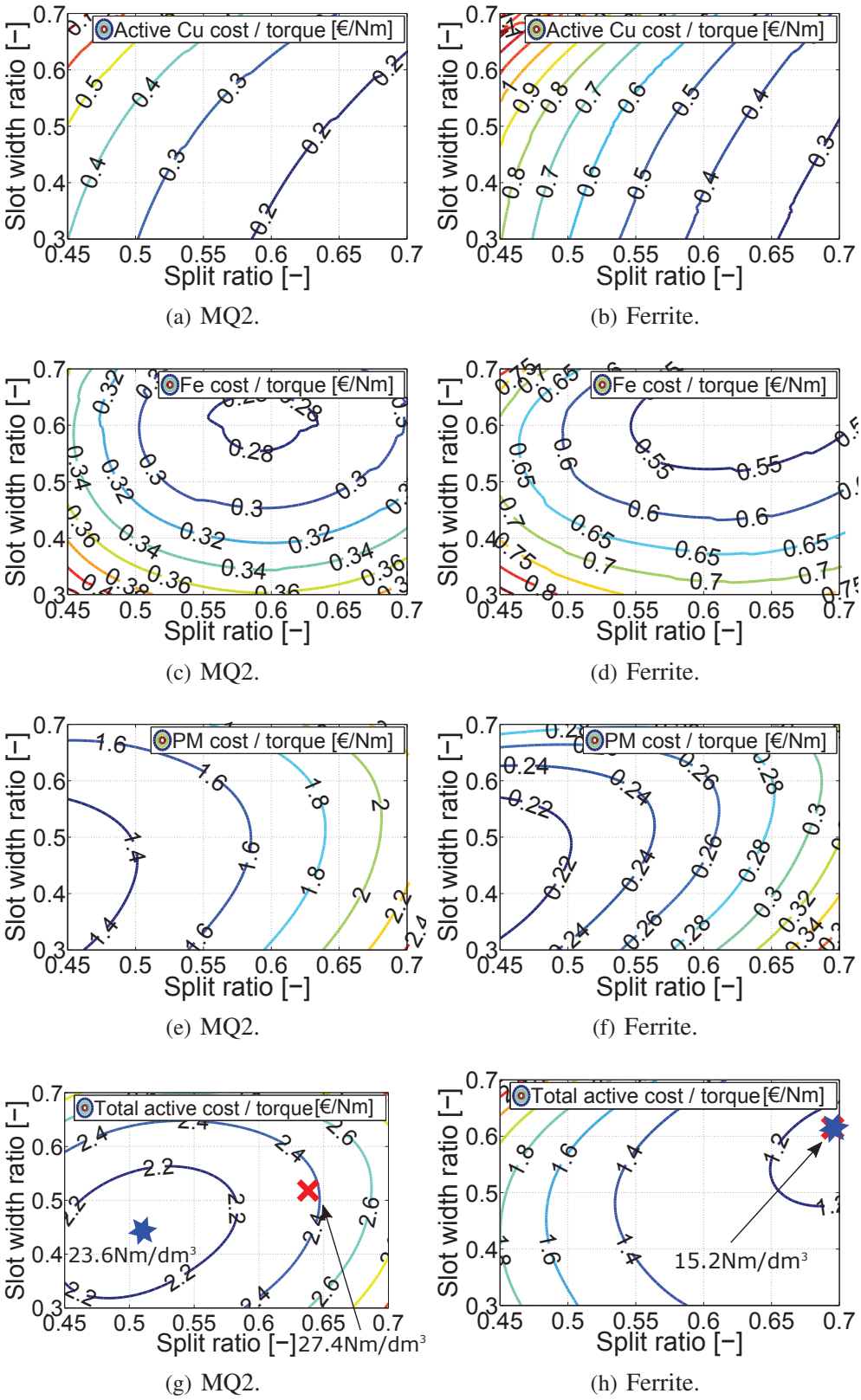

(a) MQ2. (b) Ferrite.

(c) MQ2. (d) Ferrite.

(e) MQ2. (f) Ferrite.

(g) MQ2. (h) Ferrite.

Fig. 12.3: 12-slot, 10-pole: active costs as a function of the main motor dimensions.

Table 12.2: Minimum bridge thickness.

9/6	9/8	12/8	12/10
0.114*mm*	0.086*mm*	0.086*mm*	0.067*mm*
18/12	12/14	18/14	18/16
0.057*mm*	0.049*mm*	0.049*mm*	0.043*mm*

12.3.1 Influence of the motor dimensions

A FE (Finite Element) parametric analysis has been performed for each slot-pole combination in order to highlight the influence of the split ratio and stator cross section to the torque density, airgap flux density and active cost. The slot wedge, the opening height have been kept fixed. The slot opening width has been fixed to a 40% of the tooth width in order to keep the same aspect ratio during the calculation. As regards the PM cross section, its length and width have been maximized in order to develop the highest airgap flux density, according to the rotor constraints [27]. The load simulation has been performed taking into account the actual current angle along the MTPA (Maximum Torque Per Ampere) locus. As mentioned before, with the constraint of the active copper losses, the slot current results,

$$\widehat{I_s} = \sqrt{\frac{2 \cdot k_{fill} \cdot P_{Cua} \cdot S_s}{\rho_{Cu} \cdot Q \cdot L_{stk}}} \tag{12.3}$$

where ρ_{Cu} is the copper resistivity at $80°C$ and S_s is the slot cross section area.

Fig. 12.2 shows the torque density, the load airgap flux density map as a function of the split ratio δ and slot width ratio w_{sr} (slot width w_s over the slot pitch) [152] evaluated by means of FEA. The back iron height ratio h_{bir} (back iron height h_{bi} over outer stator radius) has been evaluated in order to get the highest torque density. It is worth noticing that, regardless the PM type, for a given slot/pole combination, each (δ, w_{sr}) point corresponds to the same stator, rotor and PM cross section. For each motor topology, an optimal split ratio, slot width and back iron height ratio, which maximizes the torque, can be found. Due to the limited space in the paper, only the $12/10$ machine is shown in detail in Fig. 12.2.
As reported in Figs. 12.2(a), 12.2(b), the optimal split ratio is $\delta = 0.65$ and $\delta = 0.7$ with torque densities of $27.4 Nm/dm^3$ and $15.2 Nm/dm^3$, respectively for the MQ2 and the ferrite magnets. Regarding the slot width ratio, the ferrite design exhibits a higher value $w_{sr} = 0.61$ vs. $w_{sr} = 0.51$. In fact a reduction of the tooth width in the ferrite solution is beneficial to the torque density since it can increase the slot current, without increasing the iron saturation. Both these behaviors are related to the lower airgap flux density achievable by such a PM.

This is shown in Figs. 12.2(c), 12.2(d) which clearly highlights the increase of the flux concentration ratio as the split ratio increases. However, the airgap flux density per unit of PM area, reported in Figs. 12.2(e), 12.2(f), shows that the lower the split ratio, the higher the effectiveness of the magnet.

An analysis of the costs provides interesting remarks. In Fig. 12.3 the active cost densities (active cost per unit of motor torque) are compared. The end winding cost, being a fixed contribution to the total cost, is neglected.

Since the MQ2 machine develops a torque density almost two times that of the ferrite machine, the active copper and iron cost densities are halved going from the ferrite to the MQ2. In Figs. 12.3(a), 12.3(b), the active copper cost density increases going from higher to lower split ratio because the available slot area increases and the torque tends to decrease. The iron cost, instead, shows a global minimum for a slot width ratio $w_{sr} = 0.6$ and split ratio $\delta = 0.6$.

Conversely, the PM cost density grows as the split ratio increases and this indicates the reduction of the effectiveness of the flux concentration effect when high split ratios are employed.

Finally, as highlighted in Figs. 12.3(g), 12.3(h) a geometry with the minimum cost density exists and it can be different to that with the highest torque density. This is verified in the MQ2 motors, where the PM cost is almost 4 times the cumulative cost of the copper and iron, comparing to about $1/3$ of the ferrite design. This emphasizes that in MQ2 machines, but in general when high cost magnets are used in spoke type configurations, the cheapest solutions can be found at low split ratios. Conversely, the ferrite solution is more effective since the geometry with the highest torque density is basically in the design area of the cheapest configurations. In conclusion for each $Q/(2 \cdot p)$ combination, two representative solutions can be found: one with the highest torque density and one which shows the lowest cost. For all the considered slot/pole combinations, the above mentioned considerations results of having a general application. Since the lowest cost geometries are dependent on the actual costs of the active materials, the following analysis is focused to the highest torque density MQ2 solutions. Therefore, for the sake of the comparison, the slot opening width of each $Q/(2 \cdot p)$ combination have been adjusted in order to reach the highest torque.

12.4 Performance comparison

In this section the motor performance are compared and discussed. Fig. 12.4 reports the flux density maps at rated load of the final geometries. Table 14.9 reports the key machine

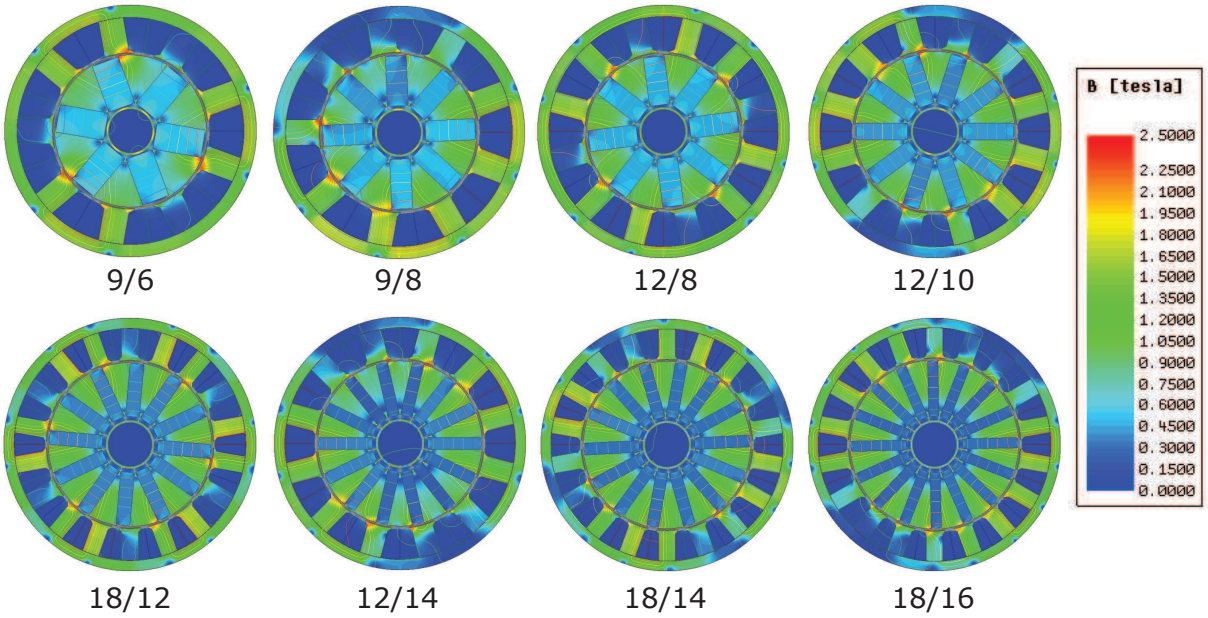

Fig. 12.4: MQ2 motors: flux density maps at rated load.

dimensions and performance data.

Regarding the motor cross section, all the slot/pole configurations show an optimal split ratio in a narrow range $\delta = 0.62 - 0.68$. The optimum split ratio increases with the number of poles and machines with the same number of poles exhibit basically the same split ratio. Since the PM cross section is different for each configuration, an evaluation of the no load airgap flux density provides an index of the effectiveness of the flux concentration. The results show that the flux concentration is less effective in the 6-pole machine, with a ratio equal to $0.104 T_{peak}/cm^2$. Conversely, a global maximum is achieved in the 12-pole machine ($0.130 T_{peak}/cm^2$) while for higher pole number such a ratio decreases [27].

12.4.1 Torque density and torque quality performance

Fig. 12.6 reports the comparison of the predicted torque density, cogging torque and torque ripple for each $Q/(2 \cdot p)$ combination.

The torque density is calculated by dividing the torque to the volume displaced by the stator $(1/4) \cdot \pi \cdot {D_e}^2 \cdot L_{stk}$. As shown in Fig. 12.5(a), the highest torque density, $30.38 Nm/dm^3$ is achieved by $12/14$ configuration while the lowest, $21.18 Nm/dm^3$ is exhibited by the $9/6$ machine. In general these results confirm that the torque density in spoke type motors benefits from a high winding factor and flux concentration since, as mentioned in Sec. 12.1

and shown in Fig. 12.5(a), the reluctance torque contribution is negligible. However, the highest saliency ratio is found in the $9/6$ (1.906), $12/8$ (1.738), $18/12$ (1.506) machines, which exhibit a number of slots per pole and phase is $q = 1/2$ [164]. Finally, in Table 14.9 the total machine cost is reported. It is worth noticing that the cost follows, in an inverse law, the trend of the torque density. Hence, the $12/14$ machine results to be the cheapest.
Fig. 12.5(b) shows the comparison of the predicted cogging torque. The trend of the cogging torque as a function of the number of poles is basically in agreement with the cogging torque index highlighted in Sec. 12.2. $12/10$, $12/14$, $18/14$, $18/16$ machines exhibit low cogging torque, in the range $25 - 100mNm$ (peak-peak). The lowest value is achieved by the $18/14$ motor.
As regards the torque ripple (under load), the predicted values are reported in Fig. 12.5(c). The trend is basically similar to that of the cogging torque, with low values in the range 2% achievable by $9/8$, $12/10$, $12/14$, $18/14$ and $18/16$ motors. The lowest torque ripple (1.77%) is predicted for the $18/14$ configuration.

12.4.2 Electromechanical performance

The machine performance have been evaluated on the basis of the synchronous space vector control in the d/q reference frame. The iron losses are taken into account in the computation. However, for such an application, the copper losses are the dominant component in the whole speed range. Fig. 12.6(a), 12.6(b) and 12.6(c) report torque, output power and power factor vs. speed, respectively. The best electromechanical characteristics are shown by the $12/14$ and $18/16$ machines while the lowest speed range is exhibited by the $9/6$ configuration. It is worth noticing that the FW range can be improved for all the machines with a different selection of the machine geometry.

Further analysis have been performed in order to verify the demagnetization at the worst operating condition in FW operation. The machines have been feed with a demagnetization current (d-axis) at the test temperature $140°C$. The PM demagnetization distribution has been frozen and a no load analysis has been subsequently performed showing a negligible reduction of the PM flux linkage. Finally, a FEA structural analysis has been carried out on each rotor, at the maximum speed. It confirms the structural integrity of the selected geometries.

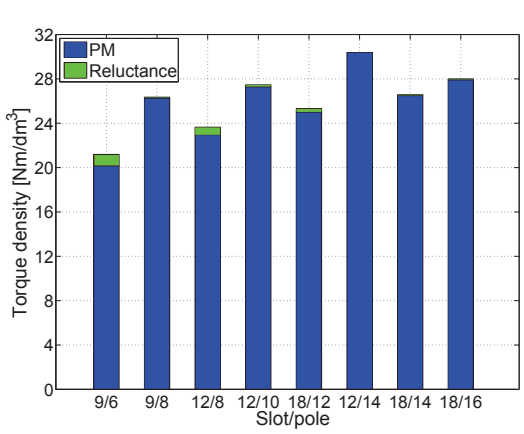

(a) Torque density.

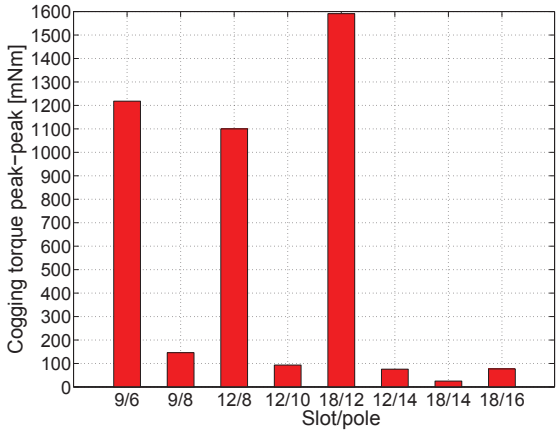

(b) Cogging torque.

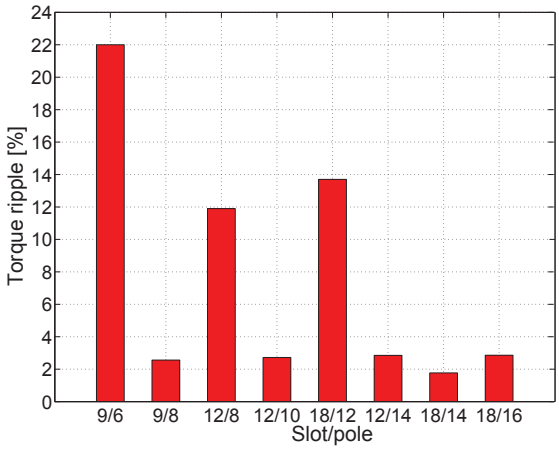

(c) Torque ripple.

Fig. 12.5: Torque density, cogging torque and torque ripple for each slot/pole combination.

12.5 Conclusions

This research investigates the influence of slot/pole combination on the performance of a FSCW IPM spoke type motors. On the basis of a preliminary evaluation of the main motor quality indexes, eight optimal configuration in the range between 6 and 16 poles have been selected and investigated.

On the basis of geometrical and electrical constraints, the influence of the geometrical dimension on the torque density and cost has been studied, comparing two different HRE-free PM solution, a hot pressed NdFeB and a ferrite magnet. Due to the different weights of the cost materials (copper, iron, PMs) and the different cost functions as regards to the motor dimensions, the optimum solution for the cost and the optimum solution for the torque can

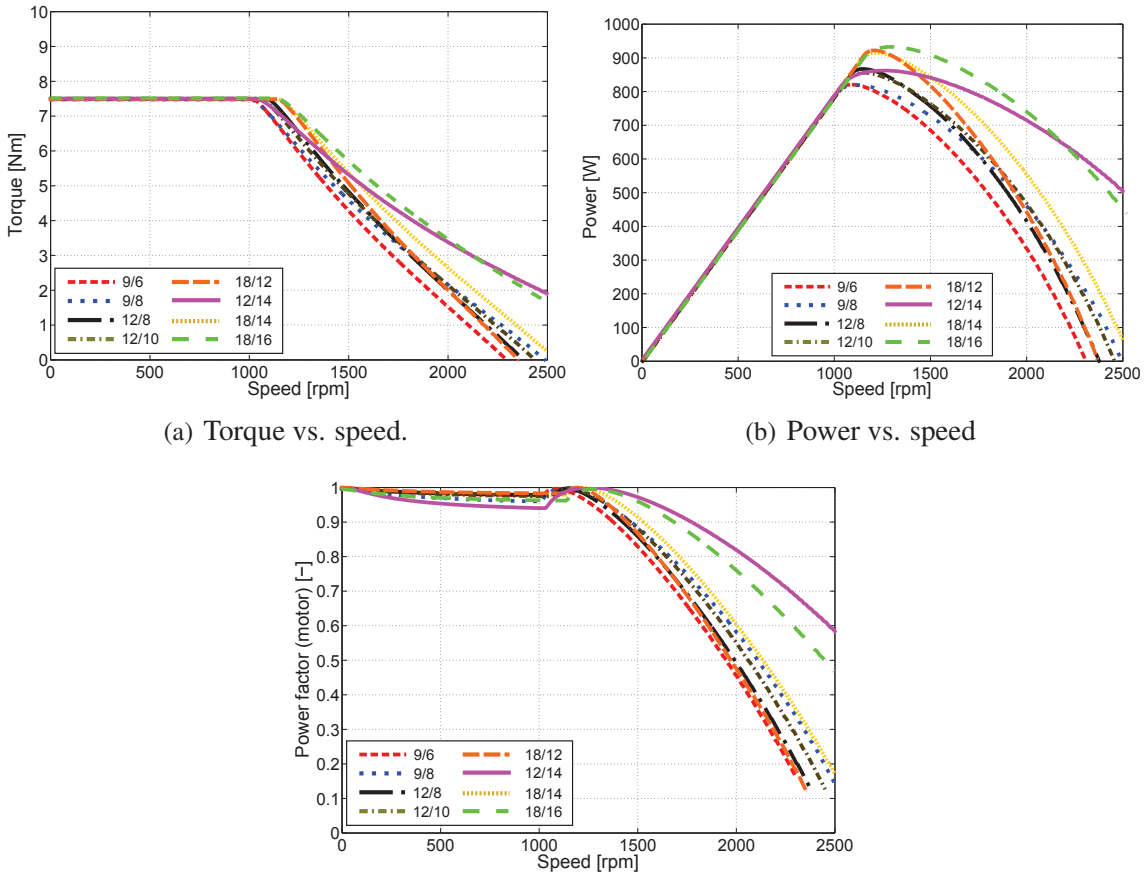

(a) Torque vs. speed.

(b) Power vs. speed

(c) Power factor vs. speed.

Fig. 12.6: Electromechanical performance.

be found in similar or different design ares. Although low cost and low remanence magnet solutions, such as with ferrite, are not able to achieve high torque density, they are more effective in a spoke type structure because they develop the highest torque density at the lowest cost. Conversely, in high cost and high remanence magnet machines, the cheapest solution is not equivalent to the highest torque density configuration. Finally, it has been shown that machines with low pole number (6- and 8-pole) develop lower torque density than those with higher pole number.

The torque density, torque quality, electromechanical performance have been finally evaluated and compared among the different slot/pole combinations. In conclusion, this research shows that, among the selected slot/pole combinations, the solution with high number of poles exhibit higher overall performance in terms of torque density, torque quality, FW performance and NV. Among them, the 12-slot 14-pole shows the best performance, with the highest torque density and lowest cost, thus representing an ideal slot/pole combination in

Table 12.3: Machine parameters comparison.

	9/6	9/8	12/8	12/10	18/12	12/14	18/14	18/16	**Unit**
Stack length	61	49	54.5	47	51	42.5	48.5	46	mm
Split ratio	0.62	0.63	0.62	0.65	0.66	0.67	0.68	0.68	–
Slot width ratio	0.56	0.56	0.51	0.51	0.45	0.54	0.47	0.48	–
Back iron ratio	0.1	0.1	0.09	0.09	0.083	0.085	0.08	0.076	–
Slot current	1265	1230	931	887	559	878	551	553	A_{peak}
# of cond./ slot, equiv. series	10	10	7	7	4	7	4	4	–
Current density	12.3	12.6	12.7	13.2	14.1	13.5	14.2	14.1	A/mm^2
Electric loading	59.3	61.4	57.7	57.0	48.8	54.7	49.0	51.1	kA_{peak}/m
No load flux dens., fund.	0.98	1.10	1.15	1.22	1.33	1.22	1.33	1.31	T_{peak}
No load flux dens., fund./PMs area	0.104	0.113	0.122	0.123	0.130	0.120	0.127	0.125	T_{peak}/cm^2
Saliency ratio (@ base point)	1.906	1.174	1.738	1.240	1.506	1	1.177	1.070	–
Torque density	21.18	26.35	23.64	27.46	25.31	30.38	26.57	27.00	Nm/dm^3
Cogging torque	1218	146	1100	93.3	1591	75.6	25.0	76.7	mNm
Torque ripple	22.0	2.56	11.9	2.72	13.7	2.85	1.77	2.86	%
End-wind. Cu cost	0.911	0.877	0.680	0.634	0.395	0.629	0.387	0.391	€
Active Cu cost	2.261	1.723	1.931	1.519	1.457	1.354	1.355	1.297	€
Iron cost	2.712	2.200	2.469	2.173	2.455	1.952	2.325	2.202	€
PM cost	17.53	14.45	15.66	14.22	15.82	13.19	15.38	14.61	€
Total cost	23.41	19.25	20.74	18.55	20.13	17.13	19.45	18.50	€

spoke type motors for mass market production.

Part IV

Acoustic analysis

Part V

Measurement methodologies and influence of the manufacturing imperfections

Chapter 14

Experimental results and model validation of EPS motors

14.1 Introduction

In this chapter the measurements on the prototypes of the EPS motors are discussed and the FEA model is validated. For the reproducibility of the results, 2 equivalent motor samples have been built for each motor type: reference, V-shape and C-shape motor. The C-shape and V-shape motor have been built sharing the same stator, therefore the measurements have been performed in subsequent phases. The measurements under load reported hereafter are related to one sample for each topology, due to a substantial uniformity of the results.
In Fig. 14.1(a) the stator assembly of the motor prototypes is shown. As discussed before, the segmented stator is made of two parts, the star of teeth and the yoke. The rotor parts are reported in Fig. 14.1(b), before and after the complete assembly with the PMs. The lamination has been manufactured by means of laser cutting technology and the stator and rotor packages has been built using backlack technologies. By means of a chemical process, the laminations are firmly "glued" together. This leads to several advantages in comparison to standard "punched" technologies, such a higher quality, mechanical strength, acoustic performance, consistency of the quality of the parts, better thermal conductivity [voestalpine Stahl GmbH].
The winding assembly is shown in Fig. 14.2. Each phase of the 3 phase winding consists of 4 coils. The adjacent coil of the same phase are connected in series. Hence two parallel branches are got connecting such a series in parallel. The coils are wound around plastic sprocket in order to ensure a proper insulation between the stator iron and the winding. In order to achieve manufacturing simplicity for mass market production and low produc-

tion cost, no bundle conductor is adopted. The star of teeth, equipped the winding, is then pressed inside the yoke. The mechanical connection between star and yoke is ensured by the intrinsic interference induced by the manufacturing tolerances. Due to the manufactur-

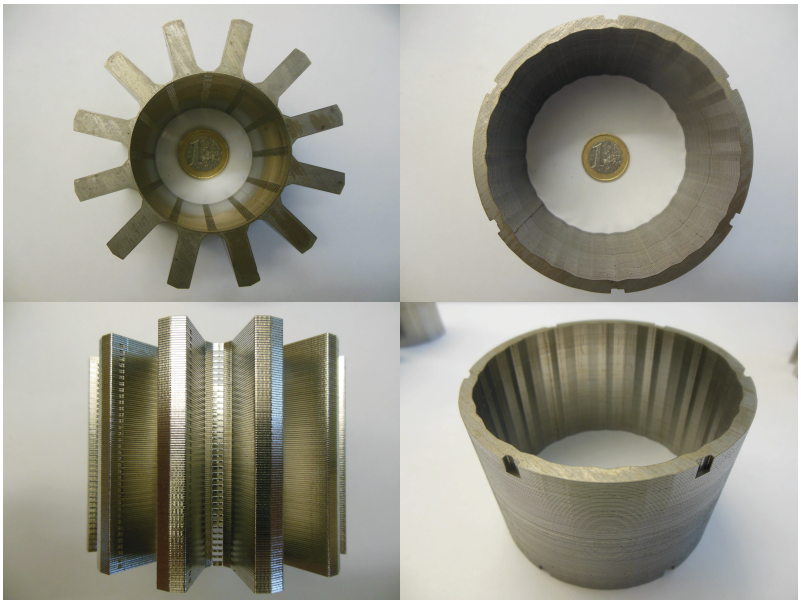

(a) Stator parts (C/V-shape motors).

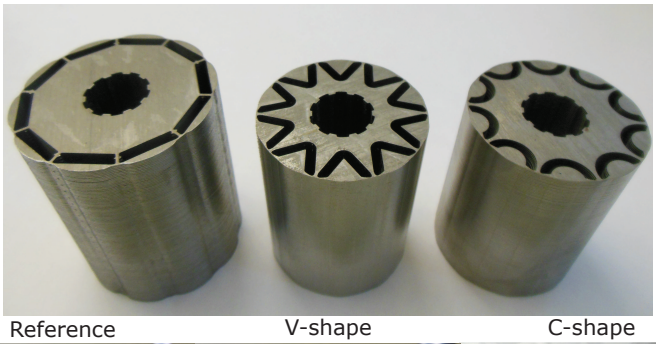

(b) Rotor parts and assembly.

Fig. 14.1: Motor packages.

ing process, components purchase and tolerance, some modifications of the original FEA designs have been introduced (star-yoke profile) and a limited discrepancies of the size and

magnetic performance of the PMs have been found, especially for the novel V-shape and C-shape design. Comparing to the rated values, it has been found a difference up to 5% of the PM dimensions. In order to ensure the equality of the stiffness of the yokes, the same profile of the reference machine has been used and this has lead to a partial redesign of the slot in order to achieve the same fill factor, in particular a reduction of the tooth width. This has caused to some discrepancy with the optimized design previously shown. Finally, two different C-shape, radially magnetized, PM technologies, 1 single piece and 4 piece design, have been studied and validated: it has been found that the ideal design, one single piece PM, does not reach the flux density waveform profile. Therefore it has been discarded for the prototyping process. At the time of the submission of this thesis further improved PM samples have been manufactured for future evaluation.

Fig. 14.2: Winding assembly.

14.2 Validation of the electrical and magnetic properties

The current section reports the validation of the main electrical motor data and magnetic properties of the PMs.

14.2.1 Stator resistance

Table 14.10 reports the phase resistance for stator topology, considering and neglecting the contribution of the connection plate. A good agreement is achieved with the calculated value, which results within about 8% higher than the computation. This discrepancy could

Table 14.1: Resistance measurement @ 20°*C* (DC value)

	Reference		**C/V-shape**		**Unit**
	#1	#2	#1	#2	
A-B	10.501	10.576	10.001	10.058	$m\Omega$
A-B with contacts	11.821	11.814	11.288	11.351	$m\Omega$
B-C	10.472	10.570	9.974	10.043	$m\Omega$
B-C with contacts	11.821	11.805	11.283	11.328	$m\Omega$
C-A	10.492	10.591	9.994	10.047	$m\Omega$
C-A with contacts	11.592	11.594	11.062	11.098	$m\Omega$
Avg. phase res.	5.244	5.290	4.995	5.025	$m\Omega$
Avg. phase res. with contacts	5.872	5.869	5.606	5.630	$m\Omega$
Avg. phase contact res.	0.628	0.579	0.611	0.605	$m\Omega$
Avg. phase res. @ 80°	6.597	6.655	6.284	6.321	$m\Omega$
Calc. phase res. @ 80°	6.237		5.839		$m\Omega$
Error (Calc.-Meas.)	−5.46	−6.28	−7.08	−7.63	%
Avg. phase res. with contacts @ 80°	7.387	7.383	7.052	7.083	$m\Omega$
Incr. (contacts -no contact)	+11.2	+10.9	+12.2	+12.1	%

be explained as follows:

- higher end winding length than the estimation: due to the requested simple and cost effective winding arrangement (direct connection between adjacent coil of the same phase, no bundle conductors) and high cross section (external conductor diameter up to 2.5*mm*) it is not possible to achieve a excellent uniformity of the conductor distributions on one of the side of the stator, as reported in Fig. 14.2.
- internal welds between the two parallel branches in each phase.

Finally, no critical asymmetries of the resistances have been found between phases. Similar differences of the phase resistance have been found betwen the reference and C/V-shape stator, in the order of 0.2% and 0.19% respectively.

14.2.2 PM magnetic properties evaluation

The characterization of the PMs has been performed by means of the following tests.

Hysteresisgraph

In this test, a PM sample is clamped between the two faces of a electromagnet, the measurement is performed in close circuit. The flux density is measured by means of a probe coil placed ar surrounding the sample. An external magnetic field is applied on the PM along the positive and negative direction of magnetization. These procedures is suitable only for PM with constant cross-section and thickness, therefore it cannot be used for complex shapes, like the C-shape design. In Fig. 14.3, the magnetization characteristic for the block NdFeB magnet (V-shape) $N45H$ grade, is shown for different temperatures including the room temperature and temperature for the demagnetization. It is compared with the simulated, rated characteristic. The measured flux density results to be around $2-3\%$ lower than the rated data, while the intrinsic coercivity H_{cJ}, which is related to the demagnetization strength, is according to the data declared by the manufacturer.

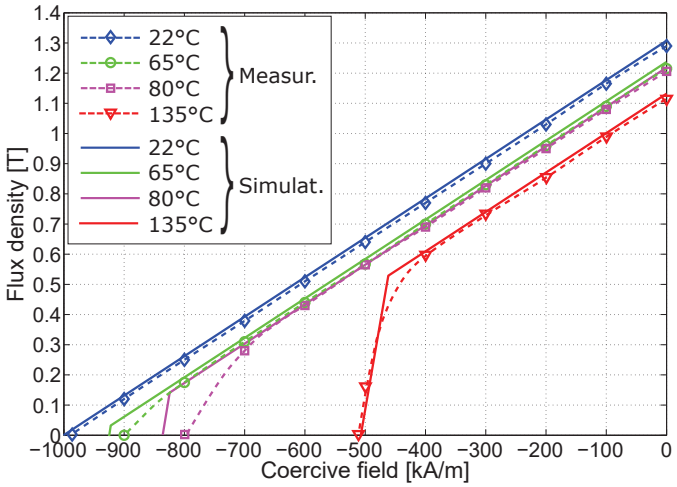

Fig. 14.3: Measurement of the B-H characteristic, $N45H$ grade, block PM (V-shape motor).

Magnetic moment (Helmholtz coil)

As discussed in Sec. 1.3.1, one of the key parameters which describes the quality of the magnetization of a PM is the magnetic moment. The measurement of this quantity is performed by means of a Helmholtz coil, reported in Fig. 14.4. This device consists of two coils separated by a distance equal to the average coil radius. This arrangement ensures the generation of a homogeneous magnetic field within about $2/3$ region of the coil area. When a PM is taken into our outside the inner area, an EMF e is induced in the coils. The open circuit polarization J_0 can be computed integrating such a EMF in the time t [166], as follows,

$$J_0 = \frac{C_H}{V_{PM}} \cdot \int e \cdot dt \tag{14.1}$$

where C_H is the coil constant, which is dependent on the geometrical properties of the device, namely the coil diameter and number of turns. The magnetic moment is therefore equal to,

$$M_m = C_H \cdot \int e \cdot dt \tag{14.2}$$

Since the Helmholtz coil can measures only magnetic fields normal to the coil plane, a modification of the coil constant equation is needed [166] when magnets with a different magnetization direction, such as the C-shape, are measured.
The magnetic moment for the V-shape and C-shape PM sample has been measured. An initial calibration of the Helmholtz coil is required at the beginning of the measurement series, by means of a reference PM, as shown in Fig. 14.4. Comparing to the hysteresisgraph, this methodology can provide a quick evaluation of the PM properties.
A validation by means of FEA 3D analysis has been performed. The magnetic moment has

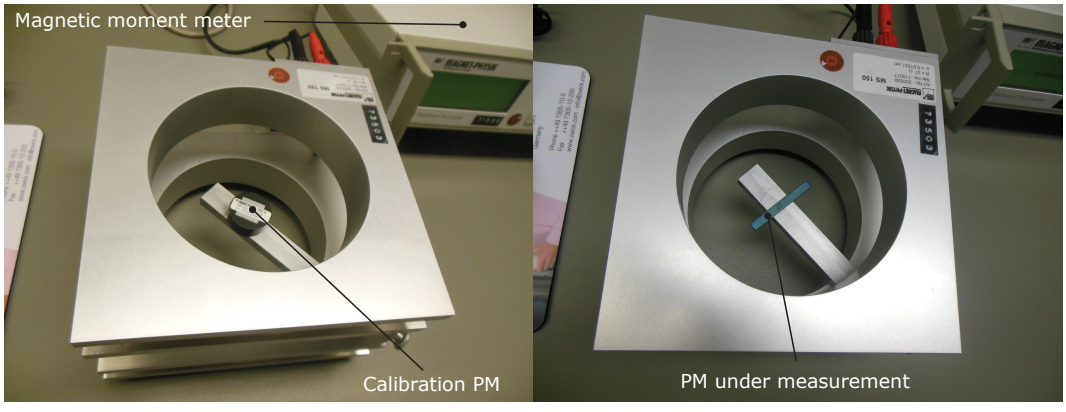

Fig. 14.4: Measurement of the magnetic moment with Helmholtz coil.

been computed both for the block type, V-shape, and C-shape PM. The magnetic moment

has been evaluated in the following manner. For each node of the mesh, the permanence coefficient *PC* is computed, as follows,

$$PC = \frac{B}{\mu_0 \cdot H} \tag{14.3}$$

The open circuit PM polarization J_0 is,

$$J_0 = B_r \cdot \frac{PC + 1}{PC + \mu_{rec}} \tag{14.4}$$

Finally, the magnetic moment M_m is obtained integrating the polarization J in the PM volume V_{PM}

$$M_m = \int_{V_{PM}} J_0 \cdot dv_{PM} \tag{14.5}$$

The discussed formulation is valid only when the magnetization has homogeneous direction in the whole PM (i.e. block PM). The magnetic moment of the C-shape PM measured with the Helmoholtz coil takes into account only the parallel component of the magnetic field to the coil axis z, being therefore lower than the actual value. On the other hand this fictitious magnetic moment can be computed by means of FEA and therefore provide a quantitative indication if the magnetic quality is according to the requirements. Therefore such a evaluation is not possible with other methodologies like the hysteresisgraph. Equations (14.6), (14.7) are modified as follows,

$$PC_z = \frac{B_z}{\mu_0 \cdot H_z} \tag{14.6}$$

$$J_{0z} = B_r \cdot cos\widehat{\overline{B}_z\overline{B}} \cdot \frac{PC_z + 1}{PC_z + \mu_{rec}} \tag{14.7}$$

Table 14.2 reports the comparison between the measurements and FEA simulations of the magnetic moment for the different PM topologies. For the C-shape magnet, has been included the calculation of the fictitious magnetic moment, which can be measured along the axial direction of the Helmoholtz coil (z-axis). The C-shape $4pcs$ and $1pcs$ have been simulated according to two different magnetization directions: radial direction, requested for the application and the parallel orientation. This has been made in order to verify the accuracy of the manufacturing and magnetization process which is critical for reaching the simulated motor performance (flux concentration). Moreover, the FEA simulation takes into account the rated and minimum value declared by the manufacture, B_r and $0.97 \cdot B_r$. It is important to remind that, for simplicity of construction, the length of the C-shape PMs is equal to half of the motor stack length (2 PM stacked along the axial direction).

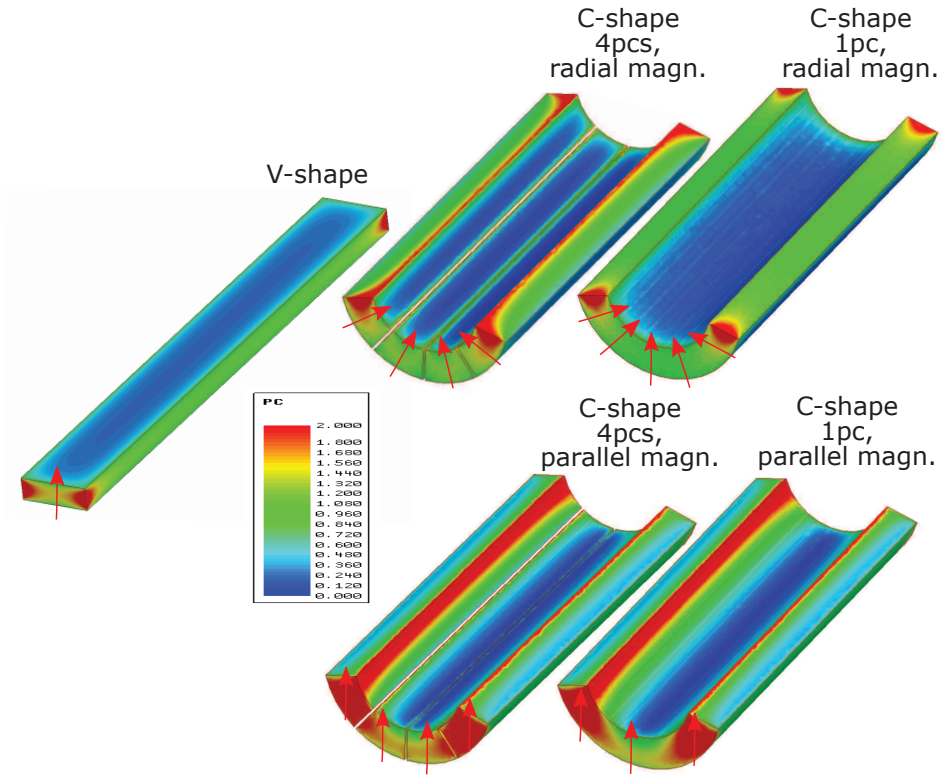

Fig. 14.5: 3D FEA analysis of the different *N*45*H* PM topologies: map of the permeance coefficient.

As confirmed by the hysteresisgraph, the V-shape block PM exhibits a magnetic moment in between the tolerance range of the remanence flux density. As regards the C-shape magnet, considering the radial direction, a simulated magnetic moment closed to the measured value would highlight that a proper radial magnetization has been achieved. Considering the parallel direction, a simulated magnetic moment closed to the measured value should highlight that the PMs has not been manufactured and magnetized properly.
Both the C-shape 4pcs and 1pc shows simulated values around 28% and 13% higher than the measured value, respectively. This emphasizes that a parallel magnetization is not reached. Conversely, considering the radial direction, the magnetic moments of the C-shape 4pcs are 1% higher than the measured value, while for the C-shape 1pc is 21% lower than the measurements. In conclusion, the C-shape 4pcs is expected to provide the requested magnetization direction, while the C-shape 1pc does not meet the requested properties.

In order to confirm in detail the previous investigation, a measurement of the flux density on the surface of the C-shape PMs has been carried out, by means of a Hall sensor and t. Fig 14.6 reports the flux density map and lines of the C-shape PM topologies with different magnetization directions. The measurement is performed in the middle line of the C-shape

Table 14.2: Magnetic moment comparison between measurement and FEA simulations of the different PM topologies (room temperature 22°C).

Sample type	**V-shape**	**C-shape 4 pcs**		**C-shape 1 pc**		**Unit**
		Radial magn.	**Parallel magn.**	**Radial magn.**	**Parallel magn.**	
Measur.	105.4	72.2		90.6		$10^{-6}Wb \cdot cm$
FEA sim. @ $B_r = 1.31T$	107.0	100.4	101.1	104.6	105.4	$10^{-6}Wb \cdot cm$
Var. to FEA	−1.50	–	−28.6	–	−14.0	%
FEA sim. @ $B_r = 1.27T$ (97%)	103.8	97.38	98.04	101.5	102.2	$10^{-6}Wb \cdot cm$
Var. to FEA	1.54	–	−26.4	–	−11.4	%
FEA sim., z-axis @ $B_r = 1.31T$	–	73.79	–	75.69	–	$10^{-6}Wb \cdot cm$
Var. to FEA	–	−2.15	–	19.7	–	%
FEA sim., z-axis @ $B_r = 1.27T$ (97%)	–	71.90	–	73.78	–	$10^{-6}Wb \cdot cm$
Var. to FEA	–	0.42	–	22.8	–	%

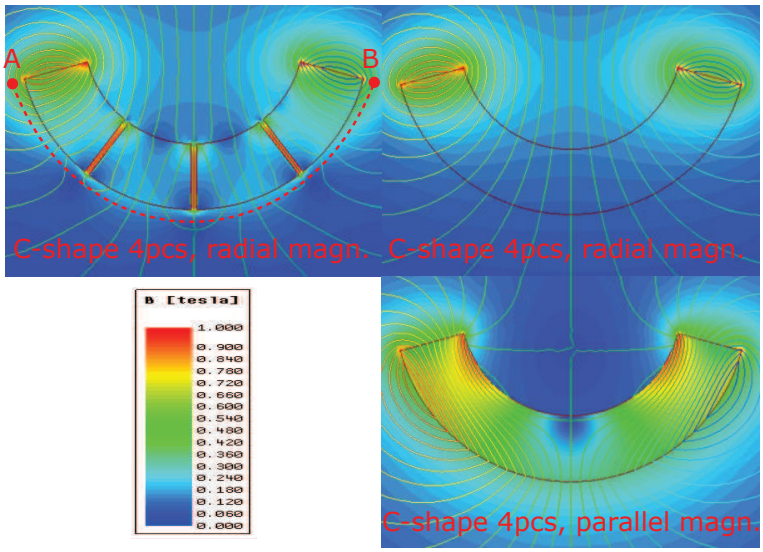

Fig. 14.6: 3D FEA analysis of the different N45H PM topologies: map of the permeance coefficient.

PM, while a monitoring line AB is placed at 0.45mm of the PM concave surface and the flux density is compared with the FEA simulation, as shown in Fig. 14.12.

Fig. 14.7(a) shows the flux density waveform of the C-shape 1pc. It is compared with two

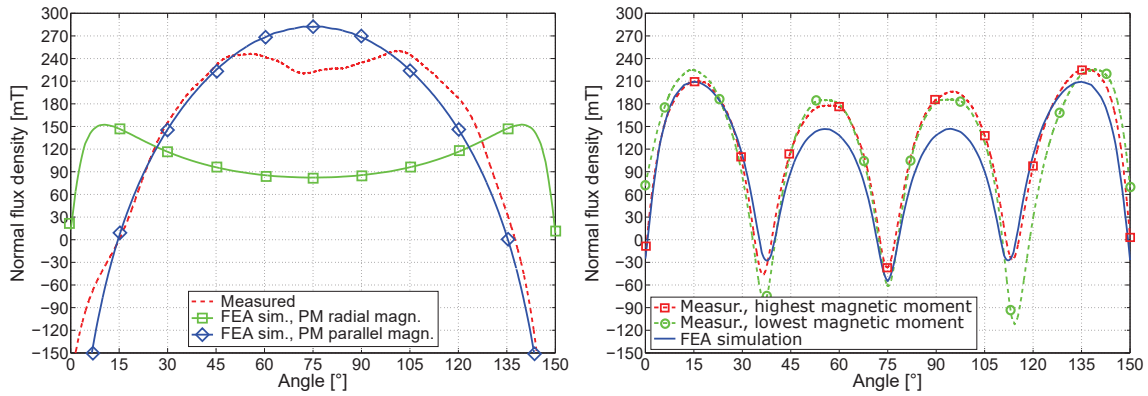

(a) C-shape 1pc. (b) C-shape 4pcs.

Fig. 14.7: Comparison between measurement and FEA simulation of the tlux density of the C-shape PM topologies (room temperature 22°C).

simulated cases, the first with radial magnetization while the second with parallel magnetization. It is worth noticing that the PM fails to meet the requested radial magnetization waveform and it is more close to the parallel magnetization result. The C-shape 1pc is therefore discarded for motor prototyping. On the other hand, it is worth noticing that the saddle area in the middle of the waveform could indicate a weak magnetization or a radial magnetization partially achieved.

As reported by Fig. 14.7(b), a good agreement is found between the measurement and the simulation for the C-shape 4pcs topology in correspondence of the external areas of the PMs. Conversely, the flux density waveform in correspondence of the inner side is 20% higher than the simulation. This highlights that the magnetization has not been performed properly and a degradation of the rotor airgap flux density (i.e. torque density) is expected. At the time of the submission of this thesis improved C-shape 1pc samples built and magnetized in a different manner, are delivered for further evaluation.

14.2.3 Rotor flux density evaluation

The rotor flux density is evaluated employing a MAGACAM ® [172] magnetic field camera. The heart of the magnetic camera is a sensor chip structured in an array of 128×128 (16384) microscopic Hall sensors, as shown in Fig. 14.8. Each sensor has an active area of $40\mu m$ and it measures locally the normal component of the airgap flux density. Each Hall pixel is electronically scanned with an acquisition time of about $50\mu s$, which leads to a total

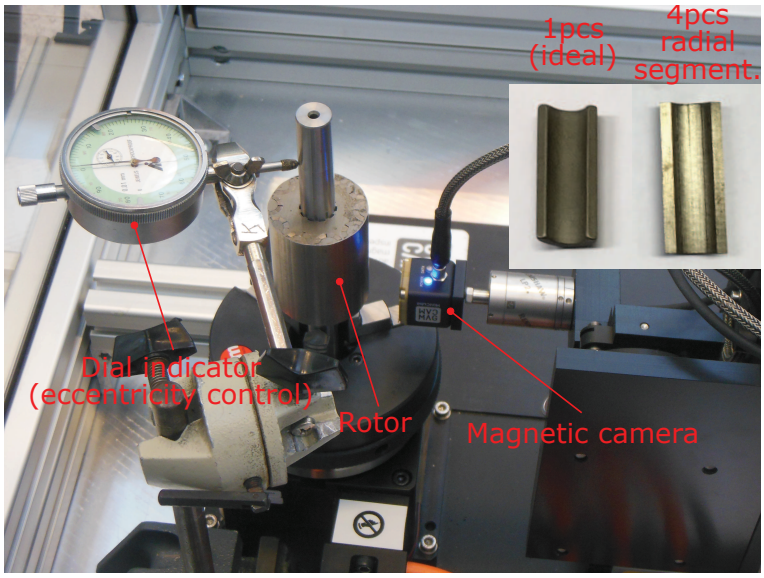

Fig. 14.8: Magnetic camera setup.

acquisition time less of $1s$ with the highest resolution of $0.1mm$. The flux density evaluated by the array provides a mapped area of $12.8 \times 12.8mm$. Finally, the sensibility of the field scanner is $\pm 0.1mT$.

In Fig. 14.8 is reported the setup for the measurement of the rotor flux quantities. It is

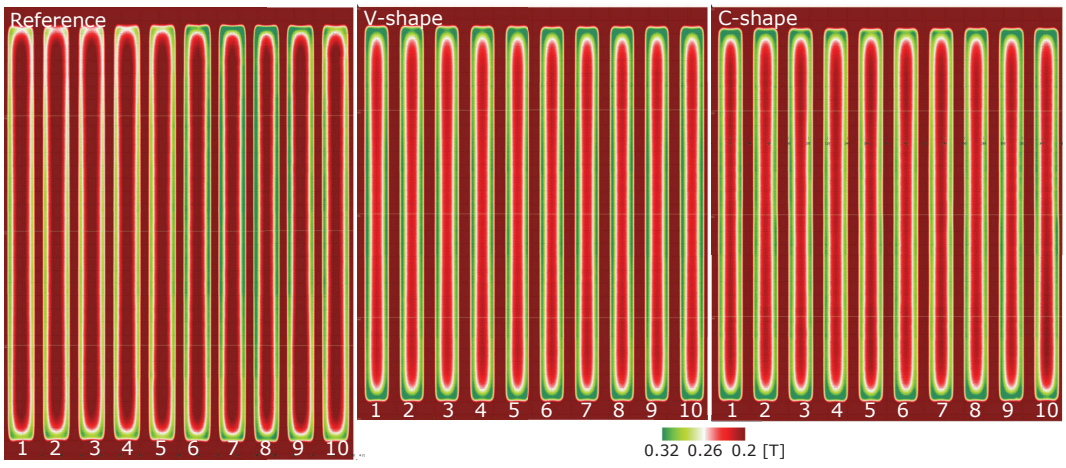

Fig. 14.9: 2D flux density map of the rotor samples (room temperature $30°C$).

based upon a field camera sensor installed in a 4-axis motorized scanner, represented by the 3 cartesian axes X, Y, Z and the rotation axis of the shaft where the rotor is placed. The distance from the Hall sensor of the magnetic field camera and the rotor is set to $0.5mm$. In this set-up only the flux density along the axial length is measured during one revolution of

the rotor. When the rotor is longer than 12.8*mm*, a mechanical scan along the rotor axial direction is performed. The angular and the axial resolution are 0.1° and 0.1*mm*.
In Fig. 14.9 the measured 2D flux density map is reported for the 3 different rotor samples. This provides a quick indication of any defects or non-uniformities of the magnetic properties of the rotors (such as PM quality, PM polarity, PM symmetry, important defects in the iron lamination). It is worth noticing that a measurable asymmetry exists between the two part of the surface of the reference rotor.

Figs. 14.10, 14.11, 14.12 report the measurement (2 sample for each motor topology) and

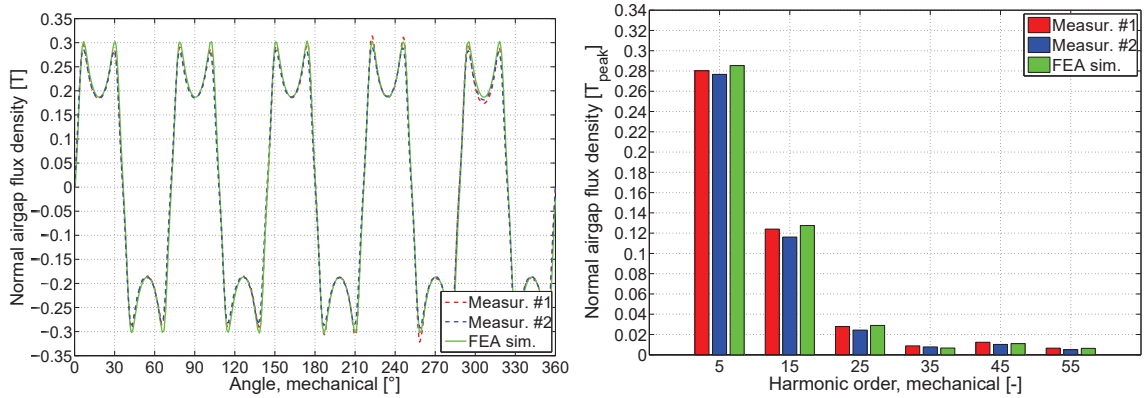

(a) Waveform. (b) Harmonic spectra.

Fig. 14.10: Reference rotor: comparison between measurement and FEA simulation of the rotor airgap flux density in open circuit (room temperature 30°*C*).

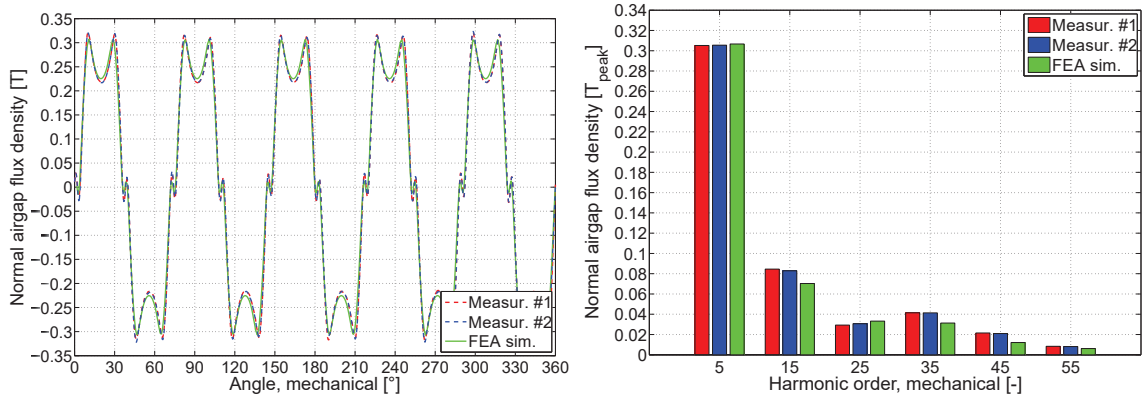

(a) Waveform. (b) Harmonic spectrum.

Fig. 14.11: V-shape rotor: comparison between measurement and FEA simulation of the rotor airgap flux density in open circuit (room temperature 30°*C*).

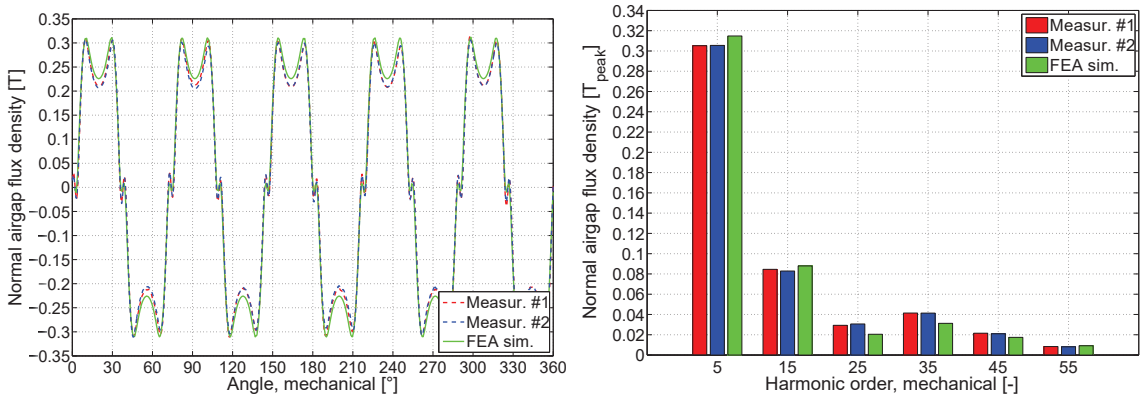

(a) Waveform.

(b) Harmonic spectrum.

Fig. 14.12: C-shape rotor: comparison between measurement and FEA simulation of the rotor airgap flux density in open circuit (room temperature 30°C).

FEA simulation of the flux density in open circuit as a function of the rotor position and its harmonic spectrum for the reference, V-shape and C-shape rotor. In order to neglect the influence of the end effects, the flux density is evaluated along a monitoring line placed in the middle of the rotor package. Table 14.10 reports the comparison between the harmonic components up to the 35^{th} mechanical order and the $THD\%$. A good agreement between the FEA simulation and measurement is shown for the reference and V-shape rotor, with an average error of the fundamental of about 1.4%. As regards the C-shape rotor, the degradation of the PM properties due to the inaccurate magnetization measured in in Sec. 14.2.2 is confirmed by the evaluation of the rotor flux density. The measured flux density of the fundamental is 6% lower than the FEA simulation. Finally, it is worth noticing the better $THD\%$ exhibited by the new rotor design, equal to an average measurement of 44.6% of the reference rotor in comparison to the 33.2% and 34.4% of the V-shape and C-shape, respectively. It is mainly due a lower 3^{th} electrical harmonic order (15^{th} mechanical) which is in average, about 28% lower for the C/V-shape rotor design. Finally in Fig. 14.13 the FEA simulation waveform and related harmonic spectrum of the airgap flux density for the different rotors is reported. Due to the flux concentration, 20% and 15% higher fundamental no load airgap flux density is achieved for the V-shape and C-shape motor, in comparison to the reference design. It is important to remind that the lower flux density of the C-shape design is caused by the degraded magnetic performance of the PM. Finally, as confirmed by the no load open circuit airgap flux density measurements, a lower distortion of the flux density is shown by the C/V-shape motor, with an average $THD\%$ of 12.7% against the 15.8% of the reference motor. From the open magnetic circuit, described before, to the

Table 14.3: Comparison of the harmonic contribution between measurement and FEA simulation (room temperature 30°C).

Harm. order	Reference			V-shape			C-shape			Unit
	Meas. #1	Meas. #2	FEA	Meas. #1	Meas. #2	FEA	Meas. #1	Meas. #2	FEA	
5^{th} (fund.)	0.280	0.277	0.285	0.305	0.306	0.307	0.299	0.294	0.315	T_{peak}
Var. to FEA	−1.8	−2.8	0	−0.7	−0.3	0	−5.1	−6.7	0	%
15^{th}	0.124	0.116	0.128	0.085	0.083	0.070	0.089	0.087	0.088	T_{peak}
Var. to FEA	−3.1	−9.4	0	21.4	19.0	0	1.1	−1.1	0	%
25^{th}	0.028	0.024	0.029	0.029	0.031	0.033	0.021	0.021	0.020	T_{peak}
Var. to FEA	−3.4	−17.2	0	−12.1	−6.1	0	5.0	5.0	0	%
35^{th}	0.009	0.008	0.007	0.041	0.041	0.031	0.038	0.037	0.031	T_{peak}
Var. to FEA	−28.6	−14.2	0	32.3	32.3	0	22.6	19.4	%	
$THD\%$	46.0	43.2	46.1	33.3	33.0	27.8	34.4	34.4	31.0	%
Var. to FEA	−0.2	−6.3	0	19.8	18.7	0	11.0	11.1	0	%

closed magnetic circuit, the higher 3^{th} harmonic order in the reference motor is maintained, as reported in Table 14.4. Moreover, additional harmonic components arise due to the stator slotting effect, following the relationship $h = (\xi \mp k \cdot Q) \cdot p$, with $\xi, k = 1,2,3...$ [43, 44].

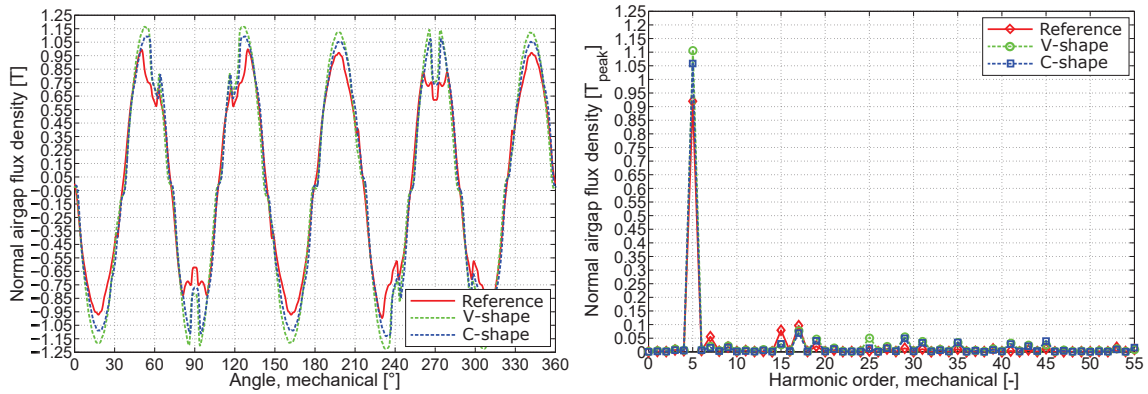

(a) Waveform. (b) Harmonic spectrum.

Fig. 14.13: FEA simulation of the airgap flux density (room temperature 30°C).

Table 14.4: FEA simulation of the harmonic spectrum (room temperature 30°C). In grey are highlighted the main harmonic components; not highlighted, the harmonic contribution due to the stator slotting effect.

Harm. order	**Reference**	**V-shape**	**C-shape**	**Unit**
5^{th} (fundamental)	0.920	1.104	1.058	T_{peak}
Variation	0	20.0	15.0	%
7^{th}	0.056	0.019	0.015	T_{peak}
15^{th}	0.079	0.025	0.029	T_{peak}
17^{th}	0.096	0.096	0.096	T_{peak}
19^{th}	0.020	0.045	0.040	T_{peak}
25^{th}	0.003	0.049	0.013	T_{peak}
29^{th}	0.013	0.053	0.049	T_{peak}
31^{th}	0.010	0.037	0.033	T_{peak}
35^{th}	0.009	0.033	0.034	T_{peak}
$THD\%$	15.8	13.0	12.3	%

14.3 FEA model

The updated FEA model of the machines is reported hereafter. The PM dimensions and their magnetic properties has been updated according to the analysis presented before. The actual profile of the star and yoke has been introduced as well. Following some dimensional analysis of profile of the contact surface of the star and yoke, the airgap between the star of teeth and yoke as been kept according to the preliminary estimation ($50\mu m$) In Fig. 14.14 and 14.15 the flux density map of the machines are reported in no load and load operation. It is worth noticing the slight difference of the saturation levels in the stator of the C-shape and V-shape designs.

14.4 No load and load tests

In this section the measurement of the motor performance in no load and load operation are summarized. The test bench setup is reported in Fig. 14.16. The motor is fed Voltage Source Inverter (VSI) with PWM modulation connected to a switching power supply at $12V$ DC and it is controlled by a dSPACE ® unit. A synchronous PI space vector control with current and speed loop, which takes into account MTPA and FW operation is implemented. The braking torque is provided by a load motor coupled with the control.
The torque is measured by a $3/30Nm$ torque-meter, accuracy class of 0.1, equivalent to uncertainty of $\pm 0.03/0.003Nm$. The maximum operating speed is $6000rpm$. The input power

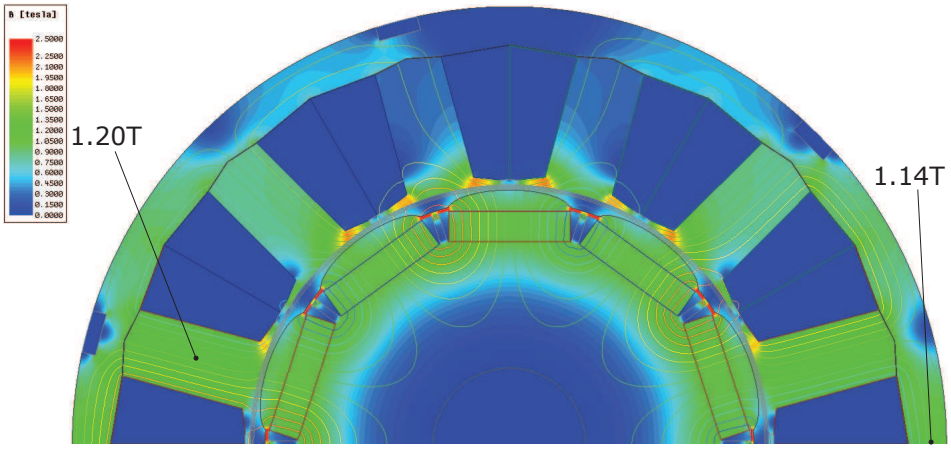

(a) Reference motor.

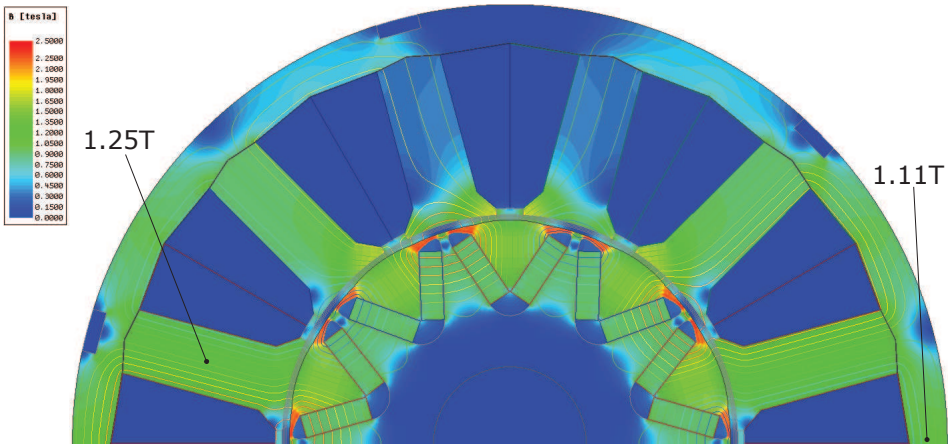

(b) V-shape motor.

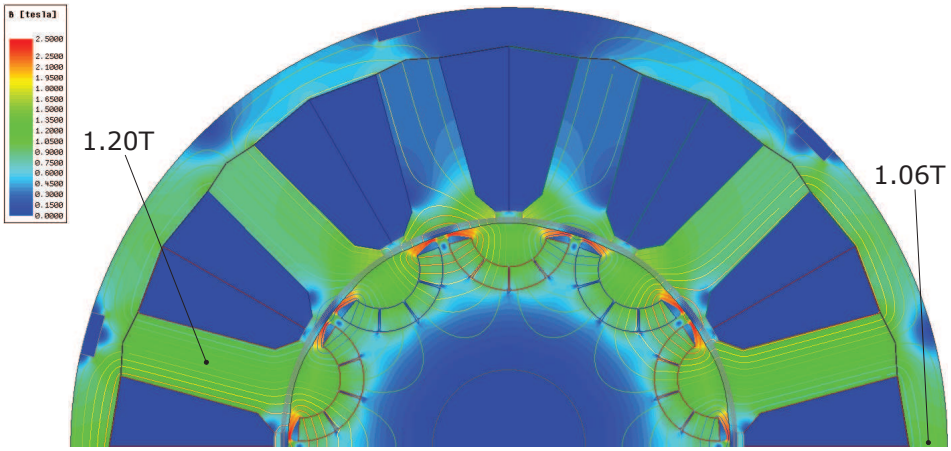

(c) C-shape motor.

Fig. 14.14: No load flux density map.

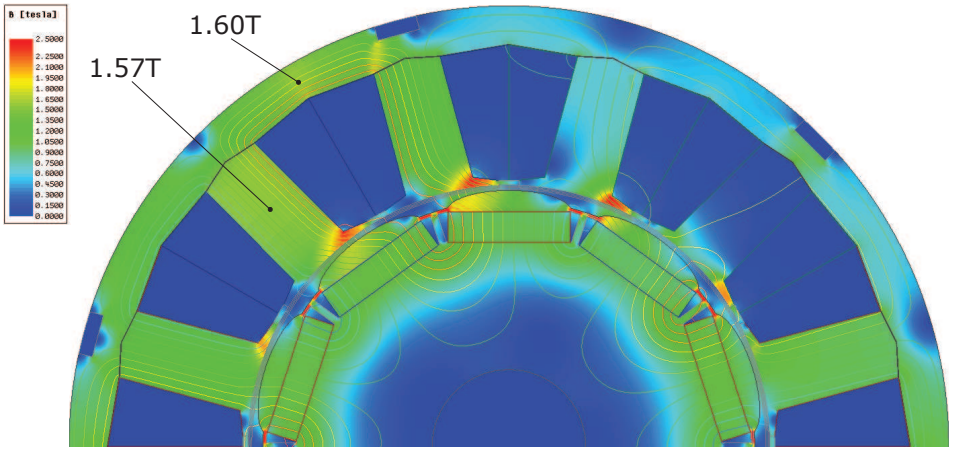

(a) Reference motor.

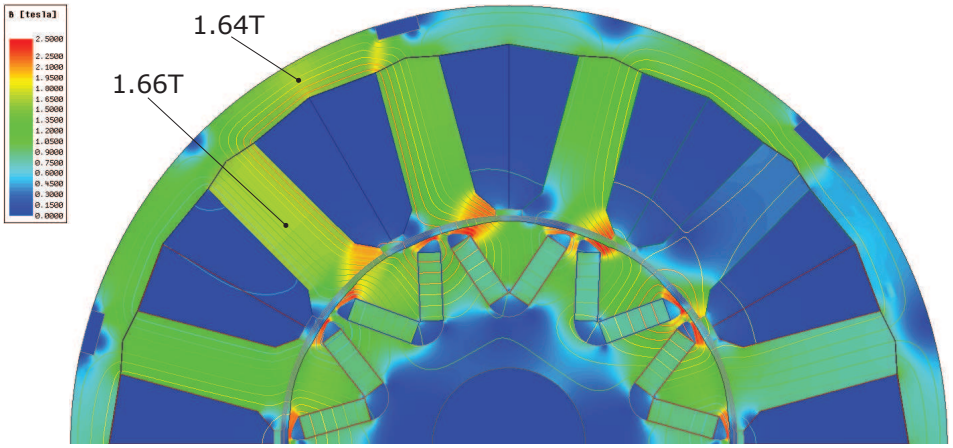

(b) V-shape motor.

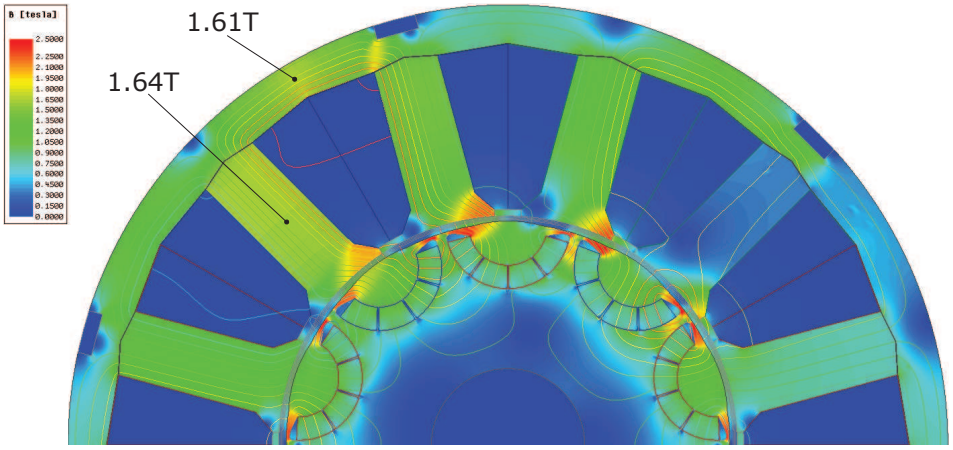

(c) C-shape motor.

Fig. 14.15: Load flux density map, $100A_{RMS}$, MTPA.

has been measured using a Yokogawa ® WT160 power analyzer.
All the measurements in load operation have been performed at a controlled average operating temperature of $30°C$. It has been controlled by means of a thermocouple been placed in correspondence of the electrical connection plate (end winding). This represents a critical aspect since the machines are designed to operate in non continuous service (current density in the order of $12A_{RMS}/mm^2$, simulated city traffic comparable to a IEC S10, which describes a discrete constant loads service).

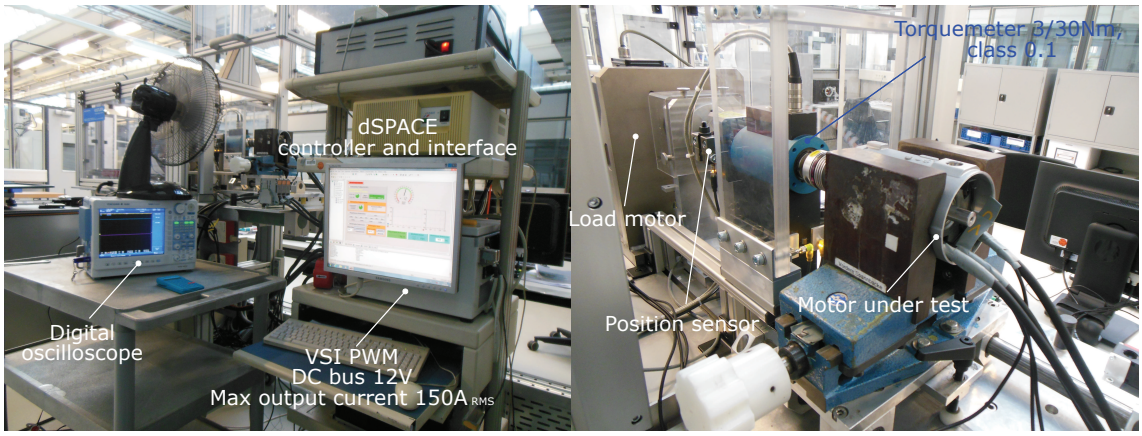

(a) Overview.

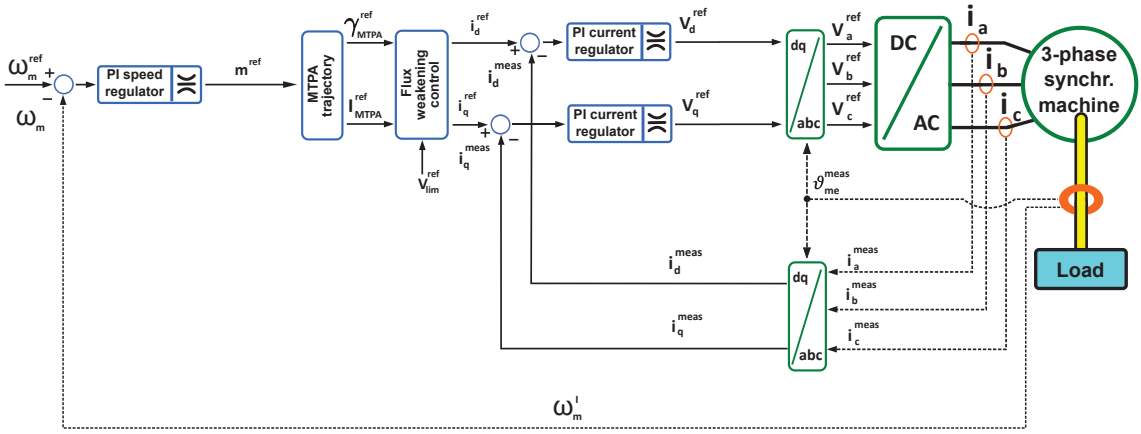

(b) d/q PI synchronous space vector control.

Fig. 14.16: Test bench setup.

14.4.1 Back EMF

The back EMF is measured at $1200rpm$. Table 14.5 summarizes the main harmonic component, $THD\%$ and another quality index, called Voltage Unbalance Factor (VUF) [132, 144]

defined as the ratio of the negative sequence voltage component V_- to the positive sequence voltage component V_+,

$$VUF\% = \frac{V_-}{V_+} \cdot 100 \tag{14.8}$$

Where,

$$\begin{cases} V_+ = \dfrac{\overline{V}_{ab} + \overline{a} \cdot \overline{V}_{bc} + \overline{a}^2 \cdot \overline{V}_{ca}}{3} & \text{(14.9a)} \\ V_- = \dfrac{\overline{V}_{ab} + \overline{a}^2 \cdot \overline{V}_{bc} + \overline{a} \cdot \overline{V}_{ca}}{3} & \text{(14.9b)} \end{cases}$$

with $\overline{a} = e^{j \cdot \frac{2}{3} \cdot \pi}$, $\overline{a}^2 = e^{j \cdot \frac{4}{3} \cdot \pi}$ A good agreement between the measurements and the FEA simulations is achieved for the reference and V-shape machine, with a average difference of the fundamental in the order of about 4% in respect to the FEA computation. As expected, a discrepancy is found for the C-shape motor due to the lower PM specifications. Finally, an analysis of the harmonic contents provides interesting remarks.

- The measured $THD\%$ of the prototypes is unexpectedly lower than the FEA simulation. In particular, the measured 3^{th} harmonic order is negligible. This could be explained by some phenomena of non ideality during the measurement, such as the effect of the stator MMF due to the induced current circulation along the two parallel branches of the same phase.
- The C/V-shape motors exhibit a $THD\%$ of the back EMF about 3 times higher than the reference design, although previous measurements and FEA simulations have proved that better harmonic content of the no load airgap flux density (in open and closed circuit) is achieved.

  Moreover, for the above mentioned machines, a higher asymmetry among the phase voltage has been measured: the measured $VUF\%$ goes from and average value of 0.29% for the reference machine to 0.54% for the C/V-shape motors. Since no remarkable differences of the winding asymmetry between the reference and C/V-shape designs have been found, this discrepancy could be induced by critical manufacturing issues in in the stator and/or rotor iron packages.

Table 14.5: Phase back EMF harmonic content ($1200rpm$, $30°C$). Measured voltage uncertainty $\pm 0.5\%$.

Motor index	1^{st}	3^{rd}	5^{th}	7^{th}	9^{th}	11^{th}	13^{th}	**Unit**	**THD%**
Reference									
#122	4.1766	0.0033	0.0075	0.0017	0.0014	0.0185	0.0083	V_{peak}	0.55%
#123	4.2187	0.0073	0.0075	0.0076	0.0008	0.0226	0.0062	V_{peak}	0.66%
FEA sim.	4.383	0.185	0.008	0.014	0.062	0.010	0.015	V_{peak}	4.57%
$VUF\%$									
#122					0.27%				
#123					0.32%				
FEA sim.					0				
V-shape									
#120	4.3815	0.0195	0.0054	0.0056	0.0018	0.0683	0.0227	V_{peak}	1.73%
#121	4.3582	0.0206	0.0068	0.0029	0.0030	0.0655	0.0244	V_{peak}	1.70%
FEA sim.	4.589	0.196	0.019	0.009	0.010	0.077	0.071	V_{peak}	4.98%
$VUF\%$									
#120					0.42%				
#121					0.59%				
FEA sim.					0				
C-shape									
#148	4.0726	0.0199	0.0089	0.0012	0.0029	0.0676	0.0253	V_{peak}	1.86%
#149	4.0650	0.0206	0.0078	0.0033	0.0018	0.0695	0.0228	V_{peak}	1.90%
FEA sim.	4.406	0.103	0.019	0.007	0.019	0.051	0.055	V_{peak}	4.98%
$VUF\%$									
#120					0.59%				
#121					0.48%				
FEA sim.					0				

14.4.2 Measurement of the PM flux linkage and d/q-axis synchronous inductance

The PM flux linkage (average value) is computed on the basis of the fundamental of the back EMF $\widehat{E}_{0,1}$ (peak value), test speed $n_m = 1200rpm$ and pole pairs p, from the equation,

$$\Lambda_{PM} = \frac{60 \cdot \widehat{E}_{0,1}}{2 \cdot \pi \cdot n_m \cdot p} \tag{14.10}$$

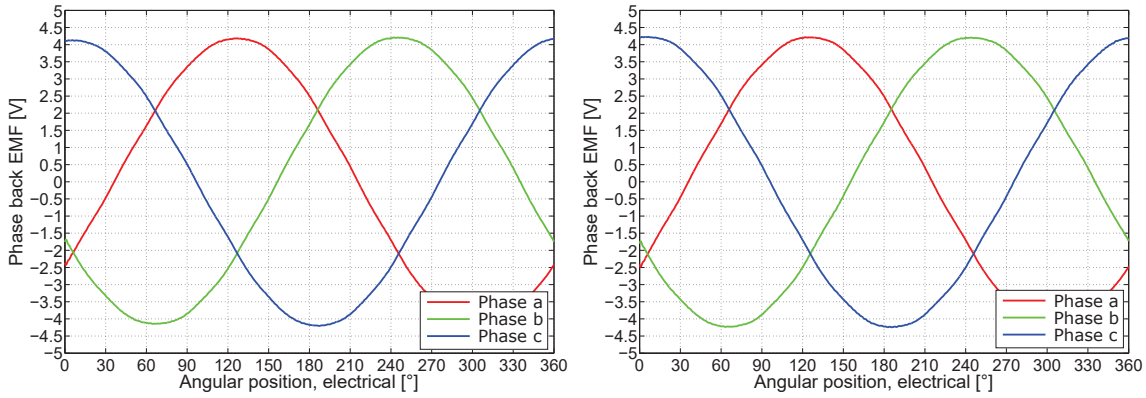

(a) Measured 3-phase back EMF, motor #122 cw. (b) Measured 3-phase back EMF, motor #123 cw.

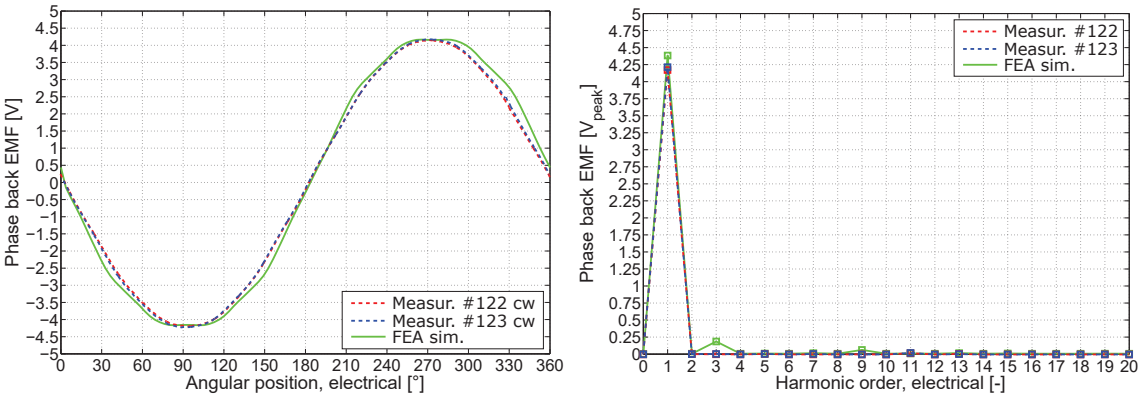

(c) Measurement vs. FEA, waveform. (d) Measurement vs. FEA, harmonic content.

Fig. 14.17: Reference motor: phase back EMF analysis.

Different methodologies have been proposed for the measurement of the synchronous inductances. These motor parameters are indirectly computed from the d-axis and q-axis flux linkage on the basis of the measurement of electrical quantities such as, voltage and current in particular circuital configuration and regime. Sorting upon the complexity of the procedure and required hardware, they are summarized in as follows. [47, 67, 113, 126, 161]

Stand-still vector control methods

- "Evaluation of the flux characteristic by means of transient response from an AC excitation" [11].

  This procedure is based upon the injection of a voltage signal separately in the d and q-axis and consequent measurement of the d/q-axis current. In order to avoid accidental rotation, a high frequency alternated signal, such as with a square wave distribution, is required. Moreover the amplitude has to be selected in order to produce a current

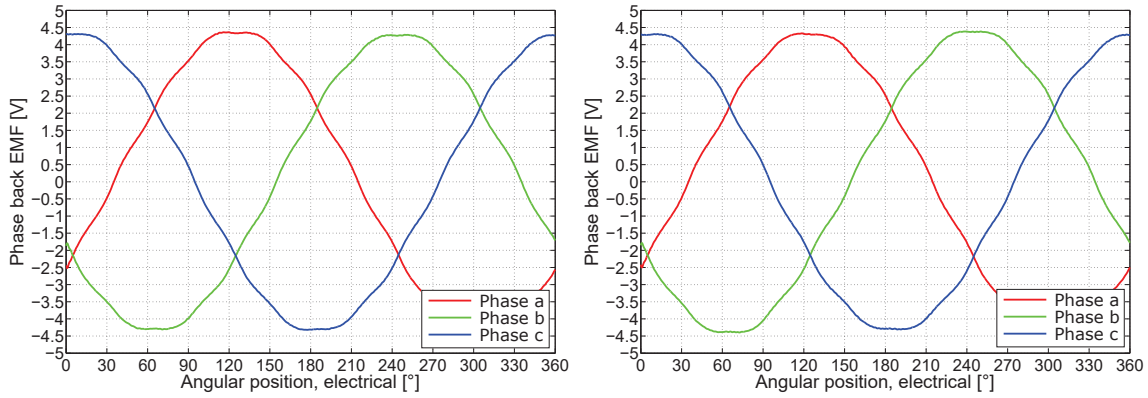

(a) Measured 3-phase back EMF, motor #120 cw. (b) Measured 3-phase back EMF, motor #121 cw.

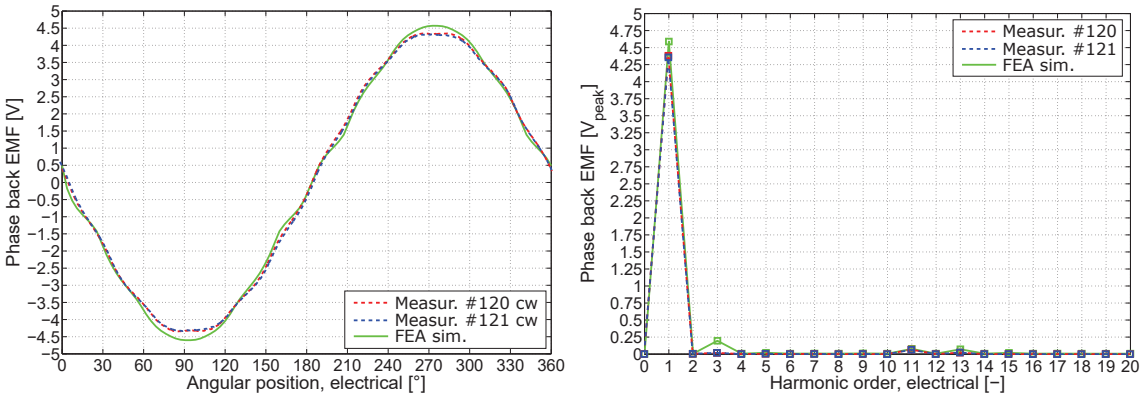

(c) Measurement vs. FEA, waveform. (d) Measurement vs. FEA, harmonic content.

Fig. 14.18: V-shape motor: phase back EMF analysis.

transient which covers all the range of interest. The voltage equations of the machines are,

$$\begin{cases} e_d = R \cdot i_d + \dfrac{d\lambda_d}{dt} - \omega_{me} \cdot \lambda_q & \text{(14.11a)} \\ e_q = R \cdot i_q + \dfrac{d\lambda_q}{dt} + \omega_{me} \cdot \lambda_d & \text{(14.11b)} \end{cases}$$

Working in stand-still operation (i.e. $\omega_{me} = 0$), the d/q-axis are decoupled. Therefore, knowing the resistance, the d/q-axis flux linkage can be indirectly evaluated by means of integration, as follows,

$$\begin{cases} \lambda_d = \displaystyle\int_0^t (e_d - R \cdot i_d) \cdot dt & \text{(14.12a)} \\ \lambda_q = \displaystyle\int_0^t (e_q - R \cdot i_q) \cdot dt & \text{(14.12b)} \end{cases}$$

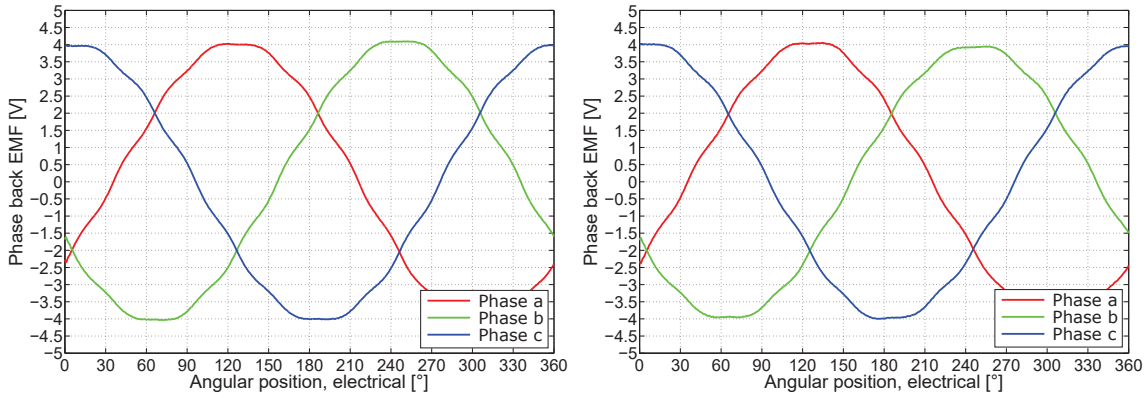

(a) Measured 3-phase back EMF, motor #148 cw. (b) Measured 3-phase back EMF, motor #149 cw.

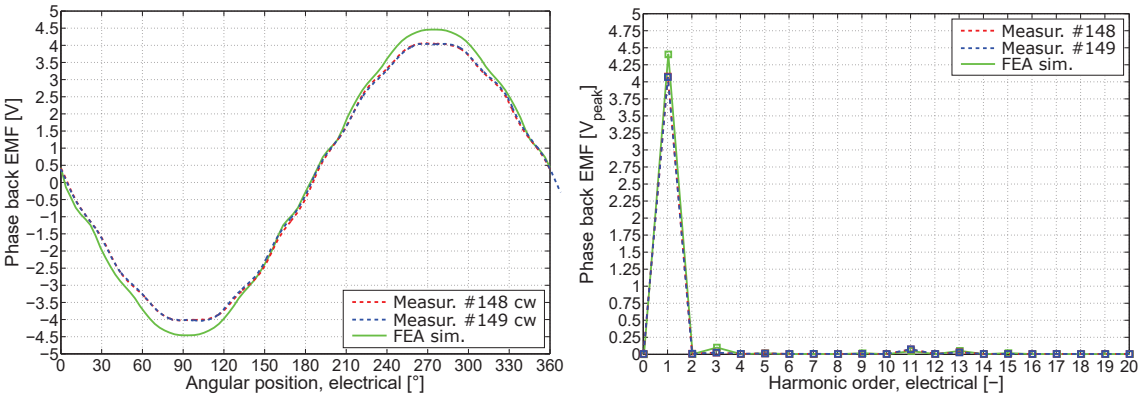

(c) Measurement vs. FEA, waveform. (d) Measurement vs. FEA, harmonic content.

Fig. 14.19: C-shape motor: phase back EMF analysis.

Therefore, the d/q-axis apparent and differential inductances can be easily computed, as follows,

$$\begin{cases} L_d = \dfrac{\lambda_d}{i_d} & \text{(14.13a)} \\ L_q = \dfrac{\lambda_q}{i_q} & \text{(14.13b)} \end{cases}$$

$$\begin{cases} L_{diff,d} = \dfrac{d\lambda_d}{di_d} & \text{(14.14a)} \\ L_{diff,q} = \dfrac{d\lambda_q}{di_q} & \text{(14.14b)} \end{cases}$$

The flux linkage vs. current curve can be approximated with a piecewise function, composed by a linear and inverse function. This representation, typical for the iron

saturation [171], reported in Fig. 14.20 and defined as follows,

$$\begin{cases} \lambda = L_0 \cdot i \rightarrow i \leq |i_{thr}| & \text{(14.15a)} \\ \lambda = sgn(i)\lambda_0 + L_1 \cdot i + \dfrac{a}{I} \rightarrow i \geq |i_{thr}| & \text{(14.15b)} \end{cases}$$

Comparing to other approximations functions, such es polynomial [149], the number

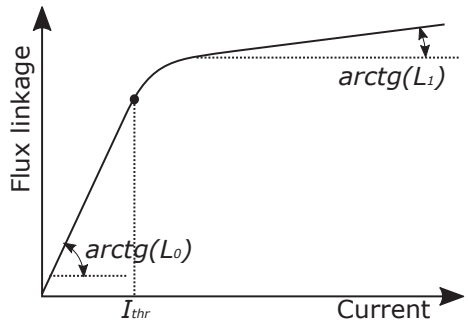

Fig. 14.20: Approximation function of the flux linkage vs. current.

of parameters which define this function are restricted to 3, L_0, L_1 and β. Therefore, especially as regards of implementation of this technique into a a self-commissioning identification, the computation is simple and it is not affected by the typical oscillatory behavior of the approximated function when a high-order polynomial function is employed with the target of increasing the accuracy. This phenomenon is more critical when an extrapolation outside the measurement range is necessary. In this model, L_0 represents the apparent or differential non-saturated inductance, L_1 is the saturated differential inductance, Λ_0 is a fictitious flux linkage of the saturated curve. Imposing the equality of the differential and apparent inductances, at the boundary point, represented by the current threshold I_{thr}, the coefficient β is equal to,

$$\beta = -\frac{\lambda_0 \cdot i_{thr}}{2} \tag{14.16}$$

Using a Multiple Linear Regression (MLR) model [73], it results,

$$\{\lambda_{d,q}\} = [i_{d,q}] \cdot \{P\} + \{\varepsilon\} \tag{14.17}$$

where:

$$\lambda_{d,q} = \begin{Bmatrix} \lambda_{d,q,1} \\ \lambda_{d,q,2} \\ \dots \\ \lambda_{d,q,n} \end{Bmatrix} \tag{14.18}$$

$$i_{d,q} = \begin{bmatrix} sgn(i_{d,q,1}) & i_{d,q,1} & \dfrac{1}{i_{d,q,1}} \\ sgn(i_{d,q,2}) & i_{d,q,2} & \dfrac{1}{i_{d,q,2}} \\ \dots & \dots & \dots \\ sgn(i_{d,q,n}) & i_{d,q,n} & \dfrac{1}{i_{d,q,n}} \end{bmatrix} \tag{14.19}$$

$$P = \begin{Bmatrix} \lambda_0 \\ L_1 \\ \beta \end{Bmatrix} \tag{14.20}$$

$$\varepsilon = \begin{Bmatrix} \varepsilon_1 \\ \varepsilon_2 \\ \dots \\ \varepsilon_n \end{Bmatrix} \tag{14.21}$$

$\{\varepsilon\}$ is the residual.

Exploiting the least square method, the estimated matrix of the regression coefficients is,

$$\{\widehat{P}\} = \left([i_{d,q}]^T \cdot [i_{d,q}]\right)^{-1} \cdot [i_{d,q}]^T \cdot \{\lambda_{d,q}\} \tag{14.22}$$

This saturation model shows some limits when the d-axis flux linkage has to be modeled in the positive range of the d-axis current. Due to the reversal of the flux linkage through the iron ribs, the d-axis flux linkage suddenly increases since the leakage flux is canceled. Moreover this model cannot take into account, for the evaluation of the flux linkage, the PM contribution since the rotational EMF is null. In order to take into account the cross saturation, the d/q-axis voltage signal has to be applied simultaneously. Then the analysis follows the procedure previously discussed.

- "Evaluation of the apparent inductance by means of an AC excitation" [121].
  This method is based upon the injection of an AC excitation at the frequency f_{inj} alternatively on the d and q-axis while the other is short-circuited by the inverter. This methodology can be applied if the mutual inductance M_{dq} is null or negligible.

The apparent inductances can be computed as follows,

$$\begin{cases} L_d = \dfrac{\widehat{E}_d - R \cdot \widehat{I}_d}{2 \cdot \pi \cdot f_{inj} \cdot \widehat{I}_d} = L_d - \dfrac{M_{dq}}{L_q} \cdot M_{dq} \cong L_d(I_d) & \text{(14.23a)} \\ L_q = \dfrac{\widehat{E}_q - R \cdot \widehat{I}_q}{2 \cdot \pi \cdot f_{inj} \cdot \widehat{I}_q} \cong L_q - \dfrac{M_{dq}}{L_d} \cdot M_{dq} \cong L_q(I_q) & \text{(14.23b)} \end{cases}$$

Constant-speed vector control methods

The constant speed vector control method has the advantage of using the existing hardware of the motor drive. The speed of the machine is kept constant and conveniently below the base speed. As the stand still methods discussed above, the constant-speed requires the knowledge of the resistance. [47]
From (14.11), the inductances can be extrapolated

$$\begin{cases} L_d = \dfrac{\dfrac{E_q - R \cdot I_q}{\Omega_{me}} - \Lambda_{PM(I_q)}}{I_d} & \text{(14.24a)} \\ L_q = \dfrac{E_d - R \cdot I_d}{\Omega_{me} \cdot I_q} & \text{(14.24b)} \end{cases}$$

Where the PM flux linkage, taking into account the cross saturation due I_q, can be evaluated measuring the q-axis EMF with $I_d = 0$, as follows,

$$\Lambda_{PM} = \frac{E_q - R \cdot I_q}{\Omega_{me}} \tag{14.25}$$

Since the measured quantities are interested by harmonic orders, the procedure requires a

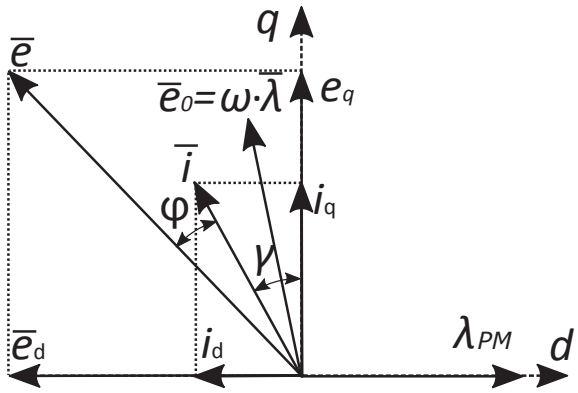

Fig. 14.21: Phasor diagram in d/q reference frame.

FFT in order to extract the fundamental components of the voltage and current in the $a/b/c$ reference frame before applying the transformation into the d/q-reference frame.

AC standstill method

The AC stand still methods require to feed the machine with an AC voltage or current excitation (sinusoidal or stepwise) with a locked rotor. There are two different procedures to evaluate the synchronous inductances.

1. "Measurement of the stator self- and mutual inductance vs. the angular position and subsequent application of the Park transformation for the computation of the d/q-axis synchronous inductance" [47, 67].
   According to Fig. 14.22(a), the phase a is feed with a AC sinusoidal voltage and the rotor is locked in different positions. The self- and mutual inductance, L_a and M_{ab} respectively, are therefore,

$$\begin{cases} L_a = \dfrac{\sqrt{\left(\dfrac{E_a}{I_a}\right)^2 - R^2}}{2 \cdot \pi f_{inj}} & \text{(14.26a)} \\ M_{ab} = \dfrac{E_b}{2 \cdot \pi f_{inj} \cdot I_a} & \text{(14.26b)} \end{cases}$$

   The abovementioned inductances can be expressed, under the hypothesis of a sinusoidal distributed winding, as follows,

$$\begin{cases} L = L_l + L_0 + L_2 \cdot cos(2 \cdot \theta_m) & \text{(14.27a)} \\ M = M_0 + M_2 \cdot cos(2 \cdot \theta_m + \dfrac{2}{3} \cdot \pi) & \text{(14.27b)} \end{cases}$$

   where:
   - L_l is the leakage inductance;
   - L_0, M_0 are respectively the average component of the self and mutual inductance, respectively;
   - L_2, M_2 is the 2^{nd} harmonic component of the inductance of the self and mutual inductance, respectively;
   By means the least square curve fitting technique, it is possible to extract the above

mentioned components. The $d-$ and $q-$ axis synchronous inductances are:

$$\begin{cases} L_d = (L_0 - M_0) - (\dfrac{L_2}{2} + M_2) & \text{(14.28a)} \\ L_q = (L_0 - M_0) + (\dfrac{L_2}{2} + M_2) & \text{(14.28b)} \end{cases}$$

2. "Measurement of the stator inductance when the d- and q-axis are aligned with the stator MMF" [67].
   As reported in Fig. 14.22(b) and Fig. 14.22(c), the d-axis and q-axis are alternately aligned on the a-phase axis. The synchronous inductances are then computed as follows,

$$\begin{cases} L_d = \dfrac{2}{3} \cdot \dfrac{v_{ab}}{i_a} \rightarrow d \equiv a & \text{(14.29a)} \\ L_q = \dfrac{2}{3} \cdot \dfrac{v_{ab}}{i_a} \rightarrow q \equiv a & \text{(14.29b)} \end{cases}$$

   It is worth noticing that the discussed methodology are not able to take into account the effect of the cross saturation.
3. Improvement method for taking into account the cross saturation [68].
   This methodology needs that the machine is fed with two different AC current sources, i_1 and i_2. These currents have to be select in order to produce, a current system $i_a/i_b/i_c$ which are related to a i_d/i_q of the operating point on interest. When the rotor is locked, as shown in the configuration I of Fig. 14.22(d), with axis $q \equiv a$ ($\theta_{me} = -90°$), the d/q-axis current are,

$$\begin{cases} i_{dI} = \dfrac{\sqrt{3}}{2} \cdot (i_c - i_b) & \text{(14.30a)} \\ i_{qI} = \dfrac{2}{3} \cdot \left(i_a - \dfrac{1}{2} \cdot (i_c + i_b) \right) & \text{(14.30b)} \end{cases}$$

   On the other hand, according to ,

$$\begin{cases} i_{dI} = -\dfrac{2}{3} \cdot \sqrt{3} \cdot i_2 & \text{(14.31a)} \\ i_{qI} = \dfrac{2}{3} \cdot i_1 & \text{(14.31b)} \end{cases}$$

Therefore, for this circuit topology, the required currents are,

$$\begin{cases} i_{1I} = \dfrac{3}{2} \cdot i_{qI} = \dfrac{3}{2} \cdot i_a & \text{(14.32a)} \\ i_{2I} = -\dfrac{\sqrt{3}}{2} \cdot i_{dI} = \dfrac{1}{2} \cdot (i_b - i_c) & \text{(14.32b)} \end{cases}$$

Likewise, for the configuration II shown in Fig. 14.22(e), where the axis $d \equiv a$ ($\theta_{me} = 0°$), it results,

$$\begin{cases} i_{1II} = -\dfrac{3}{2} \cdot i_{dI} = \dfrac{3}{2} \cdot i_a & \text{(14.33a)} \\ i_{2II} = -\dfrac{\sqrt{3}}{2} \cdot i_{qI} = \dfrac{1}{2} \cdot (i_b - i_c) & \text{(14.33b)} \end{cases}$$

Through mathematical elaborations [68], the d/q-axis inductance in the considered operating point, are given by,

$$\begin{cases} L_d = \sqrt{\left(\dfrac{V_{BCI}}{I_{1I}}\right)^2 - \left(\dfrac{P_I}{2 \cdot {I_{1I}}^2}\right)^2} & \text{(14.34a)} \\ L_q = \sqrt{\left(\dfrac{V_{BCII}}{I_{1II}}\right)^2 - \left(\dfrac{P_{II}}{2 \cdot {I_{1II}}^2}\right)^2} & \text{(14.34b)} \end{cases}$$

DC standstill method

The DC standstill test [91, 113] is based on the evaluation of the current transient as a result of a voltage step. As shown in Figs. 14.23(a) and 14.23(b) the d and q-axis are alternatively aligned with the axis of the phase a, in order to evaluate the d- and q-axis flux linkage as a function of the d- and q-axis current, respectively. The voltage has to be reversed in order to evaluate the flux linkage for $I_d < 0$ and $I_q < 0$.

$$\begin{cases} v_{d,q} = \dfrac{2}{3} \cdot \left(v_a - \dfrac{1}{2} \cdot (v_b + v_c)\right) = \dfrac{2}{3} \cdot (v_a - v_b) = v_{ab} & \text{(14.35a)} \\ i_{d,q} = \dfrac{2}{3} \cdot \left(i_a - \dfrac{1}{2} \cdot (i_b + i_c)\right) = i & \text{(14.35b)} \end{cases}$$

Using (14.12), (14.24), (14.14) the flux characteristics and synchronous inductances can be computed. The resistance R can be calculated considering the steady state voltage $v_{ab\infty}$ and current i_∞, as follows,

$$R = \frac{2}{3} \cdot \frac{v_{ab\infty}}{i_\infty} \tag{14.36}$$

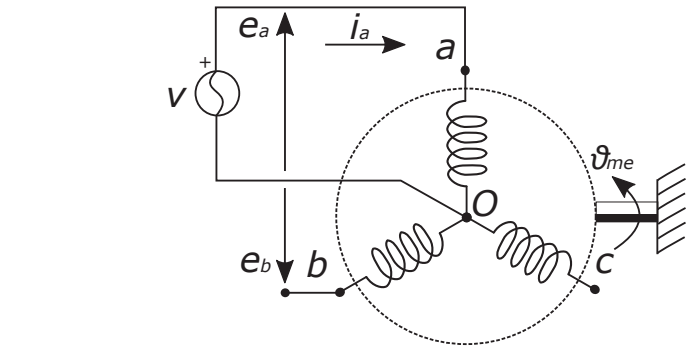

(a) Strategy 1.

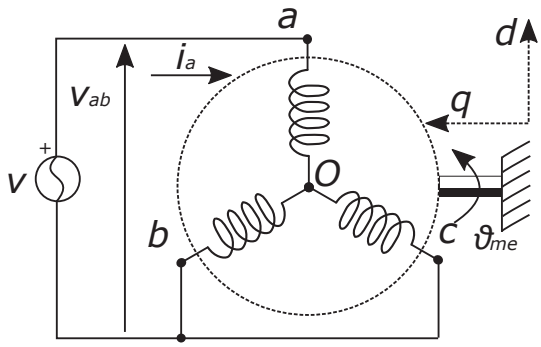

(b) Strategy 2, d-axis.

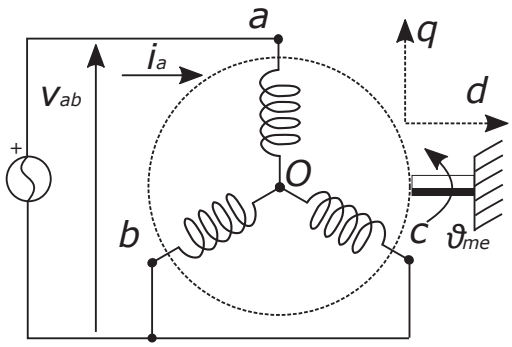

(c) Strategy 2, q-axis.

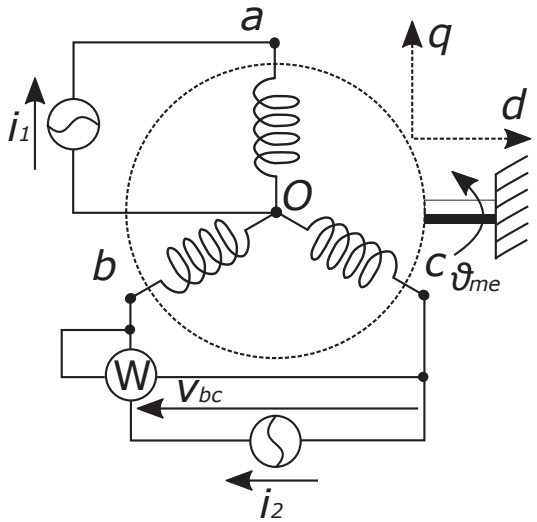

(d) Strategy 3, d-axis.

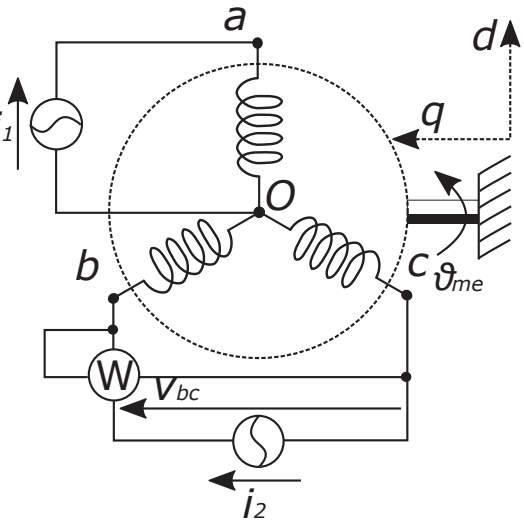

(e) Strategy 3, q-axis.

Fig. 14.22: AC standstill methods.

Fig. 14.23(c) the test bench setup. Following the alignment of the d/q-axis the rotor is firmly clamped during the measurement. It is mandatory due to the torque generated when the current is applied along the q-axis. In Fig. 14.24 is reported the measured voltage and

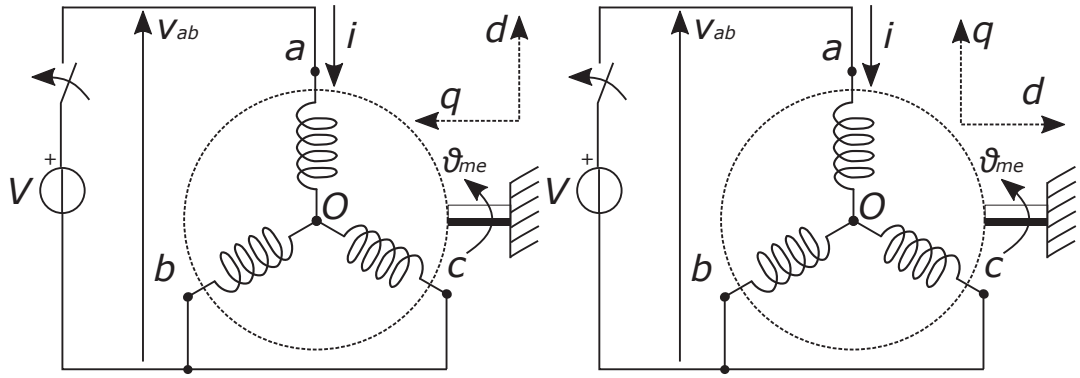

(a) d-axis. (b) q-axis.

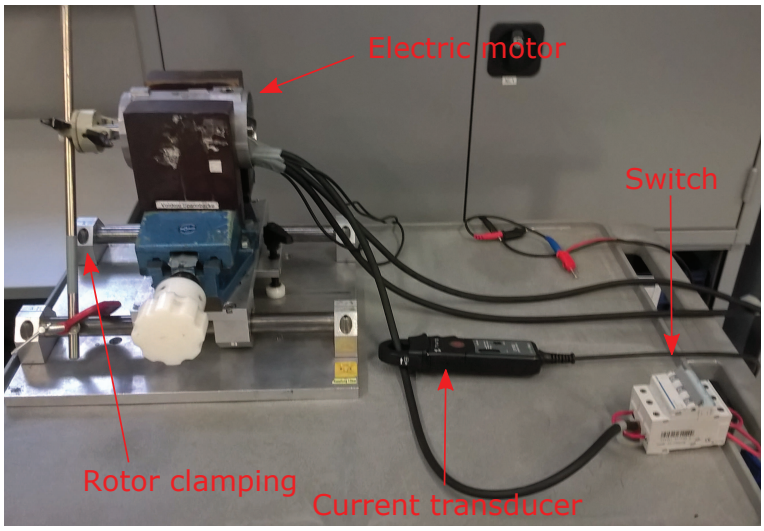

(c) Test bench setup.

Fig. 14.23: DC standstill method.

current transient for the C-shape motor. For each axis, the voltage is applied with direct and reverse the polarity, in order to measure the d/q-axis current and hence the motor parameters in the complete d/q-reference plane. The d/q-axis flux linkages, computed with (14.12), are compared with FEA simulations. They are reported in Fig. 14.25, for the reference, V-shape and C-shape machine, respectively. A dashed line band centered in the average value shows the maximum variation due to of the ripple. The PM contribution cannot be measured and it is therefore neglected for the d-axis. Finally, it is important to remind that:

- the measurement methodology cannot take into account the ripple d/q-axis flux linkage. On the other hand its negligible impact can provide a accurate indication of the average value.
- the measurement does not take into account the cross saturation since the machine is

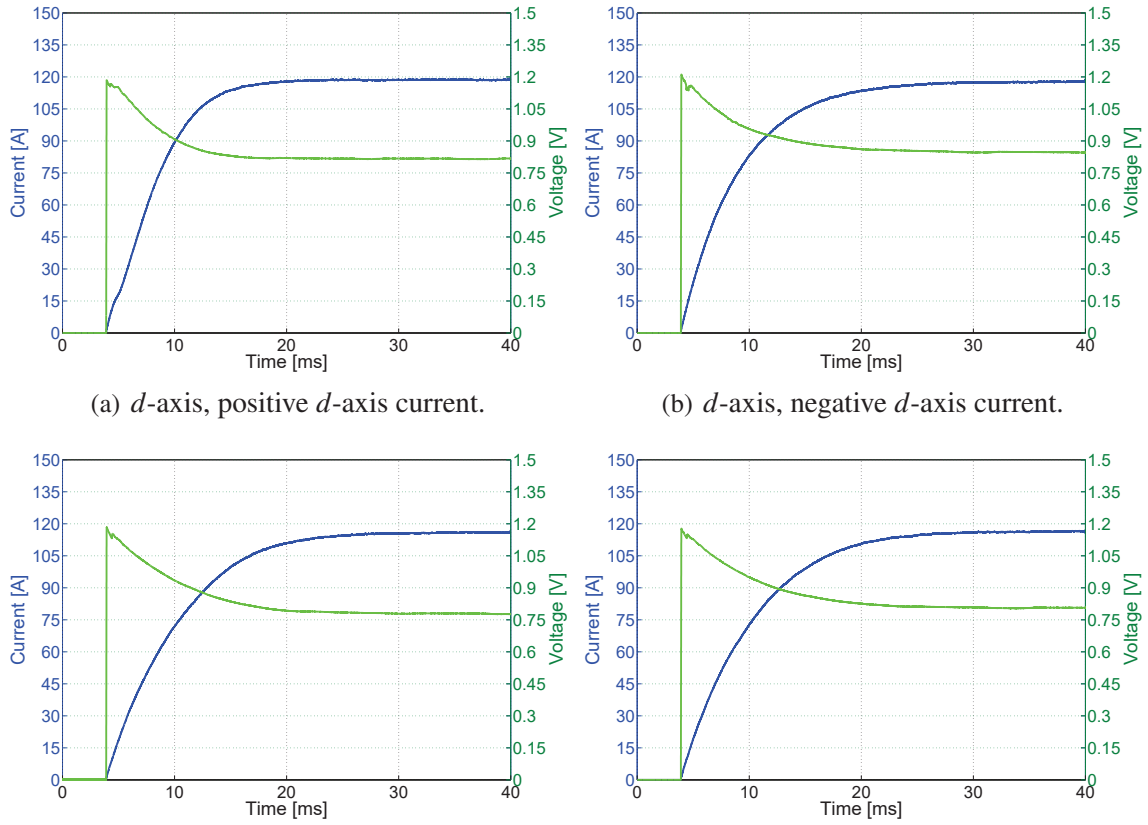

(a) d-axis, positive d-axis current.

(b) d-axis, negative d-axis current.

(c) q-axis, positive q-axis current.

(d) q-axis, negative q-axis current.

Fig. 14.24: Measured voltage and current transient, C-shape motor.

is fed alternately on the two axis.

A piecewise function, computed by means of the MLR previously discussed, has been used to approximate the d/q-axis flux linkage in the measured current range and to extrapolate the trend beyond the maximum measured current ($\sim 116A$ DC, equivalent to $\sim 82A_{RMS}$).

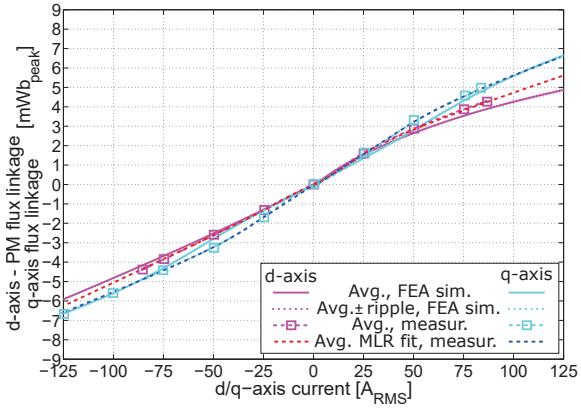

(a) Reference motor: d/q-axis flux linkages.

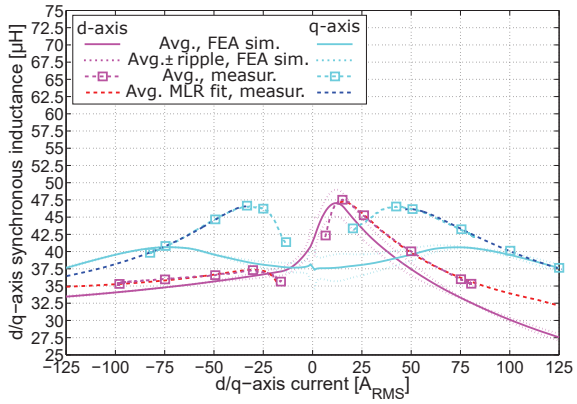

(b) Reference motor: d/q-axis synchronous inductances.

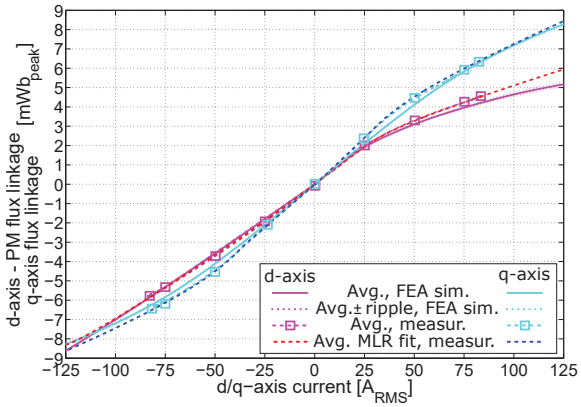

(c) V-shape motor: d/q-axis flux linkages.

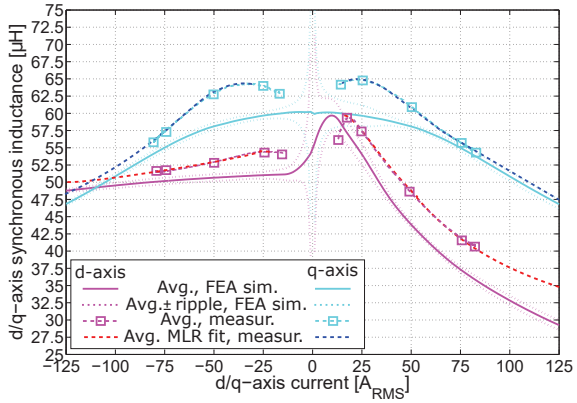

(d) V-shape motor: d/q-axis synchronous inductances.

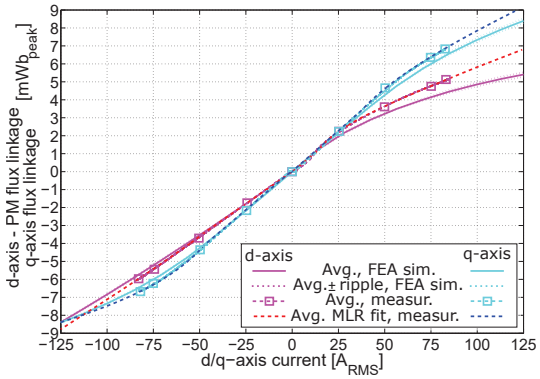

(e) C-shape motor: d/q-axis flux linkages.

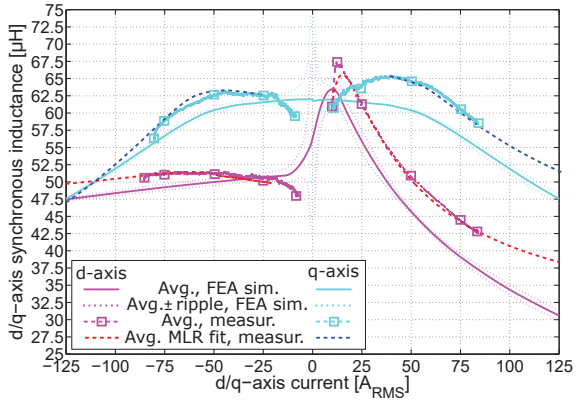

(f) C-shape motor: d/q-axis synchronous inductances.

Fig. 14.25: Measurement and FEA simulation of the d/q-axis flux linkages and synchronous inductances, no cross-saturation.

Table 14.6 summarizes the comparison between the measurements of the motor parameters evaluated by means of the methodologies proposed before, which neglects the cross saturation. In general a good agreement between FEA computation and measurement is achieved. A good agreement is achieved between the measurements and FEA simulations. A higher discrepancy is found in high current range, in particular when $I_d > 0$, in the saturation area. This phenomena could be explainable by the contribution of the end winding inductance, which cannot be computed by means of 2D FEA simulation. On the other hand, in FSCW machines the end winding leakage path (i.e. end winding inductance) is normally negligible in comparison of the active length, due the lower end winding length of the conductors. In fact, from an analytical estimation [148], the end winding inductance is,

$$L_{\sigma ew} = 0.35 \cdot \mu_0 \cdot 2 \cdot p \cdot {n_{cs}}^2 \cdot q^2 \cdot L_{ew} \tag{14.37}$$

On the basis of the calculated average end winding length L_{ew} equal to $18.6mm$ and $17.8mm$ for the reference and C/V-shape machine, respectively. Therefore the end winding inductances result $0.6\mu H$ and $0.8\mu H$ for the reference and C/V-shape motor, respectively. It is expected therefore a negligible impact of the end winding inductance to the total value.

Comparison with 3D FEA simulation: influence of the parasitic effects

In order to evaluate in an accurate way the contribution of these parasitic effects, a 3D FEA analysis has been performed. Fig. 14.26 report the comparison between the measured flux linkage (MLR approximated piecewise function) and the FEA computation. The 2D calculation is reported as well. A better agreement with the measure is achieved. Finally, Table 14.6 shows the comparison between the measurements and FEA simulations 2D/3D of the PM flux linkage, d/q-axis synchronous inductance, neglecting the cross saturation.

(a) Reference motor: d/q-axis flux linkages.

(b) Reference motor: d/q-axis synchronous inductances.

(c) V-shape motor: d/q-axis flux linkages.

(d) V-shape motor: d/q-axis synchronous inductances.

(e) C-shape motor: d/q-axis flux linkages.

(f) C-shape motor: d/q-axis synchronous inductances.

Fig. 14.26: Measurement and 2D/3D FEA simulation of the d/q-axis flux linkages and synchronous inductances, no cross-saturation.

Table 14.6: Motor parameters. $*^1$ at the base point, neglecting cross saturation (room temperature $30°C$).

		Reference	V-shape	C-shape	Unit
PM flux linkage	Measur.	6.65	6.97	6.48	
	FEA sim. 2D	6.98	7.30	7.01	mWb_{peak}
	FEA sim. 3D				
	Var. to FEA 2D/3D	-4.7	-4.5	-7.6	%
d-axis synchronous inductance $*^1$	Measur.	38.1	54.4	50.5	
	FEA sim. 2D	37.9	51.1	50.7	μH
	FEA sim. 3D				
	Var. to FEA 2D/3D	0.5	6.5	-0.4	%
q-axis synchronous inductance $*^1$	Measur.	40.7	55.8	56.7	
	FEA sim. 2D	39.6	51.4	52.5	μH
	FEA sim. 3D				
	Var. to FEA 2D/3D	2.8	8.6	8.0	%

14.4.3 Cogging torque

The cogging torque is computed at low speed ($30rpm$). The friction torque, which represents the average value of the measurement, has been extracted. In order to detect any faults of the bearings / housing coupling, the measurements have been carried out in both the rotational directions, clock-wise (cw) and counter-clock-wise (ccw).

Fig. 14.27 report the cogging torque vs. the angular position (mechanical) and the related harmonic spectra for the machines. The main results are summarized in 14.7. Comparing to the FEA simulations, the measurements show a remarkable increase of the cogging torque for all the machines up to 15 times the simulated value. This phenomena, which is investigated in the following chapter, is induced by manufacturing issues in the stator, rotor and PMs. In fact, besides the natural harmonic components, which are multiple of the $LCM(Q, 2 \cdot p) = LCM(12, 10) = 60$, additional harmonic components arise and they can be summarized in [69, 70, 94, 185]:

- harmonic orders multiple of $2 \cdot p = 10$ (10, 20,...) whenever they are induced by imperfections in the stator.
- harmonic orders multiple of the $Q = 12$ (23, 24, ...) if they are caused by faults in the PMs.

It is worth noticing the dominant contribution of the 10^{th} order which highlight clear issues in the stator package. The second prevalent harmonic order is represented by the 12^{th},

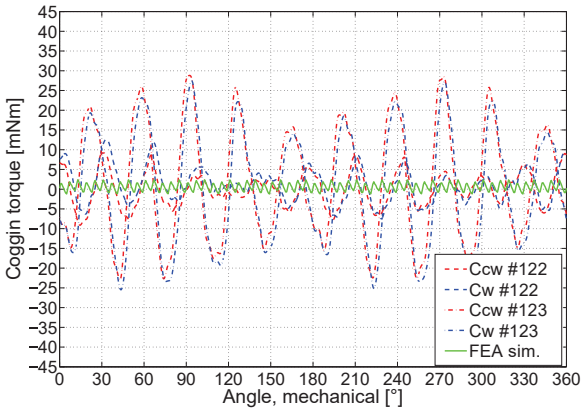

(a) Reference motor: waveform.

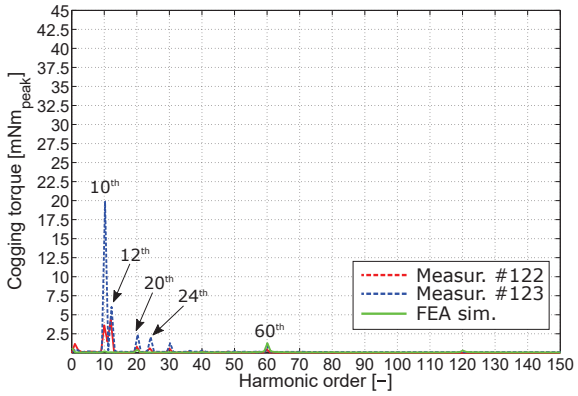

(b) Reference motor: harmonic spectrum (average of ccw and cw).

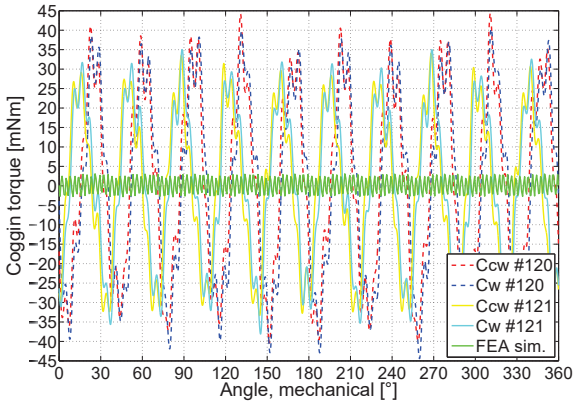

(c) V-shape motor: waveform.

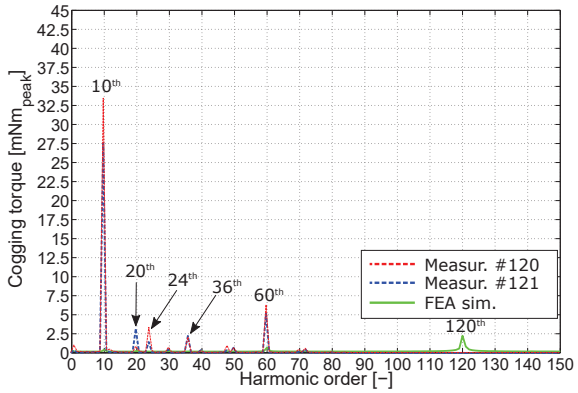

(d) V-shape motor: harmonic spectrum (average of ccw and cw).

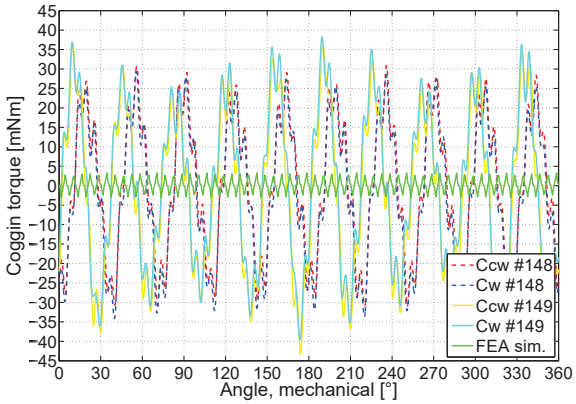

(e) C-shape motor: waveform.

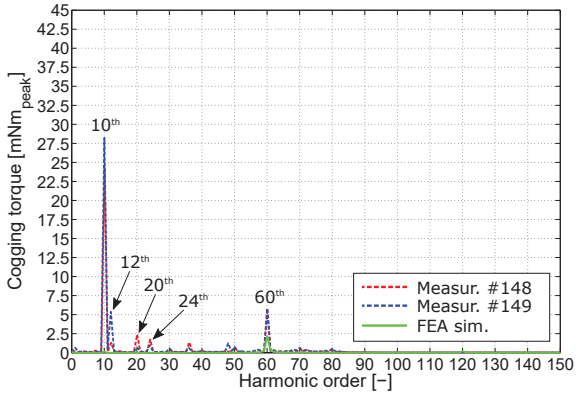

(f) C-shape motor: harmonic spectrum (average of ccw and cw).

Fig. 14.27: Measurement and FEA simulation of the cogging torque (room temperature 30°*C*).

which highlight imperfections in the rotor PMs. For the reference motor, the highest 12^{th} harmonic order has been found: this is justified by the higher inhomogeneity of the PM magnetization along the rotor, as shown in Fig. 14.9. It is worth noticing that, for the V-shape topology, this contribution is shifted to the 24^{th} and 36^{th} order. On the other hand, these discrepancies between measurements and FEA simulations are enhanced for the C/V-shape motor topology than those in the reference machine.

Table 14.7: Comparison of the measurement and FEA simulation of the cogging torque (room temperature $30°C$).

	Reference			**V-shape**			**C-shape**			
	Meas. #122	**Meas. #123**	**FEA**	**Meas. #120**	**Meas. #121**	**FEA**	**Meas. #148**	**Meas. #149**	**FEA**	**Unit**
Cogg. torque peak-peak	19.2	52.4	3.78	84.7	70.0	5.30	62.7	79.2	6.33	mNm
Var. to FEA	408	1286	0	1498	1221	0	891	1151	0	%
Harm. order										
10^{th}	3.60	19.8	0	33.4	27.6	0	24.2	28.2	0	mNm_{peak}
12^{th}	4.36	5.94	0	0.43	0.11	0	1.28	5.34	0	mNm_{peak}
20^{th}	0.81	2.32	0	0.80	3.21	0	2.35	0.66	0	mNm_{peak}
24^{th}	0.60	1.99	0	3.30	1.45	0	1.70	0.97	0	mNm_{peak}
60^{th} **(fund.)**	0.41	0.78	1.22	6.27	5.17	0.54	5.73	5.81	2.16	mNm_{peak}
Var. to FEA	−66.4	−36.1	0	1061	857	0	1653	1690	0	%

14.4.4 Friction torque

The friction torque in a electric motors is generally difficult to estimate analytically. At a given speed Ω_m, it can be described by the follow equation [165]:

$$T_f = T_f + T_v + T_d \tag{14.38}$$

where:
- T_c is the dynamic friction (or Couluomb torque);
- T_v is the viscous friction torque;
- T_d is the drag (or ventilation torque;

The Coulomb torque is not dependent of the speed, therefore it is equal to a constant K_c,

$$T_c = K_c \tag{14.39}$$

Generally constant torque is exhibited by the brushes of the motor.
The viscous friction torque is linearly function of the speed, as follows,

$$T_v = K_v \cdot \Omega_m \tag{14.40}$$

It is mainly caused by the friction of the bearings and its contribution depends on the typology (sleeve, ball, roller, etc.), their material, friction coefficient, clearances, lubricant's viscosity and temperature.
The drag or ventilation torque can be analytically estimated for simple geometries such as cylinder and disks using coefficients evaluated by means of experimental tests [1, 106, 145, 176, 178, 183]. The resistance torque of a rotating cylinder enclosed in a hollow structure is,

$$T_v = C_f \cdot \pi \cdot \rho_{air} \cdot \Omega^2 \cdot (0.5 \cdot D_r)^4 \cdot L_{stk} \tag{14.41}$$

where C_f is the air friction coefficient. Finally, in the equation the torque is function to the speed squared and it is neglected the contribution to the friction of the front and back side of the rotor. The coefficient C_f depends upon the surface condition and it is defined by,

$$C_f = \frac{\tau_{air}}{\frac{1}{2} \cdot \rho_{air} \cdot u^2} \tag{14.42}$$

where τ_{air} is the rotor shear stress and u is the fluid tangential velocity. These factors are of difficult evaluation and they are significantly dependent of the condition of the air flow which can be classified in laminar or turbulent. The condition of the flow in the airgap is defined by the Couette-Reynolds and Taylor numbers [105] equal to,

$$\begin{cases} Re_\delta = \dfrac{g \cdot \rho_{air} \cdot \Omega_m \cdot D_r}{2 \cdot \mu_{air}} & \text{(14.43a)} \\ T_a = {Re_\delta}^2 \cdot \dfrac{2 \cdot g}{D_r} & \text{(14.43b)} \end{cases}$$

Where $\mu_{air} = 1.821 \cdot 10^{-5} kg/(m \cdot s)$ is the dynamic viscosity of air at the ambient temperature. Taylor vortices appears when $T_a > 1700$. Different analytical methodologies are used for their evaluation. They are summarized in the following list:

- Yamada (1962) calculated the friction torque between concentric cylinders where the inner cylinder is in motion. He considered for his tests both smooth and grooved surfaces, speed in the range $90-5000rpm$ and for the medium he used water and spindle oil. Neglecting the axial flow, according to his work,

$$\frac{1}{\sqrt{2\cdot C_f}} = 7.54 + 11.5\cdot log\left(Re_\delta \cdot \sqrt{(2\cdot C_f)}\right) \tag{14.44}$$

  Rearranging (14.44), it results,

$$C_f = \frac{0.0152}{{Re_\delta}^{0.24}} \rightarrow 800 < Re_\delta < 6\cdot 10^4 \tag{14.45}$$

  Eq. (14.45) underestimates the actual losses and this spread increases as the airgap g. This is due the presence of circular fluid flow in the airgap, called Taylor vortices.
- Bilgen & Boulus (1973) performed measurement considering speeds in the range $300-1500rpm$ while water and water-glycerine as medium. They developed, using their results and previous works of other authors, the following equations,

$$\begin{cases} C_f = 0.515\cdot \dfrac{\left(\dfrac{2\cdot g}{D_r}\right)^{0.3}}{{Re_\delta}^{0.5}} \rightarrow 500 < Re_\delta < 10^4 & \text{(14.46a)} \\ C_f = 0.0325\cdot \dfrac{\left(\dfrac{2\cdot g}{D_r}\right)^{0.3}}{{Re_\delta}^{0.2}} \rightarrow Re_\delta > 10^4 & \text{(14.46b)} \end{cases}$$

The friction torque has been evaluated performing no load test of the machine with speed from 0 to $6000rpm$ and measuring the torque. An accurate evaluation of this contribution requires a test with an un-magnetized PMs [140], not feasible at this stage, a FEA simulation has been performed in order to segregate the iron losses and to obtain a good estimation of the mechanical losses as a function of the speed.
Fig. 14.28 reports the measured torque, cumulative of the mechanical and iron losses, and the predicted friction torque. Finally, a 2^{nd} order fitting function has be used to conveniently represent the trend of the friction torque for the calculation of the electromechanical performance, according to the theory presented above. The coefficients of the fitting function are reported in Table 14.10.

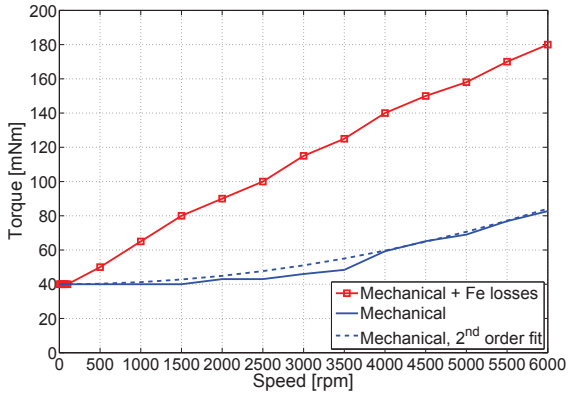

(a) Reference motor.

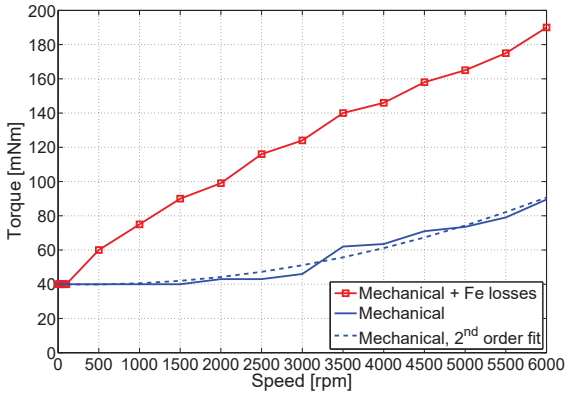

(b) V-shape motor.

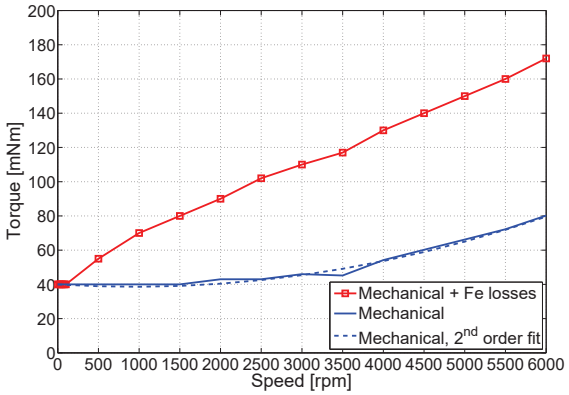

(c) C-shape motor.

Fig. 14.28: Friction and ventilation torque. Measured torque uncertainty: $\pm 3mNm$

Table 14.8: Coefficient of polynomial equation $T_{ml} = a_0 + a_1 \cdot \Omega_m + a_2 \cdot {\Omega_m}^2$

	Reference	**V-shape**	**C-shape**	**Unit**
a_0	0.04	0.04	0.04	Nm
a_1	0	0	0	Nm
a_2	1.492	1.444	1.456	$10^{-7}(Nm \cdot s^2)/rad$
C_f	1.616	2.964	2.988	–

14.4.5 Torque vs. current angle

The average torque and torque ripple have been measured at the rated current $100A_{RMS}$ varing the commutation angle between $0-90°$. Fig. 14.29 reports the comparison between the measurements and FEA simulations. The torque ripple band is also highlighted by means of the dashed lines.

As regards the average torque, a good agreement with the experimental results is achieved

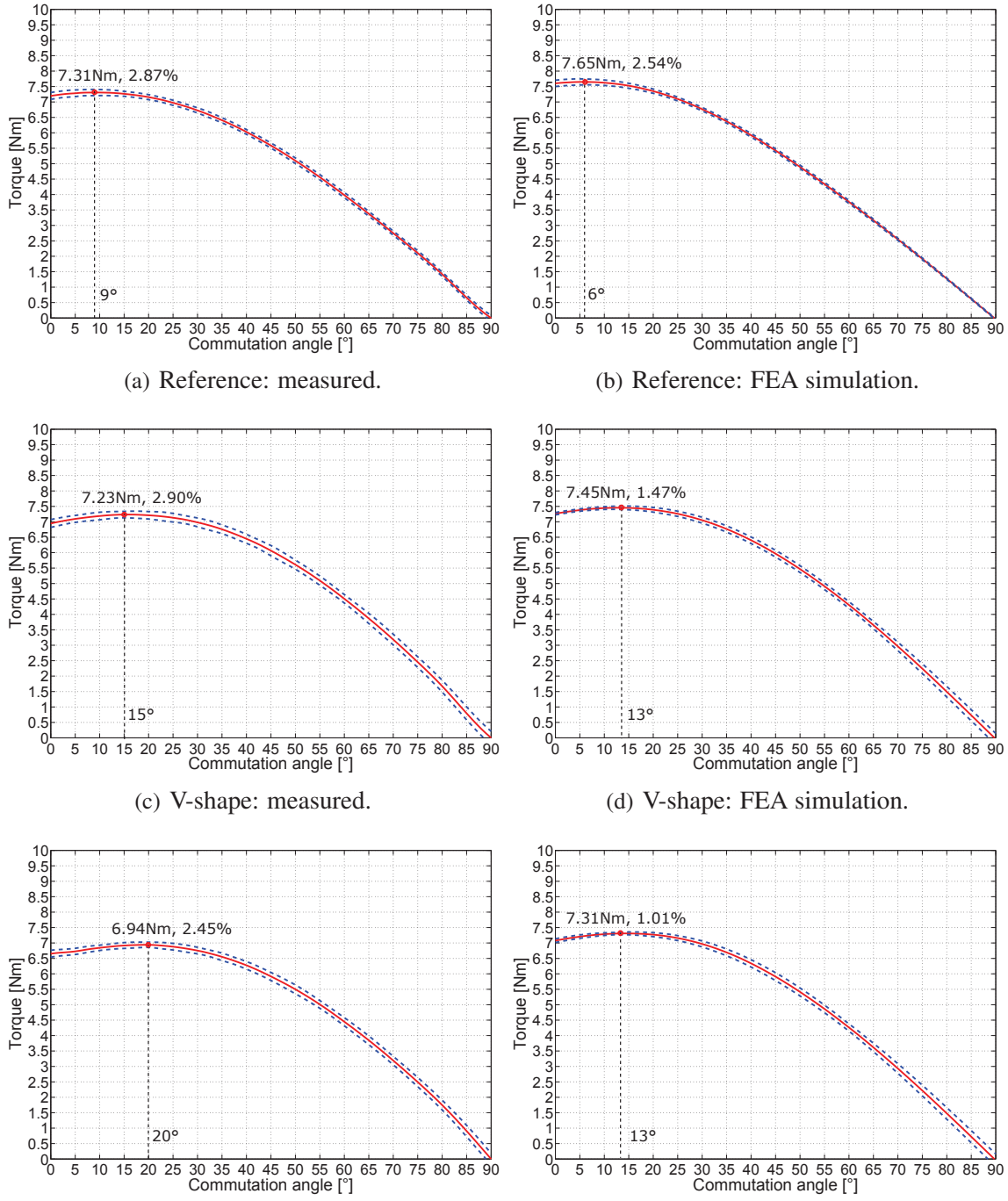

(a) Reference: measured.

(b) Reference: FEA simulation.

(c) V-shape: measured.

(d) V-shape: FEA simulation.

(e) C-shape: measured.

(f) C-shape: FEA simulation.

Fig. 14.29: Average torque as a function of the commutation angle, rated load $100A_{RMS}$. The dashed lines highlight the maximum distortion due to the torque ripple (operating temperature $30°C$).

with a difference in the order of $3-4\%$ for the reference and V-shape design. As mentioned before, due to the incomplete magnetization of the PMs, the discrepancy with the FEA

simulations increases for the C-shape motor. For this design, the base current angle is significantly higher than the simulated one, for more than 50%. This highlight the weaker contribution of the PM to the torque production.

The rated torque ripple, at the base point, is comparable among the designs, with lowest value achieved by the C-shape design of about 2.45%. On the other hand, the results are significantly different than the simulations, up to 2 times higher. In order to investigate this phenomenon, further measurements have been carried out and discussed in following section.

Table 14.9: Torque measurement along the MTPA locus.

	Reference		**V-shape**		**C-shape**		**Unit**
	Meas.	FEA	Meas.	FEA sim.	Meas.	FEA	
25% rated load - $25A_{RMS}$							
Average torque	1.76	1.82	1.86	1.90	1.76	1.82	*Nm*
Torque ripple	0.06	0.036	0.13	0.027	0.10	0.027	*Nm*
Torque ripple %	3.41	1.98	6.99	1.42	5.68	1.48	%
Commutation angle	1	0	3	3	1	6	°
50% rated load - $50A_{RMS}$							
Average torque	3.59	3.74	3.73	3.83	3.55	3.71	*Nm*
Torque ripple	0.09	0.105	0.17	0.085	0.13	0.074	*Nm*
Torque ripple %	2.51	2.81	4.56	2.22	3.66	1.99	%
Commutation angle	2	0	4	4	4	6	°
75% rated load - $75A_{RMS}$							
Average torque	5.47	5.73	5.49	5.71	5.30	5.57	*Nm*
Torque ripple	0.12	0.176	0.25	0.124	0.16	0.115	*Nm*
Torque ripple %	2.19	3.07	4.55	2.17	3.02	2.06	%
Commutation angle	7	2	6	9	8	10	°
100% rated load - $100A_{RMS}$							
Average torque	7.31	7.65	7.23	7.46	6.94	7.31	*Nm*
Torque ripple	0.21	0.194	0.21	0.11	0.17	0.074	*Nm*
Torque ripple %	2.87	2.54	2.90	1.47	2.45	1.01	%
Commutation angle	9	6	15	13	20	13	°
125% rated load - $125A_{RMS}$							
Average torque	9.06	9.49	8.68	9.07	8.44	8.92	*Nm*
Torque ripple	0.23	0.230	0.30	0.186	0.24	0.171	*Nm*
Torque ripple %	2.54	2.42	3.46	2.05	2.84	1.92	%
Commutation angle	14	9	16	16	20	18	°

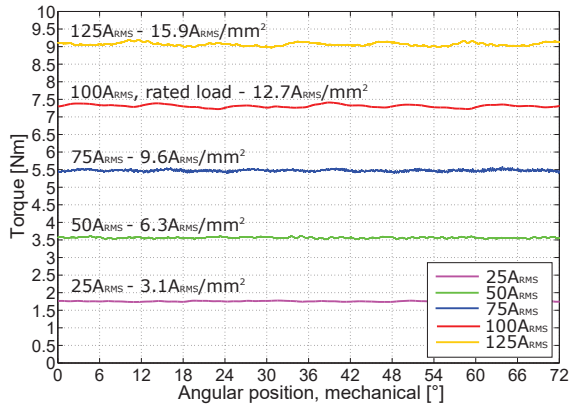

(a) Reference motor: measured torque vs. angular position, mechanical.

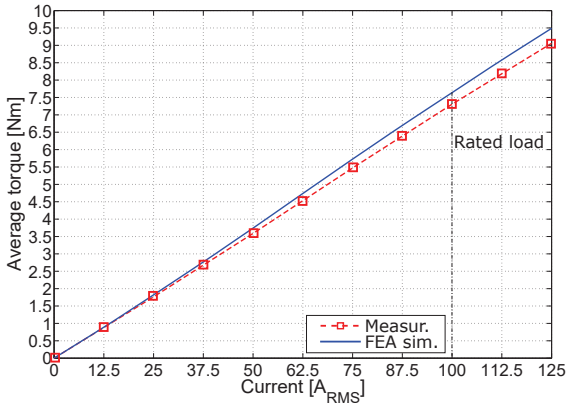

(b) Reference motor: torque vs. current.

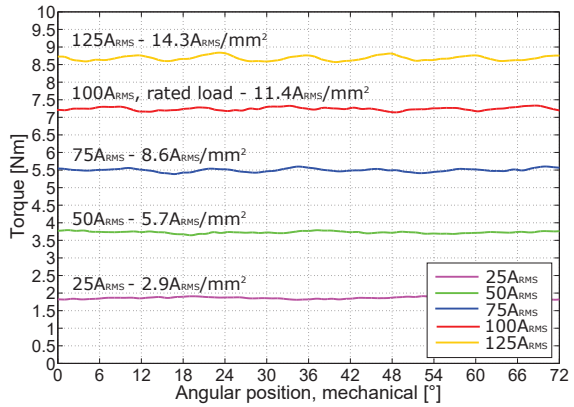

(c) V-shape motor: measured torque vs. angular position, mechanical.

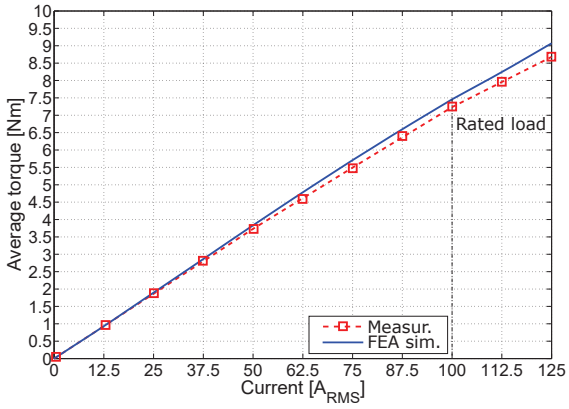

(d) V-shape motor: torque vs. current.

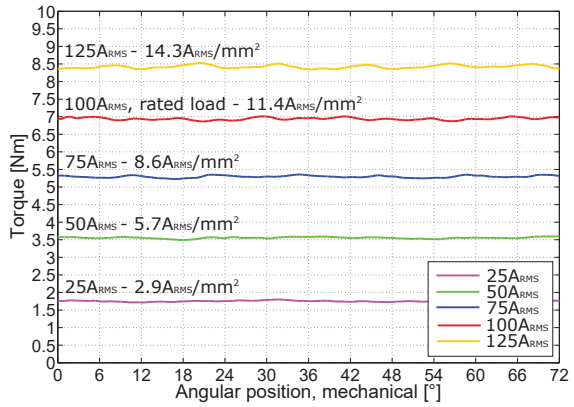

(e) C-shape motor: measured torque vs. angular position, mechanical.

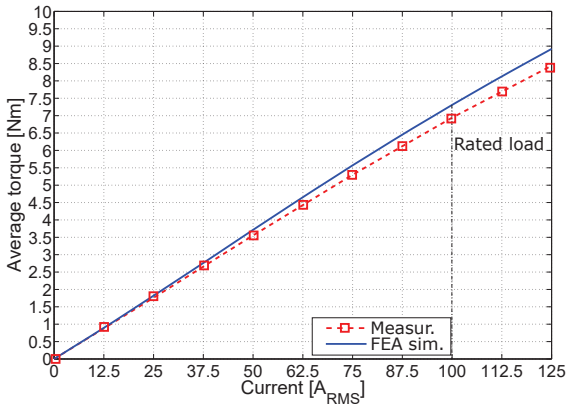

(f) C-shape motor: torque vs. current.

Fig. 14.30: Torque along the MTPA locus as a function of the current.

14.4.6 Torque and harmonic spectra

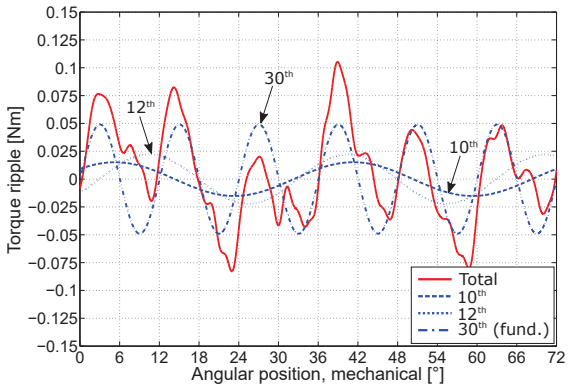

(a) Measurement.

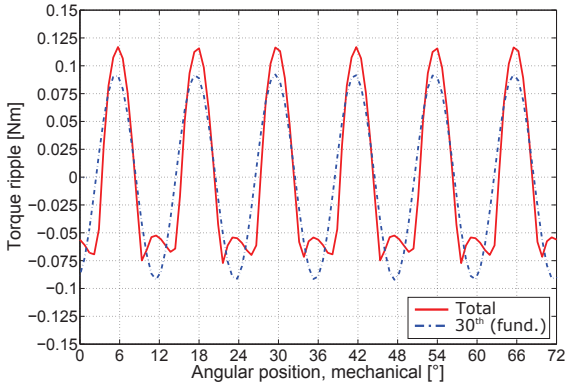

(b) FEA simulation.

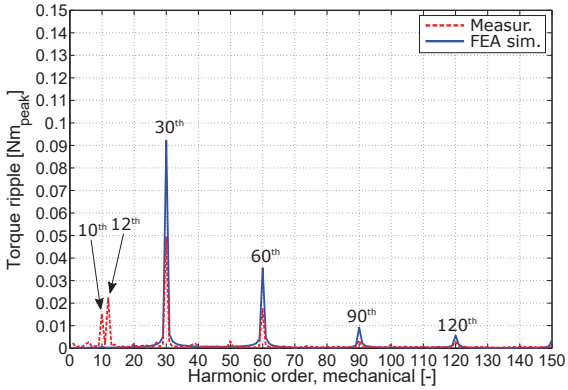

(c) Torque ripple vs. harmonic order.

Fig. 14.31: Reference motor, rated load: torque ripple.

In this section the further investigations have been performed on the torque harmonic spectrum for different loading conditions. In Figs. 14.30(a), 14.30(a), 14.30(e) the torque waveform as a function of the angular position (electrical) is reported for different loading conditions (25%, 50%, 75%, 100%, 125% of the rated current) along the MTPA locus for the machines.

There are no noticeable differences among the waveforms for the different loading conditions. Moreover a good agreement is achieved between the FEA simulations and the experimental results. According to the selected optimization criteria (constant active copper losses), at equal operating current, the current densities for the C/V-shape designs are 11% lower than the reference machine. Table 14.9 summarizes the average torque, torque ripple and commutation angle for each motor design.

Figs. 14.31, 14.32 show the harmonic analysis of the torque waveform at the rated current and the comparison with the FEA simulation for the machines. In Fig. 14.30(a), 14.30(c) 14.30(e) the waveform is reported for an electrical cycle in order to provide a clear representation of the torque oscillation. On the other hand, due to the effect of the 1^{st} harmonic order, the periodicity is not exact.

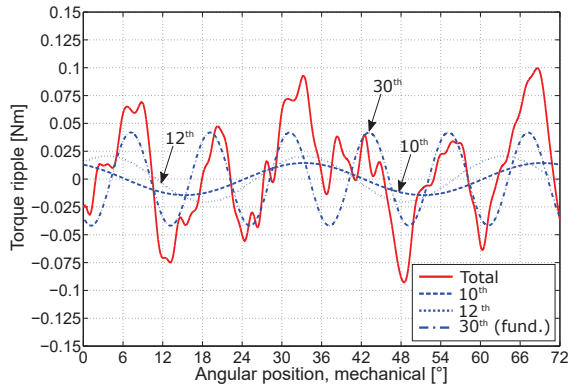

(a) V-shape motor: measurement.

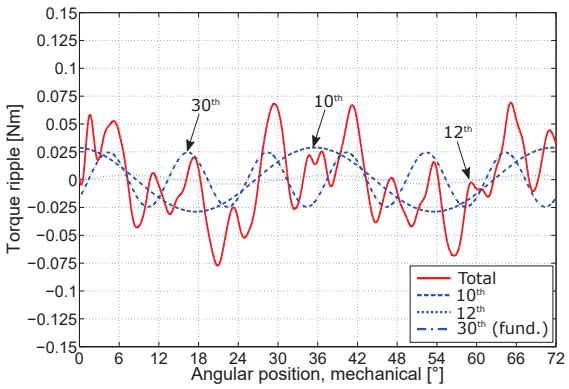

(b) C-shape motor: measurement.

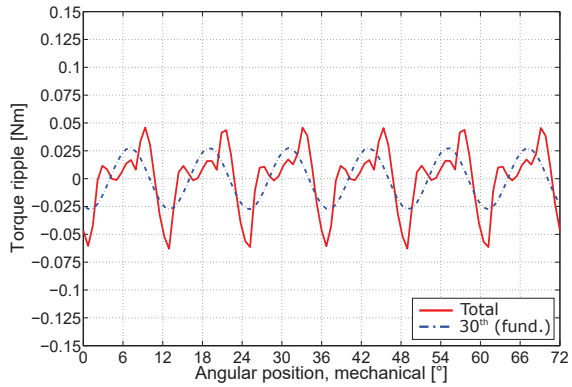

(c) V-shape motor: FEA simulation.

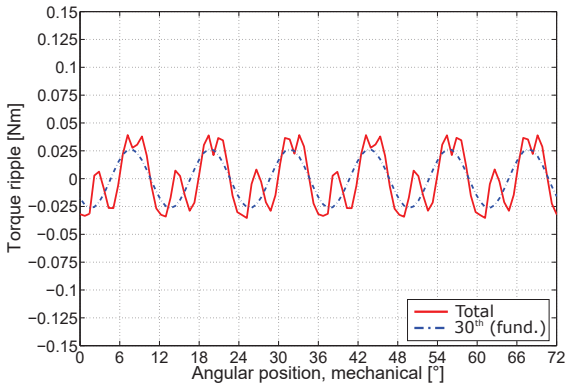

(d) C-shape motor: FEA simulation.

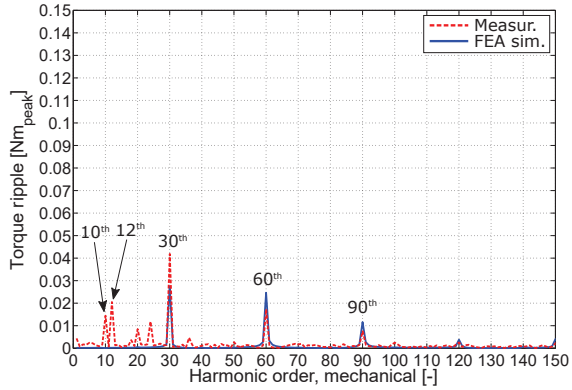

(e) V-shape motor: torque ripple vs. harmonic order.

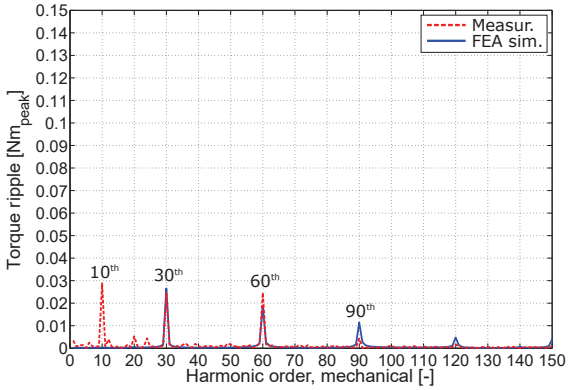

(f) C-shape motor: torque ripple vs. harmonic order.

Fig. 14.32: C/V-shape motor, rated load: torque ripple.

The main additional harmonic components, namely the 10^{th} and the 12^{th} order are highlighted. As noted for the cogging torque, the torque ripple waveform is heavily affected by these parasitic components with a magnitude comparable to the main natural harmonic (30^{th} order). It is worth noticing that:

- in the reference machine the main harmonic is overestimated.
- a good agreement between FEA simulation and experimental measurement of the natural harmonics for the C/V-shape motor is achieved.
- the 12^{th} harmonic order of the torque ripple arises in the V-shape motor although basically no 12^{th} order exists in the cogging torque. Viceversa for the C-shape motor.

The previous remarks could be justified, especially for the C/V-shape motor, by some imperfection during the disassembly and assembly operations of the motor carried out after the first round of measurements of the cogging torque.

The torque ripple harmonic spectra of the machines have been studied along the MTPA locus and as a function of the commutation angle.

Figs. 14.33(a), 14.33(c), 14.33(e) report the trend of the dominant measured harmonic components as a function of the current, evaluated along the MTPA locus. The comparison with FEA simulations are reported in Figs. 14.33(b), 14.33(d), 14.33(f). The following remarks can be done.

- Due to the impact of the stator saturation, the main harmonic torque ripple harmonics increases with the current. On the other hand while the reference machine exhibit a monotonic behavior, in the C/V-shape designs, the trend is not monotonic showing a local minimum in the area of the rated current ($100A_{RMS}$). At this current the machine has been optimized.
- The main additional harmonic component, due manufacturing imperfection in the stator (10^{th}), shows a different trend in the machines: it increases as the current increases in the reference machine, while it reduces as the current arises in the C/V-shape machines. This emphasized that the saturation in the C/V-shape motors tends to masks the effect of these imperfections at high electric loading. On the other hand the, 20^{th} order takes comparable amplitude of the 10^{th} at 125% of the rated current.
- The main additional harmonic component, due issues (12^{th}) in the PMs, has the same monotonic trend in the machines: its amplitude increase with the current following a linear relationship.

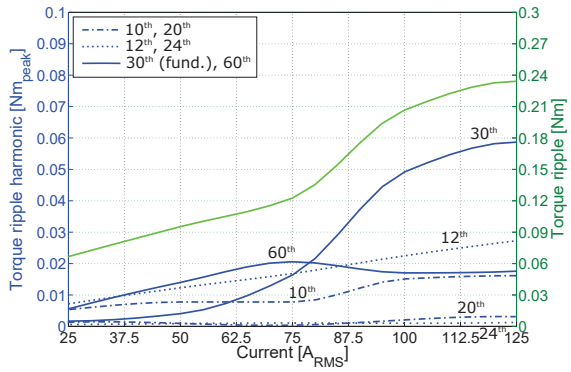

(a) Reference motor: measurement.

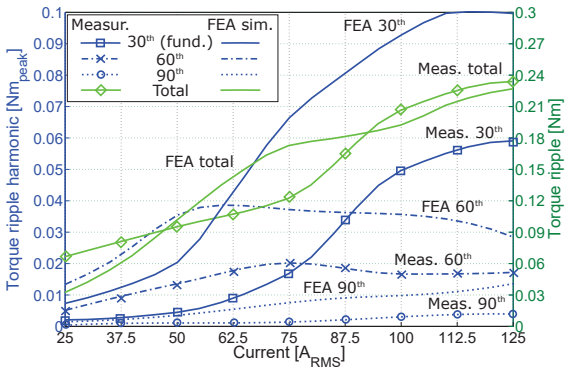

(b) Reference motor: measurement vs. FEA.

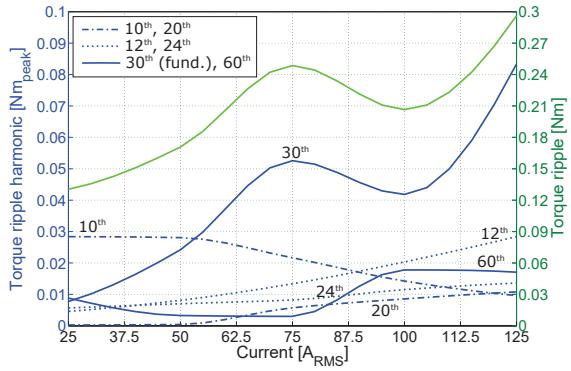

(c) V-shape motor: measurement.

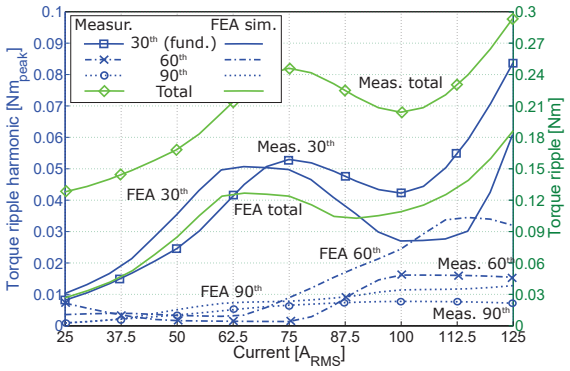

(d) V-shape motor: measurement vs. FEA.

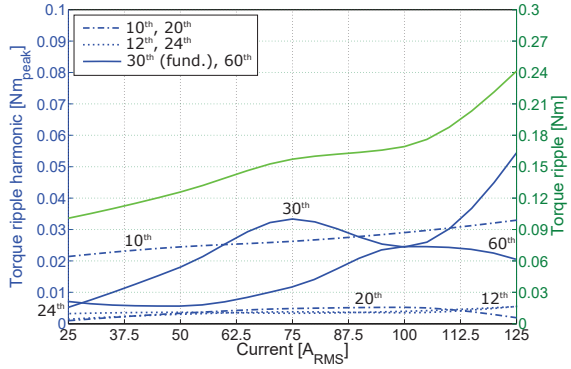

(e) C-shape motor: measurement.

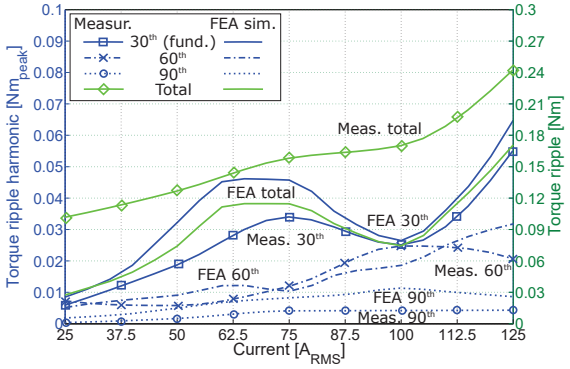

(f) C-shape motor: measurement vs. FEA.

Fig. 14.33: Torque ripple harmonic spectra as a function of the current in MTPA.

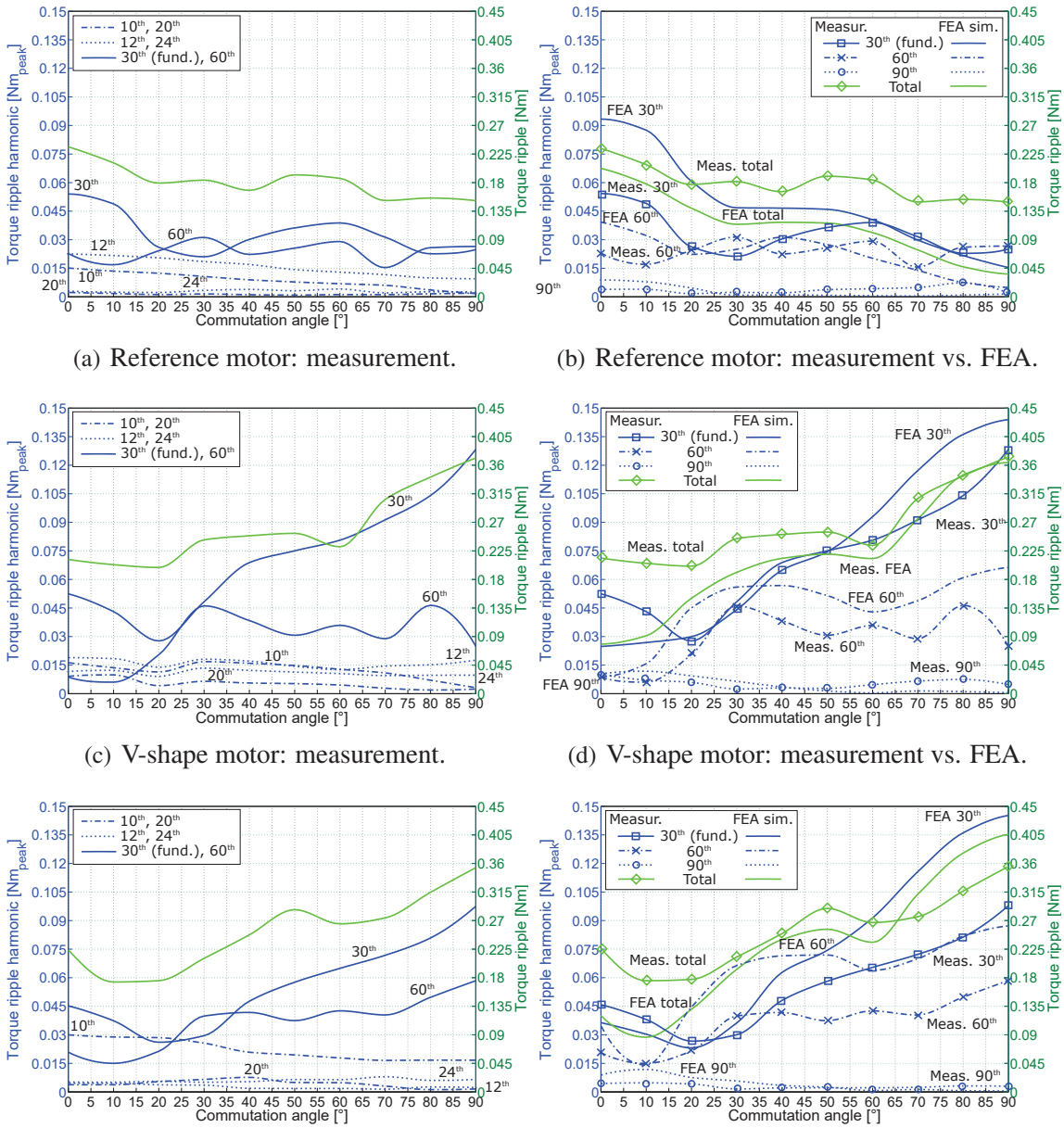

(a) Reference motor: measurement.

(b) Reference motor: measurement vs. FEA.

(c) V-shape motor: measurement.

(d) V-shape motor: measurement vs. FEA.

(e) C-shape motor: measurement.

(f) C-shape motor: measurement vs. FEA.

Fig. 14.34: Torque ripple harmonic spectra as function of the commutation angle.

Conversely, the behavior of the harmonic components as a function of the commutation angle in summarized in Figs. 14.34(a), 14.34(c), 14.34(e). The comparison with FEA simulation is is reported in Figs. 14.34(b), 14.34(d), 14.34(f). The trend harmonic components between the reference machine and C/V-shape motors exhibit noticeable differences The following remarks can be done as well.

- Thanks to the more effective shaping of the rotor poles, the reference motor shows an amplitude of the harmonics of the torque ripple witch decreases as the commutation angle increases. Conversely, it tends to increase, especially the fundamental 30^{th} order, in the C/V-shape motor designs, where the pole shaping is less evident.
- The overestimation of the natural torque ripple harmonics decreases with the commutation angle, therefore the inaccuracy might be influenced by the saturation in FW operation.
- No noticeable variations of the additional harmonic components with the commutation angle are found among the machines. This suggests that the variation of the iron saturation and PM working points due to the different current angle has a lower impact on such parasitic components.

14.4.7 Torque in the d/q-axis current plane

In Fig. 14.35 the measurements and FEA simulations of the average torque in the 2^{nd} quadrant (motor area) of the d/q-axis current plane is compared. The measurement has been performed up to a d/q-axis current of $110A_{RMS}$ with step of 10_{RMS}. For evaluating the torque in intermediate values, a 2D interpolation has been adopted. The rated current limit is highlighted in magenta.
A good agreement between the measurement and calculation is achieved in the complete working area for the reference and V-shape motors. As expected, higher discrepancy is found for the C-shape design, as discussed in the previous sections. As shown in Fig. 14.35(b), 14.35(c), it is clear the contribution of the reluctance torque to the torque production, in comparison to the reference machine. For this configuration, it is worth noticing as the gap between measurement and FEA simulations reduces as the d-axis current increases, due to the enhancement of the reluctance torque component for the total torque production.

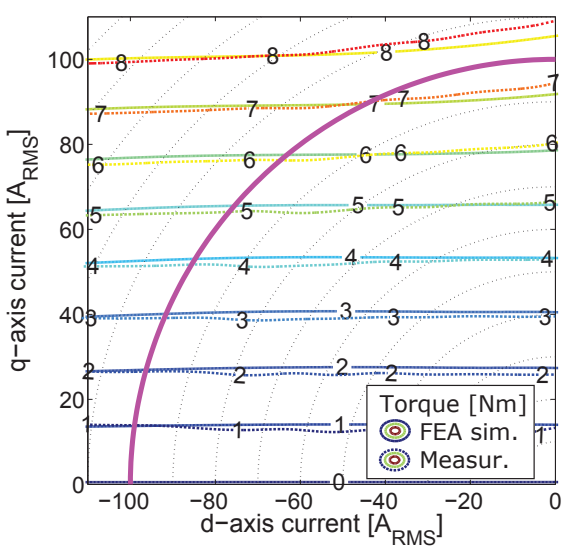

(a) Reference motor.

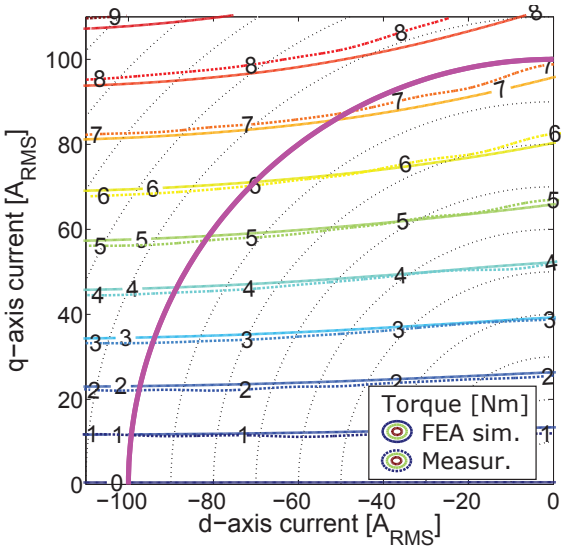

(b) V-shape motor.

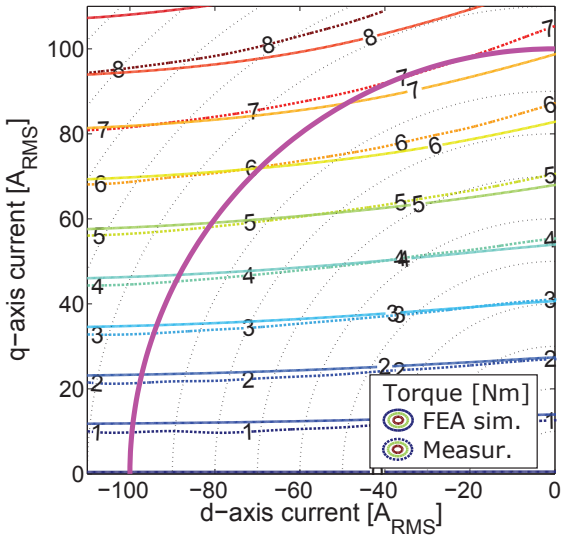

(c) C-shape motor.

Fig. 14.35: Average torque in the d/q-axis current plane, measurement vs. FEA simulation.

14.4.8 Electromechanical characteristics

In this section the main motor performance as a function of the speed are measured and compared with the FEA simulations. The measurement have been performed in steady state at different speed between $0-6000rpm$. Higher speed were not allowed by the hardware and software system. The measurement methodology is summarized below.

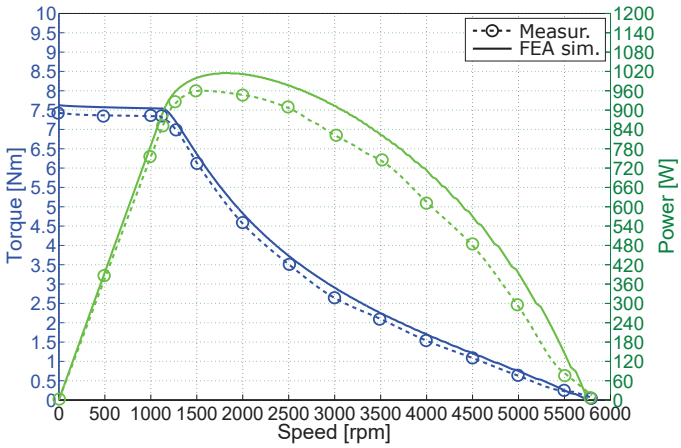

(a) Reference motor.

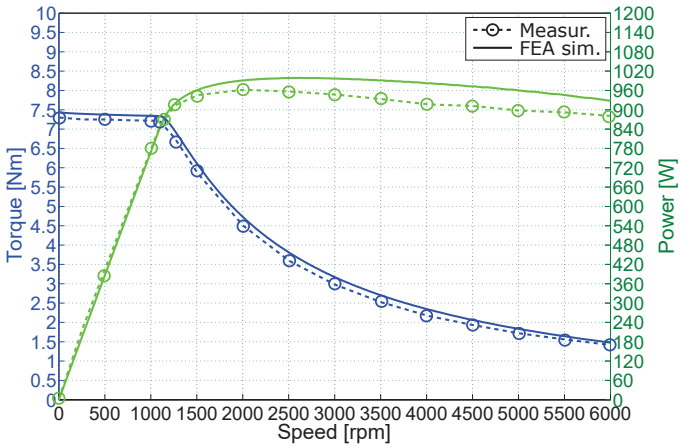

(b) V-shape motor.

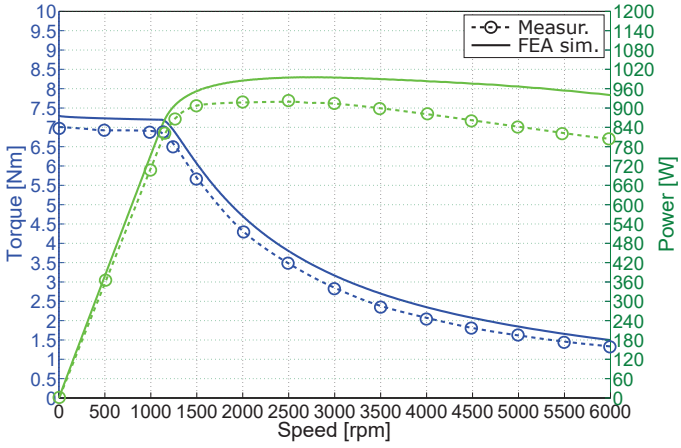

(c) C-shape motor.

Fig. 14.36: Torque vs. speed characteristic, measurement vs. FEA simulation.

For a given measured speed, the angle of the current space vector has been gradually increased up to value beyond which the control loop algorithm loses stability: in such condition it is not able to maintain null the error between the reference and the measured d/q-axis current. This working point represents therefore a point of the available working profile, in which all the electromechanical quantities can be evaluated. As regards the base and maximum speed (electrical limit, if exists, in the considered speed range), the procedure is reversed. The current space vector has been adjusted at the rated base current angle and at 180° (commutation angle 90°), respectively. At the same time the speed has been increased reaching the condition of instability of the control. This represents the measured speed for such operating points.

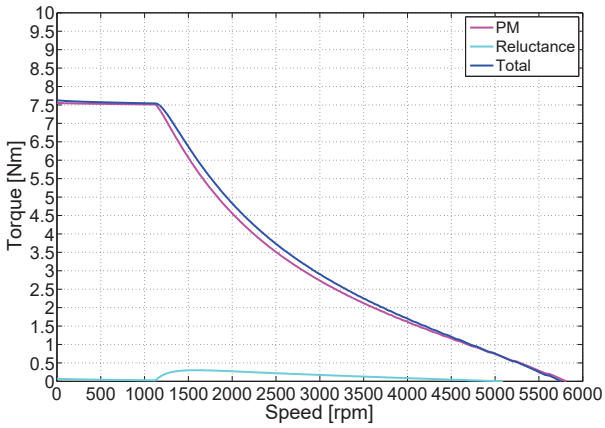

(a) Reference motor.

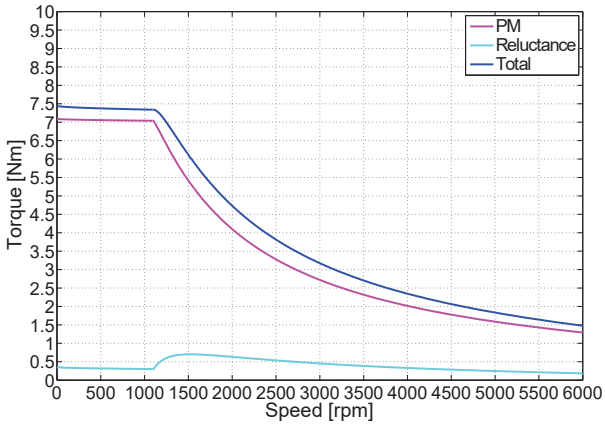

(b) V-shape motor.

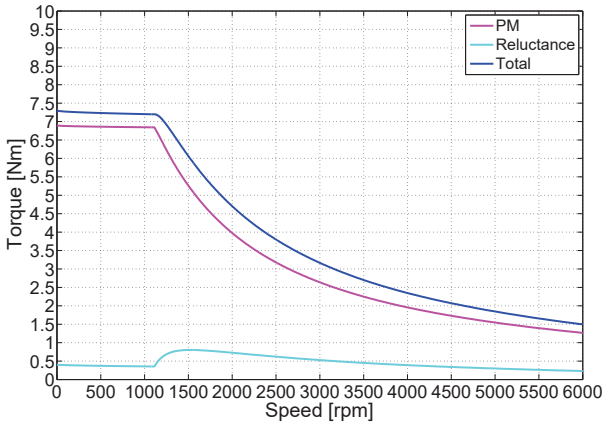

(c) C-shape motor.

Fig. 14.37: PM and reluctance torque vs. speed, FEA simulation.

Flux weakening performance

In Fig. 14.36 the measured torque vs. speed characteristics is reported and compared with the FEA simulations, showing a good agreement in the full speed range, in terms of average torque, base speed and maximum speed. It is worth noticing the extended CPSR exhibited by the C/V-shape designs in comparison to the reference machine. At $3500rpm$ the motor provides a torque and power 20% higher than those developed by the reference machine. While the measured FW range of the reference motor is slightly more than 5 times the base speed with a CPSR less than 2.5 times, the C/V-shape is predicted to deliver torque up to almost 15 times the base speed ($\sim 16000rpm$), with constant power available up to 7 times.

PM and reluctance torque

In Fig. 14.37 the contribution of the PM and reluctance torque is investigated. It is worth noticing the negligible contribution of the PM torque in the reluctance machine, especially in the constant torque region, predicted in the order of $0.03Nm$, 10 times lower than that exhibited by the C/V-shape configurations, $0.4Nm$ equal to about 6% of the total torque.
In Fig. 14.38 the distribution of the torque components in the torque vs. speed plane. The PM and reluctance torque are shown on the left and right side, respectively. The C/V-shape design provides a wider range where the reluctance torque is available, with a maximum value of about 3 times higher than the reference machine. Moreover, for the C/V-shape machines, the torque production takes advantage of the reluctance contribution starting from about 60% of the rated current, while it is negligible for the reference design.

Phase current and voltage

In Fig. 14.39 the predicted and measured trend of the d/q-axis phase current (left) and voltage (right) are reported, showing a good agreement between the measurement and simulations. For the C-shape design, a higher discrepancy in the constant torque is found due to the higher actual base commutation angle.

Power factor

The comparison between the measurements and FEA computation of the PF along the control trajectory is reported on the left side of Fig. 14.40. All the machines shows similar PF in constant torque region, with a higher value for the reference machine at the base speed (0.85 vs. 0.82). As discussed before, the enhanced FW performance of the C/V-shape machines yields to a quasi-constant PF, tending to the unity, from the base speed to the maximum speed. This is clearly reported on the right side of 14.40, where complete maps of the predicted PF constant loci in the torque vs. speed plane.

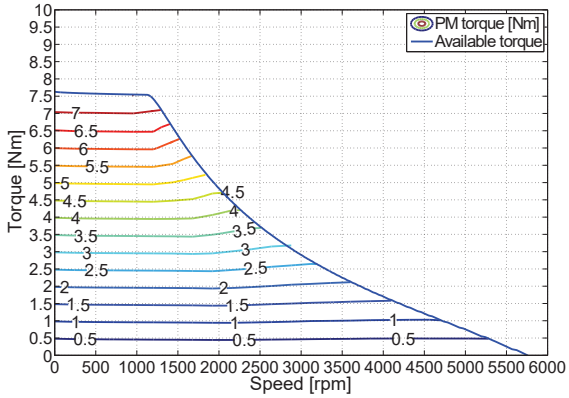

(a) Reference motor, PM torque.

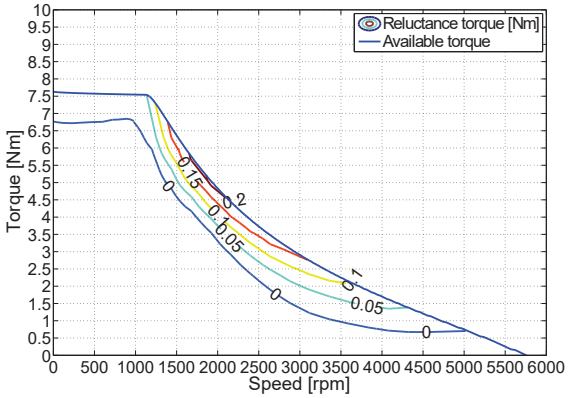

(b) Reference motor, reluctance torque.

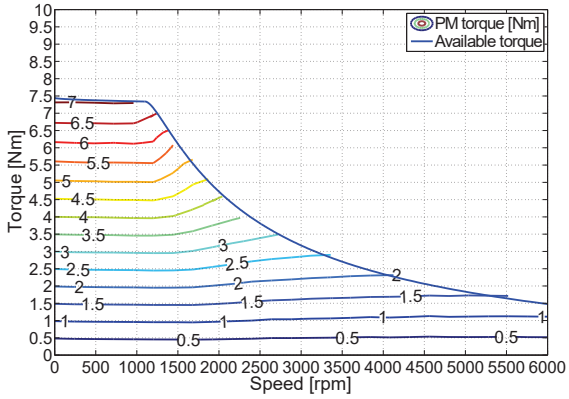

(c) V-shape motor, PM torque.

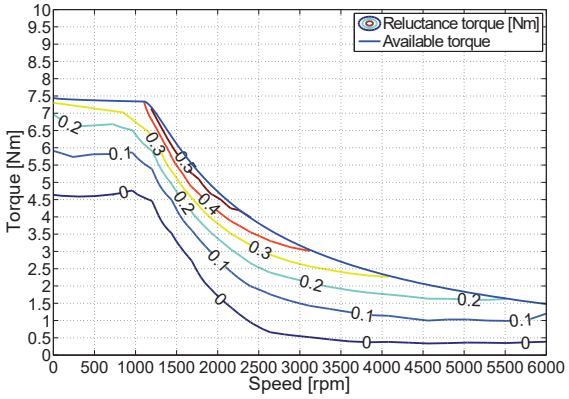

(d) V-shape motor, PM torque.

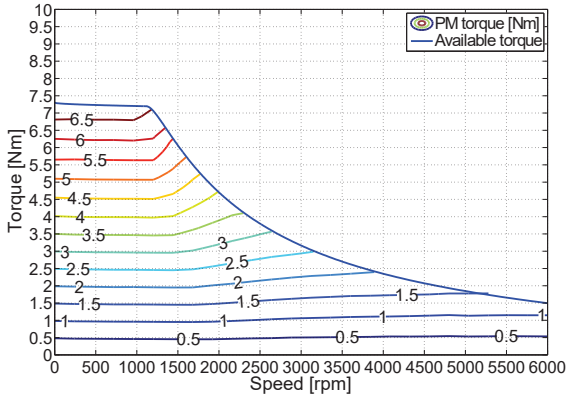

(e) C-shape motor, PM torque.

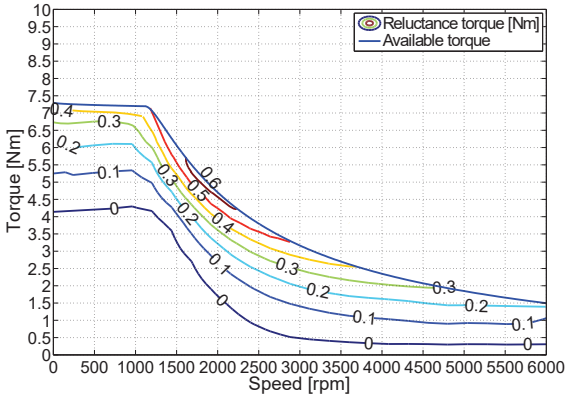

(f) C-shape motor, reluctance torque.

Fig. 14.38: PM and reluctance torque map in the torque-speed plane, FEA simulation.

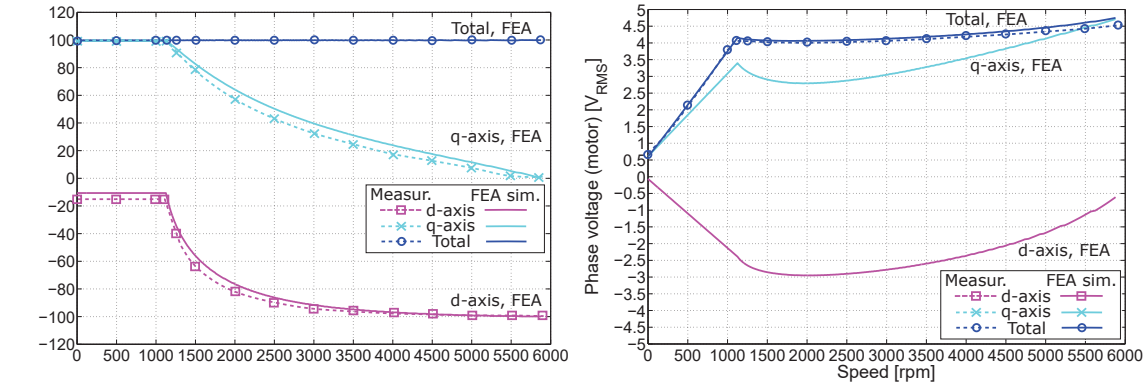

(a) Reference motor, current (b) Reference motor, voltage.

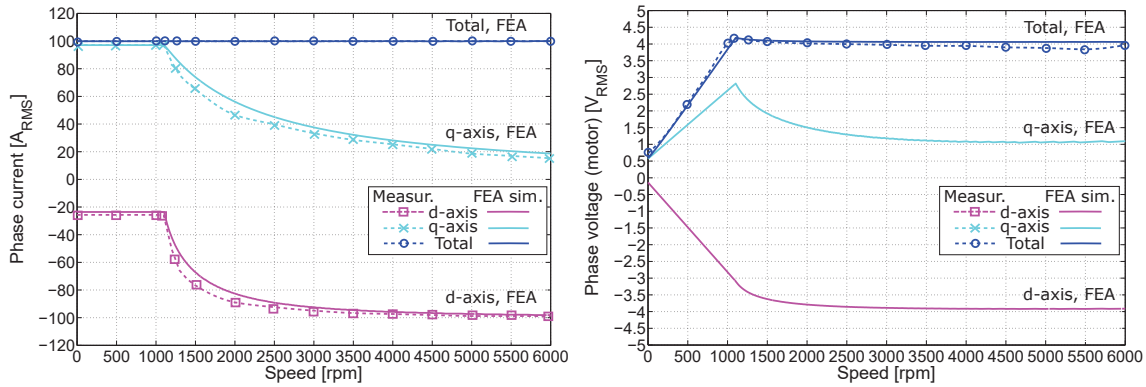

(c) V-shape motor, current. (d) V-shape motor, voltage.

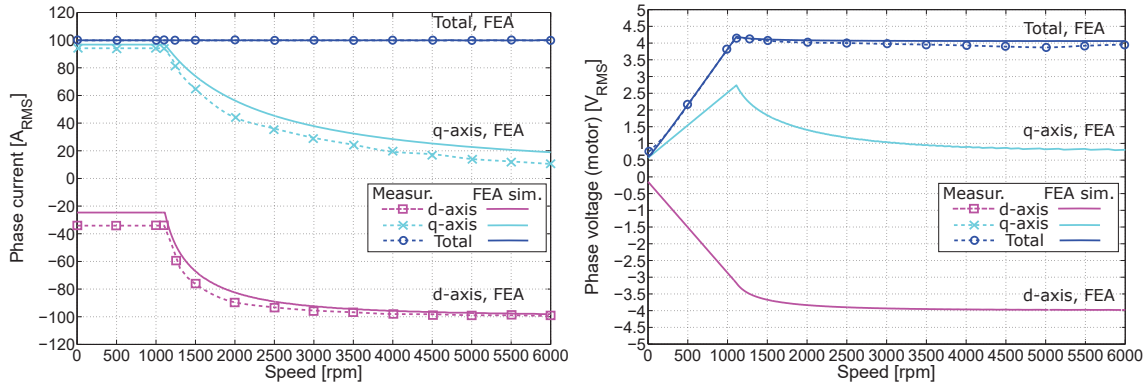

(e) C-shape motor, current. (f) C-shape motor, voltage.

Fig. 14.39: Phase current (left) and voltage (right) vs. speed, measurement vs. FEA simulation.

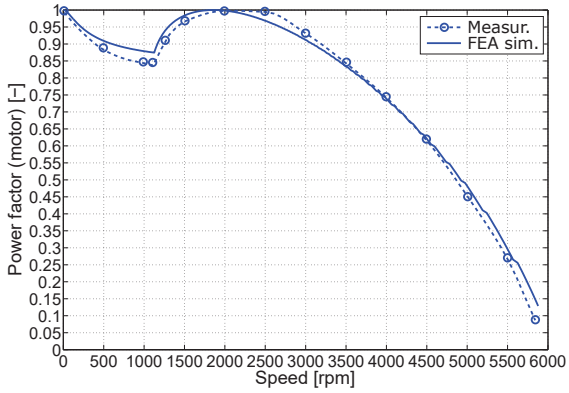

(a) Reference motor.

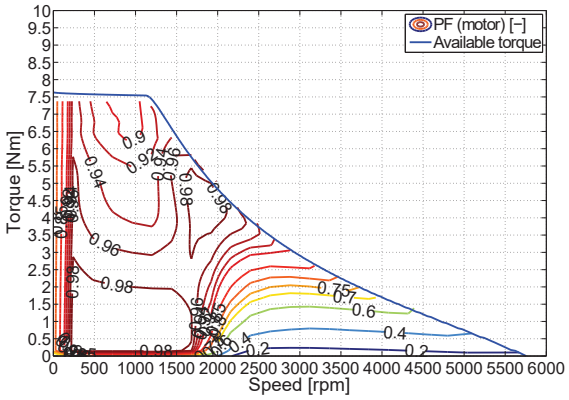

(b) Reference motor.

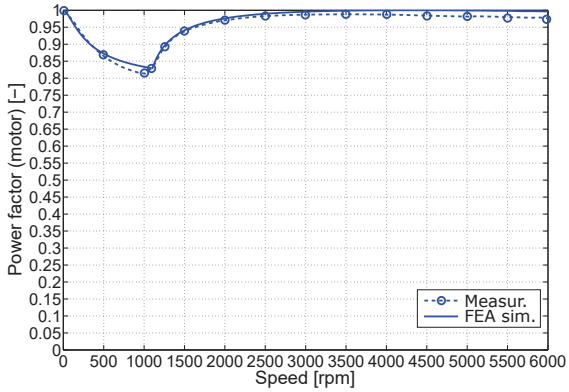

(c) V-shape motor.

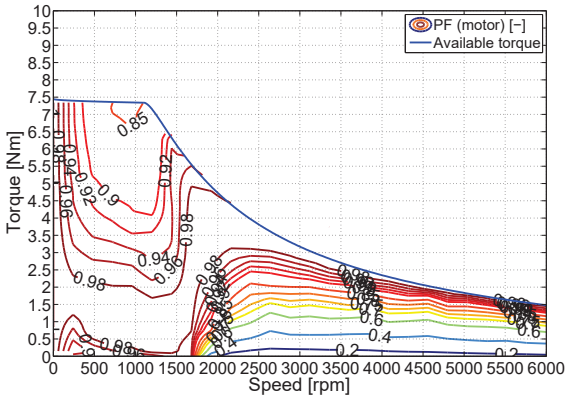

(d) V-shape motor.

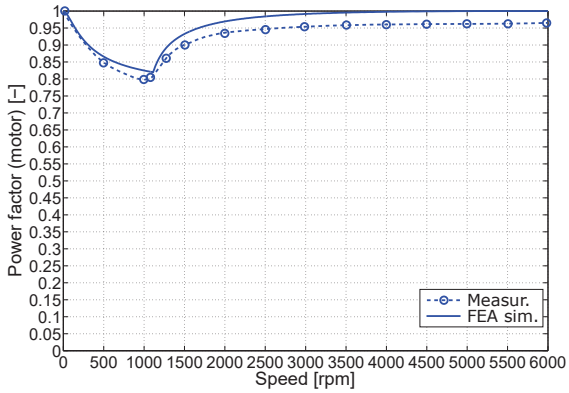

(e) C-shape motor.

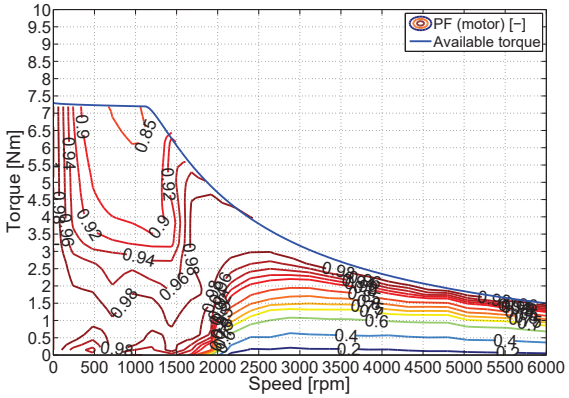

(f) C-shape motor.

Fig. 14.40: PF (motor) vs. speed, measurement vs. FEA simulation (left) and PF (motor) map in the torque-speed plane, FEA simulation (right).

Losses and efficiency

In Fig. 14.41 the FEA simulation of the losses components in the machines are reported along the available torque vs. speed profile. On the left, the copper, iron and mechanical losses are shown, while on the right, the iron losses components are highlighted.
It is worth noticing the dominant contribution of the Joule losses to the total losses, accounting for about 5% of the copper losses at the base speed, and around 20% at $\sim 6000rpm$. On the other hand, it is important to remind that due to the selected thermal design criteria, the copper losses (i.e. the active copper losses, which represents the dominant component in FSCW machines) in the C/V-shape design are lower of about 5% than those in the reference machine.
As shown in Fig. 14.41, the iron losses in the V-shape motor are predicted to be higher than those in the reference machine, accounting of about 13% and 29% at the base speed and maximum speed ($\sim 6000rpm$), respectively. Assuming a V-shape motor with the same stack length of the reference machine, these values increase to about 25% at the base speed and 43% at the maximum speed. An analysis of the iron losses components provides interesting remarks:

- In the total speed range iron losses in the teeth of the V-shape machine are about 10% (or 22% at the same stack length) higher than those in the reference motor.
- While in constant torque region, the back iron and rotor losses are comparable between the V-shape and reference motor (or about 10% higher considering the same stack length), as the speed increases, these losses arise, doubling at the maximum speed ($\sim 6000rpm$).
- Due to the radial segmentation of the PMs and better protection offered by the iron from the stator harmonics, the eddy current losses in the PMs of the V-shape design are halved as a respect of the reference machine. Per unit of PM volume, the V-shape design exhibits about 40% lower PM eddy current losses than the reference design.

As regards the C-shape motor, similar trend has been computed. It is worth noticing a lower back iron and rotor losses in comparison of the V-shape design (-20%). Moreover, the radial segmentation of the PMs drastically mitigates the eddy current losses in the magnets and the total iron losses become comparable to the total iron losses in the reference machine.

In order to investigate the source of these phenomena, a representative working points is considered. The motors are simulated at almost the maximum speed ($6000rpm$) in complete FW, with a negative d-axis rated current. In Fig. 14.42 the flux density map are shown for the machines. The saturation pattern is significantly different among the reference and C/V-

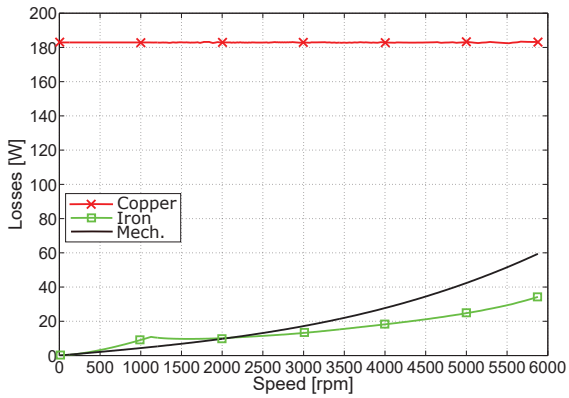

(a) Reference motor.

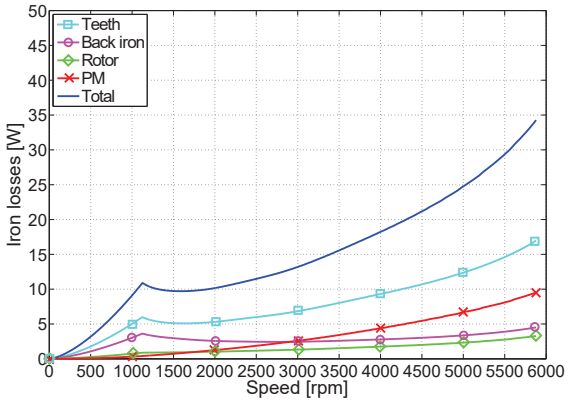

(b) Reference motor.

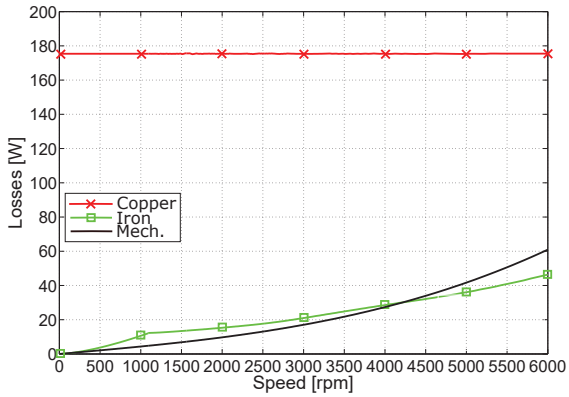

(c) V-shape motor.

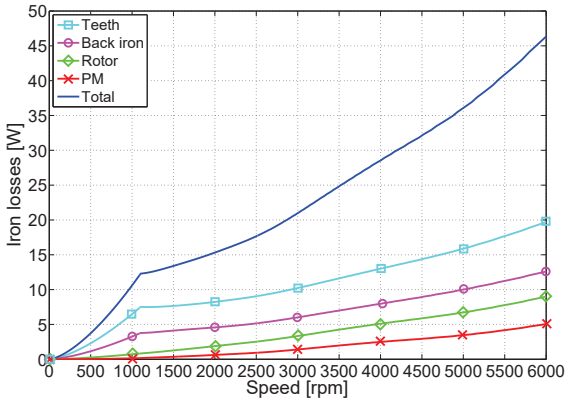

(d) V-shape motor.

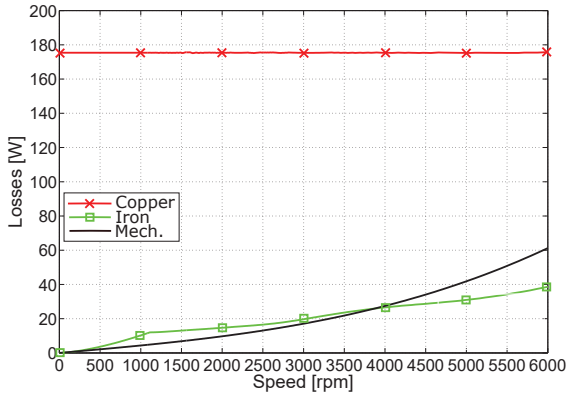

(e) C-shape motor.

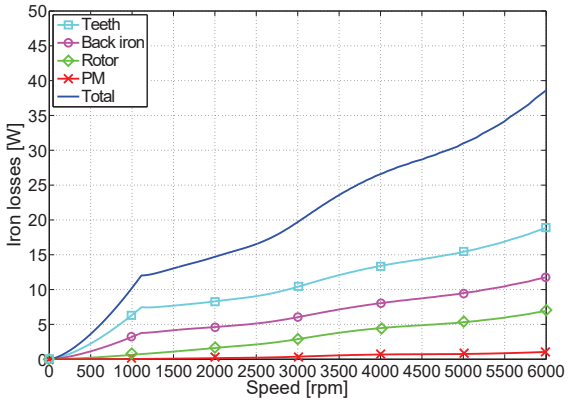

(f) C-shape motor.

Fig. 14.41: Losses (left) and iron losses (right) vs. speed, FEA simulation.

shape machines, where a 1^{st} harmonic order of the stator MMF can be detect. Simulating the reference machine with the constrain of the equality of MMF (Fig. 14.42(c)), the 1^{st} harmonic order start to appear in the reference design, therefore it is strictly related to the

iron saturation.

In Fig. 14.43 the analytical computation of the harmonic spectra of the electric loading

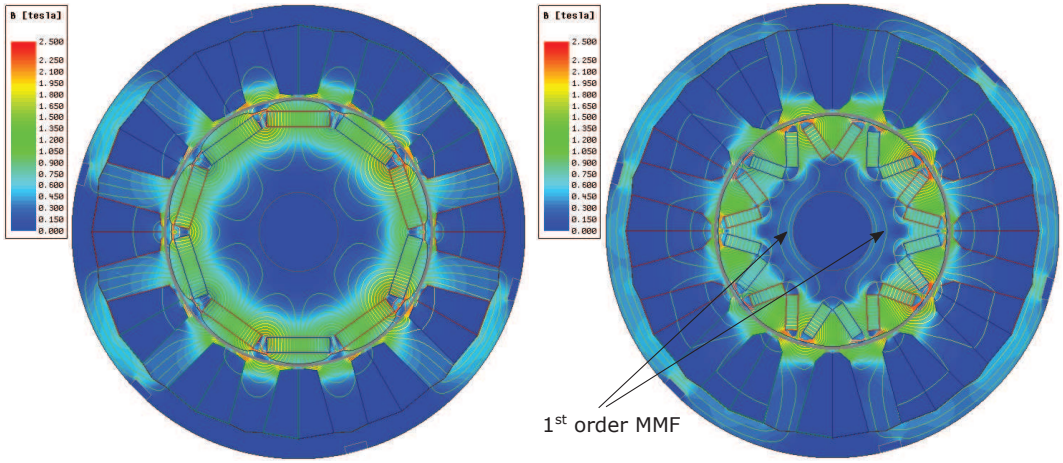

(a) Reference motor.

(b) V-shape motor.

(c) Reference motor, with equality of MMF as respect of C/V-shape motors.

(d) C-shape motor.

Fig. 14.42: Flux density map of the reference and V-shape machine at the maximum FW, $I_d = -100A_{RMS}$, $I_q = 0A_{RMS}$.

and MMF of a $12/10$ machine is reported. The amplitudes are referred to the C/V-shape design. The 1^{st} harmonic order, with the widest wavelength, is particulary adverse since it flows deeply in the rotor. This represents a subharmonic. At the rotor reference frame [15, 63], this space harmonic waveform affects the rotor, rotating backwards in respect the rotor speed (i.e. fundamental MMF), at a frequency,

$$f_{r1} = f \cdot \left| -1 - \frac{1}{p} \right| = \frac{6}{5} \cdot f = 1.2 \cdot f \tag{14.47}$$

It is worth noticing the existence of an important slot harmonic, such as the 7^{th} which affects

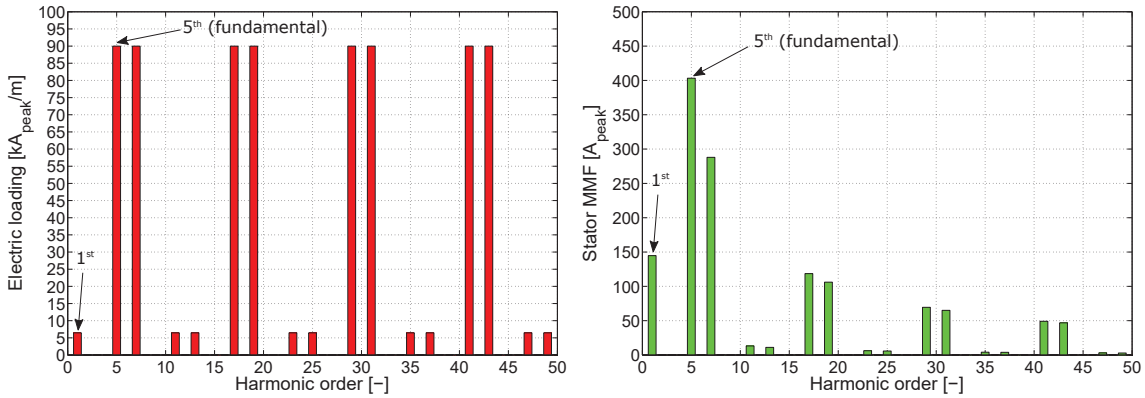

(a) Electric loading harmonic spectrum.

(b) Stator MMF harmonic spectrum.

Fig. 14.43: Analytical computation (based upon the C/V-shape configurations) of the electric loading and stator MMF harmonic spectrum for a 12-slot, 10-pole machine. The effect of the slot is neglected.

the rotor with a frequency equal to 2.4 times higher than the fundamental. On the other hand, this harmonic component tend to flow through the outer side of the rotor, therefore it contributes to arise the eddy current losses in the PMs, especially if they are placed in proximity of the surface, as it happens in the reference machine.

Figs. 14.44(a), 14.44(b) report the waveform and harmonic components of the airgap flux density in the considered working point. Likewise, for comparison, in Figs. 14.44(c), 14.44(d) is reported the computation at the base point, in the constant torque region.
Comparing to the no load airgap flux density (Fig.14.13), the fundamental of the airgap flux density exhibit, due to the effect of the saturation, comparable reduction in all the machines (3% in constant torque region, Fig.14.44(d)). Therefore, it proves that the saturation has comparable impact at the rated electric loading. Moreover, as expected, C-shape and V-shape design shows equivalent harmonic pattern. The distortion of the airgap flux density in the constant torque region is comparable between the reference and C/V-shape machines, in particular the components due to the slot harmonics (e.g. 5^{th}, 7^{th}, 17^{th}, 19^{th},...) and the 1^{st}, subharmonic order.
Comparing to the base working point, in complete FW, the $THD\%$ of the airgap flux density in the C/V-shape machines worsens of about 5%. This phenomenon is mainly caused by the doubling of the 1^{st} and 7^{th} harmonic order. In Fig. 14.44(a), the periodicity of these harmonics component can be detected and it his highlighted by the spikes of the flux density. Fig. 14.45 reports the distribution of the flux lines, in the two representative points. In the

reference machines, the narrow area of the tooth shoes is completely saturated. Conversely, in the V-shape motor, the iron works below the knee, therefore representing a preferential path for the field flow leading to such spikes. In conclusion this explain the mechanism which leads to a higher 1^{st} and 7^{th} harmonic components in the C/V-shape design and therefore higher rotor and back iron losses.

In Fig. 14.46 the iron losses map, including the eddy current losses in the PMs, at the

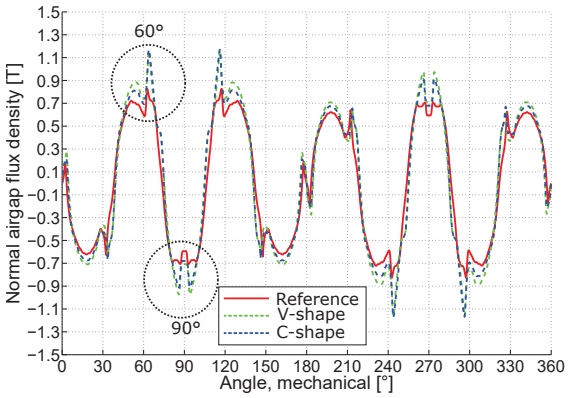

(a) Waveform, $I_d = -100A_{RMS}$, $I_q = 0A_{RMS}$.

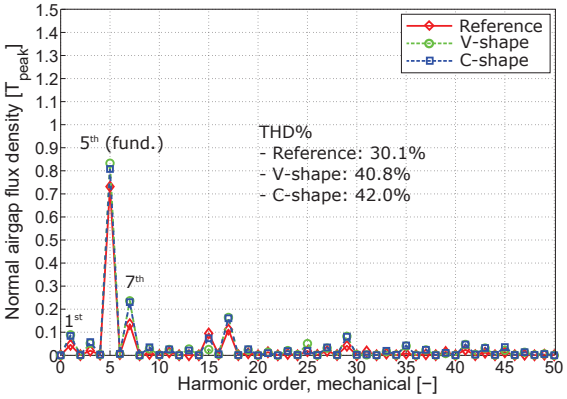

(b) Harmonic spectrum, $I_d = -100A_{RMS}$, $I_q = 0A_{RMS}$.

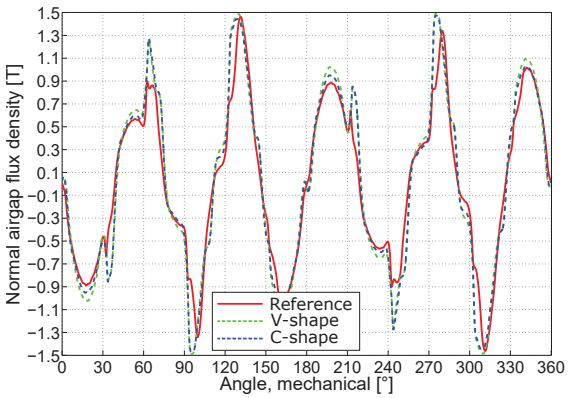

(c) Waveform, at the base point.

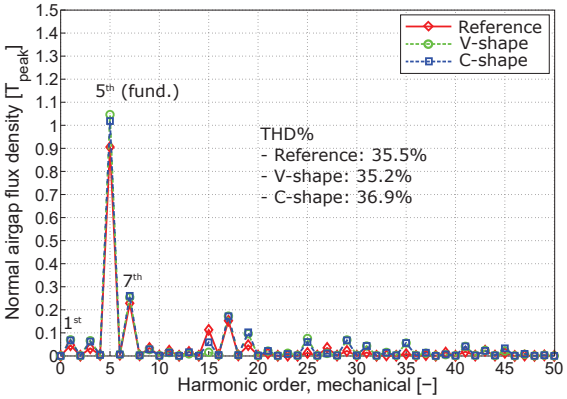

(d) Harmonic spectrum, at the base point.

Fig. 14.44: Airgap flux density in full FW and at the base point.

above mentioned FW operating point and at a speed around $6000rpm$ are shown. This map is representative of a steady state condition, at the same angular position considered in the previous analysis. The iron losses are distributed, according to the different flux density in the machines and it is clear the contribution of the subharmonic order. It is also worth mentioning the higher eddy current losses in the PMs of the reference machine.

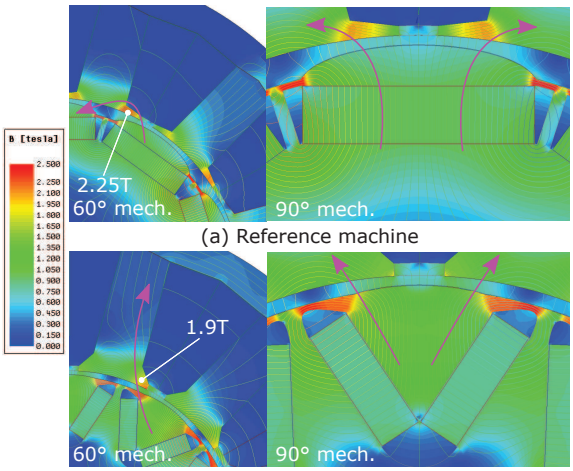

(a) Reference machine

(b) V-shape machine

Fig. 14.45: Flux density map in full FW ($I_d = -100A_{RMS}$, $I_q = 0A_{RMS}$) in the highlighted mechanical angular position, 60° and 90°.

In Fig. 14.47 the measurement and FEA simulation of the total losses, which include electrical and mechanical losses, are reported. Experimental and simulated results shows a good agreement and it is clear the dominant contribution of the copper losses. The difference contribution of the iron losses in the considered speed range is negligible. The motor efficiency is then computed and compared with the measurements along the torque vs. speed profile, as shown in Figs. 14.48(a), 14.47(d) and 14.47(f). No remarkable differences are found between the experimental and FEA computation. Higher discrepancy is found a high speed range due to the impact of the iron losses.
In Figs. 14.48(a), 14.48(c), 14.48(e) the FEA simulation of the efficiency map in the torque vs. speed plane is reported. All the machines exhibit similar efficiency at speed range lower than $2000rpm$ and in the constant torque region, with a maximum value of 90.9% at $1600rpm$ and about 33% of the rated torque. Conversely, beyond $2000rpm$, thanks to the higher FW performance, the C/V-shape motors show an efficiency up to 5% higher than the reference motor.

Torque ripple

In Figs. 14.48(b), 14.48(d) and 14.48(f) the computed torque ripple map in the torque vs. speed plane is reported. As mentioned before, the C/V-shape designs provide a better torque ripple performance in the constant torque region. while the shaping of the pole shoes of the reference motor are effective to mitigate the torque ripple in FW operation.

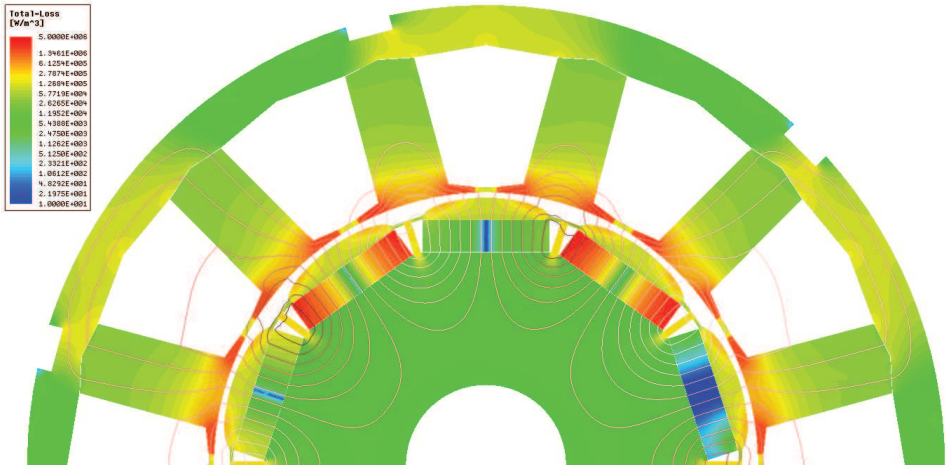

(a) Reference motor.

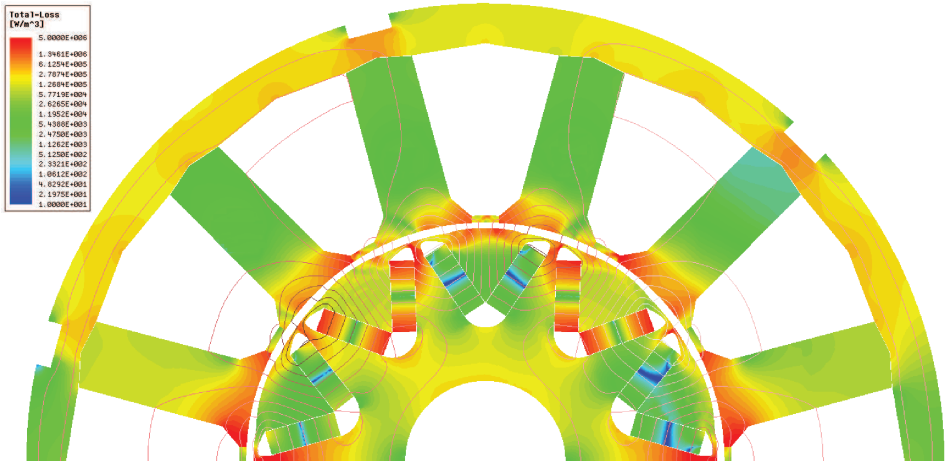

(b) V-shape motor.

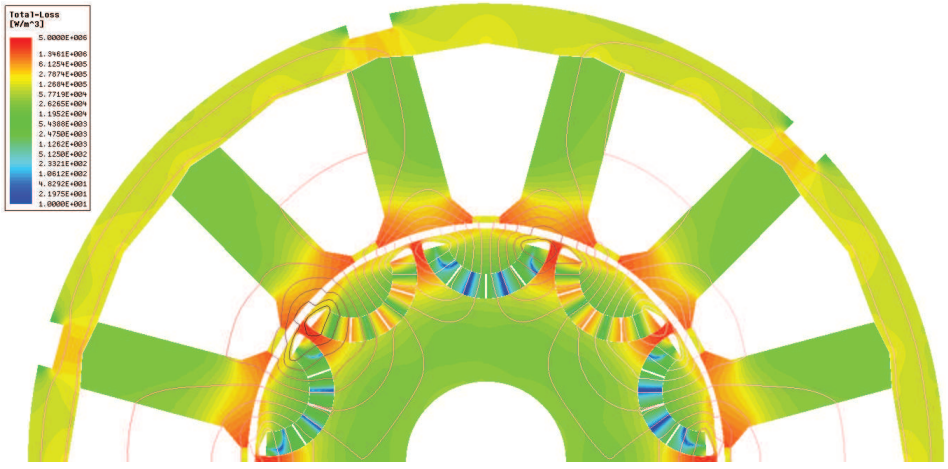

(c) C-shape motor.

Fig. 14.46: Iron losses density map at $I_d = -100A_{RMS}$, $I_q = 0A_{RMS}$, $5879rpm$. The map is representative of a steady state condition. Flux lines are superimposed and logarithmic scale is used.

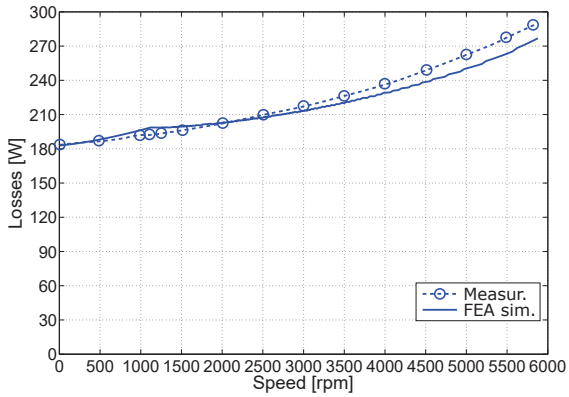

(a) Reference motor.

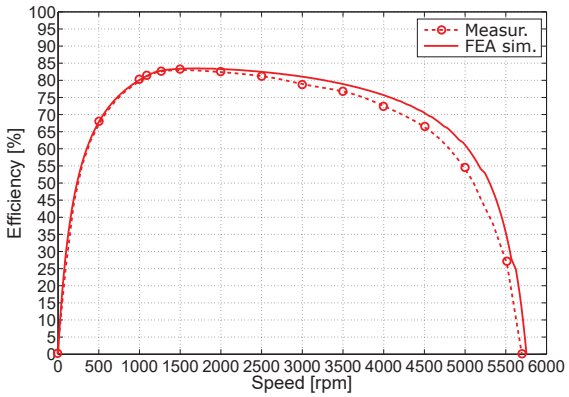

(b) Reference motor.

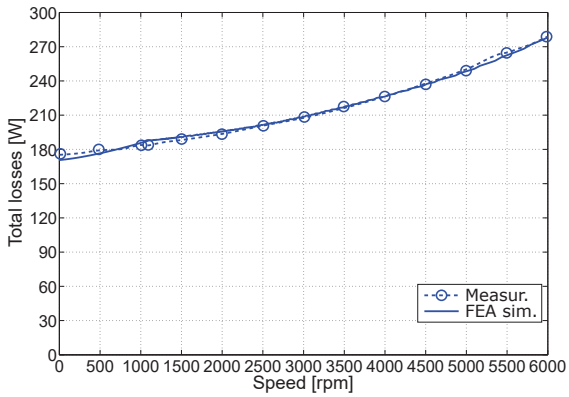

(c) V-shape motor.

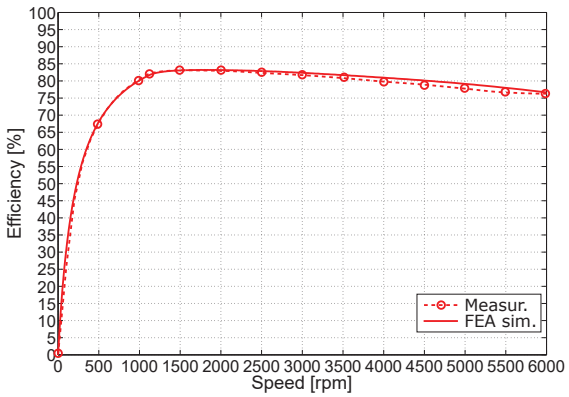

(d) V-shape motor.

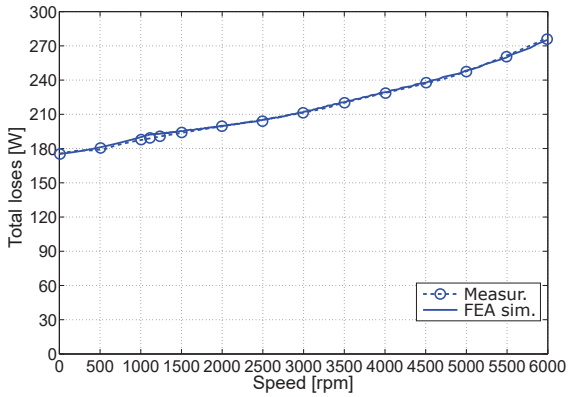

(e) C-shape motor.

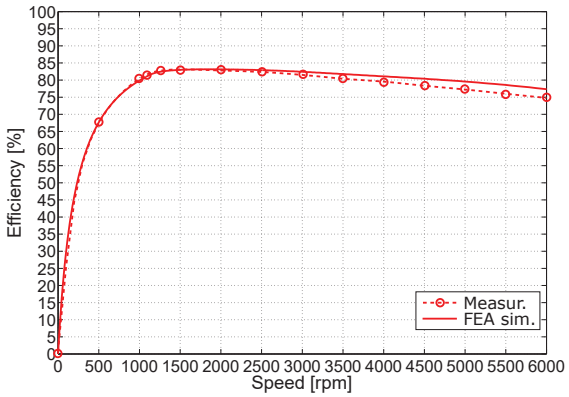

(f) C-shape motor.

Fig. 14.47: Total losses vs. speed, measurement vs. FEA simulation (left), efficiency vs. speed, measurement vs. FEA simulation (right).

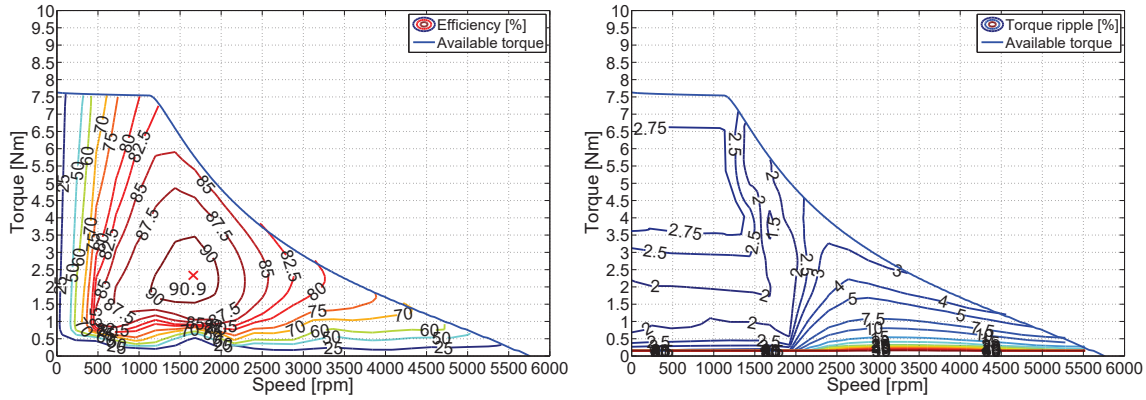

(a) Reference motor.

(b) Reference motor.

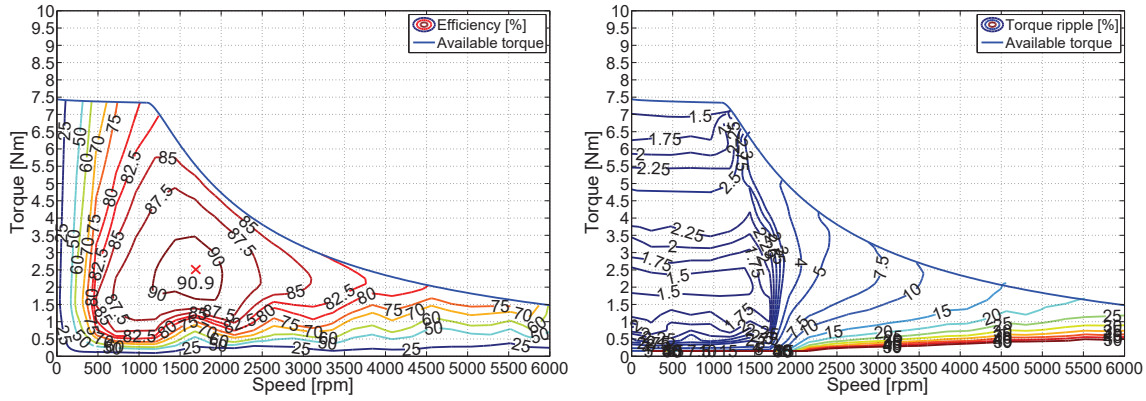

(c) V-shape motor.

(d) V-shape motor.

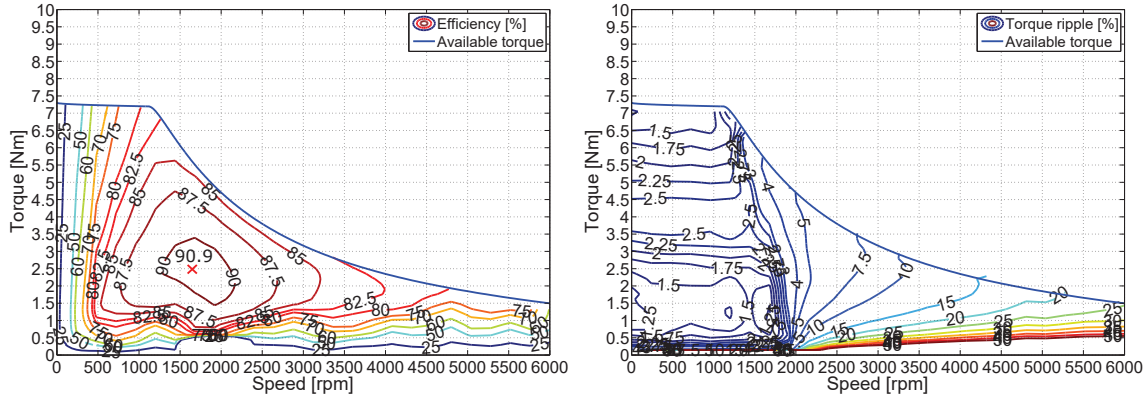

(e) C-shape motor.

(f) C-shape motor.

Fig. 14.48: Efficiency map, FEA simulation (left), torque ripple map in the torque vs. speed plane, FEA simulation (right).

14.4.9 Acoustic performance

The acoustic performance of the motors have been measured along the torque vs. speed profile. The measurement has been carried out with the complete motor setup, which includes the housing. A quantitative and accurate comparison of such experimental results with of simulations requires a complex and resource demanding multiphasic FEA computation of the mechanical structure, which takes into account the effect of several parasitic effect such as: anisotropic materials, spring and dampers connection (e.g. proprietary decoupling stator/housing rings), background noise, contribution of the torque ripple. All these elements influence the frequency response. Such an analysis is beyond the scope of this thesis. On the other hand a comparison, which takes into account only the magnetic pressure affecting the stator parts, has been already discussed in Ch. 13.

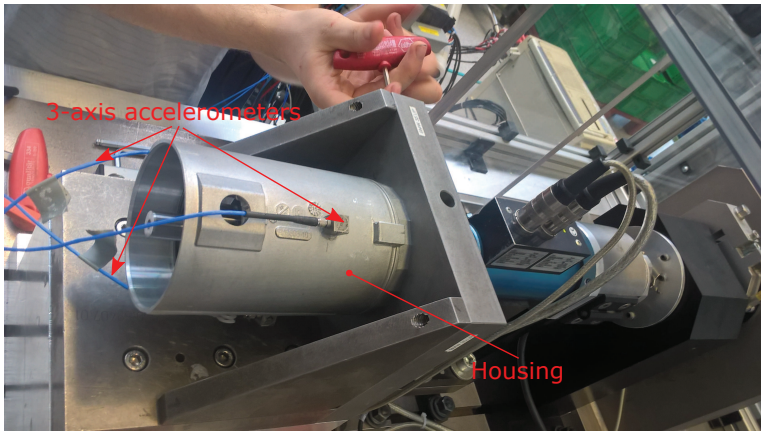

Fig. 14.49: Setup of the test bench.

In Fig. 14.49 the setup of the test bench is shown. The measurements have been carried out testing the motors along the current space vector trajectory and measuring the axial (x-axis), longitudinal (y-axis), and radial (y-axis) acceleration by means of 3 accelerometers firmly placed symmetrically (120° displacement) along the center line of the housing.
Figs. 14.50, 14.51 report, for each harmonic order, the average value of the radial and tangential accelerations (in decibel) in the 3 measurement points in the speed range $0-3000rpm$, respectively. The response among the different measurements points is comparable, proving a perfect homogeneity of the medium (housing, decoupling rings, etc.) between the active part of the motor and the outer space. The dominant contribution to the NV comes from the fundamental of the magnetic pressure with order $2 \cdot p$ and its multiples. As discussed in Ch. 13 the radial acceleration along the radial direction is normally the *primary concern* [72] of the acoustic noise since it produces a radial displacement of the stator shell

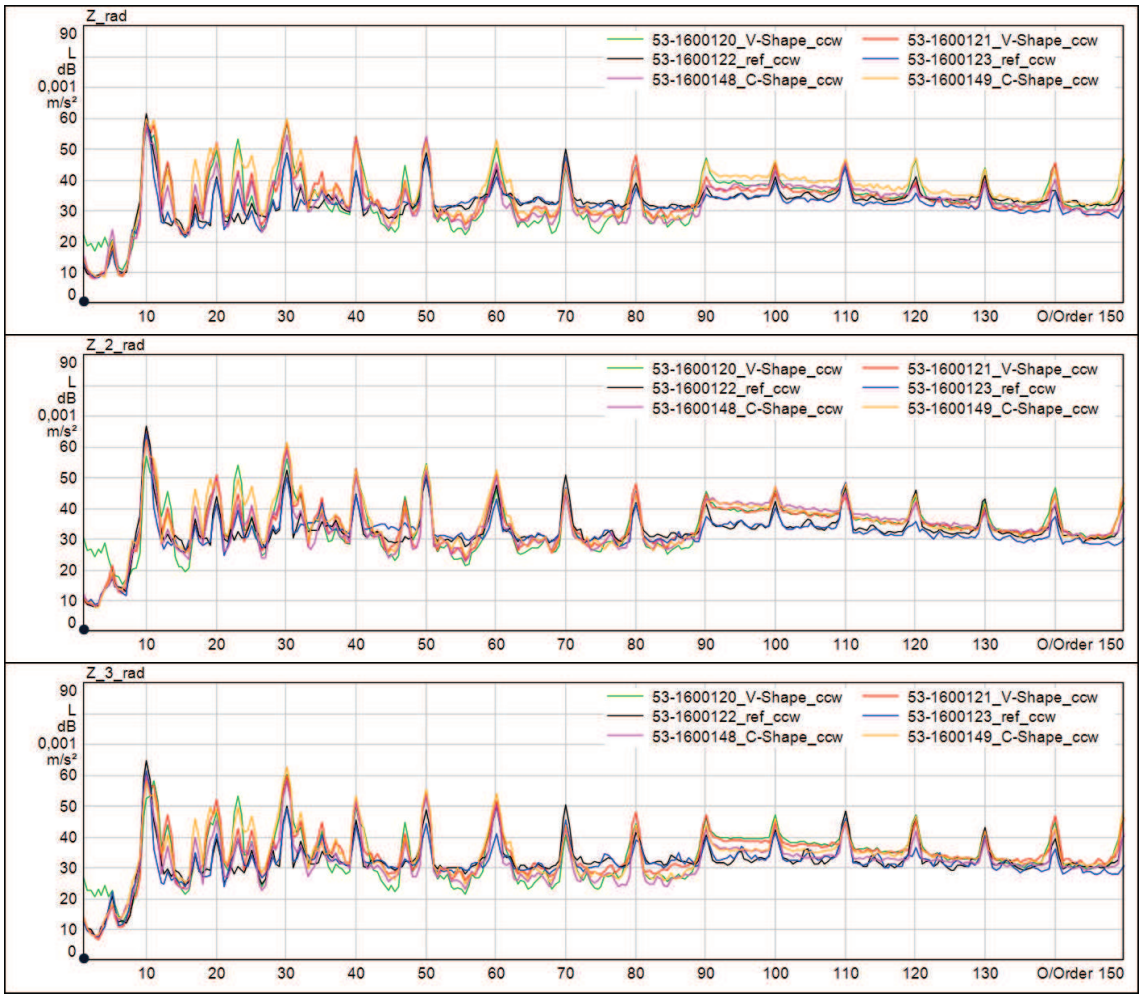

Fig. 14.50: Radial acceleration vs. harmonic order on the 3 measurement points (average value in the speed range $0-3000rpm$).

and, as result, of the medium above. For low harmonic orders, no remarkable differences between the reference and C/V-shape designs exists. The discrepancy increases for very high harmonic orders between the 90^{th} and 120^{th} order. Keeping in mind the relationship between decibel and absolute values, the dominant harmonic contributions in the spectra of the radial accelerations, are represented by the 10^{th} (fundamental) and 30^{th} order. They result about 5.6 times ($\sim 15dB$) and 3 times ($\sim 10dB$) higher than the maximum value of the remaining harmonic components.

In Figs. 14.52 14.53 the radial acceleration for the first 6 main harmonic orders (10^{th}, to 60^{th}), as a function of the speed, are reported. For the sake of presentation, higher harmonic orders are not shown since similar trends are found. The fundamental harmonic, the C/V-shape design shows a monotonic trend with a constant reduction up to about $6dB$ (50%

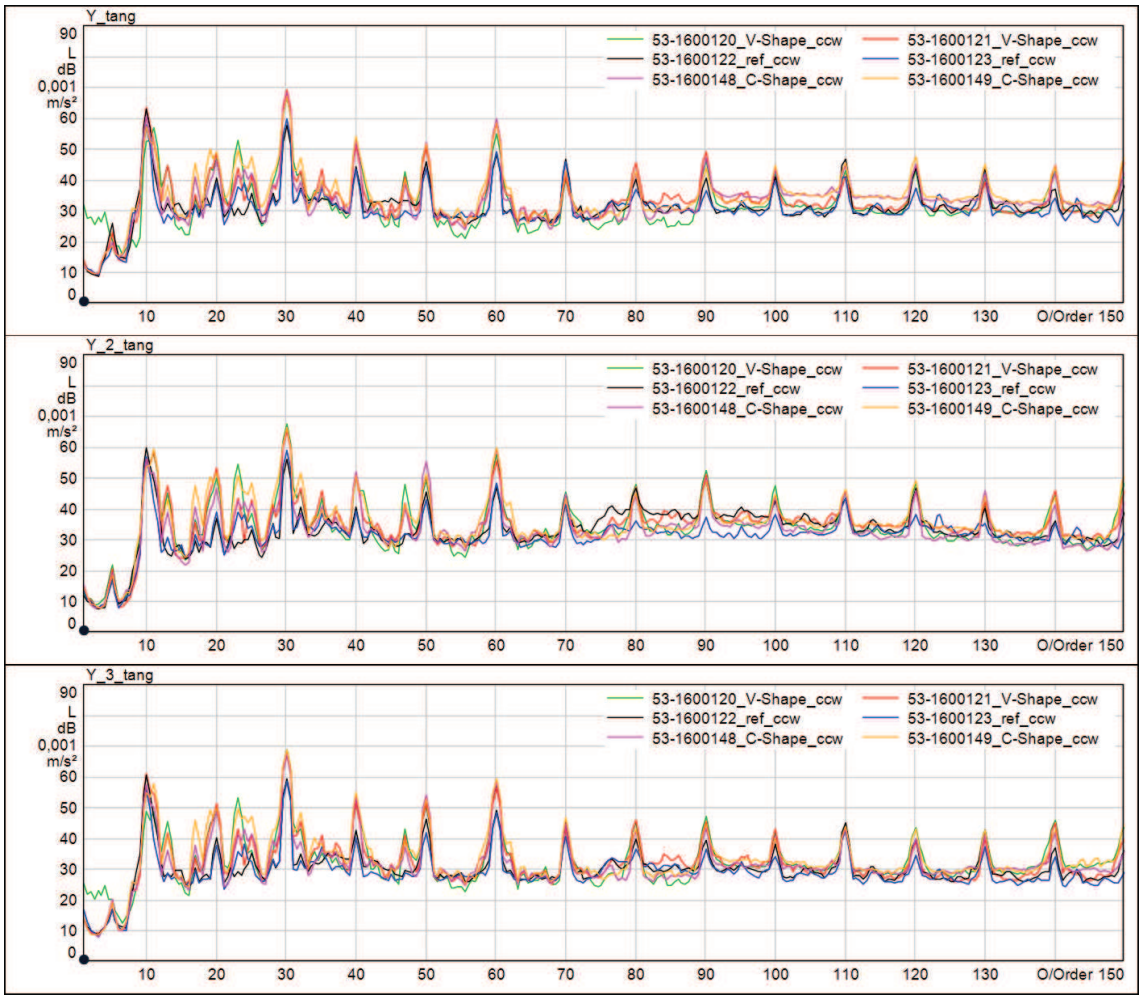

Fig. 14.51: Tangential acceleration vs. harmonic order on the 3 measurement points (average value in the speed range $0-3000rpm$).

in terms of absolute value) up to almost the maximum speed ($3000rpm$). Conversely, for higher harmonic orders, the trend is not monotonic with some local minima, which emphasizes phenomena close to resonances. For such harmonic orders, the reference motors exhibit, in general, lower radial acceleration for speed range above the base speed.

Finally, in Fig. 14.54 the Campbell diagrams provide a comprehensive picture of the acoustic performance. It represent the constant acceleration loci in a speed-frequency ($0-5kHz$). The main harmonic orders can be detected (the first six are highlighted). The axial and tangential acceleration are also included showing a similar pattern with the radial acceleration. The frequency where resonant or quasi-resonant phenomena occurs are characterized by vertical band, as highlighted in the figure by arrows. For the reference machine, these band are centered around specific frequencies: the mains are $\sim 800Hz$, $\sim 2000Hz$ besides to a

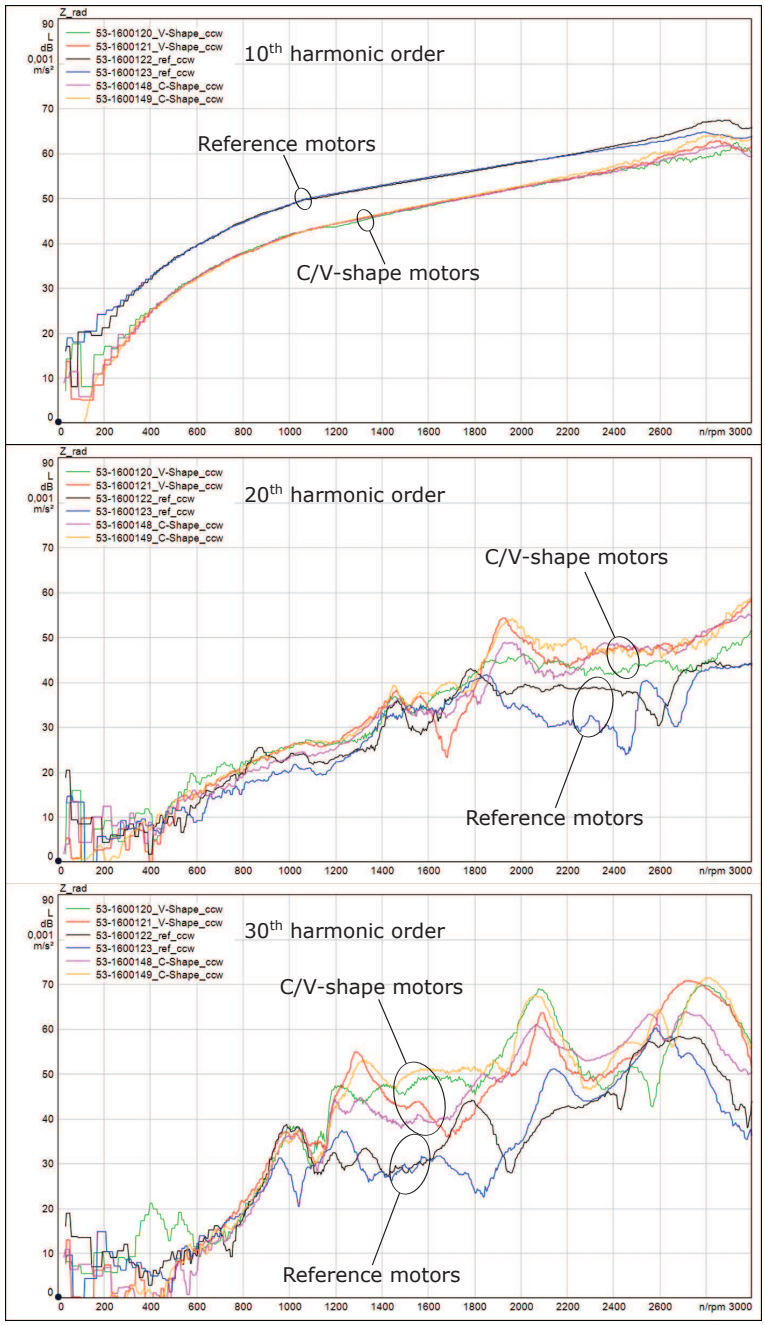

Fig. 14.52: Harmonic components of the radial acceleration vs. speed (10^{th}, 20^{th}, 30^{th}).

high frequency at $\sim 4000Hz$ which has a negligible impact. The C/V-shape motors, exhibit a comparable frequencies, with main harmonic at $\sim 1000Hz$, $\sim 2000Hz$ with a negligible at $\sim 4000Hz$. In general, V-shape motor show a higher radial acceleration than the reference machine in the area of such frequencies. Conversely, the C-shape pattern is significantly better than the V-shape design and comparable to the reference machine.

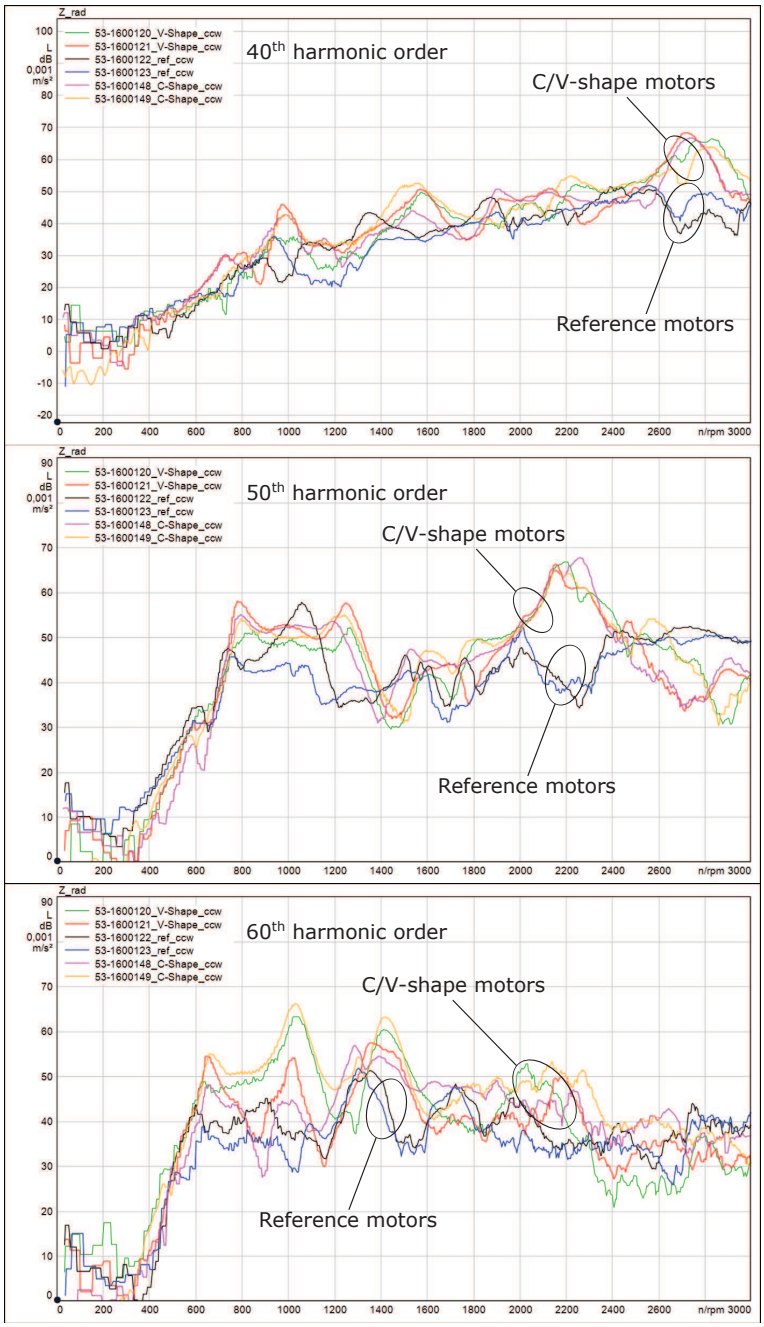

Fig. 14.53: Harmonic components of the tangential acceleration vs. speed (40^{th}, 50^{th}, 60^{th}).

Finally, it is worth mentioning the existence of an vertical band in the constant torque region up to about $1000rpm$, highlighted by the curly brace and which does not exists in batch of reference motor in series production and it is spread all over the frequency range. A possible explanation is that some coupling issues between the rotor shaft and the bearings arise, in the constant torque region, where the amplitude of the radial pressure is the highest.

14.5 Conclusions

In this chapter a detailed analysis of the experimental results has been presented. Starting from the validation of the magnet properties, a comprehensive measurements campaign which includes no load, load and acoustic tests, have been performed on the motor samples. The magnetic properties have been validated by means of measurements carried out on the single magnets and then on the complete rotor assembly. This results confirm the accuracy and the conclusions of the developed motor designs and FEA models. On the other hand it shows an unsuitable magnetization pattern of the C-shape 1pc which has been discarded for the prototyping stage in favor of the C-shape 4pcs design which partially meets the requested magnetic performance.
The measurements of the cogging torque and torque ripple have highlighted the critical impact of the manufacturing imperfections. This issue is detailed investigated in the next chapter. Following some inspections of the motor samples, some specific deficiencies have been found.

In Table 14.10 the main motor data and performance are summarized. The developed C/V-shape motors are able to provide more than 12% torque density thanks to the contribution of the flux concentration and the reluctance torque. The cost is in agreement with the original computation, showing a reduction of the active motor cost for more than 12% in the C/V-shape designs comparing to the reference machine. It is worth noticing that the cost per unit of torque is lower than the original computation, especially for the C-shape design (-12.6% and 15.6% for the V-shape and C-shape, respectively) due to the lower torque density: this is because of the lower PM quantity, in comparison of the original design. As regards the torque ripple, due possible deficiencies during the manufacturing process, no specific conclusions can be drawn. In general, the C/V-shape and reference designs exhibit similar performance in terms of cogging torque and rated torque ripple, in the constant torque region. These latter quantity is predicted to be better than the reference machine. As regards the torque ripple in FW operation, due to the beneficial impact of the pole shaping, the reference machine exhibits a torque ripple which, in absolute terms, reduces with the increase of the commutation angle. The merit of the C/V-shape machines in terms of better FW capability are confirmed by the simulation: they offer a CPSR performance more than 2 times higher than the reference configuration. As regards the acoustic performance, similar noise pattern has been found in the reference and C-shape machine, while higher values are found in the V-shape motor. On the other hand, as mentioned for the torque quality, possible manufacturing deficiencies have an important influence on such quantities.

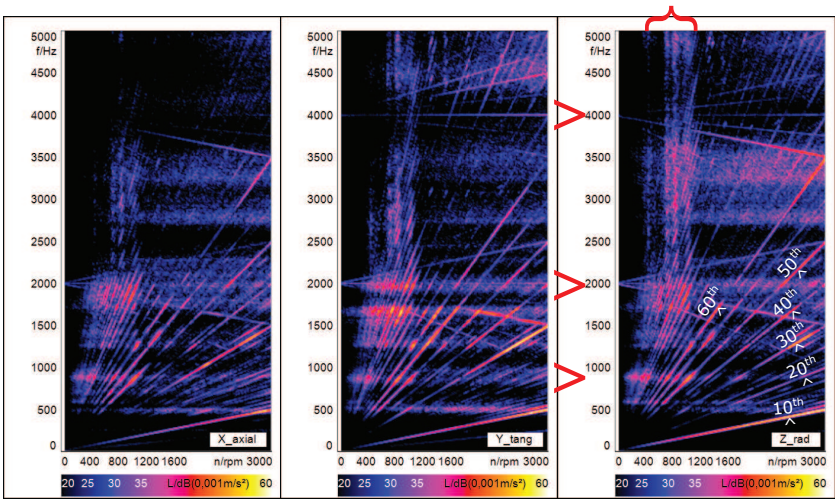

(a) Reference motor.

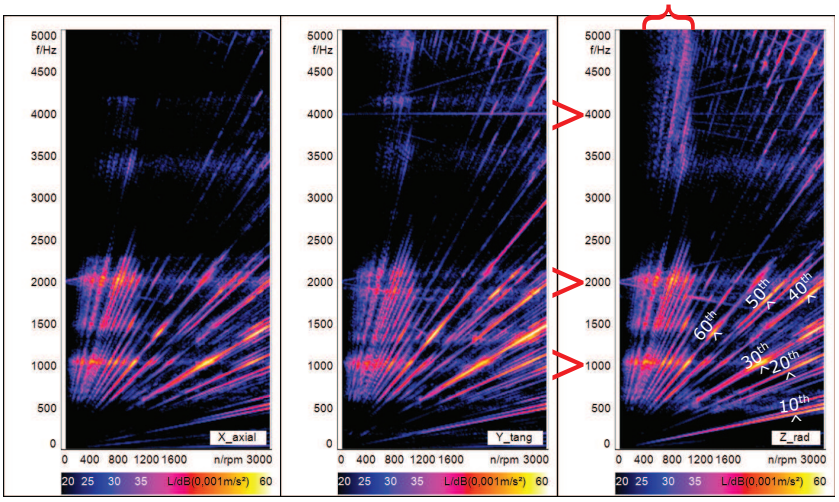

(b) V-shape motor.

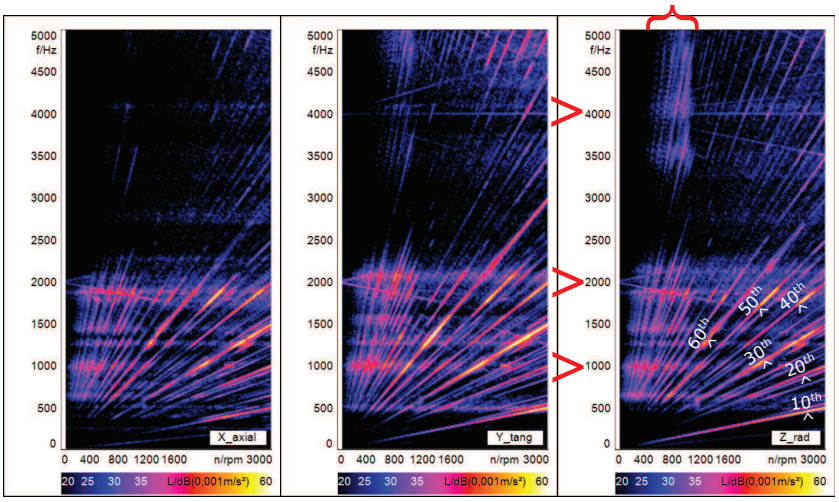

(c) C-shape motor.

Fig. 14.54: Campbell diagram.

Table 14.10: Motor performance summary @ 30°C

Quantity	Reference		V-shape		C-shape		Unit
	Meas.	FEA	Meas.	FEA	Meas.	FEA	
Stack length	62.5		56		56		*mm*
Airgap diameter	51		44.8		44.8		*mm*
Outer diameter			86				*mm*
Airgap height			0.5				*mm*
Slot area	129.8			150.9			mm^2
# cond./slot, series conf.	7			8			–
Fill factor	0.45	0.44	0.45	0.44	0.45	0.44	–
Rat. slot current	989.9		1131.4		1131.4		A_{peak}
Rat. phase current			100				A_{RMS}
Rat. current density	12.7			11.4			A_{RMS}/mm^2
Base comm. angle	9	6	15	13	20	13	°
Rat. electric loading	69044			89890			A_{peak}/m
Magn. loading, fund.	–	0.92	–	1.10	–	1.06	T_{peak}
Rated torque (static)	7.31	7.65	7.23	7.46	6.94	7.31	*Nm*
Torque density (static)	20.1	20.5	22.3	22.9	21.3	22.5	Nm/dm^3
Torque density var.	0	0	+11.0	+12.0	+6.0	+12.0	%
Cogging torque	19.2/52.4	3.78	84.7/70.0	5.30	62.7/79.2	6.33	*mNm*
Rated torque ripple	2.87	2.54	2.90	1.47	2.45	1.01	%
Base speed	1096	1126	1088	1103	1122	1112	*rpm*
Base efficiency	81.5	81.7	82.4	81.5	82.0	81.3	%
Max speed, elec. lim.	5755	5879	–	16300	–	16620	*rpm*
CPSR ratio	1 : 2.46	1 : 2.80	–	1 : 7.04	–	1 : 7.52	–
FW ratio	1 : 5.25	1 : 5.22	–	1 : 14.8	–	1 : 14.8	–
Moment of inertia	2.686		1.352		1.445		$kg \cdot cm^2$
Copper mass	0.508	0.478	0.595	0.551	0.595	0.551	*kg*
... cost	3.241	3.050	3.796	3.518	3.796	3.518	€
... variation	0	0	+17.1	+15.3	+17.1	+15.3	%
Iron mass	1.619		1.357		1.391		*kg*
... cost	3.239		2.714		2.782		€
... variation	0		−16.2		−14.1		%
PMs mass	0.167		0.128		0.116		*kg*
... cost	8.365		6.399		5.814		€
... variation	0		−23.4		−30.5		%
Total mass	2.294	2.264	2.080	2.036	2.102	2.058	*kg*
... cost	14.845	14.654	12.909	12.631	12.392	12.114	€
Cost/torque ratio	2.031	1.916	1.785	1.693	1.786	1.657	€/*Nm*
... variation	0	0	−12.1	−11.6	−12.1	−13.5	%

List of Figures

List of Tables

References

[1] Aglen, O. (2003). Loss calculation and thermal analysis of a high-speed generator. In *IEEE International Electric Machines and Drives Conference (IEMDC)*, volume 2, pages 1117–1123 vol.2.

[2] Alberti, L., Barcaro, M., and Bianchi, N. (2014). Design of a low-torque-ripple fractional-slot interior permanent-magnet motor. *IEEE Transactions on Industry Applications*, 50(3):1801–1808.

[3] Ando, K., Yamada, A., Miki, I., and Nakamura, M. (2008). Study on improvement of efficiency for outer rotor type of interior permanent magnet synchronous motor. In *International Symposium on Power Electronics, Electrical Drives, Automation and Motion (SPEEDAM)*, pages 599–602.

[4] Armando, E., Guglielmi, P., Pastorelli, M., Pellegrino, G., and Vagati, A. (2008). Performance of IPM-PMASR motors with ferrite injection for home appliance washing machine. In *IEEE Industry Applications Society Annual Meeting (IAS)*, pages 1–6.

[5] Armando, E., Guglielmi, P., Pellegrino, G., Pastorelli, M., and Vagati, A. (2009). Accurate modeling and performance analysis of ipm-pmasr motors. *IEEE Transactions on Industry Applications*, 45(1):123–130.

[6] auirgp4066d1 IGBT, International Rectifier (2012). *www.irf.com/product-info/datasheets/data/auirgp4066d1.pdf*.

[7] Azar, Z., Zhu, Z., and Ombach, G. (2012). Investigation of torque-speed characteristics and cogging torque of fractional-slot ipm brushless ac machines having alternate slot openings. *IEEE Transactions on Industry Applications*, 48(3):903–912.

[8] Barcaro, M. and Bianchi, N. (2011). Torque components in integral- and fractional-slot ipm machines. In *IEEE International Electric Machines Drives Conference (IEMDC)*, pages 1340–1345.

[9] Barcaro, M. and Bianchi, N. (2012a). Interior PM machines using ferrite to substitute rare-earth surface pm machines. In *20th International Conference on Electrical Machines (ICEM)*, pages 1339–1345.

[10] Barcaro, M. and Bianchi, N. (2012b). Torque ripple reduction in fractional-slot interior pm machines optimizing the flux-barrier geometries. In *Electrical Machines (ICEM), 2012 XXth International Conference on*, pages 1496–1502.

[11] Bedetti, N., Calligaro, S., and Petrella, R. (2015). Stand-still self identification of flux characteristics for synrm using novel saturation approximating function and multiple linear regression. In *IEEE Energy Conversion Congress and Exposition (ECCE)*, pages 2995–3002.

[12] Bianchi, N. (2011). *Industrial Electronics Handbooks, Power Electronics and Motor Drives, 2nd edition*, chapter Permanent Magnet Synchronous Motors, pages 6.1–6.35. CRC Press.

[13] Bianchi, N. and Bolognani, S. (2000). Reducing torque ripple in pm synchronous motor by pole shifting. In *Proocedings of International Conference on Electrical Machines (ICEM)*.

[14] Bianchi, N., Bolognani, S., Bon, D., and Pre, M. D. (2009). Rotor flux-barrier design for torque ripple reduction in synchronous reluctance and pm-assisted synchronous reluctance motors. *IEEE Transactions on Industry Applications*, 45(3):921–928.

[15] Bianchi, N., Bolognani, S., and Fomasiero, E. (2007). A general approach to determine the rotor losses in three-phase fractional-slot pm machines. In *IEEE International Electric Machines Drives Conference*, volume 1, pages 634–641.

[16] Bianchi, N., Bolognani, S., and Fornasiero, E. (2010). An overview of rotor losses determination in three-phase fractional-slot pm machines. *IEEE Transactions on Industry Applications*, 46(6):2338–2345.

[17] Bianchi, N., Bolognani, S., and Frare, P. (2003). Design criteria of high efficiency spm synchronous motors. In *IEEE International Electric Machines and Drives Conference (IEMDC)*, volume 2, pages 1042–1048 vol.2.

[18] Bianchi, N., Bolognani, S., and Frare, P. (2006). Design criteria for high-efficiency spm synchronous motors. *IEEE Transactions on Energy Conversion*, 21(2):396–404.

[19] Bianchi, N., Bolognani, S., and Luise, F. (2005). Analysis and design of a pm brushless motor for high-speed operations. *IEEE Transactions on Energy Conversion*, 20(3):629–637.

[20] Bianchi, N., Degano, M., and Fornasiero, E. (2013). Sensitivity analysis of torque ripple reduction of synchronous reluctance and interior PM motors. In *IEEE Energy Conversion Congress and Exposition (ECCE)*, pages 1842–1849.

[21] Bianchi, N., Fornasiero, E., Ferrari, M., and Castiello, M. (2016). Experimental comparison of pm-assisted synchronous reluctance motors. *IEEE Transactions on Industry Applications*, 52(1):163–171.

[22] Bianchi, N. and Jahns, T. (2004). *Design, analysis, and control of interior PM synchronous machines*. IEEE Industrial Application Society.

[23] Boglietti, A. (1999). A first approach for the iron losses building factor determination. In *Industry Applications Conference, 1999. Thirty-Fourth IAS Annual Meeting. Conference Record of the 1999 IEEE*, volume 1, pages 489–493 vol.1.

[24] Brisset, S., Gillon, F., Vivier, S., and Brochet, P. (2001). Optimization with experimental design: an approach using Taguchi's methodology and finite element simulations. *IEEE Transactions on Magnetics*, 37(5):3530–3533.

[25] Carraro, E. (2012). Design of a permanent magnet synchronous motor according to freedomcar specifications. Master's thesis.

[26] Carraro, E. and Bianchi, N. (2014). Design and comparison of interior permanent magnet synchronous motors with non-uniform airgap and conventional rotor for electric vehicle applications. *IET Electric Power Applications*, 8(6):240–249.

[27] Carraro, E., Bianchi, N., Zhang, S., and Koch, M. (2014a). Permanent magnet volume minimization of spoke type fractional slot synchronous motors. In *IEEE Energy Conversion Congress and Exposition (ECCE)*.

[28] Carraro, E., Degano, M., Morandin, M., and Bianchi, N. (2013). Formula SAE electric competition: Electrical motor design. In *IEEE International Electric Machines Drives Conference (IEMDC)*, pages 1142–1148.

[29] Carraro, E., Degano, M., Morandin, M., and Bianchi, N. (2014b). Pm synchronous machine comparison for light electric vehicles. In *IEEE International Electric Vehicle Conference (IEVC)*, pages 1–8.

[30] Carraro, E., Morandin, M., and Bianchi, N. (2014c). Optimization of a traction PMASR motor according to a given driving cycle. In *Transportation Electrification Conference and Expo (ITEC), 2014 IEEE*, pages 1–6.

[31] Carraro, E., Morandin, M., and Bianchi, N. (2016). Traction pmasr motor optimization according to a given driving cycle. *IEEE Transactions on Industry Applications*, 52(1):209–216.

[32] Cha, H. R., Shin, K. J., and Seo, Y. J. (2011). Design of outer rotor ipm type pmsm for 3 wheel electric vehicle. In *Electrical Machines and Systems (ICEMS), 2011 International Conference on*, pages 1–3.

[33] Chang, L. (1994). Comparison of ac drives for electric vehicles-a report on experts' opinion survey. *IEEE Aerospace and Electronic Systems Magazine*, 9(8):7–11.

[34] Charih, F., Dubas, F., Espanet, C., and Chamagne, D. (2012). Performances comparison of pm machines with different rotor topologies and similar slot and pole numbers. In *Power Electronics, Electrical Drives, Automation and Motion (SPEEDAM), 2012 International Symposium on*, pages 56–59.

[35] Chau, K. T. and Wang, Z. (2011). *Chaos in Electric Drive Systems: Analysis, Control and Application*.

[36] Chen, L., Wang, J., Lazari, P., and Chen, X. (2013). Optimizations of a permanent magnet machine targeting different driving cycles for electric vehicles. In *IEEE International Electric Machines Drives Conference (IEMDC)*, pages 855–862.

[37] Chen, L., Wang, J., Lombard, P., Lazari, P., and Leconte, V. (2012a). Design optimisation of permanent magnet assisted synchronous reluctance machines for electric vehicle applications. In *20th International Conference on Electrical Machines (ICEM)*, pages 2647–2653.

[38] Chen, Q., Liu, G., Yang, J., Gong, W., and Zhao, W. (2012b). Comparison of two interior permanent-magnet motors with improved fault-tolerance. In *IECON 2012 - 38th Annual Conference on IEEE Industrial Electronics Society*, pages 4093–4098.

[39] Chen, Y. S., Zhu, Z. Q., and Howe, D. (2006). Vibration of pm brushless machines having a fractional number of slots per pole. *IEEE Transactions on Magnetics*, 42(10):3395–3397.

[40] Chino, S., Ogasawara, S., Miura, T., Chiba, A., Takemoto, M., and Hoshi, N. (2011). Fundamental characteristics of a ferrite permanent magnet axial gap motor with segmented rotor structure for the hybrid electric vehicle. In *IEEE Energy Conversion Congress and Exposition (ECCE)*, pages 2805–2811.

[41] Chong, L. and Rahman, M. (2010). Saliency ratio derivation and optimisation for an interior permanent magnet machine with concentrated windings using finite-element analysis. *IET Electric Power Applications*, 4(4):249–258.

[42] Constantinides, S. (2014). In the loop: Understanding and using magnetic material properties. tutorial at 2014 ieee transportation electrification conference and expo (itec). Seminar.

[43] Dajaku, G. and Gerling, D. (2010). Stator slotting effect on the magnetic field distribution of salient pole synchronous permanent-magnet machines. *IEEE Transactions on Magnetics*, 46(9):3676–3683.

[44] Dajaku, G. and Gerling, D. (2012). Air-gap flux density characteristics of salient pole synchronous permanent-magnet machines. *IEEE Transactions on Magnetics*, 48(7):2196–2204.

[45] Demir, Y., Ocak, O., and Aydin, M. (2013). Design, optimization and manufacturing of a spoke type interior permanent magnet synchronous motor for low voltage-high current servo applications. In *IEEE International Electric Machines Drives Conference (IEMDC)*, pages 9–14.

[46] Dorrell, D., Hsieh, M.-F., and Knight, A. (2012). Alternative rotor designs for high performance brushless permanent magnet machines for hybrid electric vehicles. *IEEE Transactions on Magnetics*, 48(2):835–838.

[47] Dutta, R. and Rahman, M. F. (2006). A comparative analysis of two test methods of measuring d - and q -axes inductances of interior permanent-magnet machine. *IEEE Transactions on Magnetics*, 42(11):3712–3718.

[48] Duvall, M. (2010). Discussion of the benefits and impacts of plug in hybrid and battery electric vehicles. Technical report, MIT Energy Initiative.

[49] Ehsani, M., Gao, Y., and Emadi, A. (2010). *Modern electric, hybrid electric, and fuel cell vehicles : fundamentals, theory, and design*, chapter Fundamentals of Vehicle Propulsion and Brake, Ch. 2, pages 21–65. CRC Press.

[50] El-Refaie, A. (2010). Fractional-slot concentrated-windings synchronous permanent magnet machines: Opportunities and challenges. *IEEE Transactions on Industrial Electronics*, 57(1):107–121.

[51] El-Refaie, A., Alexander, J., Galioto, S., Reddy, P., Huh, K., De Bock, P., and Shen, X. (2013a). Advanced high power-density interior permanent magnet motor for traction applications. In *IEEE Energy Conversion Congress and Exposition (ECCE)*, pages 581–590.

[52] El-Refaie, A., Alexander, J., Galioto, S., Reddy, P., Huh, K.-K., de Bock, P., and Shen, X. (2013b). Reduced rare-earth flux switching machines for traction applications. In *IEEE Energy Conversion Congress and Exposition (ECCE)*, pages 581–590.

[53] El-Refaie, A., Alexander, J., Galioto, S., Reddy, P., Huh, K.-K., de Bock, P., and Shen, X. (2014). Advanced high-power-density interior permanent magnet motor for traction applications. *IEEE Transactions on Industry Applications*, 50(5):3235–3248.

[54] EL-Refaie, A. and Jahns, T. (2005). Optimal flux weakening in surface PM machines using fractional-slot concentrated windings. *IEEE Transactions on Industry Applications*, 41(3):790–800.

[55] Evans, S. A. (2010). Salient pole shoe shapes of interior permanent magnet synchronous machines. In *Electrical Machines (ICEM), 2010 XIX International Conference on*, pages 1–6.

[56] Exxon Mobil (2015). 2015 energy outlook. www.iea.org.

[57] Fasolo, A., Alberti, L., and Bianchi, N. (2012). Performance comparison between switching-flux and IPM machine with rare earth and ferrite PMs. In *20th International Conference on Electrical Machines (ICEM)*, pages 731–737.

[58] Feng, Y., Yang, K., and Gu, C. (2009). Design and optimization of external-rotor torque motor. In *Electrical Machines and Systems, 2009. ICEMS 2009. International Conference on*, pages 1–4.

[59] Ferrari, M., Bianchi, N., and Fornasiero, E. (2013). Rotor saturation impact in synchronous reluctance and PM assisted reluctance motors. In *IEEE Energy Conversion Congress and Exposition (ECCE)*, pages 1235–1242.

[60] Ferrari, M., Bianchi, N., and Fornasiero, E. (2014). Analysis of rotor saturation in synchronousreluctance and pm assisted reluctance motors. *IEEE Transactions on Industry Applications*, PP(99):1–1.

[61] Ferrari, M., Morandin, M., and Bolognani, S. (2012). Mild hybrid motorcycles: Choice of the energy storage system. In *Energy Conference and Exhibition (ENERGYCON), 2012 IEEE International*, pages 997–1002.

[62] Fornasiero, E., Alberti, L., Bianchi, N., and Bolognani, S. (2013). Considerations on selecting fractional-slot nonoverlapped coil windings. *IEEE Transactions on Industry Applications*, 49(3):1316–1324.

[63] Fornasiero, E., Bianchi, N., and Bolognani, S. (2012). Slot harmonic impact on rotor losses in fractional-slot permanent-magnet machines. *IEEE Transactions on Industrial Electronics*, 59(6):2557–2564.

[64] Fratta, A., Guglielmi, P., Villata, F., and Vagati, A. (1998). Efficiency and cost-effectiveness of ac drives for electric vehicles improved by a novel, boost dc-dc conversion structure. In *Power Electronics in Transportation, 1998*, pages 11–19.

[65] Fratta, A., Troglia, G., Vagati, A., and Villata, F. (1993). Evaluation of torque ripple in high performance synchronous reluctance machines. In *Conference Record of the IEEE Industry Applications Society Annual Meeting*, pages 163–170 vol.1.

[66] Fukushige, T., Limsuwan, N., Kato, T., Akatsu, K., and Lorenz, R. (2013). Efficiency contours and loss minimization over a driving cycle of a variable-flux flux-intensifying interior permanent magnet machine. In *IEEE Energy Conversion Congress and Exposition (ECCE)*, pages 591–597.

[67] Gao, Y., Qu, R., Chen, Y., Li, J., and Xu, W. (2014). Review of off-line synchronous inductance measurement method for permanent magnet synchronous machines. In *IEEE Conference and Expo Transportation Electrification Asia-Pacific (ITEC Asia-Pacific)*, pages 1–6.

[68] Gao, Y., Qu, R., and Liu, Y. (2013). An improved ac standstill method for inductance measurement of interior permanent magnet synchronous motors. In *International Conference on Electrical Machines and Systems (ICEMS)*, pages 927–931.

[69] Gasparin, L., Cernigoj, A., Markic, S., and Fiser, R. (2009). Additional cogging torque components in permanent-magnet motors due to manufacturing imperfections. *IEEE Transactions on Magnetics*, 45(3):1210–1213.

[70] Gasparin, L. and Fiser, R. (2009). Intensity of the native and additional harmonic components in cogging torque due to design parameters of permanent-magnet motors. In *International Conference on Power Electronics and Drive Systems (PEDS)*, pages 1062–1067.

[71] Gerling, D., Dajaku, G., and Muhlbauer, K. (2010). Cost-effective electric traction drive with high efficiency at low-load operation. In *Emobility - Electrical Power Train*, pages 1–6.

[72] Gieras, J., Wang, C., and Lai, J. (2005). *Noise of Polyphase Electric Motors*. Electrical and Computer Engineering. CRC Press.

[73] Golub, G. H. and Van Loan, C. F. (1996). *Matrix Computations*. 3rd edition.

[74] Guo, Y., Zhu, J., Lu, H., Lin, Z., and Li, Y. (2012). Core loss calculation for soft magnetic composite electrical machines. *IEEE Transactions on Magnetics*, 48(11):3112–3115.

[75] Han, S. H., Jahns, T. M., Soong, W. L., Gueven, M. K., and Illindala, M. S. (2010). Torque ripple reduction in interior permanent magnet synchronous machines using stators with odd number of slots per pole pair. *IEEE Transactions on Energy Conversion*, 25(1):118–127.

[76] Hoang, E., Lecrivain, M., Hlioui, S., and Gabsi, M. (2011). Hybrid excitation synchronous permanent magnets synchronous machines optimally designed for hybrid and full electrical vehicle. In *IEEE 8th International Conference on Power Electronics and ECCE Asia (ICPE ECCE)*, pages 153–160.

[77] Intergovernmental Panel on Climate Change (IPCC) (2010). 2010 report. www.ipcc.ch.

[78] International, S. 2013 formula sae rules.

[79] International, S. About formula sae series.

[80] International Energy Agency (IEA) (2012). 2012 energy outlook. www.iea.org.

[81] International Energy Agency (IEA) (2013). Global ev outlook. www.iea.org.

[82] Ishii, S., hasegawa, Y., Nakamura, K., and Ichinokura, O. (2012). Characteristics of novel flux barrier type outer rotor ipm motor with rare-earth and ferrite magnets. In *Renewable Energy Research and Applications (ICRERA), 2012 International Conference on*, pages 1–4.

[83] Islam, R. and Husain, I. (2010). Analytical model for predicting noise and vibration in permanent-magnet synchronous motors. *IEEE Transactions on Industry Applications*, 46(6):2346–2354.

[84] Jahns, T. (1987). Flux-weakening regime operation of an interior permanent-magnet synchronous motor drive. *IEEE Transactions on Industry Applications*, IA-23(4):681–689.

[85] Jahns, T. M. and Soong, W. L. (1996). Pulsating torque minimization techniques for permanent magnet ac motor drives-a review. *IEEE Transactions on Industrial Electronics*, 43(2):321–330.

[86] Jannot, X., Vannier, J.-C., Saint-Michel, J., Gabsi, M., Marchand, C., and Sadarnac, D. (2009). An analytical model for interior permanent-magnet synchronous machine with circumferential magnetization design. In *8th International Symposium on Advanced Electromechanical Motion Systems Electric Drives Joint Symposium (ELECTROMOTION)*, pages 1–6.

[87] Junak, J. and Ombach, G. (2010). Performance optimisation of the brushless motor with ipm rotor for automotive applications. In *Electrical Machines (ICEM), 2010 XIX International Conference on*, pages 1–5.

[88] Kakihara, W., Takemoto, M., and Ogasawara, S. (2013). Rotor structure in 50 kw spoke-type interior permanent magnet synchronous motor with ferrite permanent magnets for automotive applications. In *IEEE Energy Conversion Congress and Exposition (ECCE)*, pages 606–613.

[89] Kang, G.-H., Hur, J., Sung, H.-G., and Hong, J.-P. (2003). Optimal design of spoke type BLDC motor considering irreversible demagnetization of permanent magnet. In *6th International Conference on Electrical Machines and Systems (ICEMS)*, volume 1, pages 234–237 vol.1.

[90] Kano, Y., Inoue, Y., and Sanada, M. (2013). Current specifications of vehicle motors. In *ECCE Asia Downunder (ECCE Asia), 2013 IEEE*, pages 136–140.

[91] Kazerooni, M. and Kar, N. C. (2011). Methods for determining the parameters and characteristics of pmsm. In *IEEE International Electric Machines Drives Conference (IEMDC)*, pages 955–960.

[92] Kim, D.-H., Park, I.-H., Lee, J.-H., and Kim, C.-E. (2003). Optimal shape design of iron core to reduce cogging torque of ipm motor. *IEEE Transactions on Magnetics*, 39(3):1456–1459.

[93] Kim, W. H., Kim, K. S., Kim, S. J., Kang, D. W., Go, S. C., Chun, Y. D., and Lee, J. (2009). Optimal pm design of pma-synrm for wide constant-power operation and torque ripple reduction. *IEEE Transactions on Magnetics*, 45(10):4660–4663.

[94] Kim, Y.-B., Kim, H.-J., Jung, K.-T., and Hong, J.-P. (2014). Influence of manufacturing tolerances on cogging torque of ipmsm for eps application. In *17th International Conference on Electrical Machines and Systems (ICEMS)*, pages 382–386.

[95] kuk Lee, B., Kang, G.-H., Hur, J., and You, D.-W. (2004). Design of spoke type BLDC motors with high power density for traction applications. In *39th IAS Annual Meeting - Conference Record of the 2004 IEEE Industry Applications Conference*, volume 2, pages 1068–1074 vol.2.

[96] Kurishige, M., Kifuku, T., Inoue, N., Zeniya, S., and Otagaki, S. (1999). A control ststrategy reduce steering torque for stationary vehicles equipped with eps.

[97] Kwon, S.-O., Kim, S.-I., Zhang, P., and Hong, J.-P. (2006). Performance comparison of ipmsm with distributed and concentrated windings. In *41st IAS Annual Meeting - Conference Record of the 2006 IEEE Industry Applications Conference*, volume 4, pages 1984–1988.

[98] Larminie, J. and Lowry, J. (2003). *Electric Vehicle Technology Explained*.

[99] Laskaris, K., Chaniotis, A., and Kladas, A. (2010). High performance traction motor design and construction for small passenger electric car. In *19th International Conference on Electrical Machines (ICEM)*, pages 1–6.

[100] Lazari, P., Wang, J., and Chen, L. (2014). A computationally efficient design technique for electric vehicle traction machines. *IEEE Transactions on Industry Applications*, PP(99):1–1.

[101] Lee, R., Brewer, E., and Schaffel, N. (1985). Processing of neodymium-iron-boron melt-spun ribbons to fully dense magnets. *IEEE Transactions on Magnetics*, 21(5):1958–1963.

[102] Li, T. and Slemon, G. (1988). Reduction of cogging torque in permanent magnet motors. *IEEE Transactions on Magnetics*, 24(6):2901–2903.

[103] Liew, G. S., Tang, C., Soong, W. L., Ertugrul, N., and Gehlert, D. B. (2011). Finite-element analysis and design of a radial-field brushless pm machine utilizing soft magnetic composites. In *2011 IEEE International Electric Machines Drives Conference (IEMDC)*, pages 930–935.

[104] Lovelace, E. C., Jahns, T. M., Keim, T. A., and Lang, J. H. (2004). Mechanical design considerations for conventionally laminated, high-speed, interior pm synchronous machine rotors. *IEEE Transactions on Industry Applications*, 40(3):806–812.

[105] Luomi, J., Zwyssig, C., Looser, A., and Kolar, J. W. (2009). Efficiency optimization of a 100-w 500000-r/min permanent-magnet machine including air-friction losses. *IEEE Transactions on Industry Applications*, 45(4):1368–1377.

[106] Mack, M. (1967). *Luftreibungsverluste bei elektrischen Maschinen kleiner Baugroesse*. PhD thesis, Universitaet Stuttgart, Germany.

[107] Magnussen, F. and Lendenmann, H. (2007). Parasitic effects in PM machines with concentrated windings. *IEEE Transactions on Industry Applications*, 43(5):1223–1232.

[108] Magnussen, F. and Sadarangani, C. (2003). Winding factors and joule losses of permanent magnet machines with concentrated windings. In *IEEE International Electric Machines and Drives Conference (IEMDC)*, volume 1, pages 333–339 vol.1.

[109] Magyari, K. and Radulescu, M. (2011). Particle-swarm-optimized design of small interior-permanent-magnet synchronous motors for light electric traction applications. In *International Aegean Conference on Electrical Machines and Power Electronics and 2011 Electromotion Joint Conference (ACEMP)*, pages 663–665.

[110] Malan, J. and Kamper, M. (2001). Performance of a hybrid electric vehicle using reluctance synchronous machine technology. *IEEE Transactions on Industry Applications*, 37(5):1319–1324.

[111] McFarland, J. D., Jahns, T. M., El-Refaie, A. M., and Reddy, P. B. (2014 (in publication)). Reduced rare-earth flux switching machines for traction applications. In *IEEE Energy Conversion Congress and Exposition (ECCE)*.

[112] Mecrow, B., Jack, A., Atkinson, D., Green, S., Atkinson, G., King, A., and Green, B. (2004). Design and testing of a four-phase fault-tolerant permanent-magnet machine for an engine fuel pump. *IEEE Transactions on Energy Conversion*, 19(4):671–678.

[113] Mellor, P. H., Chaaban, F. B., and Binns, K. J. (1991). Estimation of parameters and performance of rare-earth permanent-magnet motors avoiding measurement of load angle. *IEE Proceedings B - Electric Power Applications*, 138(6):322–330.

[114] Menga, P. (2010). Battery and hybrid electric vehicles. Seminar.

[115] Mi, C., Filippa, M., Liu, W., and Ma, R. (2004). Analytical method for predicting the air-gap flux of interior-type permanent-magnet machines. *IEEE Transactions on Magnetics*, 40(1):50–58.

[116] Miayazaki, H. (2008). Technical trends in steering systems. In *Proceedings of the 7th JFPS International Symposium on Fluid Power*.

[117] Miller, T. (1989). *Brushless Permanent-Magnet and Reluctance Motor Drives*. Oxford University Press.

[118] Mitchell, W. J., Borroni-Bird, C. E., and Burns, L. D. (2010). *Reinventing the Automobile: Personal Urban Mobility for the 21st Century*.

[119] Mohan, N., Undeland, T., and Robbins, W. (2003). *Power Electronics: Converters, Applications, and Design*. 3rd edition.

[Molycorp Magnequench] Molycorp Magnequench. Rare earth hot pressed permanent magnets application guide mq2.

[120] Morandin, M. (2013). *Electric Drives with Permanent Magnet Synchronous Machines Connected to Internal Combustion Engines*. PhD thesis, Ph.D. School in Electrical Engineering, University of Padova, 2013.

[121] Morandin, M. and Bolognani, S. (2016). Locked rotor characterization tests of IPM/REL synchronous machine for sensorless drives. In *IET Power Electronics, Machines and Drives (PEMD)*.

[122] Morandin, M., Bolognani, S., Petrella, R., Pevere, A., and Calligaro, S. (2012). Mild-hybrid traction system based on a bidirectional half-bridge interleaved converter and a three-level active npc inverter-fed pmsm. In *2012 Twenty-Seventh Annual IEEE Applied Power Electronics Conference and Exposition (APEC)*, pages 1644–1651.

[123] Morandin, M., Ferrari, M., and Bolognani, S. (2013). Design and performance of a power train for mild-hybrid motorcycle prototype. In *Electric Machines Drives Conference (IEMDC), 2013 IEEE International*, pages 1–8.

[124] Morandin, M., Ferrari, M., and Bolognani, S. (2014). Power-train design and performance of a hybrid motorcycle prototype. *IEEE Transactions on Industry Applications*, PP(99):1–1.

[125] Morrison, P., Binder, A., Funieru, B., and Sabirin, C. (2009). Drive train design for medium-sized zero emission electric vehicles. In *13th European Conference on Power Electronics and Applications (EPE)*, pages 1–10.

[126] Nakatsugawa, J., Notohara, Y., Li, D., and Iwaji, Y. (2008). Inductance measurement method for permanent magnet synchronous motors using ac with dc bias. In *18th International Conference on Electrical Machines (ICEM)*, pages 1–4.

[127] Ombach, G. (2008). Challanges and requirements for high volume production electric motors. Seminar.

[128] Ombach, G. and Junak, J. (2007). Two rotors designs comparison of permanent magnet brushless synchronous motor for an electric power steering application. In *Power Electronics and Applications, 2007 European Conference on*, pages 1–9.

[129] Ombach, G. and Junak, J. (2008). Comparative study of ipm motors with different air gap flux distribution. In *Power Electronics, Machines and Drives, 2008. PEMD 2008. 4th IET Conference on*, pages 301–304.

[130] Ombach, G. and Junak, J. (2010). Weight and efficiency optimization of auxiliary drives used in automobile. In *Electrical Machines (ICEM), 2010 XIX International Conference on*, pages 1–6.

[131] Omekanda, A. (2006). Robust torque and torque-per-inertia optimization of a switched reluctance motor using the Taguchi methods. *IEEE Transactions on Industry Applications*, 42(2):473–478.

[132] P. Pillay, M. M. (2001). Definitions of voltage unbalance.

[133] Paradkar, M. and Boecker, J. (2012). Design of a high performance ferrite magnet-assisted synchronous reluctance motor for an electric vehicle. In *38th Annual Conference on IEEE Industrial Electronics Society (IECON)*, pages 4099–4103.

[134] Park, J. M., Kim, S. I., Hong, J. P., and Lee, J. H. (2006). Rotor design on torque ripple reduction for a synchronous reluctance motor with concentrated winding using response surface methodology. *IEEE Transactions on Magnetics*, 42(10):3479–3481.

[135] Pellegrino, G., Vagati, A., Boazzo, B., and Guglielmi, P. (2012a). Comparison of induction and pm synchronous motor drives for ev application including design examples. *IEEE Transactions on Industry Applications*, 48(6):2322–2332.

[136] Pellegrino, G., Vagati, A., Guglielmi, P., and Boazzo, B. (2012b). Performance comparison between surface-mounted and interior PM motor drives for electric vehicle application. *IEEE Transactions on Industrial Electronics*, 59(2):803–811.

[137] Rahman, K. M., Fahimi, B., Suresh, G., Rajarathnam, A. V., and Ehsani, M. (2000). Advantages of switched reluctance motor applications to ev and hev: design and control issues. *IEEE Transactions on Industry Applications*, 36(1):111–121.

[138] Rahman, M., Kim, K.-T., and Hur, J. (2013). Design and analysis of a spoke type motor with segmented pushing permanent magnet for concentrating air-gap flux density. *IEEE Transactions on Magnetics*, 49(5):2397–2400.

[139] Rahman, M., Kim, K.-T., and Hur, J. (2014). Design and optimization of neodymium-free SPOKE-type motor with segmented wing-shaped PM. *IEEE Transactions on Magnetics*, 50(2):865–868.

[140] Reddy, P., EL-Refaie, A., Huh, K.-K., Tangudu, J., and Jahns, T. (2012a). Comparison of interior and surface PM machines equipped with fractional-slot concentrated windings for hybrid traction applications. *IEEE Transactions on Energy Conversion*, 27(3):593–602.

[141] Reddy, P., Jahns, T., McCleer, P., and Bohn, T. (2010). Design, analysis and fabrication of a high-performance fractional-slot concentrated winding surface PM machine. In *IEEE Energy Conversion Congress and Exposition (ECCE)*, pages 1074–1081.

[142] Reddy, P. B., Huh, K. K., and EL-Refaie, A. (2012b). Effect of stator shifting on harmonic cancellation and flux weakening performance of interior pm machines equipped with fractional-slot concentrated windings for hybrid traction applications. In *2012 IEEE Energy Conversion Congress and Exposition (ECCE)*, pages 525–533.

[143] Rodrigue, J., Comtols, C., and Slack, B. (2013). *The Geography of Transport Systems*. Taylor& Francis Ltd.

[144] Roger C. Dugan, Mark F. McGranaghan, S. S. H. W. B. (2012). *Electrical Power System Quality*. McGraw-Hill Education, 3rd edition.

[145] Saari, J. (1998). *Thermal analysis of high-speed induction machines*. PhD thesis, Helsinki University of Technology.

[146] Sanada, M., Hiramoto, K., Morimoto, S., and Takeda, Y. (2003). Torque ripple improvement for synchronous reluctance motor using asymmetric flux barrier arrangement. In *Conference Record of the 38th IAS Annual Meeting*, volume 1, pages 250–255 vol.1.

[147] Sashidhar, S. and Fernandes, B. (2014). A low-cost semi-modular dual-stack PM BLDC motor for a PV based bore-well submersible pump. In *International Conference on Electrical Machines (ICEM)*, pages 24–30.

[148] Schuisky, W. (1969). *Berechnung elektrischer Maschinen*. 1st edition.

[149] Seilmeier, M. and Piepenbreier, B. (2013). Identification of steady-state inductances of pmsm using polynomial representations of the flux surfaces. In *39th Annual Conference of the IEEE Industrial Electronics Society (IECON)*, pages 2899–2904.

[150] Shriwastava, R. G. and Diagavane, M. B. (2011). Electric power steering with permanent magnet synchronous motor drive used in automotive application. In *Electrical Energy Systems (ICEES), 2011 1st International Conference on*, pages 145–148.

[151] Sneyers, B., Novotny, D., and Lipo, T. (1985). Field weakening in buried permanent magnet ac motor drives. *IEEE Transactions on Industry Applications*, IA-21(2):398–407.

[152] Soong, W. (2014). PM synchronous machine modelling and design. In *IEEE Energy Conversion Congress and Exposition (ECCE)*. Tutorial.

[153] Soong, W. and Miller, T. J. E. (1994). Field-weakening performance of brushless synchronous ac motor drives. *IEE Proceedings Electric Power Applications*, 141(6):331–340.

[154] Soong, W., Reddy, P., El-Refaie, A., Jahns, T., and Ertugrul, N. (2007a). Surface pm machine parameter selection for wide field-weakening applications. In *42nd IAS Annual Meeting Conference Record of the IEEE Industry Applications Conference, 2007.*, pages 882–889.

[155] Soong, W. L. and Ertugrul, N. (2002). Field-weakening performance of interior permanent-magnet motors. *IEEE Transactions on Industry Applications*, 38(5):1251–1258.

[156] Soong, W. L., Han, S., and Jahns, T. M. (2007b). Design of interior pm machines for field-weakening applications. In *2007 International Conference on Electrical Machines and Systems (ICEMS)*, pages 654–664.

[157] Soong, W. L. and Miller, T. J. E. (1993). Theoretical limitations to the field-weakening performance of the five classes of brushless synchronous ac motor drive. In *Electrical Machines and Drives, 1993. Sixth International Conference on (Conf. Publ. No. 376)*, pages 127–132.

[158] Sorgdrager, A. and Grobler, A. (2013). Influence of magnet size and rotor topology on the air-gap flux density of a radial flux PMSM. In *Industrial Technology (ICIT), 2013 IEEE International Conference on*, pages 337–343.

[159] Staton, D. A., Miller, T. J. E., and Wood, S. E. (1993). Maximising the saliency ratio of the synchronous reluctance motor. *IEE Proceedings B - Electric Power Applications*, 140(4):249–259.

[160] Sulaiman, E., Kosaka, T., and Matsui, N. (2011). Design optimization of 12slot-10pole hybrid excitation flux switching synchronous machine with 0.4kg permanent magnet for hybrid electric vehicles. In *IEEE 8th International Conference on Power Electronics and ECCE Asia (ICPE ECCE)*, pages 1913–1920.

[161] Sun, T., Kwon, S.-O., Lee, S.-H., and Hong, J.-P. (2008). Investigation and comparison of inductance calculation methods in interior permanent magnet synchronous motors. In *Electrical Machines and Systems, 2008. ICEMS 2008. International Conference on*, pages 3131–3136.

[162] Tangudu, J. and Jahns, T. (2011). Comparison of interior PM machines with concentrated and distributed stator windings for traction applications. In *IEEE Vehicle Power and Propulsion Conference (VPPC)*, pages 1–8.

[163] Tangudu, J., Jahns, T., and Bohn, T. (2011). Design, analysis and loss minimization of a fractional-slot concentrated winding IPM machine for traction applications. In *IEEE Energy Conversion Congress and Exposition (ECCE)*, pages 2236–2243.

[164] Tangudu, J., Jahns, T., and El-Refaie, A. (2010). Unsaturated and saturated saliency trends in fractional-slot concentrated-winding interior permanent magnet machines. In *IEEE Energy Conversion Congress and Exposition (ECCE)*, pages 1082–1089.

[165] Toliyat, H. A. and B., K. G. (2004). *Handbook of Electric Motors*. 2nd edition.

[166] Trout, S. R. (1988). Use of helmholtz coils for magnetic measurements. *IEEE Transactions on Magnetics*, 24(4):2108–2111.

[United States Environmental Protection Agency (USEPA)] United States Environmental Protection Agency (USEPA). Dynamometer drive schedules.

[167] US Department of Energy (2011). Final report on assessment of motor technologies for traction drives of hybrid and electric vehicles.

[U.S. DRIVE] U.S. DRIVE. U.s. drive.

[168] Vagati, A. (2015). 50 anni di evoluzione delle macchine a campo rotante e dei relativi azionamenti. Seminar.

[169] Vagati, A., Boazzo, B., Guglielmi, P., and Pellegrino, G. (2012). Ferrite assisted synchronous reluctance machines: A general approach. In *20th International Conference on Electrical Machines (ICEM)*, pages 1315–1321.

[170] Vagati, A., Pastorelli, M., Francheschini, G., and Petrache, S. (1998). Design of low-torque-ripple synchronous reluctance motors. *IEEE Transactions on Industry Applications*, 34(4):758–765.

[171] Vagati, A., Pastorelli, M., Scapino, F., and Franceschini, G. (2000). Impact of cross saturation in synchronous reluctance motors of the transverse-laminated type. *IEEE Transactions on Industry Applications*, 36(4):1039–1046.

[172] Vervaeke, K. (2013). Automated magnetic inspection of permanent magnet rotors. In *Electric Drives Production Conference (EDPC), 2013 3rd International*, pages 1–4.

[173] Vido, L., Gabsi, M., Chabot, F., and Lecrivain, M. (2006). Interior permanent-magnet synchronous machine design by reluctants networks approach for hybrid vehicle applications. In *3rd IET International Conference on Power Electronics, Machines and Drives*, pages 541–545.

[voestalpine Stahl GmbH] voestalpine Stahl GmbH. Backlack technology.

[174] Walker, A., Galea, M., Gerada, C., Mebarki, A., and Gerada, D. (2015a). Design considerations for high performance traction machines: Aiming for the freedomcar 2020 targets. In *International Conference on Electrical Systems for Aircraft, Railway, Ship Propulsion and Road Vehicles (ESARS)*, pages 1–6.

[175] Walker, A., Galea, M., Gerada, C., Mebarki, A., and Gerada, D. (2015b). A topology selection consideration of electrical machines for traction applications: towards the freedomcar 2020 targets. In *Tenth International Conference on Ecological Vehicles and Renewable Energies (EVER)*, pages 1–10.

[176] Wang, F., Zhang, D., Xing, J., and Xu, Y. (2009). Study on air friction loss of high speed pm machine. In *IEEE International Conference on Industrial Technology (ICIT)*, pages 1–4.

[177] Wang, J., p. Xia, Z., a. Long, S., and Howe, D. (2006). Radial force density and vibration characteristics of modular permanent magnet brushless ac machine. *IEE Proceedings - Electric Power Applications*, 153(6):793–801.

[178] Wang, J., Wang, F., and Kong, X. (2008). Losses and thermal analysis of high speed pm machine. In *Joint International Conference on Power System Technology and IEEE Power India Conference (POWERCON)*, pages 1–5.

[179] Wang, K., Zhu, Z. Q., Ombach, G., and Chlebosz, W. (2012). Optimal rotor shape with third harmonic for maximizing torque and minimizing torque ripple in ipm motors. In *Electrical Machines (ICEM), 2012 XXth International Conference on*, pages 397–403.

[180] Wong, K. P. (2009). *Electrical Engineering*, volume 3.

[181] Yamazaki, K. and Fukushima, Y. (2011). Effect of eddy-current loss reduction by magnet segmentation in synchronous motors with concentrated windings. *IEEE Transactions on Industry Applications*, 47(2):779–788.

[182] Yuan, X. and Wang, J. (2012). Torque distribution strategy for a front- and rear-wheel-driven electric vehicle. *IEEE Transactions on Vehicular Technology*, 61(8):3365–3374.

[183] Zhang, D., Wang, F., and Kong, X. (2008). Air friction loss calculation of high speed permanent magnet machines. In *International Conference on Electrical Machines and Systems (ICEMS)*, pages 320–323.

[184] Zhang, P., Sizov, G., Ionel, D., and Demerdash, N. (2015a). Establishing the relative merits of interior and spoke-type permanent magnet machines with ferrite or ndfeb through systematic design optimization. *IEEE Transactions on Industry Applications*, PP(99):1–1.

[185] Zhang, S., Carraro, E., Bianchi, N., Wang, K., and Vervaeke, K. (2015b). Industrial-scale motor cogging torque control for a high-volume motor manufacturing. In *IEEE International Electric Machines Drives Conference (IEMDC)*, pages 1235–1241.

[186] Zhang, S., Xu, J., Junak, J., Fiederling, D., Sawczuk, G., Koch, M., Schalja, A., Podack, M., and Baumgartner, J. (2012). Permanent magnet technology for electric motors in automotive applications. In *2nd International Electric Drives Production Conference (EDPC)*, pages 1–11.

[187] Zhao, C., Haihong, Qin, H., and Yan, Y. (2005a). Analysis of the pole numbers on flux and power density of ipm synchronous machine. In *International Conference on Power Electronics and Drives Systems (PEDS)*, volume 2, pages 1402–1407.

[188] Zhao, C., Li, S., and Yan, Y. (2005b). Influence factor analysis of pmsm air gap flux density. In *Proceedings of the Eighth International Conference on Electrical Machines and Systems (ICEMS)*, volume 1, pages 334–339 Vol. 1.

[189] Zhu, Z. Q. and Howe, D. (2007). Electrical machines and drives for electric, hybrid, and fuel cell vehicles. *Proceedings of the IEEE*, 95(4):746–765.